PROCEEDINGS OF THE FIRST INTERNET SYMPOSIUM ON NUCLEAR DATA

April 8-June 15, 1996, JAERI, Tokai, Ibaraki, Japan

March 1997

(Eds.) Tokio FUKAHORI, Osamu IWAMOTO
and Tsuneo NAKAGAWA

日 本 原 子 力 研 究 所
Japan Atomic Energy Research Institute

Proceedings of the First Internet Symposium on Nuclear Data
April 8 - June 15, 1996, JAERI, Tokai, Ibaraki, Japan

(Eds.) Tokio FUKAHORI, Osamu IWAMOTO and Tsuneo NAKAGAWA

Japanese Nuclear Data Committee
Tokai Research Establishment
Japan Atomic Energy Research Institute
Tokai-mura, Naka-gun, Ibaraki-ken

The First Internet Symposium on Nuclear Data (ISND-1) was held on the WWW home page of Nuclear Data Center at Tokai Research Establishment, Japan Atomic Energy Research Institute (JAERI) , from April 8 to June 15, 1996. This symposium was organized by Japanese Nuclear Data Committee and Nuclear Data Center, JAERI and was the first trial to use "Internet" for the symposium in a nuclear data field. In ISND-1, presented were 25 papers on various topics of nuclear data. Those presented papers are compiled in this proceedings as well as brief description about management of ISND-1.

第1回核データインターネットシンポジウム報文集
1996年4月8日〜6月15日，日本原子力研究所，東海村

日本原子力研究所東海研究所
シグマ研究委員会
（編）深堀 智生・岩本 修・中川 庸雄

　第1回核データインターネットシンポジウム（ISND-1）が，1996年4月8日〜6月15日の期間日本原子力研究所東海研究所核データセンターWWWホームページ上で開催された。このシンポジウムは，日本原子力研究所のシグマ研究委員会と核データセンターが主催して開いたものであり，核データの分野では初めてのインターネットを使ったシンポジウムの試みであった。本シンポジウムでは，核データに関する様々なトピックスの25件の報告があった。本報文集は，それらの発表論文及びシンポジウム運営の概略をまとめたものである。

東海研究所：〒319-11　茨城県那珂郡東海村白方白根2－4

Contents

目　　　次

目　　　次

1. Introduction

The First Internet Symposium on Nuclear Data (ISND-1) was held on the WWW home page of Nuclear Data Center at Tokai Research Establishment, Japan Atomic Energy Research Institute (JAERI), from April 8 to June 15, 1996. This symposium was organized by Japanese Nuclear Data Committee and Nuclear Data Center, JAERI and was the first trial to use "Internet" for the symposium in a nuclear data field. In ISND-1, presented were 25 papers on various topics of nuclear data on the several WWW sites. Discussions were done through e-mail-base communication. The latest information ISND-1 at the periods was located at the following URL (Uniform Resource Locator).

> http://cracker.tokai.jaeri.go.jp/ISND/index.html (English)
> http://cracker.tokai.jaeri.go.jp/ISND/index_J.html (Japanese)

Since this is the first trial to hold a symposium in nuclear data field by using the Internet, the management of ISND-1 was carried out basicly with discussion at exective committee, explaned in the chapter 2. The information on the WWW home page before strating ISND-1 was modified step by step based on the discussion. The secretariat was set at e-mail address of "ISND@cracker.tokai.jaeri.go.jp". The topics for this symposium were selected as

- Nuclear Data Measurement,
- Nuclear Data Evaluation ,
- Theory and Methodology for Nuclear Data Evaluation,
- Computer Program for Evaluation, Compilation and Processing of Nuclear Data,
- Integral Test of Nuclear Data,
- Application of Nuclear Data, and
- Status of Evaluated Nuclear Data File.

2. Brief Description of ISND-1 Management

The Exective Committee (EC) made "Paper Selection Group (PSG)" and "Technical Support Group (TSG)" to discuss paper acceptance and to support producing HTML (Hyper Text Make-up Language) pages of particpant papers, respectively. The members of EC, which also played a role of PSG, and TSG are listed below.

Exective Committee (* Secretariat)

Mamoru BABA (Tohoku University)

Tokio FUKAHORI* (JAERI)

Katsumi HAYASHI (Hitachi Engineering Co. Ltd.)

Masayuki IGASHIRA (Tokyo Institute of Technology)

Osamu IWAMOTO* (JAERI)

Yasuyuki KIKUCHI (JAERI)

Katsuhei KOBAYASHI (Kyoto University)

Norihiko KOORI (Tokushima University)

Tsuneo NAKAGAWA* (JAERI)

Kazuhiro OYAMATSU (Nagoya University)

Takahiro TACHIBANA (Waseda University)

Akito TAKAHASHI (Osaka University)

Yukinobu WATANABE (Kyushu University)

Naoki YAMANO (Sumitomo Atomic Energy Industries, Ltd.)

Technical Support Group

Ken-ya SUYAMA (JAERI)

Soji SHIMAKAWA (JAERI)

Tokio FUKAHORI (JAERI)

Tsuneo NAKAGAWA (JAERI)

Osamu IWAMOTO (JAERI)

Discussions of EC were held by using so to say "EMROOM1", which is the first electric meeting room and constructed at the e-mail address of emroom1@cracker.tokai.jaeri.go.jp by mailing-list system. The one of decided rules for discussion using maling list system was that "no reply" means "yes" and WWW home page of internal information for EC was produced and limited to be accessed only for the members with password. For the paper selection, submitted abstract

was forwarded to EMROOM1 and accepted if it has no objection within 2 working days by the members.

By using WWW, information such as texts (sentenses, numerical data, etc.) and glaphics (plots, photographes, etc) is connected through hyper-link and can be obtained from internet terminals of all over the world. The basic concept of the method for ISND-1 was that system combined WWW and e-mail was used to present and discuss the paper. The actual samples are shown in Appendix. In principle, following procedure was used.

- The author made the poster in HTML and opened it on the Internet as a WWW home page. TSG can help to produce the home page for the authors not familiar with HTML. It was just linked from the home page of Nuclear Data Center at JAERI. The author's pages were allowed to be modified during the conference period only for the quality-up caused by discussion. To get the information how to create the author's home page, the special home page for authors was produced and the home page of the other author can be seen only by author group even before the beginning of the conference.

- Participants could see the home page by their browser program like MOSAIC, Netscape, Internet Exprolar, etc. and send their questions and comments to the author by e-mail. For attend the e-mail-base discussion, registration was necessary. Registered participants can join the discussion by using the system like mailing list system. However the system was not perfectly same as mailing list system, because all the questions would be delivered to all registrated perticipants, if the same system was used. Hence then new shell script was written to manege this registration and discussion.

- This e-mail was not only reached the author but also uploaded to WWW home page to be seen by the others, simultaniously. Reply from the author was treated as same way.

- The manuscripts of proceedings was prepared basicly from the home page by computational way such as TeX, LaTeX, Postscript and published by JAERI-Conf Report Seriese and on the WWW Home page.

The merits of this method were following.

- Conference fee and travel expence were not needed.

- Many people can see the conference, because the conference can be held for long period.

- This was a trial to examine the Internet possibility.
- The Internet was made widly known for scientists in the nuclear data field.

Before summary, the statistics of access to the papers is summarized in Table 1. In the table, the column of "Paper" was counted by a free software named "Web Counter". The symbol "-" means the paper did not have statistics, since it did not include this system and was not located at the server of Nuclear Data Center. The other columns were counted from "log file" at the server of Nuclear Data Center. Though the numbers of accesses to "Abstract", "Paper" and "Discussion" were 0.5 per day, those to "Question" and "Reply" were few. This means papers were seen but questions and comments were not sent. Though active discussion was expected, however it was not at this moment, since

- It was not easy to read paper on the computer display, and it took time to move next page of WWW caused by low speed connection.
- Though 30 registrations to attend discussions were done, participants might not like discussion through e-mail so much.

From the results of inquiry about ISND-1 after finished, the ISND-1 impression was following.

- The reason not to see were 1) not enough time and 2) low speed connection. So, ISND-1 itself was acceptable at least to Japanese scientist related to nuclear data field.
- Many people thought the face-to-face discussion was more important.

The less discussion was one of the consideration points. However much more people saw the papers than the ordinary symposium. ISND-1 was the first trial of symposium on nuclear data through the Internet. Only from these two points, it can be concluded that ISND-1 gave a strong impact to many fields.

The editors wish to thank paper authors, members of exective committee and technical support group, and participants for their kind and warm supports.

Table 1 Accesses to the Papers Participating to ISND-1

Paper No.	Abstract	Paper	Discussion	Question	Reply
p001	29	43	67	0	0
p002	30	68	59	0	0
p003	35	–	46	0	0
p004	19	17	36	0	0
p005	34	–	82	0	0
p006	43	29	73	1	0
p007	25	65	57	0	0
p008	20	42	43	0	0
p009	18	45	38	0	0
p010	29	48	41	0	0
p011	41	–	32	0	0
p012	18	34	75	0	0
p013	26	24	70	0	0
p014	24	65	55	0	0
p015	32	54	70	0	0
p016	27	54	49	0	0
p017	19	–	50	0	0
p018	22	–	37	0	0
p019	22	–	48	0	0
p020	31	19	30	0	0
p021	27	53	68	0	0
p022	25	47	55	0	0
p023	21	23	45	0	0
p024	28	66	129	1	1
p025	24	–	33	0	0
total	675	796	1388	2	1

Number of People Registrating to Discussion: 30

3. Papers Presented in ISND-1

The First Internet Symposium on Nuclear Data: Paper No. 001

3.1 Analysis of proton-induced fragment production cross sections by the Quantum Molecular Dynamics plus Statistical Decay Model

Satoshi Chiba[1,2], Osamu Iwamoto[2], Tokio Fukahori[1,2], Koji Niita[1,3],
Toshiki Maruyama[1], Tomoyuki Maruyama[1] and Akira Iwamoto[1]

[1]*Advanced Science Research Center, Japan Atomic Energy Research Institute,*
Tokai-mura, Naka-gun, Ibaraki-ken 319-11, Japan
[2]*Nuclear Data Center, Japan Atomic Energy Research Institute,*
Tokai-mura, Naka-gun, Ibaraki-ken 319-11, Japan
[3]*Research Organization for Information Science and Technology*
Tokai-mura, Naka-gun, Ibaraki-ken 319-11, Japan

Abstract

The production cross sections of various fragments from proton-induced reactions on ^{56}Fe and ^{27}Al have been analyzed by the Quantum Molecular Dynamics (QMD) plus Statistical Decay Model (SDM). It was found that the mass and charge distributions calculated with and without the statistical decay have very different shapes. These results also depend strongly on the impact parameter, showing an importance of the dynamical treatment as realized by the QMD approach. The calculated results were compared with experimental data in the energy region from 50 MeV to 5 GeV. The QMD+SDM calculation could reproduce the production cross sections of the light clusters and intermediate-mass to heavy fragments in a good accuracy. The production cross section of ^{7}Be was, however, underpredicted by approximately 2 orders of magnitude, showing the necessity of another reaction mechanism not taken into account in the present model.

1 Introduction

Recently we have developed a framework of the quantum molecular dynamics (QMD) plus statistical decay model (SDM) that takes account of the relativistic kinematics and relativistic correction for interaction term, Lorentz boost of the initial and final states, realistic momentum distribution in the ground state, and comprehensive nucleon-nucleon (N-N) collision term /1/. It was shown /1/ that this framework could reproduce the measured double-differential (p,xn), (p,xp') and (p,x π) reactions from 100 MeV to 3 GeV in a systematic way. In the subsequent papers /2, 3/, we have given detailed analyses of the pre-equilibrium (p,xp') and (p,xn) reactions in terms of the QMD in the energy region of 100 to 200 MeV. It was demonstrated that the Fermi motion including the high-momentum component, surface refraction, multi-step effect and the multiple pre-equilibrium emission were the key issues in understanding the angular distributions of neutrons and protons emitted during the pre-equilibrium process. In these analyses a single set of parameters was selected, and no adjustment was attempted.

The success obtained in the previous studies has shown the ability of the QMD+SDM approach for the study of the nucleon-induced nuclear reactions. However, the previous

analyses have been concentrated on the inclusive particle spectra, and a fine selection of the final reaction products was not performed. It is therefore the purpose of this work to carry out an analysis of proton-induced reactions for the production of specific final states, i.e., fragments, with the same formulae and the same set of parameters as the previous works/1, 2, 3/ to investigate further the validity of the QMD+SDM approach. Such fragmentation phenomena themselves have been a matter of long and intensive studies to extract the basic reaction mechanisms of nucleon induced reactions /4, 5, 6, 7, 8, 9/, e.g., multifragmentation, liquid-gas phase transition, sideward peaking of fragment angular distribution, properties of nuclei at high temperature, etc. Reliable estimations of fragment production are also important in many application fields /10, 11, 12, 13, 14, 15, 16/.

In this work,the fragment production cross sections from p + ^{56}Fe and p + ^{27}Al reactions were calculated. These targets were selected because 1) they are mono-isotopic or nearly mono-isotopic in the natural elements, therefore the data are abundant, 2) they are popular elements among the structural materials with high importance from the practical point of view, and 3) effects of the fission and multifragmentation become significant for heavier elements, where an analysis is too complicated. Moreover, the computation time, proportional to the square of the mass number, is kept manageable for these target materials. Special emapasis was placed for the proton energy of 1.5 GeV because this energy attracts special attention as a possible candidate energy of application of a high-intensity proton accelerator for researches on transmutation of radioactive wastes and basic sciences/17/. The maximum energy was chosen to be 5 GeV: above this energy many nucleon-nucleon inelastic channles, which are not considered in our model, are open.

In the next section, a brief explanation of the QMD plus SDM approach is given. The comparison of the calculation with the experimental data and discussions on the reaction mechanisms are given in section 3. Summary of this work is given in section 4.

2 Essence of the QMD plus SDM Model

The details of the QMD and SDM calculations are given in Ref. /1/, so only the basic principles of them will be repeated here. In the QMD calculation, each nucleon is expressed with a Gaussian wave packet in both the coordinate and momentum spaces in the following way:

$$f_i(\mathbf{r}, \mathbf{p}) = 8 \cdot \exp\left[-\frac{(\mathbf{r} - \mathbf{R}_i)^2}{4L} - \frac{2L(\mathbf{p} - \mathbf{P}_i)^2}{\hbar^2} \right] \tag{1}$$

where L is a parameter which represents the spacial spread of a wave packet, $\mathbf{R}_i$ and $\mathbf{P}_i$ corresponding to the centers of a wave packet in the coordinate and momentum spaces, respectively. The total one-body phase-space distribution function is taken to be simply a sum of these single-particle wave packets. Initially, we distribute the $\mathbf{R}_i$ and $\mathbf{P}_i$ to produce a stable target ground state with realistic density and momentum distributions. The time evolution of $\mathbf{R}_i$ and $\mathbf{P}_i$ is determined based on the Newtonian equation and the N-N collision term, latter satisfying the Pauli exclusion principle. A Skyrme-type interaction parameterized in Ref. /1/ is used as the effective interaction. In addition, the symmetry and the Coulomb forces are included.

The QMD calculation is carried out up to a time scale 100 (fm/c), which is referred to as the switching time, t_{sw}. The position and momentum of each nucleon is then used to calculate the distribution of mass and atomic numbers, kinetic energy and direction of motion of the remaining fragments (referred to as "prefragments") as well as those of the emitted nucleons and π-mesons. In determining the mass and atomic numbers of the prefragments, the phase-space minimum-distance-chain method/18/ is employed.

The prefragments thus identified are then Lorentz boosted into their rest frames to evaluate their excitation energies. When the prefragment is in the excited state, the statistical decay via n, p, d, t, ^3He and α emissions is considered based on the Weisskopf-Ewing approximation, the emission probability of particle x being given as

$$P_x = (2J_x + 1)m_x \epsilon \sigma_x(\epsilon)\rho(E)d\epsilon \tag{2}$$

where J_x, m_x and ϵ are the spin, mass and kinetic energy of the emitted particle, while $\sigma_x(\epsilon)$ and $\rho(E)$ denote the inverse cross section and the level density of the residual nucleus at the excitation energy E, respectively. The level density has been assumed to be proportional to $\exp(2\sqrt{aE})$ with $a = A/8$ MeV^{-1}. The inverse cross section is taken to be of the form $\sigma_x(\epsilon) = (1 - U_x/\epsilon)\pi R^2$ if $\epsilon > U_x$ and $\sigma_x(\epsilon) = 0$ otherwise, where R denotes the absorption radius and U_x is the empirical Coulomb barrier for particle x/19/.

The separation of the QMD and SDM calculations as performed in this approach can give the individual production cross sections of various residues before and after the statistical decay, the former being called as the prefragment, the latter as the fragment. This possibility gives information on the relation of the dynamical and statistical processes as a function of projectile energy and impact parameter. On the contrary, this hybrid approach introduces an ambiguity because the switching time t_{sw} is an arbitrary parameter. As described above, we have selected t_{sw} to be 100 (fm/c), because this value was enough to obtain stable neutron spectra from the (p,xn) reaction against a change of t_{sw} as shown in Ref./1/. However, it does not necessarily mean that this value is also appropriate to obtain stable values for more exclusive observables as the fragment production cross sections. Therefore, we have carried out calculations by changing the value of t_{sw}, and investigated how various fragment production cross sections would vary as a function of this parameter. The result is shown in Fig. 1 for the production of ^{4}He, ^{24}Na, ^{38}Ar and ^{54}Mn for 1.5-GeV p + ^{56}Fe reaction. This is a result of the QMD plus SDM calculation. This figure demonstrates that the cross section values given by the present approach are very robust against the change of the switching time t_{sw}, therefore defines the cross sections in a unique way at around $t_{sw} = 100$ (fm/c).

Calculations with event number of 50,000 for each combination of target and proton energy have been performed to get enough statistical accuracy. The computation time was approximately 24 hours for p + ^{56}Fe reaction on HP9000/735 work station.

3 Results and Discussion

Calculated cross sections for the production of various prefragments and fragments are shown for 1.5-GeV p + ^{56}Fe reaction in Fig. 2. Here the upper figure shows the production cross sections calculated only by the QMD, while the lower one is obtained including the statistical decay. In this and the subsequent figures, the cross sections before and
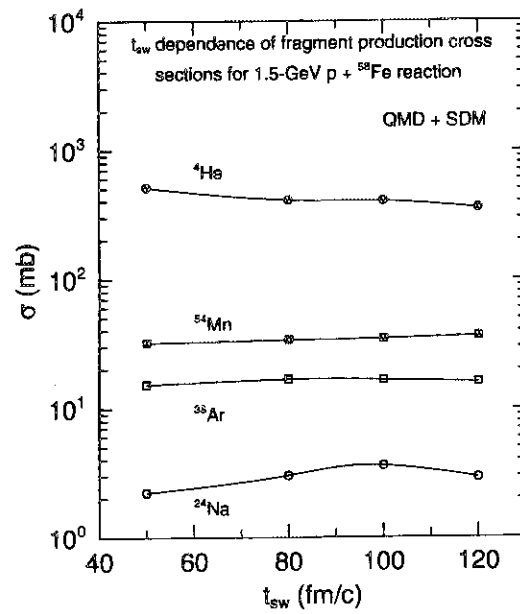
Figure 1: Dependence of the production cross sections of ^{4}He, ^{24}Na, ^{38}Ar and ^{54}Mn on the switching time, t_{sw}, from the QMD to SDM calculation for 1.5-GeV p + ^{56}Fe reaction.
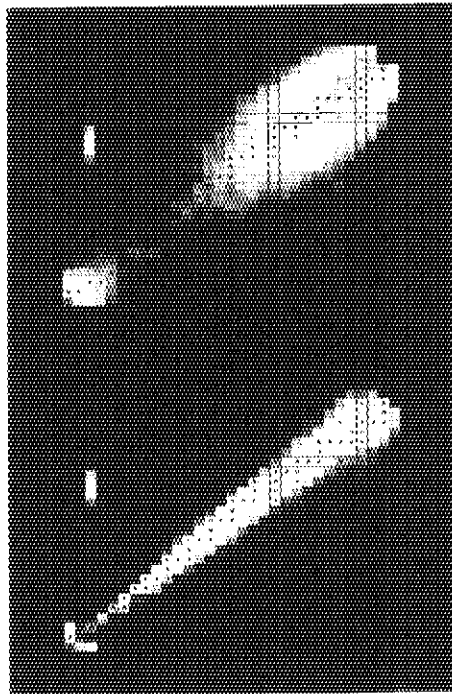
Figure 2: Distribution of various fragments in N-Z plane from the QMD alone (top) and QMD+SDM(bottom) calculations for 1.5-GeV proton + ^{56}Fe reaction. The small squares indicate positions of stable isotopes, while vertical and horizontal lines at N,Z=20 and 28 denote the magic numbers.
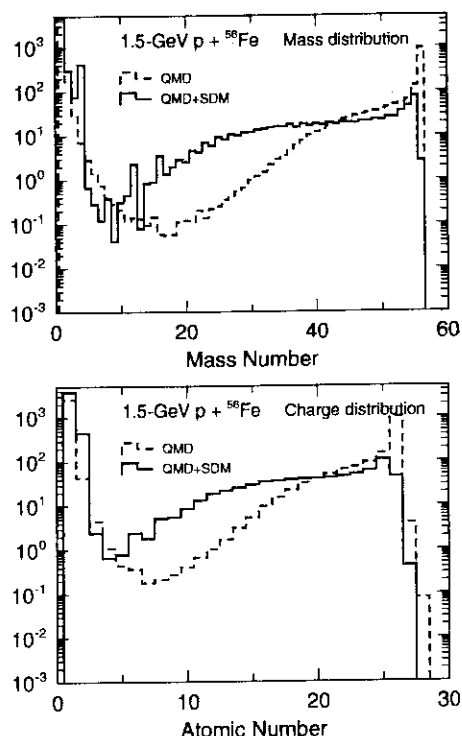
Figure 3: Calculated mass (top) and charge (bottom) distributions of fragments for 1.5-GeV p + ^{56}Fe reaction. The broken histograms show the results for QMD calculation only, while the solid ones corresponding to QMD+SDM results.

after the statistical decay process is denoted as the "QMD" and "QMD+SDM", respectively. The small squares indicate the positions of stable nuclei, while the lines at $N, Z = 20$ and 28 show the locations of major magic numbers. The upper part of Fig. 2 shows that the prefragments are produced primarily in mass $A = 1 \sim 10$ and $A_T/2 \leq A \leq A_T$ regions, with A_T as the target mass. In the cascade model approach/20, 21/, the light mass fragments ($A \leq 10$) are produced only as a result of the statistical decay or as a spallation residue, whereas the QMD describes the dynamical emission of such light mass fragments as shown in Fig. 2. This is a clear advantage of the QMD approach. The intermediate-mass-fragment (IMF) corresponding to mass 10 to $A_T/2$ are very rare (about an order of $10 \sim 100 \, \mu$ barn) in the QMD result alone. In the target region, the prefragments are distributed in a broad area of the N-Z plane. This distribution, then, is changed via the statistical decay to the bottom figure which is more localized along the stability line. The IMF region is primarily filled by the statistical decay of heavier prefragments, and the final isotopic distribution becomes significantly flattened in the direction of stability line as a result of the statistical decay. At the same time, yield of the light mass fragment becomes much larger, in particular of α particle. Figure 2 demonstrates clearly the importance of both the dynamical and statistical processes which are included in the QMD+SDM approach.

Figure 3 shows the total mass (top figure) and charge (bottom figure) distributions from the QMD and QMD+SDM calculations for the same projectile/target combination. This figure again confirms that the QMD calculation predicts dynamical production of
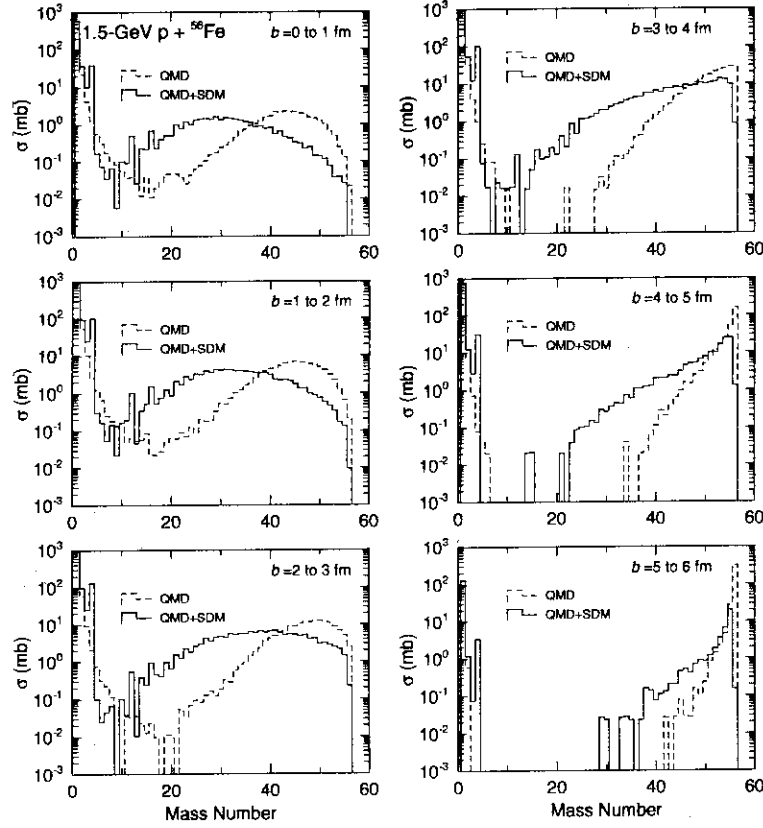
Figure 4: Calculated mass distributions for 1.5-GeV p + ^{56}Fe reaction with different impact parameters.

the light ($A \leq \sim 10$) and target mass/charge regions. The statistical decay then makes the distributions much smoother and flatter. The IMF is produced primarily by the statistical decay.

In Fig. 4, the mass distributions obtained for 1.5-GeV p + ^{56}Fe reaction with different impact parameter events are shown. In this figure the impact parameter (denoted as b) varies from 0 to 1 fm in the left-top figure, then the impact parameter range is increased in steps of 1 fm toward the right-bottom one. The total mass-yield distributions given in the upper part of Fig. 3 were obtained by integrating the contributions from the whole impact parameter range given in Fig. 4. Figure 4 indicates that the mass distribution changes significantly as a function of the impact parameter. For the events having smaller impact parameters, the QMD distribution has a broad maximum centered around a mass of 45. Then this distribution becomes much broadened by the statistical decay, shifting the peak to around mass $\sim A_T/2$. As the impact parameter increases, the distribution is shifted toward higher masses; at the peripheral events ($b \geq 4$ fm) the QMD distribution has a sharp peak at the target mass. In this impact parameter region, the incident proton interacts with a nucleon by grazing the target near the surface. Therefore the chance that one of these 2 nucleons is emitted from the target without further collisions is very high due to a smaller nucleon density than in the central region. For such a reaction, which may be referred to as "1-step" reaction, the cross section is determined by the magnitude of the basic nucleon-nucleon cross section. Furthermore, Fig. 4 shows
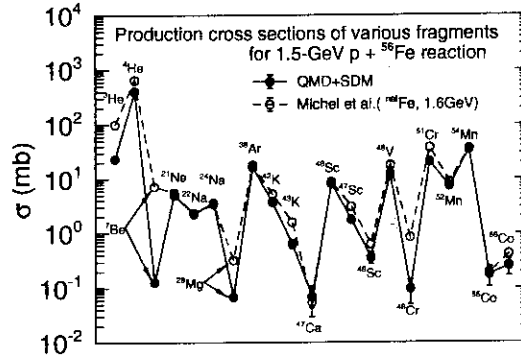
Figure 5: Production cross sections of various fragments for 1.5-GeV proton + ^{56}Fe reaction. The full circles connected by a solid line denote the result of QMD+SDM calculation, while the open circles connected by a broken line were obtained experimentally by Michel et al. measured at 1.6 GeV for ^{nat}Fe

that the rather smooth and monotonic distributions seen in Figs. 2 and 3 are the results of superpositions of contributions from different impact parameters which have quite different shapes. Therefore, the dynamical approach as realized by QMD is essential in predicting such fragment distributions.

In Fig. 5 shown are the production cross sections of various fragments for 1.5-GeV p + ^{56}Fe reaction. The data were measured by Michel et al/16/ at 1.6 GeV for ^{nat}Fe. It is clearly concluded that the QMD+SDM approach reproduces the fragment production cross sections in the whole mass region well, including the light clusters such as α and IMF ($A \sim 20$ to 30) except for ^{7}Be where the present result underestimates the data by approximately 2 orders of magnitude.

A similar comparison was made for 2.6-GeV p + ^{56}Fe reaction in Fig. 6. In this case, again, the overall agreement of the theoretical results with the data of Michel et al/16/ is encouraging. However, the production cross sections of ^{7}Be is underpredicted more than one order of magnitude as was the case at 1.5 GeV. Furthermore, the theory could not predict any production of ^{10}Be. Agreement at the IMF region is somewhat worse than the 1.5-GeV result, in particular shape of the production cross sections of Ne isotopes is not reproduced correctly. These problems, together with the problem of ^{7}Be production at 1.5 GeV, may by accounted for by the multifragmentation mechanism not included in the present model/16/. An explanation of the origin of the disagreement for ^{55}Co and ^{56}Co production cross sections will be given later.

The calculated isotope production cross sections from proton induced reaction on ^{56}Fe and ^{27}Al are compared with experimental data in Figs. 7 and 8 for various residual nuclei as a function of incident energy in the energy region of 50 MeV to 5 GeV. We did not distinguish the experimental data for ^{56}Fe and ^{nat}Fe in order to enhance the experimental database. In these figures, the results of the QMD calculation is given by the broken curves, the QMD+SDM result by the full curves, the experimental data by the open circles with error bars. The error bars in the QMD and QMD+SDM calculations indicate the statistical uncertainty. The experimental data have been retrieved from the CHESTOR (Charged Particle Experimental Data Storage and Retrieval System) database at Nuclear Data Center of JAERI /22/ supplemented by available literatures
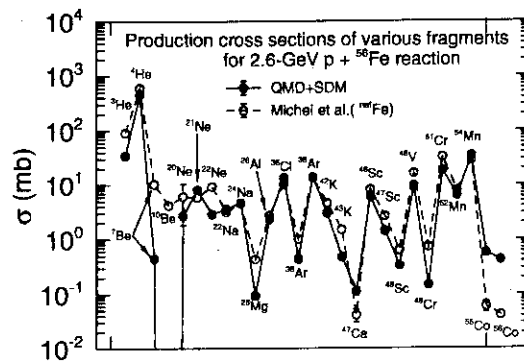
Figure 6: Production cross sections of various fragments for 2.6-GeV proton + ^{56}Fe reaction. The full circles connected by a solid line denote the result of QMD+SDM calculation, while the open circles connected by a broken line were obtained experimentally by Michel et al.

including the recent data reported by Michel et al/16/.

The ^{56}Fe(p,x) cross sections shown in Fig. 7 again reveals the general accuracy of the QMD+SDM approach for the a-priori estimation of production cross sections of target-like fragment for a very wide incident energy range; the QMD+SDM calculation reproduces the experimental data within a factor of 2. In most cases, shapes of the prefragment production cross sections (the broken curves) are quite different from those of the final cross sections (solid curves) except for such a simple reaction as the (p,n) case where the prefragment production cross section is always larger than the final cross section by a constant ratio. The difference between the "QMD" and "QMD+SDM" calculations shows that the production of these fragments is a result of subtle balance between the dynamical formation and the statistical decay processes. The dynamical process acts as a "source" of "hot" prefragments at the target mass region, followed by the production of nuclides with smaller masses due to particle evaporation. It is intersting to note that the calculated ^{56}Fe(p,n)^{56}Co reaction cross section increases at energies above several hundred MeV. The same energy dependence was obtained for ^{56}Fe(p,2n)^{55}Co and ^{59}Co(p,n)^{59}Ni reactions. It is natural to assume that such reactions leading to the formation of prefragments which are very close to the target take place mostly at the peripheral region (as Fig. 4 clearly demonstrates). For these events the number of collisions in the compound system may be only 1 or 2. Then, the cross section for such events will be roughly proportional to the basic nucleon-nucleon cross sections adopted in the calculation. Indeed, the p-n cross section used in our calculation increases at the energy above 400 MeV due to contributions of the inelastic channels (see Fig. 1 of Ref. /1/). On the contrary, the recent data measured by Michel et al./16/ shows a steep drop above 1 GeV. However, the ^{nat}Fe(p,xn)^{57}Co and ^{nat}Fe(p,xn)^{58}Co reactions reported by them have a clear increase above several hundred MeV, although they attribute this energy dependence to the influence of secondary reactions. We hope that further experimental investigation of such reactions would be carried out to obtain information on this subject because it could be a direct measure of the N-N inelastic collision in nuclei.

Figure 8 exhibits a result of the similar analysis for ^{27}Al target. The cross sections for
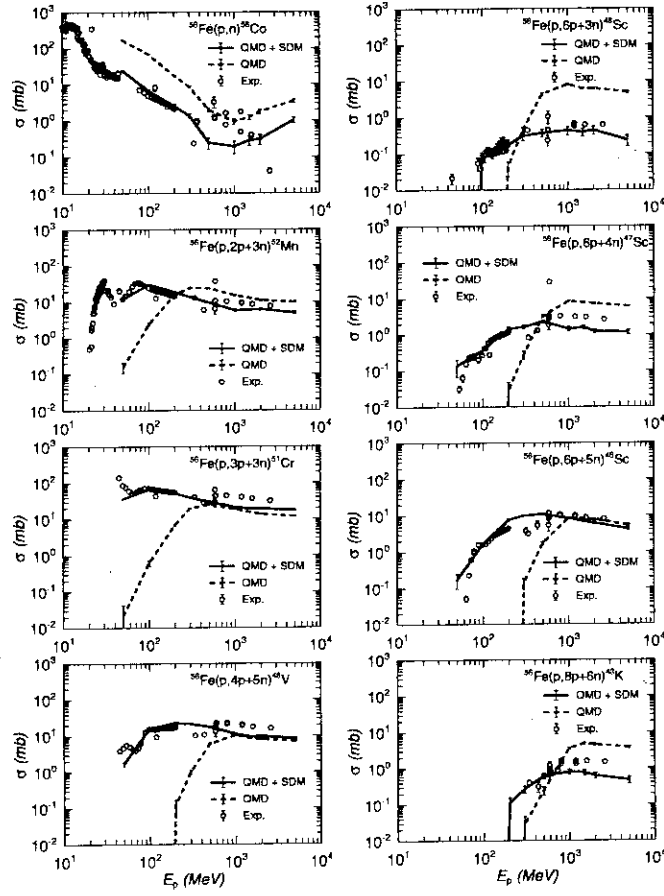
Figure 7: Calculated and measured fragment production cross sections for p + ^{56}Fe reaction as a function of incident energy.
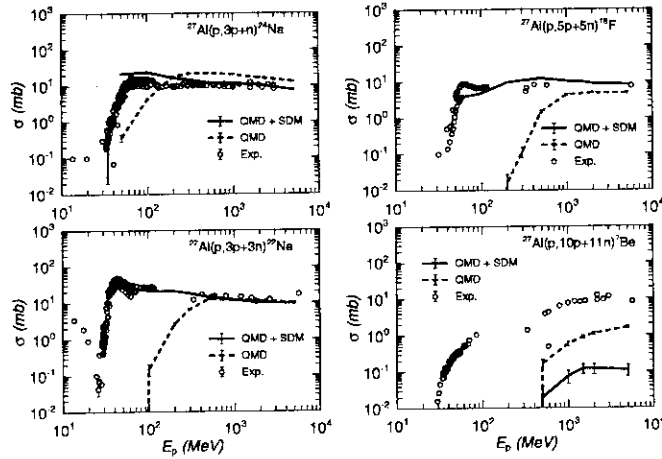
Figure 8: Same as Fig. 7 but for p + ^{27}Al reaction.

production of target-like fragments are reproduced very well by the QMD+SDM calculation. On the contrary, the production cross section of ^{7}Be is noticeably underestimated, even the threshold energy not being reproduced correctly. These results are consistent with the case for p+Fe reaction as shown in Figs. 5 and 6. Other reaction mechanisms which are not taken into the present model, including the multifragmenttaion, might be the origin of production of such "heavy" clusters as ^{7}Be.

4 Summary

We have calculated the production cross sections of various residues for 1.5-GeV proton-induced reactions on ^{56}Fe in terms of the Quantum Moleculear Dynamics (QMD) and the Statistical Decay Model (SDM). It was found that the distribution of the fragments calculated by QMD alone and QMD+SDM differs considerably. The distribution after the QMD calculation alone has a broad maximum close to the target mass and a maximum at the very light mass region. This distribution is then smoothed out by the statistical decay along the stability line, filling the gap at the intermediate-mass-fragment (IMF) region.

The QMD calculation predicts the dynamical production of light fragments which is not possible with the ordinary cascade model approach. Furthermore, it was found that the distribution of the fragments depends strongly on the impact parameter, showing the importance of the dynamical treatment as realized by QMD. It was also demonstrated that the present QMD+SDM results are quite robust against the change of the switching time from the QMD to SDM approach.

The calculated results for proton-induced fragment production cross sections on ^{56}Fe and ^{27}Al have been compared with experimental data in the energy range of 50 MeV to 5 GeV. A satisfactory overall agreement of the QMD+SDM calculation with the measured data is obtained, which confirmed the basic validity of the model and underlying parameters adopted in the present approach. The production cross sections of heavy clusters such as ^{7}Be, however, were underpredicted by about 2 orders of magnitude. These problems would show that other production mechanisms which are not included in this model may be needed to improve the agreement between the theory and experimental data. This problem, together with the high energy behavior of the ^{56}Fe(p,n)^{56}Co reaction, should be investigated further for a better understanding of the phenomena.

Th authors wish to thank Drs. Hiroshi Takada and Peter P. Siegler of JAERI, and Dr. Shiori Furihata of Mitsubishi Research Institute for valuable discussions and comments.

References

[1] K. Niita, S. Chiba, T. Maruyama, T. Maruyama, H. Takada, T. Fukahori, Y. Nakahara and A. Iwamoto, Phys. Rev. C **52**, 2620(1995).

[2] M.B. Chadwick, S. Chiba, K. Niita, T. Maruyama and A. Iwamoto, Phys. Rev. C **52**, 2800(1995).

[3] S. Chiba, M.B. Chadwick, K.Niita, T. Maruyama, T. Maruyama and A. Iwamoto, Phys. Rev. C **53**, 1824(1996).

[4] J. Hüfner, Phys. Rep. **125**, 129(1985).

[5] H.W. Barz, J.P. Bondorf, R. Donangelo, I.N. Mishustin and H. Schulz, Nucl. Phys. **A448**, 753(1986).

[6] A.S. Botvina, A.S. Iljinov and I.N. Mishustin, Nucl. Phys. **A507**, 649(1990).

[7] L.G. Moretto and G.J. Wozniak, Ann. Rev. Nucl. Part. Science **43**, 379(1993).

[8] E. Gadioli and P.E. Hodgson, "Pre-Equilibrium Nuclear Reactions", Clarendon Press, Oxford (1992).

[9] K.H. Tanaka, Y. Yamanoi, H. Ochiishi, H. Akiyoshi, S. Kouda, H. Nakamura, S. Morinobu, Y. Tanaka, K. Kimura, T. Shibata, Y. Sugaya, K. Yasuda, H. Ito and T. Murakami, Nucl. Phys. **A583**, 581(1995).

[10] T. Nishida, Y. Nakahara and T. Tsutsui, "Development of a Nuclear Spallation Simulation Code and Calculations of Primary Spallation Products", JAERI-M 86-116 (1986), in Japanese.

[11] S. Pearlstein, Astrophys. J. **346**, 1049(1989).

[12] L. Sihver, C.H. Tsao, R. Silbergerg, T. Kanai and A.F. Barghouty, Phys. Rev. **C47**, 1225(1993).

[13] H. Vonach, private communication (1995).

[14] N. Shigyo, S. Sakaguchi, K. Ishibashi and Y. Wakuta, Jour. Nucl. Sci. Technol. **32**, 1(1995).

[15] R. Michel and P. Nagel, *Specifications for an International Codes and Model Intercomparison for Intermediate Energy Activation Yields*, NEA/NSC/DOC(95)8, OECD/NEA (1995).

[16] R. Michel, M. Gloris, H.-J. Lange, I. Leya, M. Lüpke, U. Herpers, B. Dittrich-Hannen, R. Rösel, Th. Schiekel, D.Filges, P. Dragovitsch, M. Suter, H.-J.Hogmann, W. Wölfli, P.W. Kubik, H. Baur and R. Wieler, Nucl. Instr. Methods in Physics Research, **B103**, 183(1995).

[17] M. Mizumoto and S. Tanaka (ed.), JAERI-Conf 95-017 (1995).

[18] T. Maruyama, A. Ohnishi and H. Horiuchi, Phys. Rev. **C45**, 2355(1992).

[19] R.J. Charity, M.A. McMahan, G.J. Wozniak, R.J. McDonald, L.G. Moretto, D.G. Sarantites, L.G. Sobotka, G. Guarino, A. Pantaleo, L. Fiore, A. Gobbi and K.D. Hildenbrand, Nucl. Phys. **A483**, 371(1988).

[20] H.W. Bertini, "Monte Carlo Calculations on Intranuclear Cascades", ORNL-3383 (1963).

[21] Y. Nakahara and T. Tsutsui, "A Simulation Code System for High Energy Nuclear Reactions and Nucleon-Meson Transport Processes", JAERI-M 82-198 (1982), in Japanese.

[22] T. Fukahori, "CHESTOR", Charged Particle Experimental Data Storage and Retrieval system, unpublished.

The First Internet Symposium on Nuclear Data: Paper No.02

3.2 Evaluation of cross sections and calculation of kerma factors for neutrons up to 80 MeV on ^{12}C

M. Harada[#], Y. Watanabe, S. Chiba[*] and T. Fukahori[*]

Department of Energy Conversion Engineering, Kyushu University,
Kasuga, Fukuoka 816

[*] *Japan Atomic Energy Research Institute, Tokai-mura, Naka-gun, Ibaragi 319-11*
[#] *Email : harada@ence.kyushu-u.ac.jp*

We have evaluated the cross sections for neutrons with incident energies from 20 to 80 MeV on ^{12}C for the JENDL high-energy file. The total cross sections were determined by a generalized least-squares method with available experimental data. The cross sections of elastic and inelastic scattering to the first 2^+ were evaluated with the theoretical calculations. The optical potentials necessary for these calculations were derived using a microscopic approach by Jeukenne-Lejeune-Mahaux. For the evaluation of double differential emission cross sections (DDXs), we have developed a code system SCINFUL/DDX in which total 35 reactions including the 3-body simultaneous breakup process (n+^{12}C $\longrightarrow$ n+α+^{8}Be) can be taken into consideration in terms of a Monte Carlo method, and have calculated the DDXs of all light-emissions (A$\leq$ 4) and heavier reaction products. The results for protons, deuterons, and alphas showed overall good agreement with experimental data. The code is also applicable for calculations of total and partial kerma factors. Total kerma factors calculated for energies from 20 to 80 MeV were compared with the measurements and the other latest evaluations from the viewpoints of medical application and nuclear heating estimation.

1 Introduction

Intermediate energy nuclear data for ^{12}C are requested with high priority in several applied fields, such as radiation therapy using fast neutron or proton beam and accelerator-based transmutation/1, 2/. In particular, double differential emission cross sections (DDXs) are important for transport calculations of secondary neutrons and accurate dose calculations in matter. Various types of experimental data including the DDXs , however, are scarce in the intermediate energy range above 20 MeV because of few intense neutron sources suitable for the measurements. Some progress has recently been made in the measurement of DDXs/3, 4/, but the experimental data are still not sufficient compared with those for energies below 20 MeV. Moreover, the theoretical model calculations for light nuclei is not so well-established as those for medium-heavy nuclei because many-body breakup processes, such as simultaneous 3 α-decay process in the n+^{12}C reaction, are involved. Therefore, it is also necessary to develop the methods of model calculations available for intermediate energy nuclear data evaluation for light nuclei. In the present work, we have evaluated the cross sections of ^{12}C in the neutron

energy range up to 80 MeV, in connection with the evaluation activities of the JENDL high energy file/5/ which is now in progress in Japan. Our work is summarized as below:

1. Evaluation of total, elastic, and total reaction cross sections on the basis of the experimental data and the microscopic optical model calculations.

2. Development of a practical code system to calculate the DDXs of all emitted particles (n, p, d, t, ^{3}He, α, and heavier reaction products) and kerma factors using a Monte Carlo method based on the SCINFUL code/6/ which is used for the neutron efficiency calculation for organic scintillators.

3. Application of the code system to calculation of the DDXs and the kerma factors.

2 Evaluation methods and code development

2.1 Outline of Evaluation methods

Total cross sections are determined by a generalized least-squares method with the experimental/7/-/10/. The details have been described in Ref./11/.

The spherical optical model is applied to evaluate elastic scattering cross sections. DWBA calculation is also made for inelastic scattering to the first 2^+ state. The ECIS77 code/12/ is used in both calculations. As the optical potentials necessary in these calculations, we use microscopic optical potentials derived by the Jeukenne-Lejeune-Mahaux (JLM) approach/13/ of calculating the optical potentials with the non-relativistic G-matrix theory and the local density approximation. The details of the calculational method based on the JLM model have been described elsewhere/14/. Total reaction cross sections are evaluated by the subtraction of the elastic cross section from the total cross section. The cross sections for the other reaction channels, e.g., the DDXs of all emitted particles, are evaluated with a Monte Carlo simulation method explained in the following subsection.

2.2 Monte Carlo code system developed in this work

The n+^{12}C reaction processes can be classified by combination of 9 primary reaction processes and the following sequential or simultaneous decay processes as shown in Fig.1. The primary reactions considered in the present calculation are elastic scattering, inelastic scattering to the first 2^+ state, (n,α), (n,n')3α, (n,^{3}He), (n,p), (n,2n), (n,d), and (n,t) reactions. Total 35 processes of the n+^{12}C reaction are taken into account as in the SCINFUL code.

The main part of our code system consists of a Monte Carlo simulator of the n+^{12}C reaction in which several subroutines of the SCINFUL code are used. In the simulation, the cross section for each primary reaction, the angular distribution for each particle emitted in the primary reaction and branching ratios of the following decay processes are needed as the main input data. We employ the same data as those used in the SCINFUL code, except for the major reaction channels: the elastic scattering, the inelastic scattering to the first 2^+ state, and the (n,n')3α reaction. Using a Monte Carlo method, the energy and angle of all emitted particles are calculated on the basis of the two-body or three-body kinematics and are recorded event by event in a file. Finally, we calculate the DDXs, the energy differential cross sections, the production cross sections and the

kerma factors using the output data from the simulator. In the development of our code system, we have checked the data and assumptions used in the original SCINFUL code. As a result, the following modifications were made in the Monte Carlo simulator to improve the agreement between the calculated results and the experimental data:

- Limitation of the maximum order of the Legendre coefficients for elastic and inelastic(2^+) angular distributions was removed and the newly evaluated differential cross sections were used.

- Underestimation of the total reaction cross sections seen in the original SCINFUL code was improved by increase in the (n,n')3α cross sections, as will be presented in the next section.

- Three-body simultaneous breakup (3BSB) process/15/ (n+^{12}C $\longrightarrow$ n+ α + ^{8}Be) was taken into account to improve the shape of energy spectra of neutron and alpha particle emitted with intermediate outgoing energies.

- Kalbach systematics/16/ was applied to reproduce well the forward-peaked angular distributions of light mass particles emitted from the primary reactions. Note that the angular distributions of all particles emitted in the following secondary stage are assumed to be isotropic.

An advantage of the use of such a Monte Carlo method is that the many-body breakup processes characteristic in the reaction with light-nuclei can be taken into account in a rather simple way and the energy conservation important in the kerma factor calculation can be also treated correctly.

3 Results and discussion

3.1 Total, Elastic and Reaction Cross Sections

The evaluated total, elastic and reaction cross sections are compared with the experimental data/10/,/17/-/26/ in Fig.2. The data of the original SCINFUL are also plotted by the dotted lines. The present results shown by the solid lines are in fairly good agreement with the measurements. On the other hand, the original SCINFUL data of total and reaction cross sections underestimate obviously the experimental data in the whole energy region.

3.2 Emission spectra and production cross sections

Calculated energy spectra of the (n,n') reaction at 40 MeV are compared with experimental (p,p') data/27/ in Fig.3. The dotted line represents the result with the same input data as used in the original SCINFUL code. Remarkable underestimation seen at intermediate outgoing energies is improved by the present calculation. This is due to the inclusion of the 3BSB process mentioned above.

Figure 4 shows a comparison between the calculated DDXs of the 26 MeV (n,n') reaction and the experimental (p,p') data/28/. As in Fig.3, the present calculation is in better agreement with the experimental data in the continuum region than the

original SCINFUL. From Figs.3 and 4, we can point out that the 3BSB process plays an important role in nucleon emission from nucleon-induced reaction on ^{12}C.

Double differential emission cross sections (DDXs) of other charged particles (p, d, t, and α) are compared with the latest experimental data by Slypen et al./29/ in Fig.5 at 42.5MeV. The calculated DDXs are in overall good agreement with the experimental data, except for the proton emission with medium outgoing energies to forward angles and deuteron emission with high outgoing energies.

Figure 6 shows comparisons of the calculated (n,n')3α cross sections and α production cross sections with the experimental data/15, 30/ . The dotted line in Fig.6(a) presents the data used in the original SCINFUL code. They are much smaller than the experimental data. From the comparison between Fig.2(c) and Fig.6(a), one can see that the underestimation in total reaction cross sections used in the original SCINFUL code is due mainly to the underestimation in the (n,n')3α cross sections. Therefore, we have re-evaluated the (n,n')3α cross sections as given by the solid line in Fig.6(a). As a result, the α production cross sections calculated with the evaluated (n,n')3α cross sections are in good agreement with the experimental data/31, 29, 32, 33/ as shown in Fig.6(b).

3.3   Kerma factors

Figure 7 shows comparisons of the calculated total kerma factors with the experimental data /34/-/38/ and the other calculations/39/-/45/, respectively. Our result looks somewhat large in the energy range between 30 and 60 MeV compared with the experimental data and the other calculations. However, the present calculation is almost within the experimental errors and is at most 10% different from the recent calculation by Chadwick et al./40/. In Fig.8, we decompose the total kerma factor into the partial kerma factors corresponding to emitted particles and recoiled nuclei in order to see how the most dominant component changes with energy. For low incident energies, the contribution of α particles from the (n,n')3α reaction is the largest as expected from Fig.7(a) and amounts to about 60 % at 30 MeV. As the incident energy increases, it decreases gradually and the contributions from protons and deuterons become important. They amount to about 60 % of the total kerma factor at 80 MeV.

4   Conclusions

We evaluated the cross sections of ^{12}C and calculated the kerma factors for neutrons up to 80 MeV:

- The total cross section, the elastic cross section, and the total reaction cross section were evaluated on the basis of the generalized least-squares method with the experimental data and the calculation with the microscopic optical potentials.

- The Monte Carlo simulation code system was developed to calculate the DDXs of all emitted particle for the n+^{12}C reaction. The calculated DDXs showed overall good agreement with the latest experimental data.

- The kerma factors were calculated using the Monte Carlo code and compared with the experimental data. It was found that the calculation reproduces the measurements well within the error.

- All evaluated cross sections including the DDXs are scheduled to be stored in the JENDL high energy file.

The code system developed in this work can be extended for proton-induced reactions on ^{12}C. In the future, we plan to start the work on nuclear data evaluation of ^{12}C for proton energies up to 200 MeV using the extended code system, in parallel with the measurements of the DDXs of all emitted light-charged particles.

Acknowledgments
We wish to thank Dr. M.B. Chadwick for valuable discussions. We are also grateful to Drs. J. P. Meulders and I. Slypen for sending numerical data of their latest experiments of (n,p), (n,d), (n,t), and (n,α) reactions on ^{12}C.

References

[1] A.J. Koning, "Requirements for an evaluated nuclear data file for accelerator-based transmutation", ECN-C-93-04 (1993).

[2] Y. Kikuchi and T. Fukahori, "Recent of Inquiry on Intermediate Energy Nuclear Data Needs for Various Applications as Start-up Task of SG13", NEANSC/WPIEC/SG13 meeting, NEA Data Bank, Dec. 9, 1994.

[3] I. Slypen et al., Nucl. Instr. and Meth., **A337**, 431 (1994).

[4] M. Baba et al., Proc. Int. Conf. on Nucl. Data for Sci. and Technol., Gatlinburg, Tennessee, USA, May 9-13, 1994, Ed. J. K. Dickens (1994), p.90.

[5] T. Fukahori and S. Chiba, Proc. of the second specialists' meeting on high energy nuclear data, Jan. 26-27, 1995, JAERI, Tokai, Japan, JAERI-Conf 95-016 (1995), p. 46.

[6] J. K. Dickens, ORNL-6402, Oak Ridge National Laboratory (1988); Computers in Physics, Nov/Dec, 62 (1989).

[7] J. D. Kellie et al., Proc. of Int. Conf. on Nuclear Data for Technology, Oct. 22-26, 1979, Knoxvill, U.S.A., (1980), p.48.

[8] S. Cierjacks et al., Nucl. Instr. Meth. **169**, 185 (1980).

[9] D. C. Larson, Proc. of Symp. on Neutron Cross Sections from 10 - 50 MeV, May 12-14, 1980, BNL, U.S.A., (1981), p.277.

[10] R. W. Finlay et al., Phys. Rev. C **47**, 237 (1993).

[11] S. Chiba et al., Proc. of the 1993 Nuclear Data Symp., Nov. 18-19, 1993, JAERI, Tokai, Japan, JAERI-M 94-019, (1994), p.300.

[12] J. Raynal., ECIS79 code, unpublished.

[13] J. P. Jeukenne, A. Lejeune and C. Mahaux, Phys. Rev. C **16**, 80 (1977).

[14] S. Chiba and M. Harada, J. Nucl Sci. and Technol. **33**, 346 (1996).

[15] B. Antolkovic and Z. Dolenec, Nucl. Phys. **A237**, 235 (1977); B. Antolkovic, Proc. Int. Conf. on Nucl. Data for Sci. and Technol., Jülich, Germany, May 13-17, 1991, Ed. S. M. Qaim (Springer-Verlag, 1992), p.594.

[16] C. Kalbach, Phys. Rev. C37, 2350 (1988).

[17] F. Boreli et al., Phys. Rev. 174, 1147 (1968).

[18] R. P. DeVito, Ph.D. thesis, Michigan State University (unpublished) (1979).

[19] A. S. Meigooni et al., Phys. Med. Biol. 29, 643 (1984).

[20] N. Olsson et al., Phys. Med. Biol. 34, 909 (1989).

[21] Y. Yamanouti et al.,Proc. Int. Conf. on Nucl. Data for Sci. and Technol., Jülich, Germany, May 13-17, 1991, Ed. S. M. Qaim (Springer-Verlag, 1992), p.717.

[22] E. L. Hjort et al., Phys. Rev. C 50, 275 (1994).

[23] J. Dejuren and N. Knable, Phys. Rev. 77, 606 (1950).

[24] R. G. P. Voss and R. Wilson, Proc. Royal Soc. A236, 41 (1956).

[25] M. H. Macgregor et al., Phys. Rev. 111, 1155 (1958).

[26] C. I. Zanelli et al., Phys. Rev. C 23 1015 (1981).

[27] F.E. Bertrand and R.W. Peelle, Phys. Rev. C 8, 1045 (1973).

[28] Y. Watanabe et al., Proc. Int. Conf. on Nucl. Data for Sci. and Technol., Gatlinburg, Tennessee, USA, May 9-13, 1994, Ed. J. K. Dickens (1994), p.574.

[29] I. Slypen et al., Phys. Rev. C 51, 1303 (1995); I. Slypen et al., ibid. 53, 1309 (1996).

[30] B. Antolkovic et al., Nucl. Phys. A394, 87 (1983).

[31] T. S. Subramanian et al., Phys. Rev. C 28, 521 (1983).

[32] Y. Takao, Ph.D. thesis, Kyushu University (1996).

[33] D. W. Kneff et al., Nucl. Sci. Eng. 92, 491 (1986).

[34] J. L. Romero et al., Rad. Effects 94, 13 (1986).

[35] H. Schuhmacher et al., Phys. Med. Biol. 37, 1265 (1992).

[36] P. Pihet et al., Phys. Med. Biol. 37, 1957 (1992).

[37] C. L. Hartmann et al., Rad. Prot. Dos. 44, 25 (1992).

[38] I. Slypen et al., Phys. Med. Biol. 40, 73 (1995).

[39] U. J. Schrewe et al., in Chalk River Conference, to be published in Rad. Prot. Dos. (1994).

[40] M. B. Chadwick et al., Nucl. Sci. and Eng., 123, 17 (1996).

[41] E. N. Saviskaya and A. V. Sannikov, Rad. Prot. Dos. 60, 135 (1995).

[42] P. J. Dimbylow, Phys. Med. Biol. 27, 989 (1982).

[43] M. A. Behrooz et al., Phys. Med. Biol. 26, 507 (1981).

[44] P. J. Dimbylow, Phys. Med. Biol. 25, 637 (1980).

[45] R. S. Caswell et al., Radiat. Res. 83, 217 (1980).

(1) n + ^{12}C-> n + ^{12}C (elastic)

(2) n + ^{12}C-> n' + ^{12}C (2$^+$)

(3) n + ^{12}C-> α + ^{9}Be

(4) n + ^{12}C-> n' + 3$^\alpha$(Sequential decay, 3BSB)

(5) n + ^{12}C-> ^{3}He + ^{10}Be

^{3}He + n + ^{9}Be

^{3}He + 2n + 2$^\alpha$

^{3}He + n + p + ^{8}Li

^{3}He + 2n + p + ^{7}Li

^{3}He + 2n + p + t + α

(6) n + ^{12}C-> p + ^{12}B

p + α + ^{8}Li

p + n + ^{11}B

p + n + α + ^{7}Li

p + 2n + ^{10}B

p + 2n + α + ^{6}Li

p + 2n + d + 2$^\alpha$

p + n + t + 2$^\alpha$

2p + ^{11}Be

2p + n + ^{10}Be

2p + 2n + ^{9}Be

(7) n + ^{12}C-> 2n + ^{11}C

2n + p + ^{10}B

(8) n + ^{12}C-> d + ^{11}B

d + α + ^{7}Li

d + n + ^{10}B

d + n + p + ^{9}Be

d + n + α + ^{6}Li

2d + n + 2$^\alpha$

(9) n + ^{12}C-> t + ^{10}B

t + p + ^{9}Be

t + d + 2$^\alpha$

t + α + ^{6}Li

t + p + n + 2$^\alpha$

t + p + d + ^{7}Li
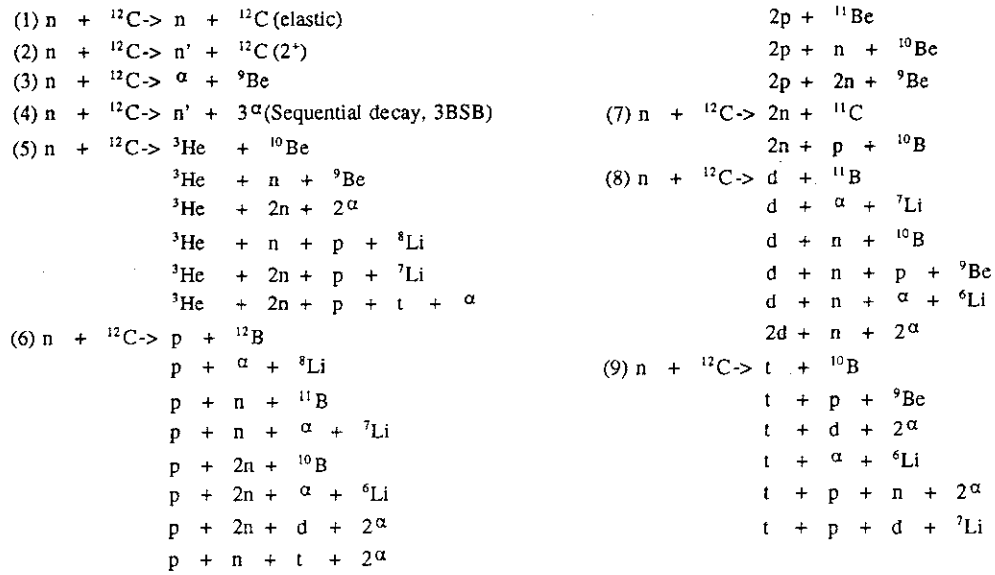
Figure 1: All n+^{12}C reaction processes considered in this work
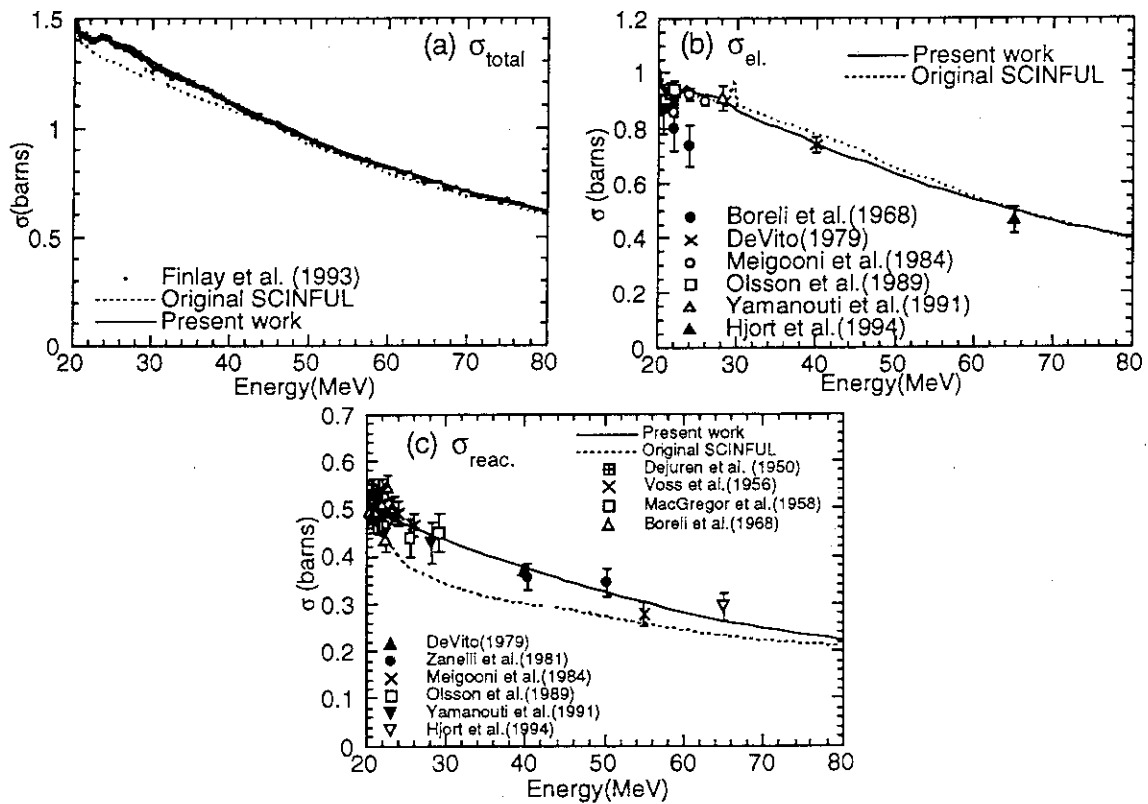
Figure 2: All comparisons of the evaluated cross sections with the experimental ones. (a) total, (b) elastic, and (c) total reaction cross sections
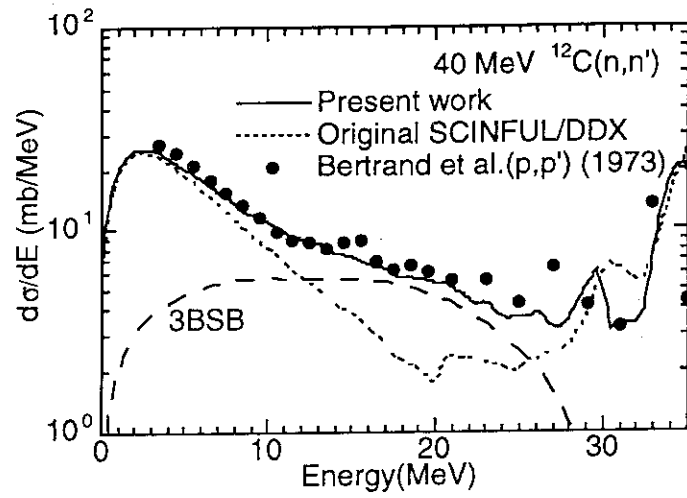
Figure 3: Comparisons of the calculated energy spectra of the 40 MeV (n,n') reaction with the measured (p,p') spectrum.
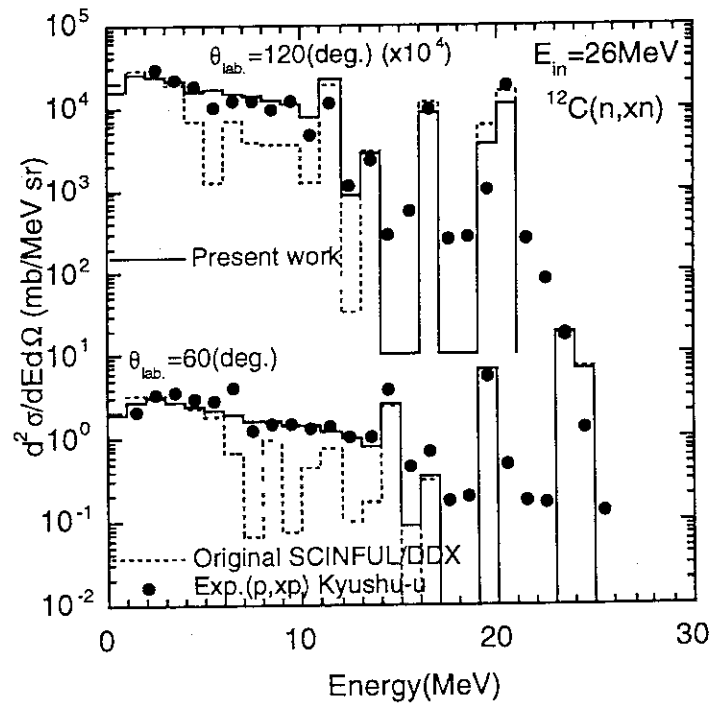
Figure 4: Comparisons of the calculated DDXs of the 26 MeV (n,n') reaction with the measured ones for (p,p') reaction.
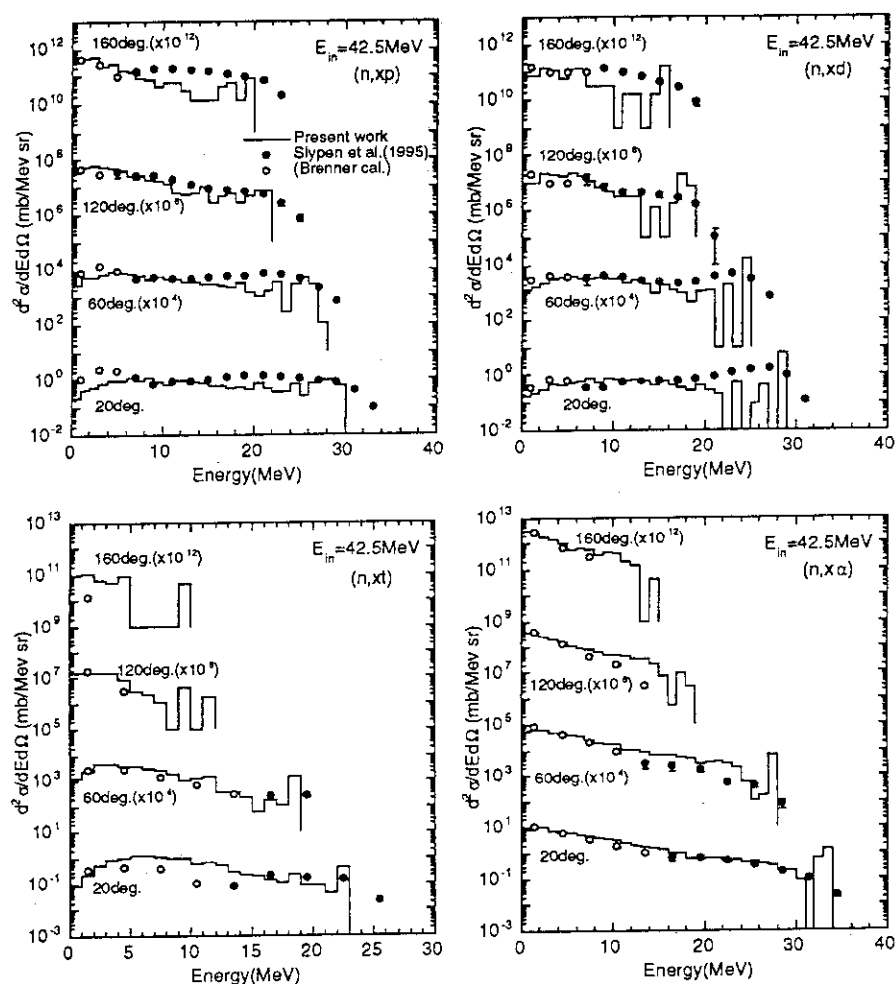
Figure 5: Comparisons of the calculated DDXs of (n,charged particles) reactions at 42.5 MeV with the measured ones.
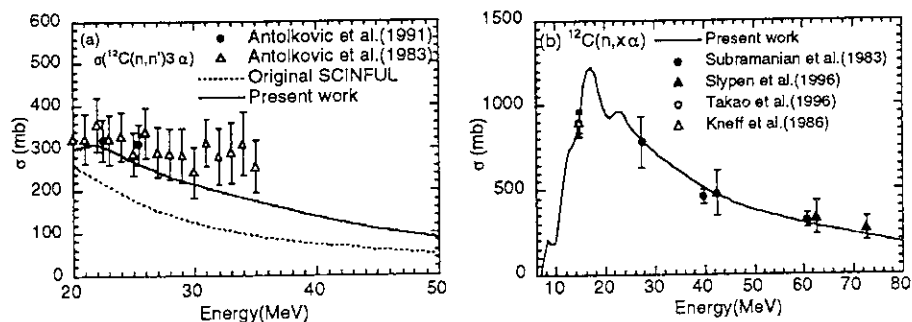
Figure 6: (a)(n,n')3α cross section and (b)α production cross section
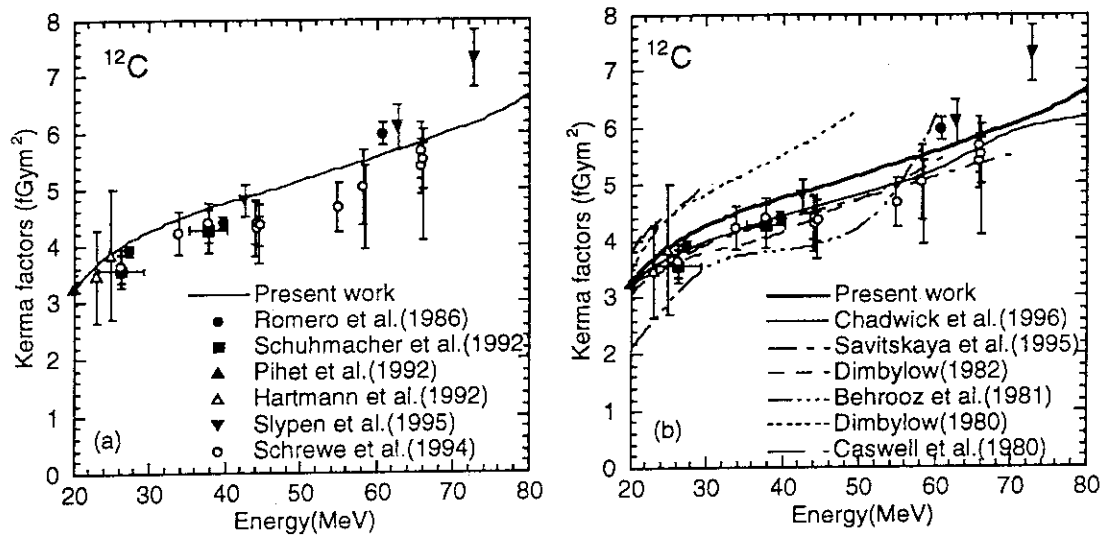
Figure 7: Comparisons of the calculated total kerma factor with (a)the experimental data and (b)the other evaluations.
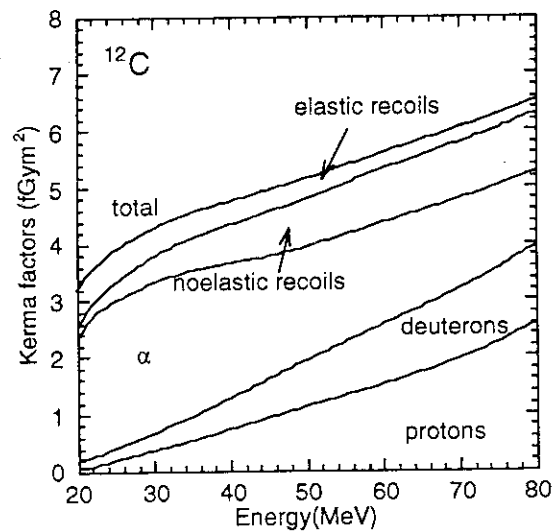
Figure 8: Calculated partial kerma factors

3.3 Effect of U-238 and U-235 Cross Sections on Nuclear Characteristics of Fast and Thermal Reactors

Hiroshi Akie and Hideki Takano
Japan Atomic Energy Research Institute
Tokai-mura, Naka-gun, Ibaraki-ken, 319-11, JAPAN
e-mail : akie@mike.tokai.jaeri.go.jp

Kunio Kaneko
Integrated Technical Information Research Organization
Ryogoku City Core, 2-10-14 Ryogoku, Sumida-ku, Tokyo, 130, JAPAN

Benchmark calculation has been made for fast and thermal reactors by using ENDF/B-VI release 2(ENDF/B-VI.2 and JENDL-3.2 nuclear data. Effective multiplication factors(k_{eff}s) calculated for fast reactors calculated with ENDF/B-VI.2 becomes about 1% larger than the results with JENDL-3.2. The difference in k_{eff} is caused mainly from the difference in inelastic scattering cross section of U-238.

In all thermal benchmark cores, ENDF/B-VI.2 gives smaller multiplication factors than JENDL-3.2. In U-235 cores, the difference is about 0.3%dk and it becomes about 0.6% in TCA U cores. The difference in U-238 data is also important in thermal reactors, while there are found 0.1-0.3% different v values of U isotopes in thermal energy range between ENDF/B-VI.2 and JENDL-3.2.

1. Introduction

Benchmark calculation has been made for fast and thermal reactors by using ENDF/B-VI release 2 (ENDF/B-VI.2) nuclear data, and the results are compared with those of JENDL-3.2 benchmark test. In the benchmark calculation, there are still found discrepancies between these files even in the data of the most important nuclides in reactor calculations such as U-235 and U-238. In this paper, the effect of the discrepancies in uranium nuclear data is described on nuclear characteristics of fast and thermal benchmark reactors.

2. Fast Reactor Benchmark

The benchmark cores are the large LMFBR mock-up core ZPPR-9 and the 1-dimensional benchmark cores of VERA, ZPR, ZEBRA, SNEAK, etc. Diffusion calculation was made on 2-dimensional(ZPPR-9) or 1-dimensional geometry model.

Effective multiplication factors(k_{eff}s) and reaction rate ratios calculated for ZPPR-9 are shown in Table 1. The multiplication factor calculated with ENDF/B-VI.2 becomes about 0.8% larger than the results with JENDL-3.2. There are 2-3% differences in reaction rate ratios of U-238 capture and fission to Pu-239 fission(C8/F9 and F8/F9).

By comparing U-238 cross sections between both files, differences are found in inelastic scattering cross section in 2-6MeV energy region(Fig.1) and in capture cross section in MeV region.

Figure 2 summarizes the k_{eff}s of 1-D benchmark cores. Similarly to the case in ZPPR-9, ENDF/B-VI.2 gives 1-2% larger k_{eff}s than JENDL-3.2. It was also compared the k_{eff}s

Table 1 Calculation/Experiment(C/E) values of
k_{eff} and reaction rate ratios for ZPPR-9

		ENDF/B-VI	JENDL-3.2
k_{eff}		1.007	0.9986
Reaction rate ratio			
	F5/F9	1.010	1.003
	C8/F9	1.037	1.046
	F8/F9	0.975	0.955

F9: Pu-239 fission rate, F5: U-235 fission rate,
C8: U-238 capture rate, F8: U-238 fission rate.
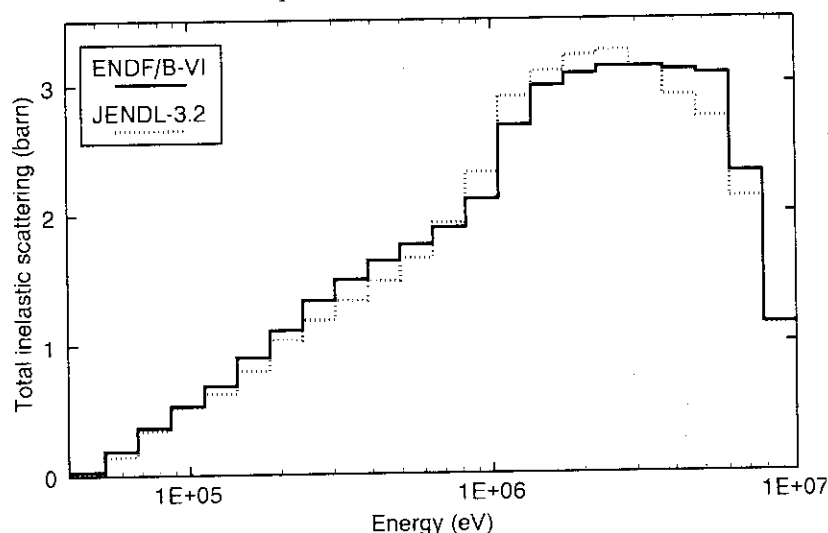
Fig. 1 Total inelastic scattering cross section of U-238

calculated with the following data :

(1) J32+B6(U8): JENDL-3.2 + U-238 cross section from ENDF/B-VI.2.
(2) B6(U8)+J32(U8mtx): (1) + secondary neutron energy distribution of U-238 inelastic scattering from JENDL-3.2

In (2), total inelastic scattering cross section of U-238 is that of ENDF/B-VI.2. From these calculations, it is observed when the U-238 data in JENDL-3.2 is replaced by those of ENDF/B-VI.2, the calculated k_{eff} agree well with that calculated by using ENDF/B-VI.2 ("J32+ B6(U8)" and "ENDF/B-VI.2"). The difference in U-238 inelastic scattering matrix leads to the k_{eff} difference of about 1% (comparison between "J32+ B6(U8)" and "B6(U8)+J32 (U8mtx)"). The effect of U-238 capture cross section difference is not shown in this figure, but was much smaller to be about 0.1%.

Figure 3 compares the secondary neutron energy distribution of U-238 inelastic scattering obtained by using a typical neutron spectrum of large FBR. ENDF/B-VI.2 gives harder neutron spectrum than JENDL-3.2 because of the different secondary neutron energy distribution of U-238 inelastic scattering. The discrepancy between the k_{eff}s calculated with ENDF/B-VI.2 and JENDL-3.2 is caused from the difference in U-238 cross section data, mainly of inelastic scattering matrix.
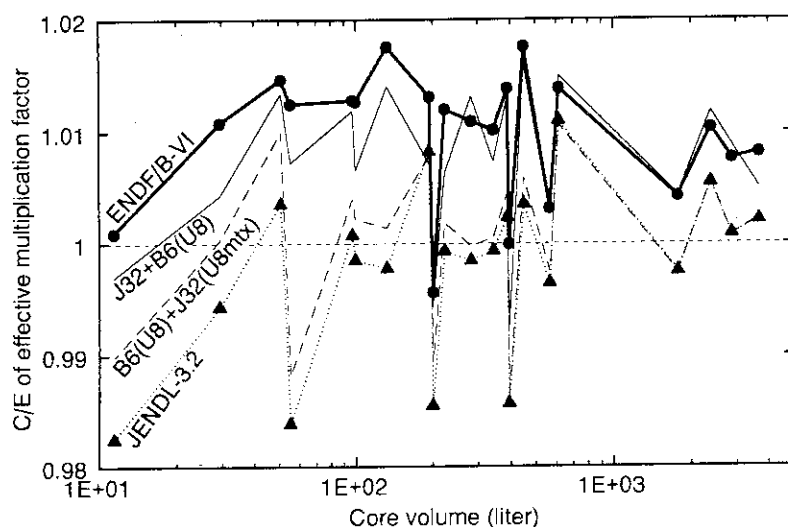
Fig. 2 Calculation/Experiment(C/E) values of effective multiplication factors for 1-D benchmark cores

(B6: ENDF/B-VI.2, J32: JENDL-3.2, U8: U-238 cross section, mtx: secondary neutron energy distribution of inelastic scattering)
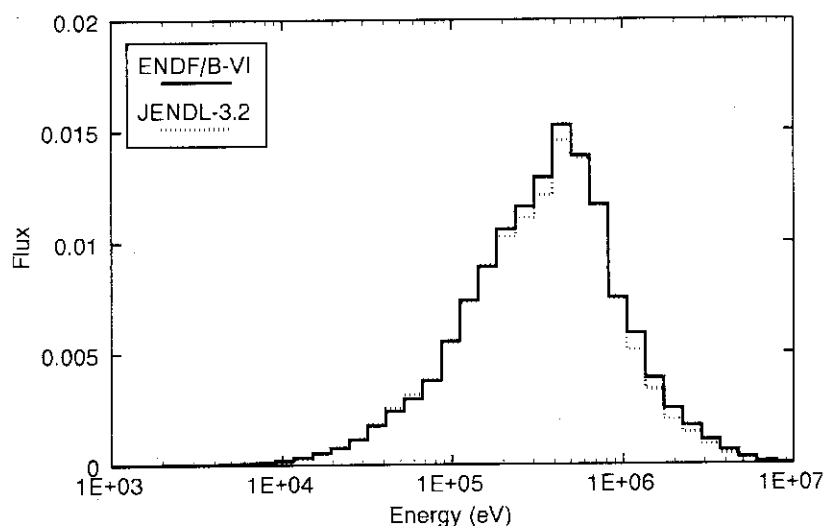
Fig. 3 Secondary neutron energy distribution of U-238 inelastic scattering calculated with the neutron spectrum of a typical large fast reactor

3. Thermal Reactor Benchmark

The thermal reactor benchmark cores are TRX, BAPL and TCA with water moderated lattice, and critical safety experiments ORNL and McNeany&Jenkins series. Unit cell calculation was made for TRX, BAPL and TCA by using critical bucklings. One-dimensional Sn calculation was made for critical safety experiments.

Effective multiplication factors(k_{eff}s) are shown in Figs.4 and 5, respectively for critical safety experiments and water moderated lattice cores. In all thermal benchmark cores, ENDF/B-VI.2 gives smaller multiplication factors than JENDL-3.2. In TRX and BAPL cores, the difference is about 0.3%dk and it becomes about 0.6% in TCA U cores.
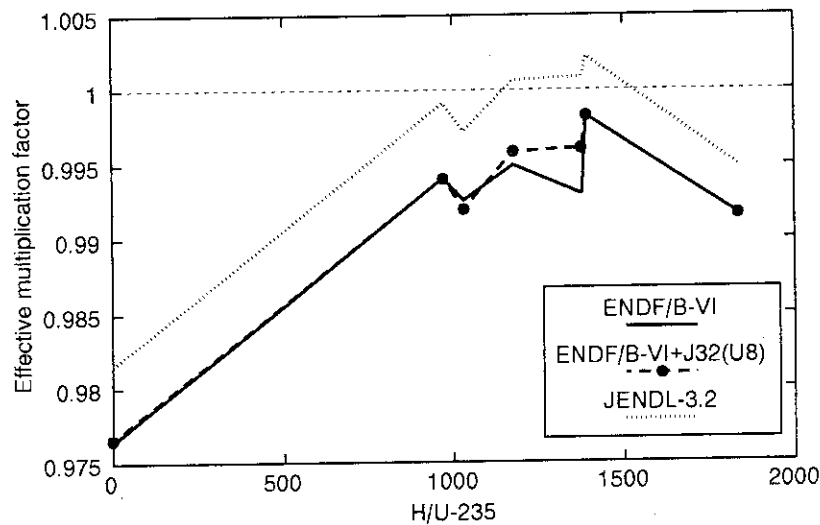
Fig. 4 Effective multiplication factors of U-235 fueled critical safety experiments
(B6: ENDF/B-VI.2, J32: JENDL-3.2, U8: U-238 cross section)
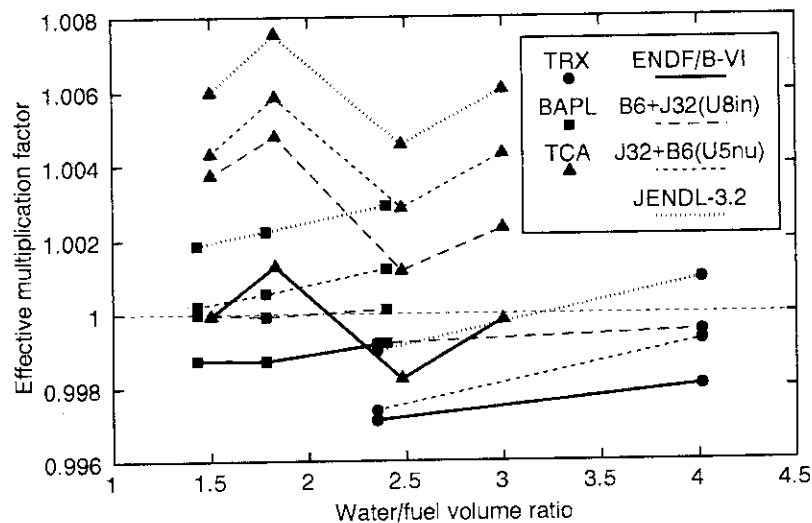
Fig. 5 Effective multiplication factors of U-235 fuel cores
(B6: ENDF/B-VI.2, J32: JENDL-3.2, U8 and U5: U-238 and U-235 cross section, in: inelastic scattering cross section, nu: ν value in thermal energy range)

By comparing the cross sections, there are found 0.1-0.3% different ν values of U isotopes in thermal energy range between ENDF/B-VI.2 and JENDL-3.2(Fig. 6). As discussed in fast reactor benchmark, the difference of U-238 cross section between ENDF/B-VI.2 and JENDL-3.2 is found in fast energy range(Fig.1).
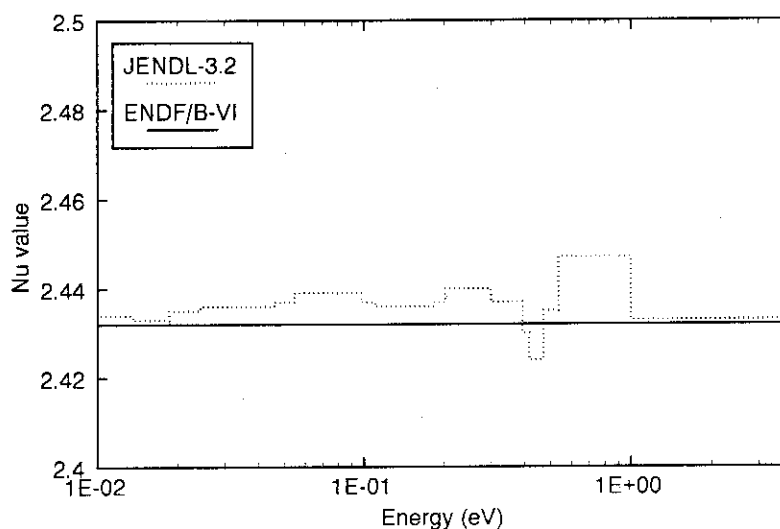
Fig. 6 ν values of U-235 in thermal energy range

Additional calculations were made for TRX, BAPL and TCA cores with the following data :

(1) B6+J32(U8in): ENDF/B-VI.2 + U-238 inelastic scattering cross section from JENDL-3.2.
(2) J32+B6(U5-Nu): JENDL-3.2 + U-235 ν value in thermal energy range from ENDF/B-VI.2.

The results are also shown in Fig.5. By replacing U-235 ν value in thermal energy range, there is found about 0.2%dk difference in all cores. The effect of U-238 cross section is significant(0.2-0.4%dk) in TCA cores, and 0.1% or less in TRX and BAPL.

Table 2 summarizes the critical bucklings of TRX, BAPL and TCA-U cores. From these bucklings, it can be observed the TCA cores are smaller than the other cores. Furthermore, the neutron spectra in TCA 3.00U core calculated with ENDF/B-VI.2 and JENDL-3.2 are compared in Fig.7. The fast neutron spectrum calculated with ENDF/B-VI.2 is harder than JENDL-3.2, because of the difference in secondary neutron energy distribution of U-238 inelastic scattering. The large effect of U-238 in TCA cores is therefore assumed to the neutron leakage effect in fast energy range.

Table 2 Critical bucklings of TRX, BAPL and TCA cores

core name	$B^2(10^{-3}/cm2)$
TRX-1	5.7
TRX-2	5.469
BAPL-1	3.259
BAPL-2	3.547
BAPL-3	3.422
TCA 1.50U	8.70
TCA 1.83U	9.33
TCA 2.48U	9.89
TCA 3.00U	9.68
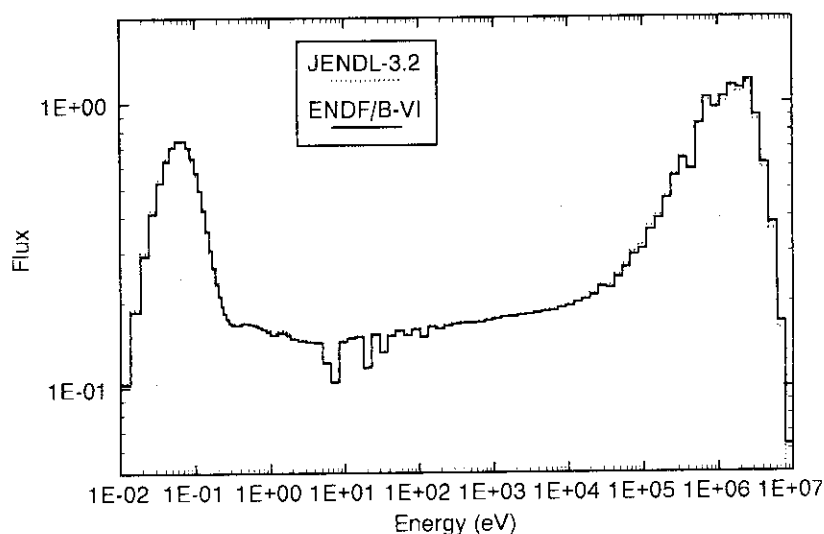
Fig. 7 Neutron spectrum calculated for TCA 3.00U core

Central reaction rate ratios in TRX cores are shown in Table 3. The effect of the difference in U-238 data is found in delta-28, which is sensitive to the change in fast neutron spectrum.

Table 3 C/E of central reaction rate ratios in TRX cores

	ENDF/B-VI	JENDL-3.2
TRX-1		
ρ-28	1.0138	1.0123
δ-25	0.9925	0.9873
δ-28	1.0597	1.0127
C^*	0.9956	0.9976
TRX-2		
ρ-28	0.9971	0.9965
δ-25	0.9788	0.9745
δ-28	1.0264	0.9897
C^*	0.9890	0.9909

ρ-28: epi-thermal/thermal U-238 capture rate ratio
δ-25: epi-thermal/thermal U-235 fission rate ratio
δ-28: fission rate ratio of U-238/U-235
C^*: ratio of U-238 capture/U-235 fission

4. Conclusion

By comparing ENDF/B-VI.2 and JENDL-3.2 it is found in fast reactors that ENDF/B-VI.2 gives 1-2% larger k-eff than JENDL-3.2 The difference is mainly caused from U-238 cross sections. Inelastic scattering cross section of U-238 leads to 1% or larger difference in k_{eff}. From the difference in the secondary neutron energy distribution of U-238 inelastic scattering, the neutron spectrum calculated with ENDF/B-VI.2 becomes harder than that calculated with JENDL-3.2. The effect of U-238 capture cross section is smaller to be

0.1-0.4%.

In thermal reactors, ENDF/B-VI.2 gives about 0.3% smaller k_{eff} than JENDL-3.2, and the difference becomes 0.6%dk in TCA cores. The difference in U-235 ν value in thermal energy range cause 0.2%dk. The difference in U-238 data also gives 0.2%dk in TCA cores. The cross section discrepancy of U-238 in high energy range, especially of inelastic scattering, is assumed to lead the difference in the neutron leakage effect in the TCA cores, which are smaller in size than the other benchmark cores.

The first Internet Symposium on Nuclear Data: Paper No. 004

3.4 Evaluation of the 2039 keV level property in ^{124}Te

J. Katakura

Nuclear Data Center

Japan Atomic Energy Research Institute

Tokai-mura, Naka-gun, Ibaraki-ken, 319-11

E-mail : katakura@cracker.tokai.jaeri.go.jp

One of the purposes of the mass chain evaluation is to provide reliable level properties of isobars based on available experimental data. In the work of A=124 mass chain evaluation, we have faced some confusing data relating to confirming the level properies of the 2039 keV level in ^{124}Te: (1) inconsistent intensity ratios of emitted gamma rays between reaction gamma ray and decay gamma ray data, (2) placement of 2039 keV gamma ray transition and (3) gamma ray angular correlation data relating to the level. In the evaluation work, we have to reconcile the confusing data and to provide the adopted ones derived from the available data. In this report, the problems relating to the level properties are described and the reanalyses of the measured data are presented for providing the adopted data.

1 Introduction

The level scheme and gamma transitions in ^{124}Te has been studied by a lot of experiments and the information on the low-lying levels of this nucleus has been accumulated in different investigations /1/-/15/. The experimental data derived from these investigations, however, are not always consistent with each other. As a typical example of the inconsistency the partial level schemes relating to the level at 2039 keV in ^{124}Te and the gamma transitions are shown in Figs. 1 through 5.
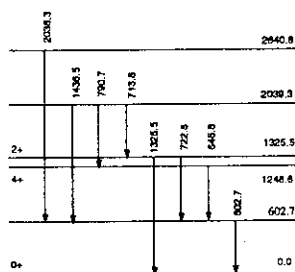
Fig. 1. Partial decay scheme of ^{124}I ϵc decay/1/.
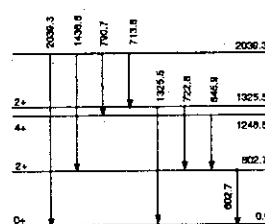
Fig. 2. Partial decay scheme of ^{124}Sb β^- decay/7/.
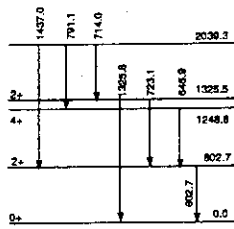
Fig. 3. Partial decay scheme of $(\alpha, 2n\gamma)$ reaction/10/.
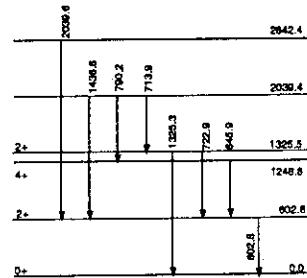
Fig. 4. Partial decay scheme of (n, γ) reaction/12/.
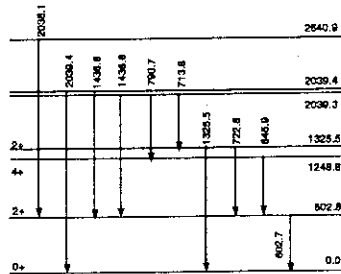
Fig. 5. Partial decay scheme of $(n, n'\gamma)$ reaction/14/.

In these level schemes the levels and gamma rays not relating to the present discussion are omitted. These figures show the level schemes proposed by different types of experiment the data of which are most recent ones in the category. As seen in the figures the level at 2039 keV shows different gamma transitions. In the experiments of [124]I decay, $(\alpha, 2n\gamma)$, (n, γ), 2039 keV gamma transition from this level is not given, but the transition is placed between the levels at 2642 and 603 keV in [124]I decay and (n, γ) and the same gamma transition is not reported in $(\alpha, 2n\gamma)$. The 2039 keV gamma, however, is placed between the levels at 2039 keV and the ground state in [124]Sb decay and 2642 keV level is not reported in the experiment. The most interesting case is the level scheme in $(n, n'\gamma)$ in which two levels at 2039 keV is proposed and the lower level emits three gamma rays and the higher level emits two gamma rays, one of which is the 2039 keV gamma and the other is the 1437 keV gamma that is also emitted from the lower level. And more the 2038 keV gamma is placed between the 2641 and 603 keV levels.

In the evaluation of the mass chain, we have to provide the adopted data as most convincing level data. We, therefore, reexamined the available data and tried to reconcile the existing inconsistent level properties to give the adopted ones.

2 Problems of 2039 keV level

The problems about the 2039 keV level was first indicated by Demidov et al./13/ in 1980 through examining the data of their $(n, n'\gamma)$ reaction and other experiments. They found out that there existed inconsistency in the intensity ratios of gamma transitions from the level in then available data. The inconsistency is still remained in the recently measured data. In Table 1 shows the intensity ratios derived from the measured data normalizing the 714 keV gamma to be 100.0 and two doubly placed 2039 keV gammas in $(n, n'\gamma)$ are set to be single transitions here.

Table 1: Comparison of relative intensities of gamma rays relating to the 2039 keV level

E(keV)	^{124}I decay	^{124}Sb decay	$(\alpha, 2n\gamma)$	(n, γ)	$(n, n'\gamma)$
714	100(4)	100(1)	100(7)	100(21)	100(10)
791	36(5)	33.1(4)	60(7)	57(9)	33(3)
1437	118(39)	55.1(4)	147(7)	191(38)	152(15)
2039	463(25)	2.91(9)	—	74(13)	70(7)

The numbers in parentheses are errors in the least significant digits.

As seen in the Table the relative intensities of the 1437 and 2039 keV gammas are scattered among the experiments. In the table the data from the ^{124}I decay are obtained from recent ones /2/ except for the 2039 keV transition, the intensity of which is derived by renormalizing old data because recent data work reports only the gamma rays with energy up to 1720 keV. According to the old data that Demidov et al. used in their analysis the relative intensities of the 791, 1437 and 2039 keV transitions are 26, 61, and 311 respectively. Other data are also recent ones, but the intensity ratios are consistent with the old data. Important point seen in the table is that the intensity of the 2039 keV gamma observed in each experiment is not considered to be the transition from the same level as Demidov et al. indicated, because the intensity ratio to the 714 keV gamma is too different from each other if the 2039 keV gamma is the same transition. The 2039 keV transitions in each experiment were confirmed by coincident experiment. In the ^{124}I decay the gamma ray was placed between the 2641 and 603 keV levels. In the ^{124}Sb decay there was the coincident data in which the transition was placed between the 2641 and 603 keV levels /8/, but the placement was denied from another experiment /9/ and was placed from 2039 keV level to the ground state. The placement was the key point to determine the spin of the level, because angular correlation data showed two possibilities of the spin assignment 2 and 3. If the spin is 3 the transition to the ground state is hardly possible and the spin of 2 is acceptable. However, according to Demoidiv et al., their angular distribution from $(n, n'\gamma)$ suggested 3 for the 714 and 791 keV transitions and a mixture of two types of transition 2-2 and 3-2 for the 1436 keV transitions from which they proposed the doublet at 2039 keV. Recently Georgii et al. published (n, γ) reaction data in which they reported that they did not confirm the doublet.

We as evaluators take these facts into account and have to obtain the evaluated data including spin and multipolarity assignments. We reanalyzed the available data to get the spin assignments and the multipolarities of the relating transitions.

3 Reanalyses of angular correlation and distribution data

The gamma rays emitted from the 2039 keV level are 714, 791, 1437 and 2039 keV as seen Figs. 1 through 5. Except for the 2039 keV gamma ray angular correlation data are available for the ^{124}Sb decay, (n, γ) reaction. Angular distribution data are also given for the $(n, n'\gamma)$ and $(\alpha, 2n\gamma)$ reactions. They are usually given by the coefficients, A_2 and A_4, of

$$W(\theta) = 1 + A_2 P_2(\cos\theta) + A_4 P_4(\cos\theta).$$

Table 2: Angular Correlation Data

Cascade	A_2	A_4	References
714-*723*	0.220(19)	0.000(28)	/4/
	0.220(15)	-0.026(30)	/3/
	0.143(14)	0.042(17)	/5/
	0.201(15)	0.040(19)	/6/
	0.39(19)*	0.40(25)*	/11/
714-(723)-*603*	0.094(25)	0.010(30)	/7/
791-*645*	0.280(31)	-0.187(44)	/7/
	1.00(77)*	0.28(67)*	/11/
791-(645)-*603*	0.104(58)	-0.116(79)	/7/
	0.307(65)	-0.114(95)	/5/
1437-*603*	-0.112(64)	-0.214(86)	/7/
	-0.240(60)	0.340(100)	/4/
	0.12(26)*	-0.20(10)*	/11/

The italic figure represents the energy of the gating transition.

*Coefficients of the first gamma rays in the cascades, not including
the coefficient of the gating gamma rays.

Table 3: Angular Distribution Data

Transition	A_2	A_4	References
714	-0.210(11)	0.100(13)	/14/
	-0.09(7)	-0.10(10)	/10/
791	0.012(11)	0.020(16)	/14/
	0.19(7)	-0.02(17)	/10/
1437	0.291(5)	0.055(7)	/14/
	0.11(6)	-0.11(10)	/10/

The measured coefficients are tabulated in Table 2 for the angular correlation data and in Table 3 for the angular distribution data.

The problem is if we can obtain the definitive spin assignment of the level and multipolarities of the transitions from those listed data. As an example the angular correlation and distribution data of the 791 kev transition whose placement in the level scheme has been confirmed was reanalyzed by non-linear fitting taking the mixing ratio as a parameter by the method indicated by Robinson/16/. In the method the parameter is obtained so as to minimize the statistic,

$$S^2 = \sum_i \left[\frac{W(\theta_i)_{exp} - W(\theta_i)_{th}}{\Delta W(\theta_i)_{exp}} \right]^2 ,$$

where $W(\theta_i)_{exp}$ is the measured distribution probability, $W(\theta_i)_{th}$ the theoretical one and $\Delta W(\theta_i)_{exp}$ the error of $W(\theta_i)_{exp}$.

The experimental data, however, are usually given by the A_2 and A_4 values and their errors only as in Table 2 and Table 3. Then the S^2 statistic is calculated using

the covariance of A_2 and A_4 which are able to be estimated from the experimental information as indicated by Robinson /16/.

In this case S^2 is estimated as

$$S^2 = (1 - \rho_{xy}^2)^{-2}(X^2 + Y^2 - 2\rho_{xy}XY).$$

Here
$$X = \frac{A_2 - A_{2,exp}}{\Delta A_{2,exp}}, \quad Y = \frac{A_4 - A_{4,exp}}{\Delta A_{4,exp}}$$
and
$$\rho_{xy} = \frac{\sigma_{24}}{\Delta A_{2,exp}\Delta A_{4,exp}}$$
where σ_{24} is the covariance of $A_{2,exp}$ and $A_{4,exp}$.

The S^2 values for two possible spin assignments taking into account the second (and third) transition's multipolarity that is determined by separate experiment are shown in Figs. 6 through 12.
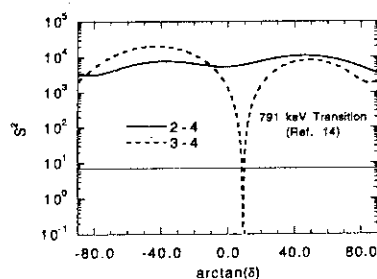
Fig. 6. S^2 curves of angular distribution of 791 keV transition in $(n, n'\gamma)$ reaction.
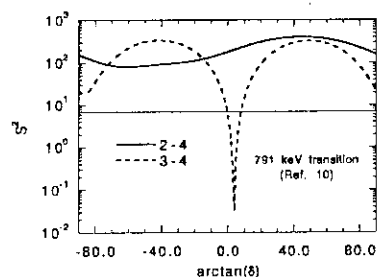
Fig. 7. S^2 curves of angular distribution of 791 keV transition in $(\alpha, 2n\gamma)$ reaction.
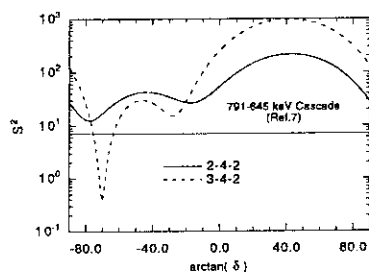
Fig. 8. S^2 curves of angular correlation of 791-645 keV cascade.
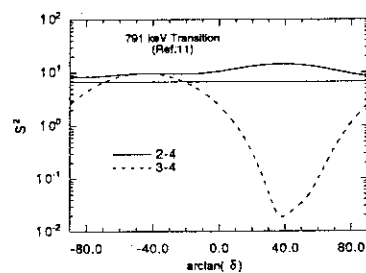
Fig. 9. S^2 curves of angular correlation of 791-645 keV cascade. The coefficients of 645 keV transition are not included as indicated in Table 2.
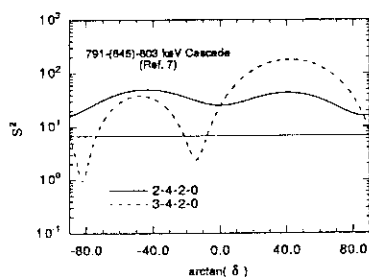
Fig. 10. S^2 curves of angular correlation of 791-(645)-603 keV cascade.
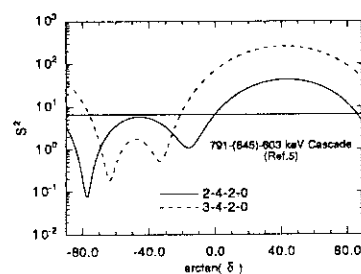
Fig. 11. S^2 curves of angular correlation of 791-(645)-603 keV cascade.
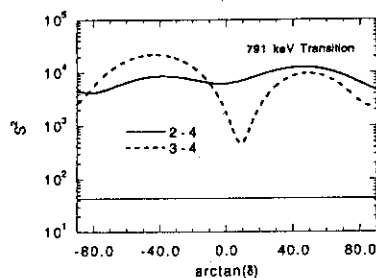
Fig. 12. Averaged S^2 curves of 791 keV transition.

In these figures the horizontal axis is arctan(δ) in unit of degree and the confidence level of 99 % is indicated by straight line. Figures 6 and 7 show the S^2 curves of the angular distribution of the $(n, n'\gamma)$ and $(\alpha, 2n\gamma)$ reactions respectively and Figs. 8 through 11 S^2 curves of the gamma-gamma angular correlation. The distribution and gamma-gamma angular correlation show quite different behavior. According to the S^2 curves of the $(n, n'\gamma)$ and $(\alpha, 2n\gamma)$ reactions spin 3 of the 2039 keV level seems to be acceptable but it is not possible from the angular correlation data to deny the possibility of spin 2. The average of all the data given in Fig. 12 shows no possibility for both of spin 2 and 3. This seems to mean that the data are not consistent with each other. So it is difficult to derive the conclusive remark on the level spin property from those angular correlation and distribution data only. The similar situation is seen in the other transitions.

Angular distribution data generally are more difficult to be obtained than angular correlation data because the orientation information of the level from cascade transitions is not so clear. When the angular correlation data are available, they are generally considered to be more reliable than the angular distribution data. So the angular correlation data are examined. However, even if we limit the arguments on the angular correlation data, the situation is not made clear. The averaged S^2 curves of angular correlation for spin assignments of 2 and 3 are shown in Figs. 13 through 15.
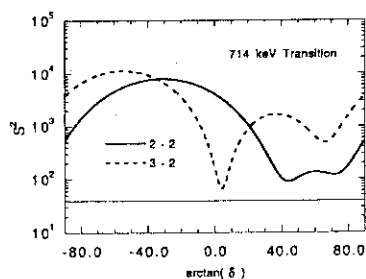
Fig. 13. Averaged S^2 curves of angular correlation for 714 keV transition.
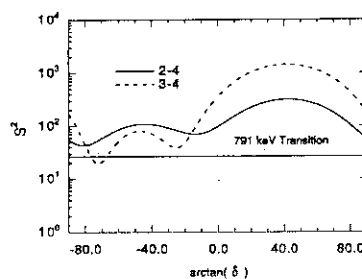
Fig. 14. Averaged S^2 curves of angular correlation for 791 keV transition.
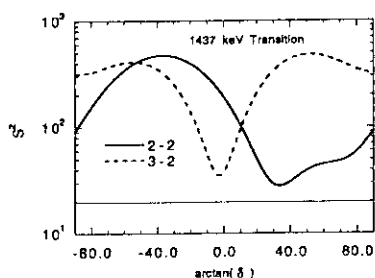
Fig. 15. Averaged S^2 curves of angular correlation for 1437 keV transition.

Figure 13 shows the average of the 714 keV transitions, Fig. 14 that of the 791 keV transitions and Fig. 15 that of the 1437 keV transitions. The confidence level of 99 % is indicated by straight line.

As seen in these figures definitive spin assignment of the 2039 keV level is not able to be derived. To see more detail the parameter plots of A_2-A_4 are shown as a function of mixing ratio δ in Figs. 16 through 22.
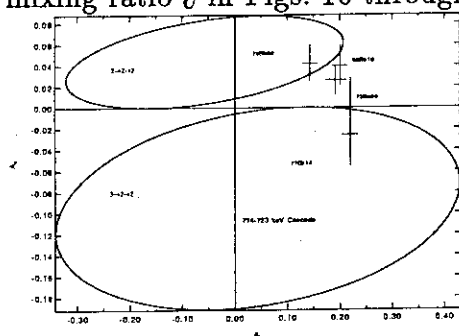
Fig. 16. A_2-A_4 plots for 714-723 keV cascade. Measured data are indicated as 71Gr14/3/, 72Ba38/4/, 79Sh08/5/ and 90Su10/6/. Averaged A_2 and A_4 values are also shown.
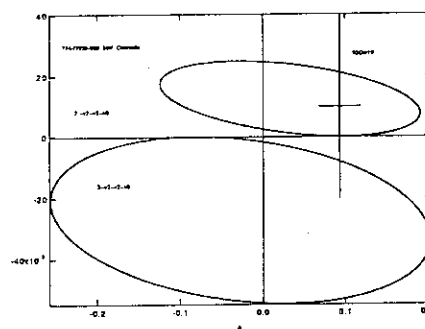
Fig. 17. A_2-A_4 plots for 714-(723)-603 keV cascade. Measured data are indicated as 93Go10/7/.
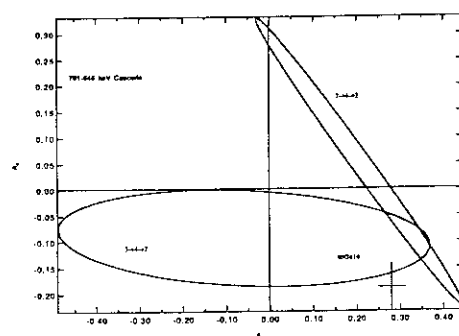
Fig. 18. A_2-A_4 plots for 791-645 keV cascade. Measured data are indicated as 93Go10/7/.
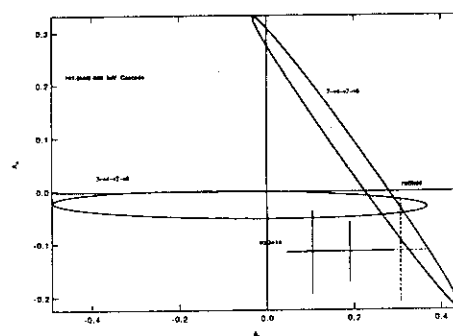
Fig. 19. A_2-A_4 plots for 791-(645)-603 keV cascade. Measured data are indicated as 79Sh08/5/ and 93Go10/7/. Averaged A_2 and A_4 values are also shown.
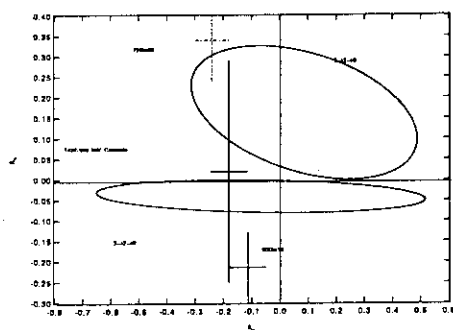
Fig. 20. A_2-A_4 plots for 1437-603 keV cascade. Measured data are indicated as 72Ba38/4/ and 90Su10/6/. Averaged A_2 and A_4 values are also shown.
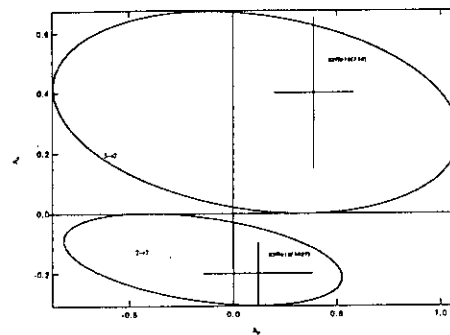
Fig. 21. A_2-A_4 plots for 714 and 1437 keV cascade. 83Ro13(714) is for 714 keV and 83Ro13(1437) for 1437 keV transition/11/.
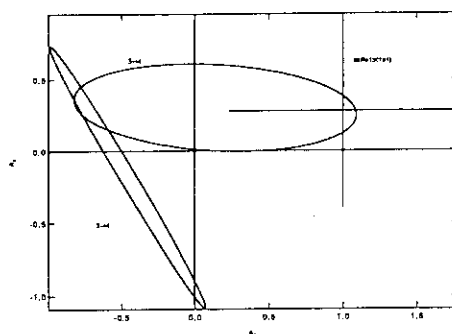
Fig. 22. A_2-A_4 plots for 791 keV transition/11/.

Figure 16 shows the A_2-A_4 plots for the 714-723 keV cascade for the two possible spin sequences 2-2-2 and 3-2-2 with measured data which are designated as 71Gr14 /3/, 72Ba38 /4/, 79Sh08 /5/ and 90Su10 /6/. Of these measured data 71Gr14 and 72Ba38 prefer 3-2-2 transition to 2-2-2 transition, but 79Sh08 and 90Su10 show completely opposite behavior, that is, they prefer 2-2-2 transition. Their averaged A_2 and A_4 values in the figure don't match any of the two spin sequence. The S^2 curves shown in Fig. 13 seem to reflect this situation even if the effects of the 714-(723)-603 keV cascade in Fig. 17, which favors spin sequence of 2-2-2-0 but does not exclude spin sequence of 3-2-2-0 and the 714 keV transition in Fig. 21 which favors 3-2 spin sequence, are taken into account. Similar situation is seen for the 791 keV transition in Figs. 18, 19 and 22. For the 1437 keV transition seen in Figs. 20 and 21 measured data are also scattered. In the 1437-603 keV cascade shown in Fig. 20 one measurement (72Ba38) fits 2-2-0 spin sequence, but another one (93Go13 /7/) prefers 3-2-0 spin sequence. They are inconsistent with each other. Their average taking χ^2 test into account lies on curves of both of the spin sequences.

Taking these results into consideration it seems to be difficult to derive definitive spin assignment from available angular correlation and distribution data. These results, however, are obtained by taking the same energy transition with different cascades such as the 714-723 and 714-(723)-603 keV cascades as equivalent. Then each cascade was treated as different one and the mixing ratio δ of the common transition was compared for the two kinds of spin assignment. Table 4 shows the results for the 714 and 791 keV transitions.

From Table 4 it is said that mixing ratio δ for the 714 keV transition is consistent with each other for the 714-723 and 714-(723)-603 keV cascades of 2-2 spin sequence but

Table 4: Comparison of multipole mixing ratios

	714-723 keV Cascade	714-(723)-603 keV Cascade
714(2-2)	0.96 (+20 -14)	1.14 (+189 -56)
714(3-2)	< -3.26	-0.83 (+40 -224)
	791-645 keV Cascade	791-(645)-603
791(2-4)	-4.00 (+151 -390) or -0.34 (+19 -29)	-5.15 (+222 -880) or -0.33 (+18 -25)
791(3-4)	-2.67 (+41 -54) or -0.69 (+22-542)	-3.94 (+182 -580) or <0.30

not of 3-2 spin sequence. In the case of the 791 keV transition both of the 2-4 and 3-4 spin sequences are consistent for the 791-645 and 791-(645)-603 keV cascades. Therefore the spin of the 2039 keV level is assigned as 2. This assignment is consistent with the gamma transition to the ground state proposed in the [124]Sb decay.

4 Summary

Because the spin of the level emitting the 714 and 791 keV gamma rays was thus confirmed to be 2, the doublet proposal by Demidov et al. lost one of it's footing. As mentioned in Section 2, recent (n, γ) measurement /12/ could not confirm the doublet. From these facts the doublet at 2039 keV is not able to be accepted. The finally determined level scheme is shown in Fig. 23 where the 2039 keV gamma rays are doubly placed; one is between the 2039 keV level and the ground state and the other one between the 2642 and 602 keV levels.
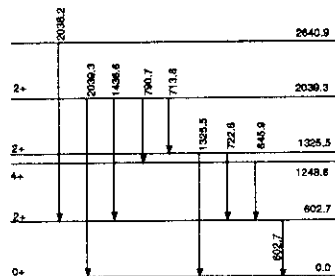
Fig. 23. Partial level scheme of "adopted data" of [124]Te nuclide.
Levels and gamma rays not discussed are omitted.

The intensity of the former gamma ray is weak comparing to the 714 keV gamma ray as seen in the [124]Sb decay in Table1 where the latter gamma ray is not observed. The 2039 keV gamma ray observed in the [124]I decay, (n, γ) and $(n, n'\gamma)$ reactions is mainly from the 2642 keV level. This interpretation is able to explain the inconsistency of the 2039 keV gamma ray intensity observed in different types of experiment.

Acknowledgment

References

[1] R. C. Ragaini, W. B. Walters, and R. A. Meyer, *Phys. Rev.*, **187**, 1721(1969)

[2] D. H. Woods et al. , *Appl. Radiat. Isot.*, **43**, 551(1992)

[3] Z. W. Grabowski, K. S. Krane, and R. M. Steffen, *Phys. Rev.*, **C3**, 1649(1971)

[4] K. R. Baker et al. , *Nucl. Phys.*, **A186**, 493(1972)

[5] A. K. Sharma et al. , *J. Phys. Soc. Japan*, **46**, 1057(1979)

[6] S. S. Rao et al. , *Nuovo Cimento*, **103**, 803(1990)

[7] J. Goswamy et al. , *Appl. Radiat. Isot.*, **44**, 541(1993)

[8] G. Mardirosian and N. M. Stewart, *Z. Phys.*, **A315**, 213(1984)

[9] Y. Jianming, L. Yunzuo, and H. Dailing, *Z. Phys.*, **A331**, 391(1988)

[10] C. S. Lee et al. , *Nucl. Phys.*, **A530**, 58(1991)

[11] S. J. Robinson, W. D. Hamilton, and D. N. Snelling, *J. Phys.*, **G9**, 961(1983)

[12] R. Georgii et al. , *Nucl. Phys.*, **A592**, 307(1995)

[13] A. M. Demidov et al. , *Izvestiya Akademii Nauk SSSR. Ser. Fiz.*, **44**, 135(1980)

[14] L. I. Govor, A. M. Demidov, and I. V. Mikhalov, *Problems of Nuclear Physics and Cosmic Rays*, **32**, 3(1989)

[15] T. Tamura, K. Miyano, and S. Ohya, *Nucl. Data Sheets*, **41**, 413(1984)

[16] S. J. Robinson, *Nucl. Instr. and Meth.*, **A292**, 386(1990)

The First Internet Symposium on Nuclear Data:Paper No.5

3.5 Measurement of Thermal Neutron Cross Section for ^{241}Am(n,f) Reaction

Katsuhei Kobayashi/1/, Shuji Yamamoto/1/, Mitsuharu Miyoshi/2*/,
Itsuro Kimura/2/, Ikuo Kanno/2/, Nobuo Shinohara/3/, and Yoshiaki Fujita/1/

1 Research Reactor Institute, Kyoto University
Kumatori-cho, Sennan-gun, Osaka 590-04, Japan
2 Department of Nuclear Engineering, Kyoto University
Yoshida-honmachi, Sakyo-ku, Kyoto 606-01, Japan
* Present address: GE and Yokogawa Medical System Inc.
4-chome, Asahigaoka, Hino-shi, Tokyo 191, Japan
3 Department of Radioisotopes, Japan Atomic Energy Research Institute
Tokai-mura, Naka-gun, Ibaraki 319-11, Japan

e-mail:koba@rri.kyoto-u.ac.jp

Making use of a standard neutron spectrum field with a pure Maxwellian distribution, the thermal neutron cross section for the ^{241}Am(n,f) reaction has been measured relative to the reference value of 586.2b for the ^{235}U(n,f) reaction. For the present measurement, electrodeposited layers of ^{241}Am and ^{235}U have been employed as back-to-back type double fission chambers. The present result at neutron energy of 0.0253 eV is 3.15 ± 0.097b. The ENDF/B-VI data is in good agreement with the present value, while the JENDL-3.2 data is lower by 4.2%. The evaluated data in JEF-2.2 and by Mughabghab are higher by 0.9% and 1.6%, respectively than the present result. The ratios of the earlier experimental data to the present value are distributed between 0.89 and 1.02.

1. Introduction

Most of the experimental data of the thermal neutron cross section for the ^{241}Am(n,f) reaction were obtained in 1950's to 1970's, and their values were distributed between 2.8 and 3.2 b. These data have mainly measured with reactor neutrons or in a graphite thermal column, and have not always been measured with a pure Maxwellian neutron spectrum field/1-7/. Recently, the new evaluated data have been provided/8-11/.

Measurement of the cross section for the ^{241}Am(n,f) reaction has often confronted with the difficulty by strong alpha-particle activity due to its short half-life of 432 years as alpha-decay. Another suffering for the fission cross section measurement is due to the lack of isotopically pure samples, though utilization of high purity samples is one of the most important things for the nuclear data measurement. Wagemans suggests the usefulness of thermal neutron experiments to check the sample quality/12/. We had experience in obtaining the larger fission cross section of ^{241}Am by using the sample on the market/13/. Through the careful and steady investigation of the ^{241}Am sample by the alpha-ray spectrometry, we found that the problem was mainly caused by the plutonium impurities in the sample/14/.

In the present measurement, after the chemical purification of the ^{241}Am sample, making use of back-to-back (BTB) type fission chambers/15/ with the ^{241}Am and the ^{235}U deposits, the thermal neutron cross section for the ^{241}Am(n,f) reaction has been measured relative to that for the ^{235}U(n,f) reaction in a standard neutron spectrum field of pure Maxwellian distribution of the Kyoto University Reactor (KUR) at Research Reactor Institute, Kyoto University (KURRI), as performed before/16/.

2. Thermal Neutron Spectrum Field

The Kyoto University Reactor (KUR) at KURRI has a thermal neutron facility with a heavy water tank of 1.4 m in length/17,18/. The irradiation room is about 2.4 × 2.4 × 2.4 m^3 and is surrounded by 90 cm thick heavy water concrete shields. The leakage neutrons from the heavy water tank can be used as a thermal neutron source of plane-type in a large space.

Kanda et al. measured the neutron spectrum from the heavy water tank by the time-of-flight technique using a fast chopper/17/. The obtained spectrum showed good agreement with a Maxwellian distribution having neutron temperature of 60°C. The Cd-ratio measured by Au foils with and without Cd-cover of 0.7 mm in thickness was more than 5,000 and epi-thermal neutrons could be almost negligible/17/.

3. Experimental Method

3.1 ^{241}Am and ^{235}U Samples

Americium solution obtained from IAEA was purified at Isotope Products Laboratory, Japan Atomic Energy Research Institute by anion-exchange method using nitric acid-methyl alcohol mixed media/19/, in order to remove uranium, neptunium, plutonium and curium from the americium sample. The purified americium solution and isopropyl alcohol were mixed thoroughly and electrolyzed on a stainless steel disk (28 mm in diameter and 0.2 mm in thickness) for preparing an americium deposit (radioactive area of 20 mm in diameter)/20/. After electrodeposition, the sample was sintered with a gas burner to fix the americium layer on the disk by making americium oxide.

Alpha-ray from the deposit was measured with a silicon surface barrier detector. Impurities of ^{237}Np, $^{238-240}$Pu, ^{243}Am and ^{242}Cm on the americium deposit were not observed in the measured alpha-ray spectrum. Therefore, the isotopic composition of ^{241}Am for the deposit was estimated to be greater than 99.9 %. The number of the ^{241}Am atoms was determined by analyzing the alpha-rays of 5.322 to 5.544 MeV. The 59.5 keV gamma-ray from ^{241}Am was also measured with a HPGe detector. The number of ^{241}Am atoms obtained by both detectors was in good agreement with each other. The result was (1.734±0.020) × 10^{16}, where the errors were estimated by taking account of (i) statistics of the activity measurements, (ii) geometrical detection efficiencies and (iii) uncertainties of the decay data used.

Highly enriched uranium sample (99.91 % of ^{235}U) was also prepared at KURRI by the electrodeposition method. The number of ^{235}U atoms was determined to be (3.283±0.036) × 10^{17} with the alpha-rays of 4.152 to 4.597 MeV and the gamma-ray of 185.7 keV.

3.2 Fission Chambers

The fission chambers employed in the present experiment are composed of two identical parallel plate-type ionization chambers/15/, as shown in Fig.1. Since the back sides of the Am deposit on the stainless steel plate and the reference one are faced each other, it is called back-to-back (BTB) type. The double fission chambers were made of aluminum and filled with a mixed gas of 97 % Ar and 3 % N_2 at the pressure of 1 atm. Since we used the thin ^{241}Am and the thin ^{235}U deposits, fission pulses were clearly discriminated from background ones caused by the alpha-rays.

3.3 Data Taking and Electronics

The chambers were set in the irradiation room and exposed to thermal neutrons for about 10 hours during the nominal power operation of 5 MW of the KUR. The irradiation was repeated by exchanging the ^{241}Am and the ^{235}U sample positions in the chambers. Two identical electronic circuits were employed for both fission chambers, as seen in Fig.2. Fission pulses from the samples were led to their 2048 channel pulse height analyzers through the amplifiers and the discriminators. Each of the fission counts was obtained by integrating the pulse height distribution above the discrimination level.

4. Measurement of the Cross Section

The thermal neutron cross section σ_{th} averaged over the Maxwellian distribution spectrum is defined as

$$\sigma = \frac{\sigma_{th}(V_0)}{1.128}g(T_n)\sqrt{\frac{T_0}{T_n}}$$

where V_0=2,200 m/s, T_0=293.6, T_n is the neutron temperature, and $g(T_n)$ the g-factor. The thermal neutron cross section σ_{Am} for the ^{241}Am(n,f) reaction at a neutron energy of 0.0253 eV (corresponding to a velocity of 2,200 m/s) is obtained as before/16/, by rewriting the above relation as follow:

$$\sigma_{Am} = \frac{C_{Am}}{C_U}\frac{N_U}{N_{Am}}\frac{g_U(T_n)}{g_{Am}(T_n)}\sigma_U$$

where, C_{Am}: fission counts of ^{241}Am, C_U: fission counts of ^{235}U, $g_U(T_n)$: g-factor of ^{235}U(0.9761 ± 0.0012), $g_{Am}(T_n)$: g-factor of ^{241}Am(0.996), σ_U: fission cross section at 0.0253 eV of ^{235}U. The reference fission cross section was taken from the evaluated data file of ENDF/B-VI/8/, and the g-factors were referred to the literature/11/, although Gryntakis/21/ gave 1.0220 for ^{241}Am and 0.9665 for ^{235}U, respectively. The ratio of C_{Am}/C_U data obtained by exchanging the deposit positions of ^{241}Am and ^{235}U in the BTB chambers was 1.04 ± 0.03. We took an average of the values before and after the deposits were exchanged to derive the fission cross section.

5. Results and Discussion

The fission cross section of ^{241}Am for 2,200 m/s neutrons was obtained relative to the reference value of 586.2 b appeared in ENDF/B-VI. The present result is 3.15±0.097 b. Main sources of the uncertainties in the present measurement are due to the statistical

error (0.04 to 0.4 %), assignment of C_{Am} and C_U by integrating the pulse height spectrum above the discrimination level (estimated to be about 1.5 and 1.1 %, respectively), the g-factors for ^{241}Am and ^{235}U, the reference cross section for the ^{235}U(n,f) reaction (estimated to be less than 1 %)/8,11/, the number of atoms in the ^{241}Am and ^{235}U deposits (1.2 % and 1.1 %, respectively), and the assigned correction for the setting position of ^{241}Am and ^{235}U deposits in the BTB chambers (0.25 %). We have estimated that the uncertainty of the g-factor for ^{241}Am is ±1.3 %, because we could see such a difference between the g-factors by Mughabghab/11/ and Gryntakis/21/, while the g-factor for ^{235}U is well determined/11/. Some other uncertainties and corrections may be small and be negligible as before/16/. The total experimental uncertainty of the thermal neutron cross section for the ^{241}Am(n,f) reaction was derived to be about 3.1 % as the root of square sum of the above uncertainties.

The measured result is given in Table 1, and is compared with earlier evaluated and experimental data. The evaluated value in ENDF/B-VI/8/ is in good agreement with the present result, and the JEF-2.2/10/ and the Mughabghab's data are also close to the measurement. The data appeared in JENDL-3.2/9/ and measured by Dabbs et al./7/ are lower by 4.2 % and 2.9 %, respectively. Although the average value of other six earlier experimental data is in agreement with the present measurement within the uncertainty, the data by Gavrilov et al./5/ seem to be lower by 11 % than the present data.

Since we could carefully prepare the ^{241}Am sample and make it pure, the measured cross section may not be disturbed by the undesirable reactions due to the impurities. This would be implied by the fact that the present measurement of the thermal neutron cross section for the ^{241}Am(n,f) reaction is in good agreement with most of the recent evaluated values at 0.0253 eV.

Acknowledgement

References:

1) G. C. Hanna, et al., Phys. Rev., 81, 893 (1951).

2) B. B. Cunningham and A. Ghiorso, Phys. Rev., 82, 558 (1951).

3) E. K. Hulet, et al., Phys. Rev., 107, 1294 (1957).

4) M. A. Bak, et al., Atomnaya Energiya, 23, 316 (1967).

5) V. D. Gavrilov, et al., Atomnaya Energiya, 41, 85 (1975).

6) K. D. Zhuravlev, et al., Atomnaya Energiya, Vol.39, No.4, 285 (1975).

7) J. W. T. Dabbs, et al., Nucl. Sci. Eng., 83, 22 (1983).

8) R. F. Rose(Compiled and Edited), "ENDF-201, ENDF/B-VI Summary Documentation", BNL-NCS-17541, 4th Ed. (ENDF/B-VI) 1991.13.

9) T. Nakagawa, et al., J. Nucl. Sci. Technol., Vol.32, No.12, 1259 (1995), and "Evaluation of Nuclear Data for Americium Isotopes", JAERI-M, 89-008 (1989).

10) C. Nordborg and M. Salvatores, "Status of the JEF Evaluated Data Library", Proc. of International Conf. on Nucl. Data for Sci. and Technol., Gatlinburg, USA, 1994, ORNL, Vol.2, p.680 (1994).

11) S. F. Mughabghab, "Neutron Cross Sections", Vol.1, Neutron Resonance Parameters and Thermal Cross Sections, Part B:Z=61-100, Academic Press. Inc., New York (1984).

12) C. Wagemans, Nucl. Instr. Methods in Phys. Res., A236, 429 (1985).

13) K. Kobayashi, et al., "Fission Cross Section Measurement of Am-241 between 0.1 eV and 10 keV with Lead Slowing-down Spectrometer", Gatlinburg, Tenn., May 1994, J. K. Dickens(Ed.), ORNL, Vol.1, p.242 (1994).

14) M. Miyoshi, "Measurement of Neutron Energy Dependent Fission Cross Section of ^{241}Am", Master Thesis in Japanese, Department of Nuclear Engineering, Kyoto University, 1995.

15) M. Obu, JAERI-M 9757 (1981).

16) A. Yamanaka, et al., J. Nucl. Sci. Technol., Vol.30, No.9, 863 (1993).

17) K. Kanda, et al., Nucl. Instrum. Methods, 148, 535 (1978).

18) K. Kobayashi, et al., J. Nucl. Sci. Technol., Vol.31, No.12, 1239 (1994).

19) S. Usuda and N. Kohno, Separation Science and Technology, 23, 1119 (1988).

20) N. Shinohara and N. kohno, Appl. Radiat. Isot., 40, 41 (1989).

21) E. M. Gryntakis, et al., Radiochimica Acta, 22, 128 (1975).

Table 1 Thermal neutron cross section (2,200 m/s value) for ^{241}Am(n,f) reaction.

Cross Section (b)	Reference	
3.15 ± 0.097	Present	
3.153	ENDF/B-VI('91)	Ref(8)
3.019	JENDL-3.2('95)	Ref(9)
3.177	JEF-2.2('94)	Ref(10)
3.20 ± 0.09	Mughabghab('84)	Ref(11)
3.06 ± 0.19	Dabbs('83)	Ref(7)
3.0	Hanna('51)	Ref(1)
3.0 ± 0.2	Cunningham('51)	Ref(2)
3.13 ± 0.15	Hulet('57)	Ref(3)
3.15 ± 0.10	Bak('67)	Ref(4)
2.8 ± 0.25	Gavrilov('75)	Ref(5)
3.20 ± 0.15	Zhuravlev('75)	Ref(6)
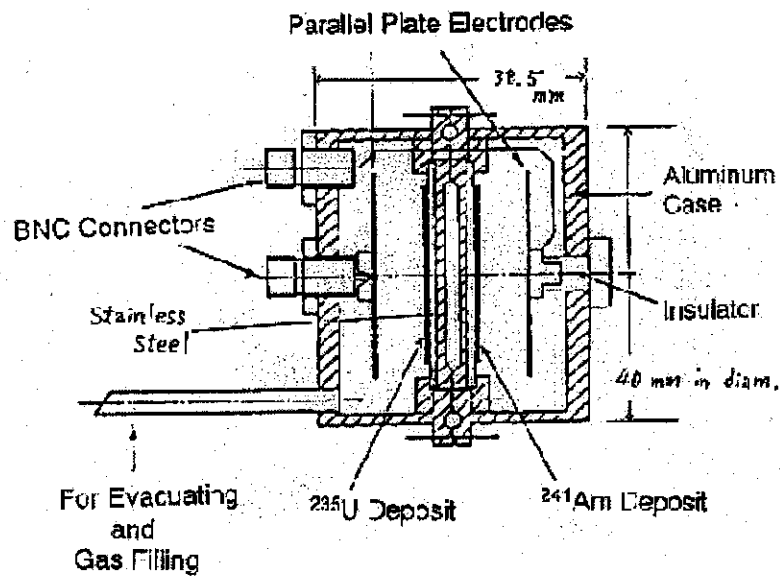
Fig. 1 Cross sectional view of back-to-back type
double fission chambers.
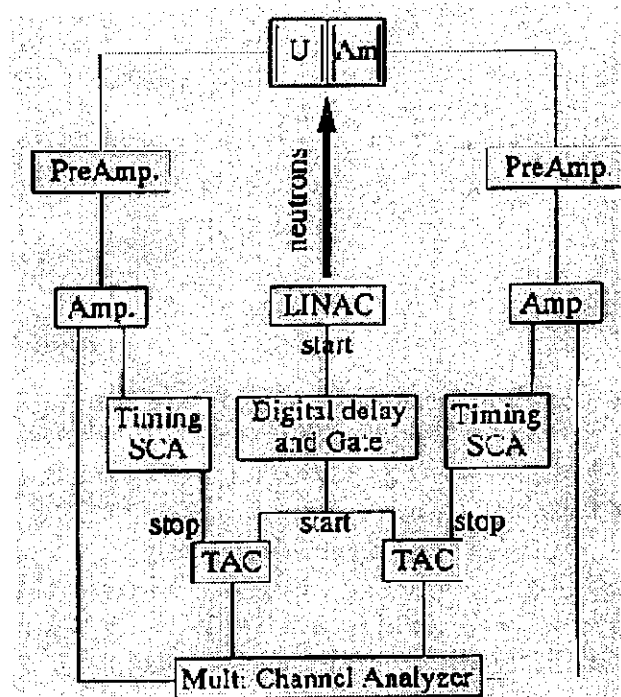
Fig. 2 Block diagram of electric circuit
to measure fission counts with
back-to-back type fission chambers.

The First Internet Symposium on Nuclear Data: Paper No. 006

3.6 Compositional Change of Some First Wall Materials by Considering Multiple Step Nuclear Reaction

Tetsuji NODA, Misako UTSUMI and Mitsutane FUJITA

National Research Institute for Metals

1-2-1, Sengen, Tsukuba, Ibaraki 305 Japan

noda@nrim.go.jp

Abstract

The conceptual system for nuclear material design is considered and some trials on WWW server with functions of the easily accessible simulation of nuclear reactions are introduced. Moreover, as an example of the simulation on the system using nuclear data, transmutation calculation was made for candidate first wall materials such as 9Cr-2W steel, V-5Cr-5Ti and SiC in SUS316/Li_2O/H_2O(SUS), 9Cr-2WLi_2O/H_2O(RAF), V alloy/Li/Be(V), and SiC/Li_2ZrO_3/He(SiC) blanket/shield systems based on ITER design model. Neutron spectrum varies with different blanket/shield compositions. The flux of low energy neutrons decreases in order of V-SiC-RAF-SUS blanket/shield systems. Fair amounts of W depletion in 9Cr-2W steel and the increase of Cr content in V- 5Cr-5Ti were predicted in SUS or RAF systems. Concentration change in W and Cr is estimated to be suppressed if Li coolant is used in place of water. Helium and hydrogen production are not strongly affected by the different blanket/shield compositions.

1 Introduction

Many phenomena cased by neutron irradiation under thermal, fast and fusion reactors can be little understood except through the examination. Easily accessible material information system is required for design of nuclear materials and analyses or simulations of the phenomenon. In order to construct such a system, a project, "Data-Free-Way", has been under way from April in 1990 under the cooperation of National Institute for Metals (NRIM), Japan Atomic Energy Research Institute (JAERI) and Power Reactor and Nuclear Fuel Development Corporation (PNC) /1, 2/. In NRIM besides the cooperated construction of the distributed database for nuclear materials, a simulation system of nuclear transmutation and radioactivation has been created. On the other way, the new system is created on the basis of the substantial concept and data used in IRAC /3/. IRAC was developed in 1984, however the use of it is limited to the inside of NRIM. Therefore, the system as was improved to be easily used mutually through the network. The system consists of a nuclide database with several tables storing the data on nuclear reaction and two simulation processes on transmutation and radioactivation integrated under user-friendly interface. In the near future, the system will be combined with "Data-Free-Way". Transmutation resulting in change of composition, helium and
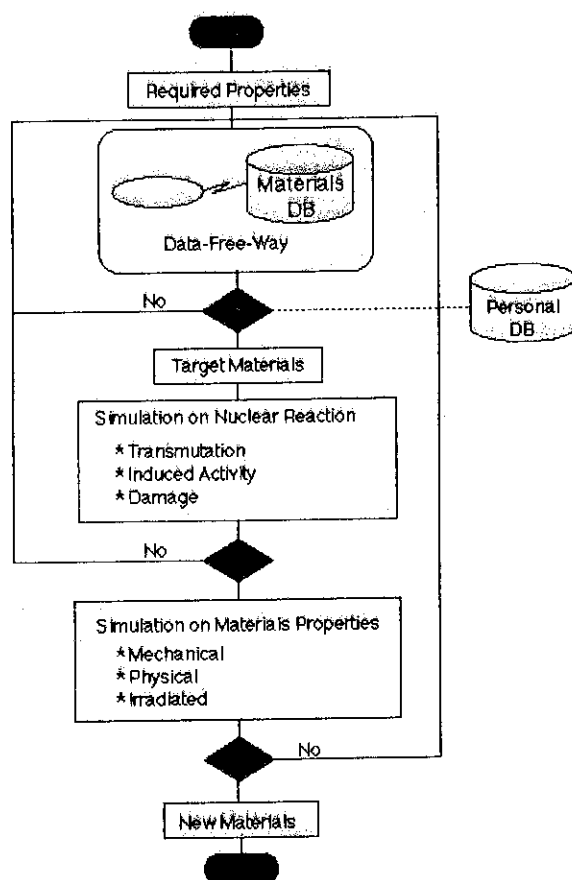
Figure 1: Flow diagram on the concept of the ata system for nuclear material design and selection.

hydrogen production, and induced activity under neutron irradiation is considered as one of severe problems for first wall materials of fusion reactors. The compositional change and gaseous products lead the degradation of materials and induced activity should be lowered from the viewpoint of reactor and environmental safety. Since the degree of transmutation depends on the neutron spectrum /3/, designs of fusion reactor structures such as blanket and shield must be considered to understand the transmutation behaviors of materials. Recently, high burn-up of some metals such as Mo, Re, W, Ta, V are predicted under fusion neutron irradiation conditions /3, 4/. In the present paper, the outline of the new simulation system for nuclear transmutation is introduced. Then, the necessary functions of the system are discussed. Moreover, in order to verify the simulation using the system, the transmutation behaviors of several candidate first wall materials such as 9Cr-2W steels, V-5Cr-5Ti and SiC have been examined for various types of blanket and shields based on ITER design structures /5/ using the simulation calculations /6/.

2 Conceptual Material Information System for Nuclear Materials Design

In the system for nuclear materials, it has to be considered that irradiation in various reactors produces radiation damage as a consequence of the formation of impurity nuclide by transmutation and the displacement of atoms from their equilibrium lattice positions by high energetic neutron or atom collision. Moreover, induced radioactivity by transmutation is an important problem from the viewpoints of the reduction of radiological hazards such as contact maintenance, waste management and environmental safety. The calculation code for the simulation and various databases required for the system is as follows:
Code:

1. Neutron spectrum calculation,

2. Transmutation and Induced activity calculations,

3. Damage calculation.

Database:

1. Facts Material Database,

2. Nuclear Database,

3. Reactor Operation Database,

4. Reactor Design Database,

5. Safety criteria Database.

We are unable to employ readily all of them because these many database are now under construction. Thus, in the present situation, the conceptual flow diagram of a information system for the alloy design and selection of nuclear materials is shown in Fig.1. At the first, candidate materials are selected by using material database such as "Data-Free-Way" /1, 2/. The properties of the materials under irradiation are checked by the three types of simulations and then the other properties will be evaluated. In the data system, it is necessary for the functions for analysis of data retrieved from database and the simulation of various phenomenon in material field. An example of the simulation of transmutation on WWW server is shown in Fig.2. In this system, the results of simulation of the compositional change are easily obtained by the operation of mouse-click.

3 Effect of neutron spectra on the transmutation of first wall materials

3.1 Reactor designs and neutron spectra

The neutron spectrum calculation was made using ANISN for ITER inboard structure design /5/. Fig.3 shows the one dimensional model of mid-plane of the reactor used

Figure 2: Screen of WWW shown the results of simulation on the compositional change by transmutation.

for calculation. The main structures are composed of carbon armor of 2cm, first wall of 1.5cm, blanket/shield of around 150cm, SUS 316 vacuum vessel, super-conducting magnet, and liquid helium vessel. In the present study, the compositions of first wall and blanket/shield materials were changed. In Fig.3, several combinations of blanket/shield materials are shown. ITER originally adopts the blanket(SUS blanket) made of stainless steel, Li_2O with condensed ^6Li, Be and water, and the shield materials made of stainless steel and water, respectively. In the RAF blanket, SUS316 was replaced by 9Cr-2W steel. V blanket was one of options for ITER where V-5Cr-5Ti was considered as the first wall and liquid lithium is used as breeder and coolant. The composition of SiC blanket was taken from ARIES-1 blanket model /7/. The blanket for nuclear material design and selection. is composed of SiC, Li_2ZrO_3, Be and He gas. In the shield, B_4C is added to SiC and He gas to improve the shielding efficiency. Nuclear data library with respectively 42 and 21 energy groups of neutron and gamma ray used was FUSION-40 /8/ based on JENDL-3. The calculation was made with scattering order of P5 and angular quadrature order of S8.

3.2 Transmutation calculation

Transmutation calculation of materials was conducted based on the neutron spectra obtained ANISN using IRAC /4/ code considering several step reactions if reactions have large cross sections. Nuclear data with 42 energy groups used for the transmutation calculation were CROSSLIB /9/, JENDL-3 and FENDL/GA-1.1 /10/. The neutron wall loading was assumed to be 1MW/m^2.
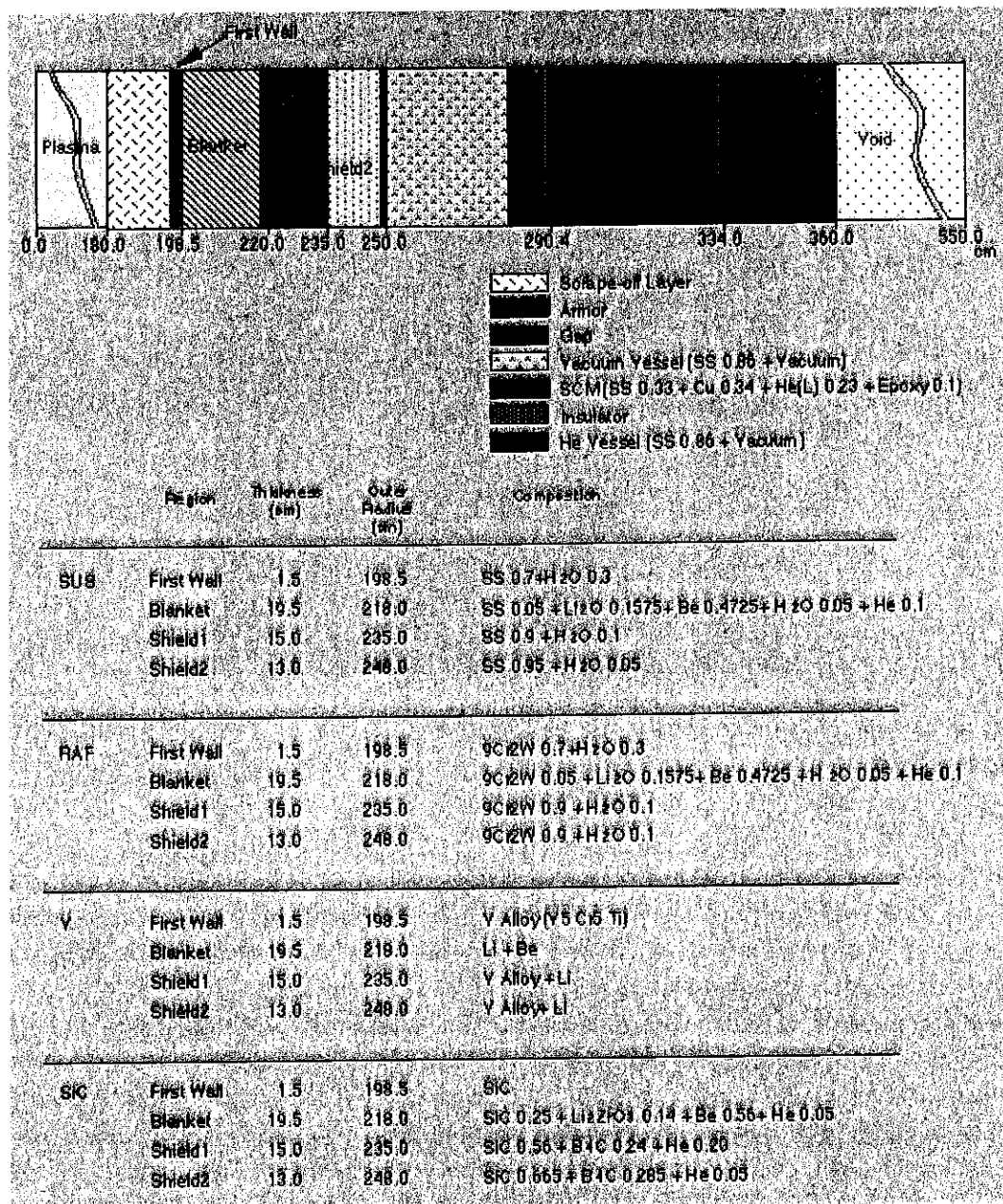
Figure 3: One dimentsional inboard model of a fusion wall reactor based on ITER design and material compositions of several first wall, blanket and shield models.
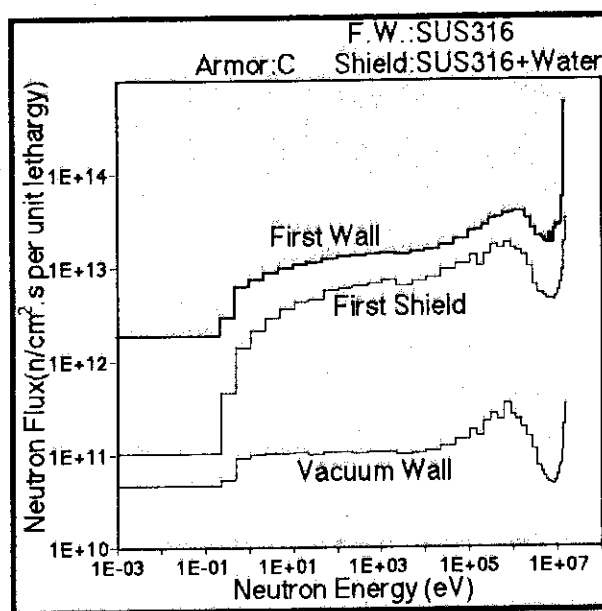
Figure 4: Neutron spectra at first wall, shield and vacuum position under 1 MW/m^2 wall loading.

4 Results

Fig.4 shows the typical neutron spectra at the first wall, the first shield and the vacuum wall for SUS blanket system. The flux of 14 MeV neutron remarkably decreases with the distance from plasma. The relations between 14 MeV neutron flux and the distance from the plasma center for various blanket systems are shown in Fig.5. The flux almost linearly decreases with the distance from the armor. The decay slope is around one order magnitude per 15-17cm independently on the blanket/shield compositions. Fig. 6 shows the neutron spectra at the position of first wall for various blanket/shield compositions. There is a large difference in neutron flux at low energy region between blanket/shield materials. Especially, in the V blanket/shield system where liquid Li is used as a coolant, the sharp decrease of the neutron flux is observed with decreasing neutron energy. Compositional changes of 9Cr-2W steel, V-5Cr-5Ti and SiC for the respective blanket/shield systems with neutron fluence are shown in Fig. 7. The concentration of main constituents does not change remarkably for V-5Cr-5Ti and SiC except helium and hydrogen production. On the other hand, tungsten content in 9Cr-2W steels decreases with the neutron fluence. Next the effect of neutron spectrum on the compositional change of 9Cr-2W steel, V-5Cr-5Ti and SiC were examined for various blanket/shield systems by changing the first wall materials. Table 1 and 2 show the concentration change of some elements in 9Cr-2W steel, V-5Cr-5Ti, and SiC for different blanket/shield systems after 10 MWy/m^2 irradiation. In 9Cr-2W steel, W is transmuted to Re and Os and reduces the concentration below half of an initial value in SUS and RAF systems, while the transmutation is suppressed in V blanket/shield system. Chromium, another main alloying element, is hardly affected in concentration by neutron spectrum, though it is slightly transmuted to Mn. If V-5Cr-5Ti is used as a first wall in SUS or RAF blanket/shield system, Cr content increases by about 40% in contrast to V blanket/shield system where only several % of the increase is predicted.
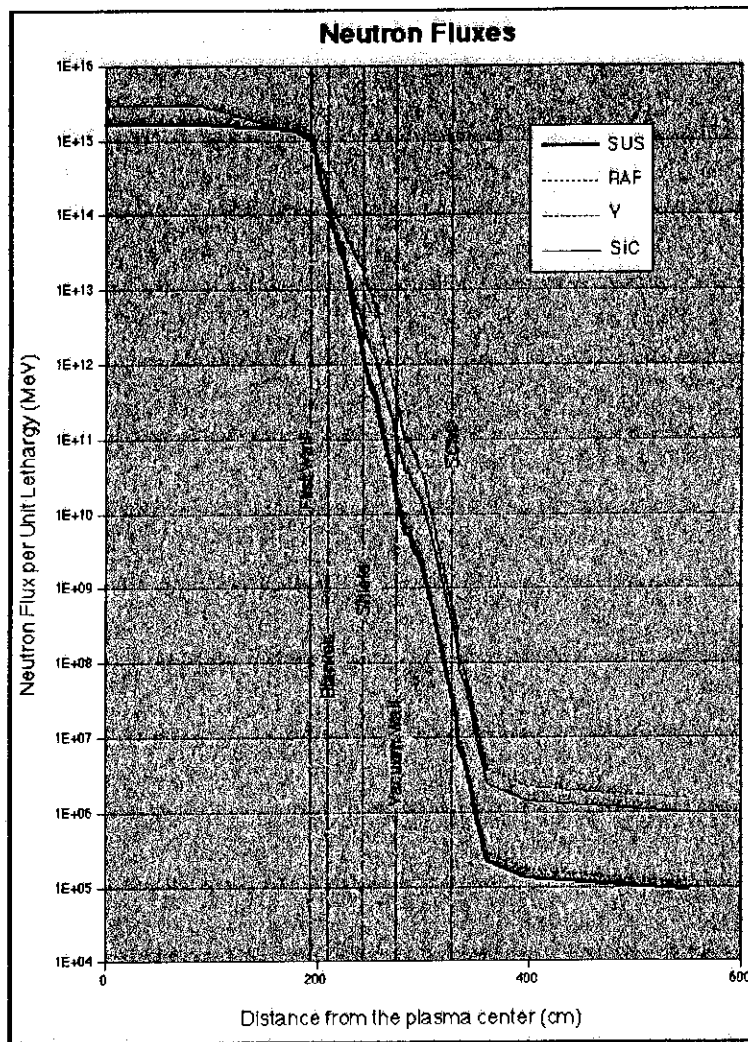
Figure 5: Neutron flux of 14 MeV as a function of the distance from the plasma center.
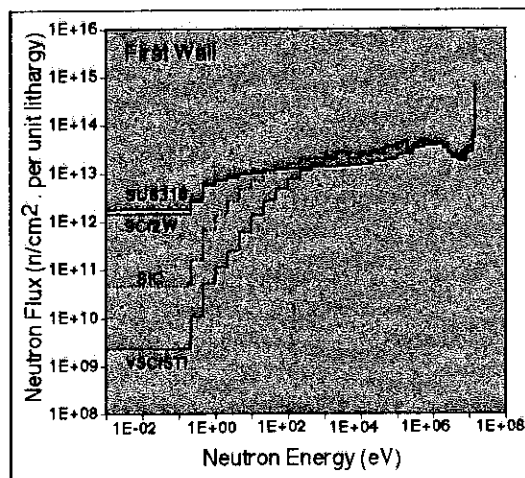
Figure 6: Comparison of neutron spectra at first wall for various blanket/shield compositions.
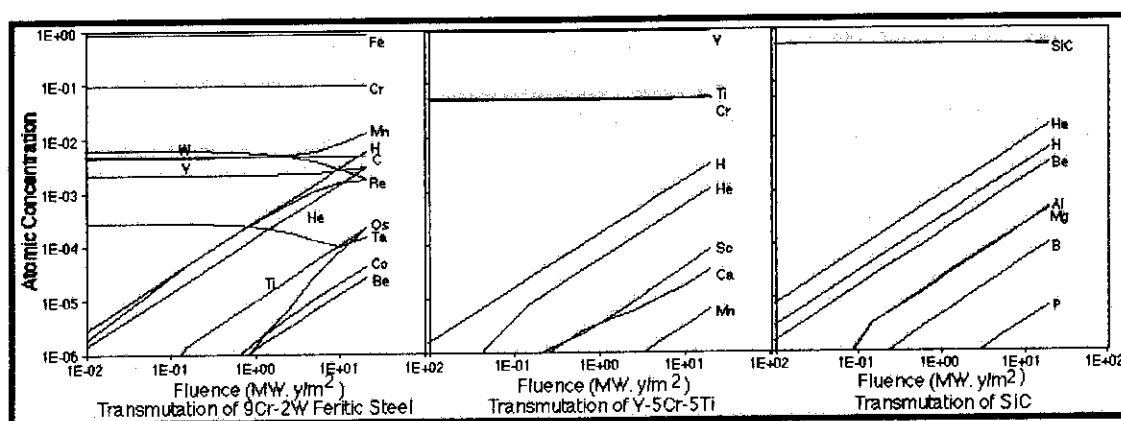
Figure 7: Compositional change of 9Cr-2W steel for RAF, V-5Cr-5Ti for V and SiC for SiC blanket/shield system as a function of neutron fluence.

Titanium concentration is not affected by the neutron spectrum as seen in Table 1. Regarding SiC, compositional change except gaseous products is not obvious. However substantial He formation occurs in SiC for any blanket/shield systems. Helium of about 0.7-0.8 $(appm)$ is produced after 10 MWy/m^2 irradiation. The results in Table indicates that the amounts of He and H are produced in V and SiC blanket/shield systems where fluxes with energies of 100 $keV - 1MeV$ are rather higher than other systems.

Table.1: Concentration change of some elements for candidate first wall materials after 10 MWy/m^2 irradiation in various blanket/shield systems $(appm)$.

Material		Blanket	/	Shield	
	before	SUS	RAF	V	SiC
9Cr2Wsteel					
W	0.61	0.27	0.27	0.48	0.32
Re+Os	0.00	0.17	0.16	0.06	0.14
Cr	9.71	9.80	9.80	9.81	9.81
Mn	0.46	0.81	0.81	0.84	0.81
V5Cr5Ti					
Cr	4.89	6.77	6.47	5.13	5.35
Ti	5.31	5.36	5.36	5.40	5.39
SiC					
Si	50.0	49.6	49.6	49.5	49.5
C	50.0	49.2	49.2	49.1	49.2

Table.2: Helium and hydrogen production for candidate first wall materials after 10 MWy/m^2 irradiation in various blanket/shield systems $(appm)$.

Material	Blanket	/	Shield	
	SUS	RAF	V	SiC
9Cr2Wsteel				
He	1510	1510	1710	1630
H	3020	3020	3440	3300
V5Cr5Ti				
He	476	475	509	537
H	1420	420	1620	1550
SiC				
He	7310	7310	8250	7800
H	2740	2740	5970	3130

5 Discussion

The concentration change of W in 9Cr-2W steel and Cr in V-5Cr- 5Ti due to the trans-
mutation is affected by the neutron spectrum. Especially significant transmutation of
W and V occurs when the neutron flux with low energy is considerably high in such
case of SUS blanket/shield system. As have pointed out in the previous works /1, 2/,
stable isotopes of W have a large cross section for (n, γ) reaction in low energy region
of neutrons. W is composed of 0.135% ^{180}W, 26.4% ^{182}W, 14.4% ^{183}W, 30.6% ^{184}W and
28.4% ^{186}W. Re and Os productions mainly occur through following paths:

$$^{184}\text{W } (n, \gamma) \ ^{185}\text{W } (75.1\text{days}) \rightarrow \ ^{185}\text{Re } (n, \gamma) \ ^{186}\text{Re } (90.64\text{h}) \rightarrow \ ^{186}\text{Os} \qquad (1)$$

$$^{184}\text{W } (n, \gamma) \ ^{185}\text{W} \rightarrow \ ^{185}\text{Re } (n, \gamma) \ ^{186}\text{Re } (n, \gamma) \ ^{187}\text{Re } (n, \gamma) \ ^{188}\text{Re } (16.98\text{h}) \rightarrow \ ^{186}\text{Os}$$
$$(2)$$

$$^{186}\text{W } (n, \gamma) \ ^{187}\text{W } (23.9\text{h}) \rightarrow \ ^{187}\text{Re } (n, \gamma) \ ^{188}\text{Re} \rightarrow \ ^{188}\text{Os} \qquad (3)$$
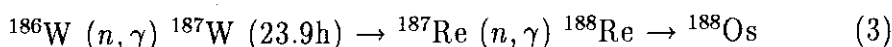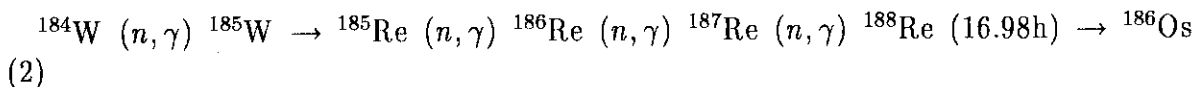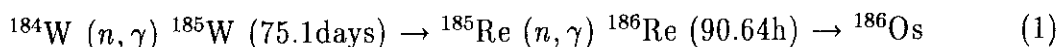
Most Os is produced through reaction of (3). Neutron capture is also significant for the
transmutation of vanadium. Chromium is formed according to the following reaction:

$$^{51}\text{V } (n, \gamma) \ ^{52}\text{V } (3.75\text{min}) \rightarrow \ ^{52}\text{Cr} \qquad (4)$$
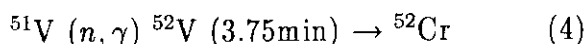
As have seen in Table 2, W depletion and Cr accumulation caused by the trans-
mutation are much affected by the neutron spectrum. Especially neutron fluxes with
energies below around 100 eV determine the degree of concentration change of these
elements. Returning to the neutron spectra of various blanket/shield compositions, it
is necessary to examine the factors controlling spectrum changes. In the present study,
V blanket/shield system showed the lowest flux at low energies of neutrons. In order
to clarify the compositional dependence of the spectrum, V-5Cr-5Ti, structural material
of V blanket/shield system, was replaced by 9Cr-2W steel and the neutron spectrum
was calculated. Fig.8 shows the comparison of neutron spectra for RAF blanket/shield
systems with different coolant and breeder. It is clear that H$_2$O softens the neutron
spectrum resulting the production of more neutrons with low energies than Li. The neu-
tron spectra in this figure suggest that W depletion in 9Cr-2W steel is minimized if Li
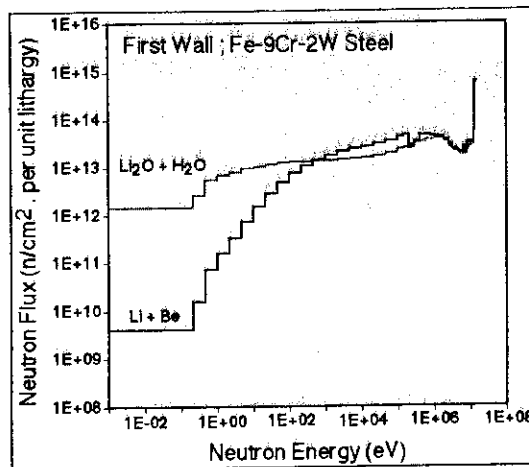
Figure 8: Neutron spectra at the first wall of 9Cr-2W/Li$_2$O H$_2$O and 9Cr-2W/ Li/Be blanket/shield systems.

coolant is used. Considering the real first wall/blanket/shield system, the combination of V alloy/Li$_2$O/H$_2$O is not necessary realistic because vanadium is not stable in water. Therefore Cr accumulation in V alloys will not be significant so far as V alloy/Li/Be system is considered.

6   Conclusion

Concept of data system for nuclear material design was considered. It is necessary that the system consists of a nuclide database storing the data on nuclear reaction and two calculating processes for the simulation of transmutation and radio activation. The transmutation of 9Cr-2W steel, V-5Cr-5Ti and SiC for SUS316/Li$_2$O/H$_2$O(SUS), 9Cr-2W/Li$_2$O/H$_2$O(RAF), V-5Cr-5Ti/Li/Be(V), and SiC/Li$_2$ZrO$_3$/He(SIC) blanket/shield systems were examined by using the simulation calculation code. Conclusions are as follows:

1. Neutron spectrum depends on the composition of blanket/shield materials.

2. The flux of neutrons with energies lower than around 100 eV decreases in order of V

3. Fair amounts of W depletion in 9Cr-2W steel and Cr accumulation in V-5Cr-5Ti were predicted for H$_2$O coolant system.

4. Transmutation of W and V is suppressed if Li coolant is used.

5. Helium and hydrogen production are not strongly affected by the different blanket/shield systems.

References

[1] H.Nakajima, N.Yokoyama, F.Ueno, S.Kano, M.Fujita, Y.Kurihara and S.Iwata, *J. Nucl. Mat.*, **212-215** (1994) 117.

[2] F.Ueno, S.Kano, M.Fujita, Y.Kurihara, H.Nakajima, N.Yokoyama and S.Iwata, *J. Nucl. Sci. Tech.*, **31** (1994) 1314.

[3] L.R.Greenwood and F.A.Garner,*Nucl. Mat.*, **212-215** (1994) 634.

[4] C.B.A.Forty, G.J.Butterworth, J.-Ch.Sublet, *Nucl. Mat.*, **212- 215** (1994) 640.

[5] K.Maki, H.Takatsu, T.Kuroda,Y.Seki, M.Kajiura, N.Tachikawa, R.Saito, H.Kawasaki, *JAERI-M* **91-017** (1991).

[6] T.Noda, H.Araki, F.Abe, and M.Okada, *Trans NRIM,* **30**(1988) 185.

[7] S.Sharafat, C.P.C.Wong and E.E.Reis, *Fusion Technol.*, **19** (1991) 901.

[8] K.Maki, K.Kosako, Y.Seki, and H.Kawasaki, *JAERI-M* **91-072** (1991).

[9] Y.Seki, H.Iida and H.Kawasaki, *JAERI-1280,* (1982).

[10] A.Pashchenko and P.Maclauglin, *FENDL/GA-1.1, IAEA-NDS-148* **Rev.**1 (1993).

The first internet Symposium on Nuclear Data: ISND-1-p007

3.7 Benchmark Validation by means of Pulsed Sphere Experiment at OKTAVIAN

Chihiro ICHIHARA, *Research Reactor Institute, Kyoto University,*
Kumatori, Sennan-gun, Osaka 590-04, Japan
e-mail: chihiro@kuca.rri.kyoto-u.ac.jp

Shu A. HAYASHI, *Institute for Atomic Energy, Rikkyo University,*
2-5-1 Nagasaka, Yokosuka, Kanagawa 240-01, Japan
e-mail: i02220@sinet.or.jp

Itsuro KIMURA, *Department of Nuclear Engineering, Kyoto University,*
Yoshida Honmachi, Sakyoku, Kyoto 606-01, Japan
e-mail: kimura@n-grp.nucleng.kyoto-u.ac.jp

Junji YAMAMOTO *Department of Electric Engineering, Setsunan University,*
17-8 Ikedanakamachi, Neyagawa, Osaka 572, Japan
and
Akito TAKAHASHI *Department of Nuclear Engineering, Osaka University,*
2-1 Yamada-oka, Suita, Osaka 565, Japan
e-mail: akito@nucl.eng.osaka-u.ac.jp

Abstract

The new version of Japanese nuclear data library JENDL-3.2 has recently been released. JENDL Fusion File which adopted DDX representations for secondary neutrons was also improved with the new evaluation method. On the other hand, FENDL nuclear data project to compile nuclear data library for fusion related research has been conducted partly under auspieces of International Atomic Energy Agency (IAEA). The first version FENDL-1 consists of JENDL-3.1, ENDF/B-VI, BROND-2 and EFF-1 and has been released in 1995. The work for the second version FENDL-2 is now ongoing. The Bench mark validation of the nuclear data libraries have been performed to help selecting the candidate for the FENDL-2. The benchmark experiment have been conducted at OKTAVIAN of Osaka university. The sample spheres were constructed by filling the spherical shells with sample. The leakage neutron spectra from sphere piles were measured with a time-of-flight method. The measured spectra were compared with the theoretical calculation using MCNP 4A and the processed libraries from JENDL-3.1, JENDL-3.2, JENDL Fusion File, and FENDL-1. JENDL Fusion File and JENDL-3.2 gave almost the same prediction for the experiment. And both prediction are almost satisfying for Li, Cr, Mn, Cu, Zr, Nb and Mo, whereas for Al, LiF, CF2, Si, Ti Co and W there is some discrepancy. However, they gave better prediction than the calclations using the libary from FENDL-1, except for W.

1 Introduction

Nuclear data libraries are of essential importance for designing nuclear fusion reactors. For selecting an suitable evaluated nuclear data set for the future requirement including a fusion task, FENDL nuclear data project is now being carried out under the auspices of nuclear data section of IAEA. After the first release of FENDL/E-1.0 /1/, the selection of the next candidate file had already started. Recently, several nuclear data files have been published in the world. JENDL-3.2 /2/ has been released in 1995 as the second revision of JENDL-3 /3/. JENDL Fusion File /?/ has been released as the special purpose file of JENDL-3.2 by adding DDX representation of secondary neutrons. As these files are positive candidate for the next FENDL libraries, it is important to make benchmarking these data files. In this paper, the calculations using cross section libraries processed from JENDL Fusion File, JENDL-3.2 and FENDL/E-1.0 are compared with the pulsed sphere experiment conducted at OKTAVIAN /5/ of Osaka university in order to validate neutron cross section data for several nuclide and elements including important elements for fusion reactors.

2 OKTAVIAN Experiment

Experiment have been conducted at OKTAVIAN, an intense neutron source facility of Osaka university. Leakage neutron spectrum measurement from spherical samples has been performed by means of time-of-flight technique. The measured samples were Li, LiF, (CF2)n, Al, Si, Ti, Cr, Mn, Co, Cu, Zr, Nb, Mo and W. All samples were packed in spherical shells made of stainless steel or normal steel. The outer radii of the sample piles were 28 cm for Nb, 40 cm for Li, (CF2)n, Al, Si, Ti, Cr, Co and W, 60 cm for Si, and 61 cm for LiF, Cu, Mn and Mo. The 40 cm piles and 60 cm pile are equipped with a spherical void 10 cm in radii at their centers and a cylindrical hole for a OKTAVIAN beam duct, whereas 28 cm and 61 cm piles have only cylindrical hole for a beam duct. The geometris of 40 cm piles, 60 cm pile and 61 cm piles are shown in **Figs. 1, 2 and 3**, respectively.
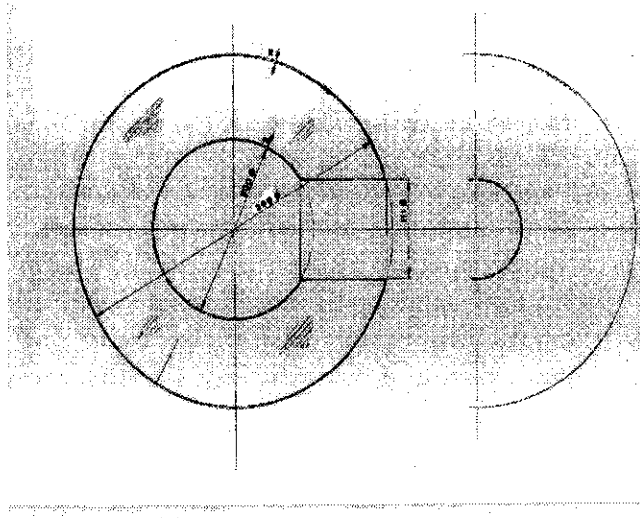
Figure 1: Geometry of 40 cm pile

In the Table-1, apparent density, thickness of the sample in cm and units of mean free path for 14 MeV neutrons of each sample materialare listed. The experimental arrangement is shown in **Fig.1**. An NE218 liquid scintillation counter of 12.7 cm in diameter and 5.1 cm thick was used as a neutron detector and was located about 11 m from the center of a spherical sample. The detector was shielded with B4C, paraffin blocks and heavy concrete

Table 1: List of sample piles

sample	diameter (cm)	weight (kg)	apparent density (g/cm3)	sample (cm)	(MFP)
Li	40	14.3	0.534	9.8	2.9
LiF	61	198.0	1.79	27.5	3.5
TEFLON	40	34.7	1.30	9.8	0.7
Al	40	32.8	1.22	9.8	0.5
Si	40	34.85	1.30	9.8	0.55
Si	60	138.05	1.30	20.0	1.1
Ti	40	41.20	1.54	9.8	0.5
Cr	40	99.7	3.72	9.8	0.7
Mn	61	480.0	4.37	27.5	24.7
Co	40	52.0	1.94	9.8	0.5
Cu	61	675.0	6.01	27.5	4.7
Zr	61	311.9	2.84	27.5	2.0
Nb	28	47.7	4.39	11.2	1.1
Mo	61	236.0	2.15	927.5	1.5
W	40	118.6	4.43	9.8	0.8

blocks as shown in **Fig.4**.

A pre-collimator made of polyethylene and iron multi-layers was used to reduce background neutrons (**Fig.5**). The detail of the experiment have been explained previously /6/ and /7/.
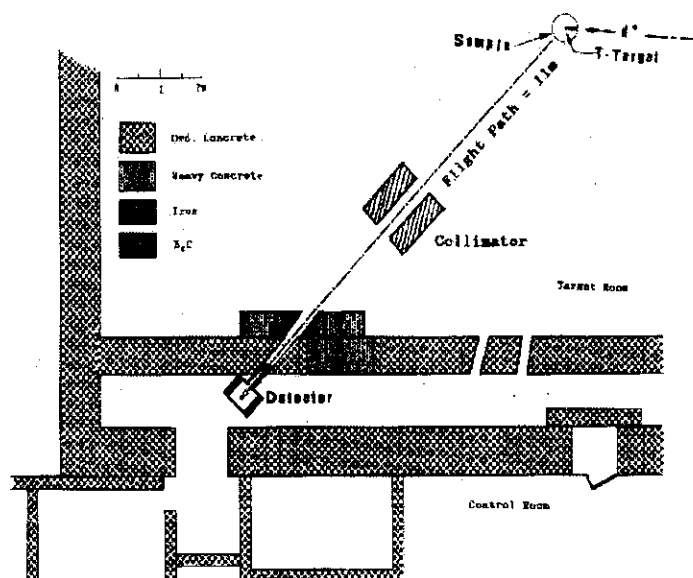
Figure 6: Experimental arrangement at OKTAVIAN
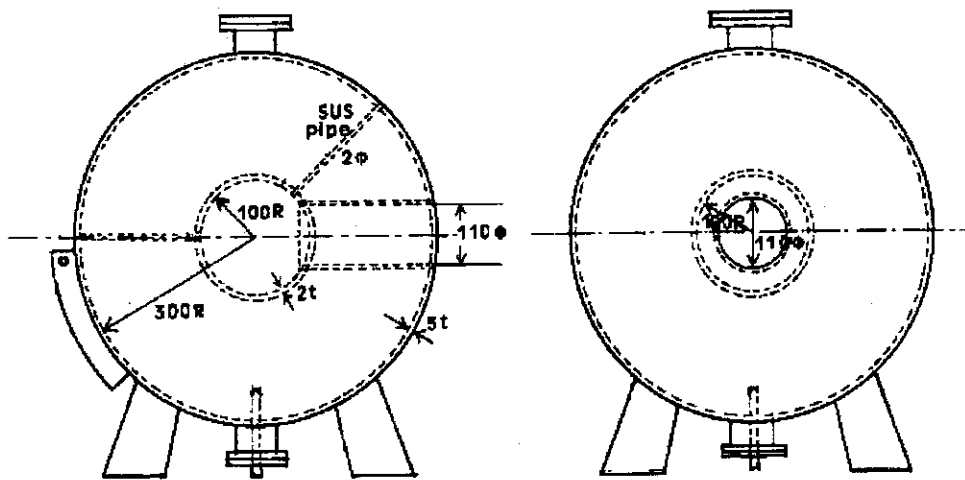
Figure 2: Geometry of 60 cm pile
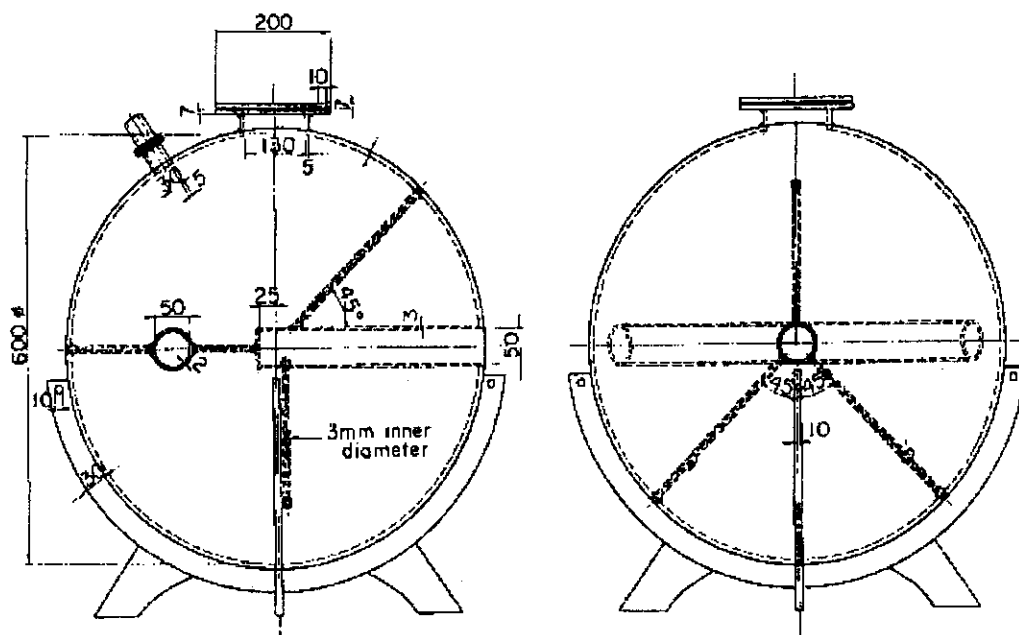
Figure 3: Geometry of 61 cm pile

Figure 4: Neutron detector and surrounding shielding
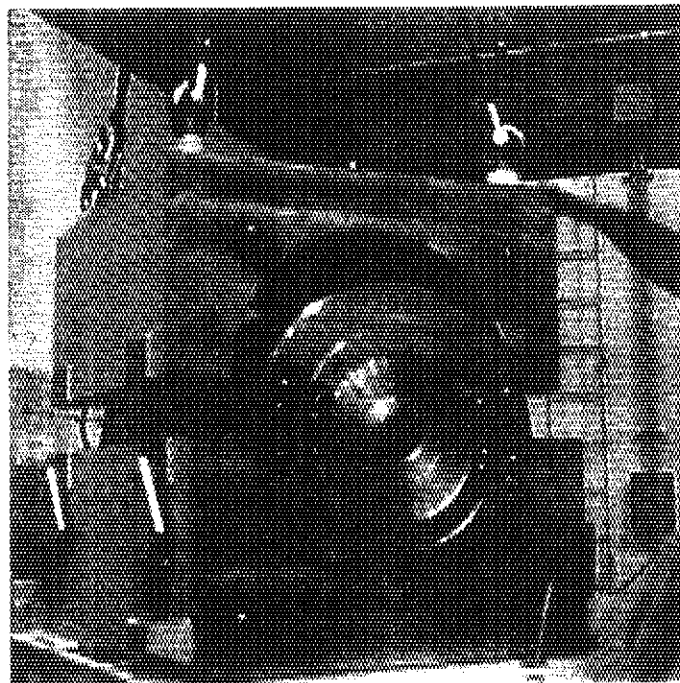
Figure 5: Polyethilene-iron pre-collimator

3 calculation

3.1 Data libraries

Neutron libraries used for the calculation were, 1) three JENDL based libraries - FSXLIB-J3 /10/ from JENDL-3.1, FSXLIB-J3R2 /11/ from JENDL-3.2 and FSXLIB-JFF /12/ from JENDL Fusion File and FENDL/MC1 /13/ from FENDL/E-1.0 which consists of ENDF/B-VI /14/, JENDL-3.1 and BROND-2 /15/. JENDL-3.2 consists of revised evaluation after the variety of benchmark tests of JENDL-3.1. JENDL-3.2 employs ENDF-6 format instead of ENDF-5 format which is used in JENDL-3.1. JENDL Fusion File was released as one of a special purpose file of JENDL-3.2 by adopting DDX representation in File 6 and with including several new evaluations.

3.2 Calculation code

The theoretical calculation was performed using a continuous energy Monte Carlo code MCNP4A /9/. The source was assumed as an isotropic point source and surface crossing tally was adopted to get the calculated results.

4 Results

The measured and calculated results are given in the Figs.7 to 21. Each figure consists of experimental result, calculation using MCNP4A and JENDL Fusion File, JENDL-3.2, JENDL-3.1 and FENDL-1. In adition to the measured and calculated spectra, C/E values of the integrated neutron flux between 16 and 10 Mev, 10 and 5 MeV, 1 and 5 MeV, 0.1 and 1 MeV are given at the bottom of the figure.

4.1 Li 40 cm sphere
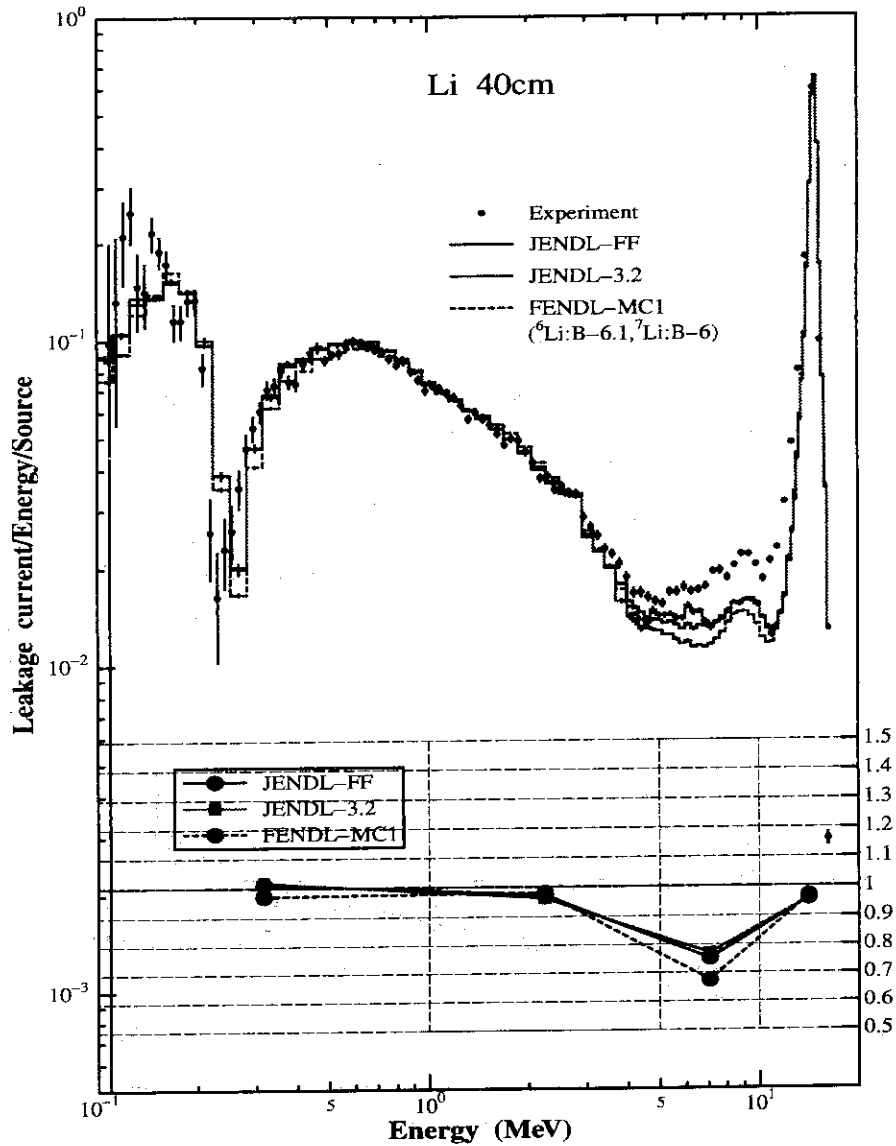
Figure 7: Experimental and calculated spectrum from Li 40 cm sphere

There is little difference among calculations using different nuclear data. Except for minor disagreement between experiment and calculations between 4 MeV and 12 MeV, each calculation predicts the experiment pretty well. It can be concluded that all data can predict the experiment satisfactorily.

4.2 LiF 40 cm sphere
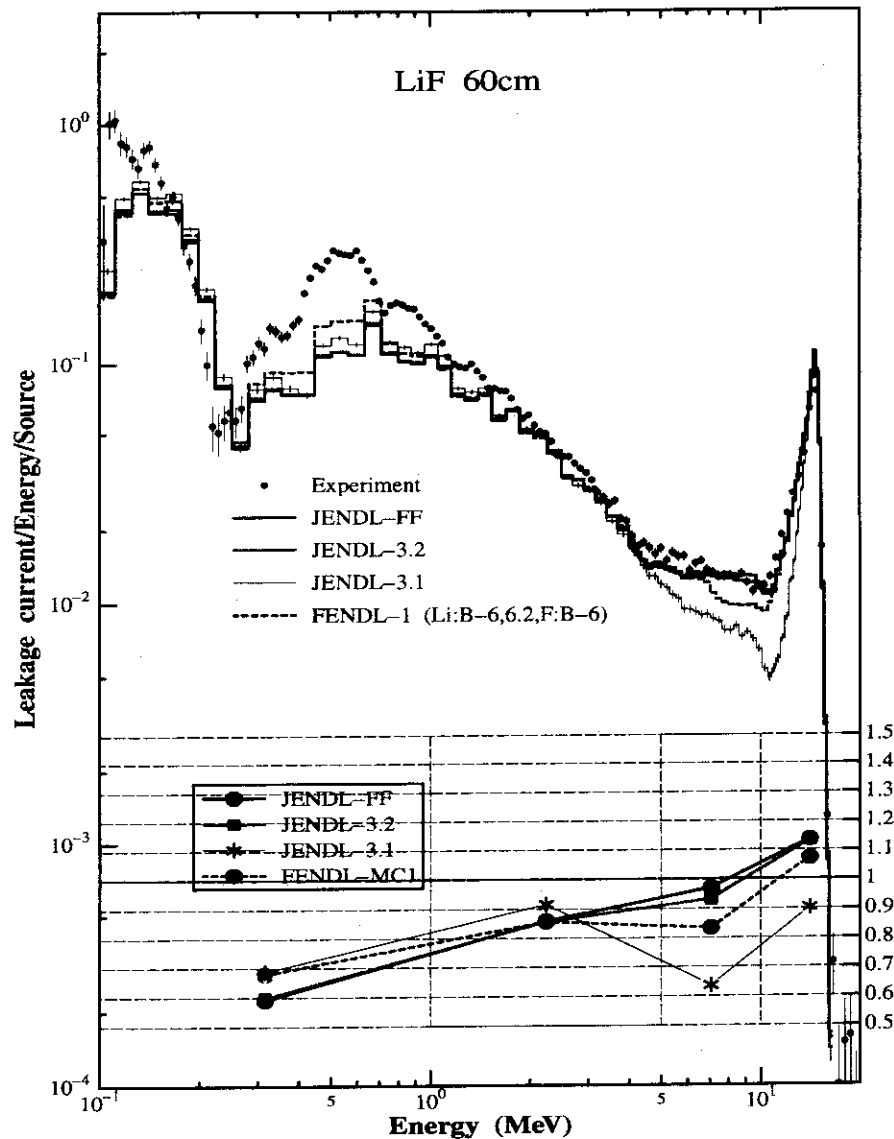
Figure 8: Experimental and calculated spectrum from LiF 61 cm sphere

Though all Li nuclear data predict the experiment pretty well, all calculations for LiF are unsatisfactory. There is little difference among calculations using JENDL-3.2, JENDL Fusion-file and EENDL-MC1. There is severe discrepancy between 4 and 12 MeV, and below 1 MeV region. It can be considered that the fluorine nuclear data in all libraries are responsible for such large discrepancy.

4.3 CF2
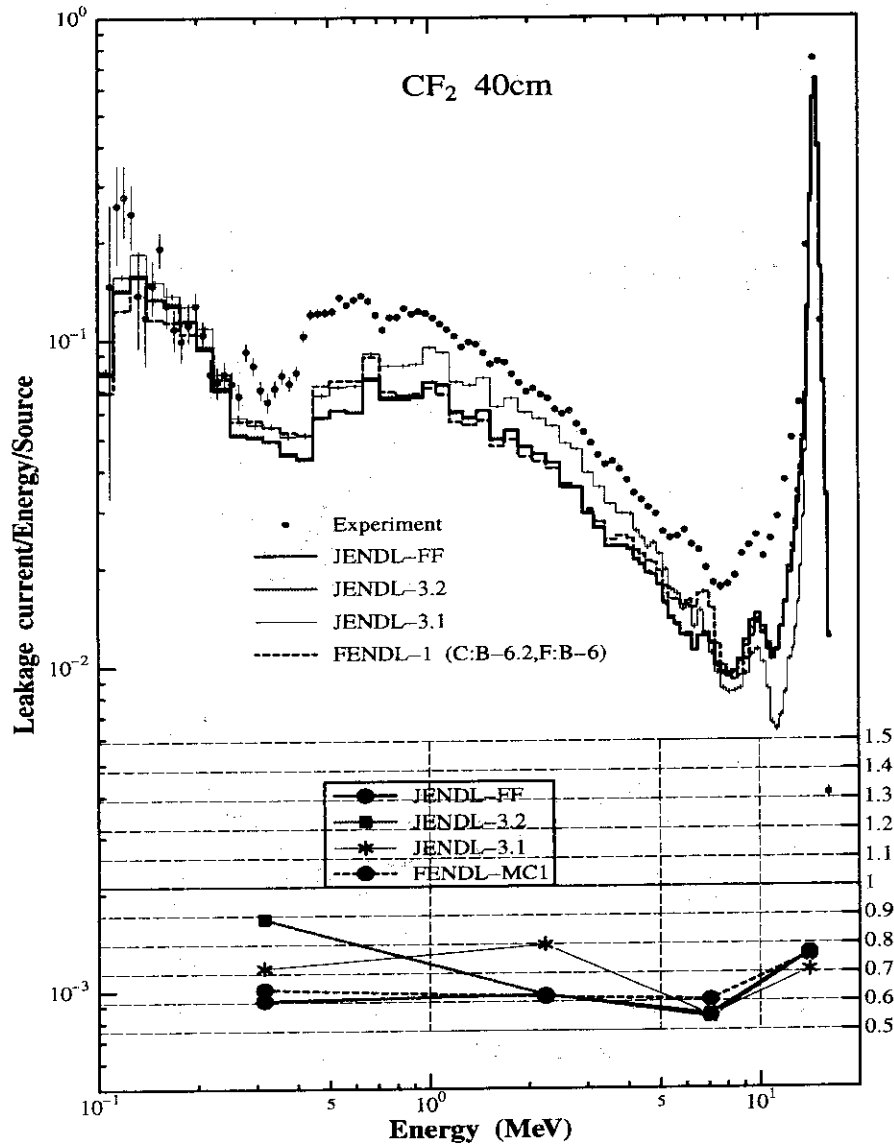
Figure 9: Experimental and calculated spectrum from TEFLON 40 cm sphere

Similar to the LiF case, all calculations can not give satisfactory prediction. The agreement is even poorer than the LiF calculation. The calculations underestimate the experiment for overall energy region. Fluorine nuclear data can be responsible for the discrepancy.

4.4 Al
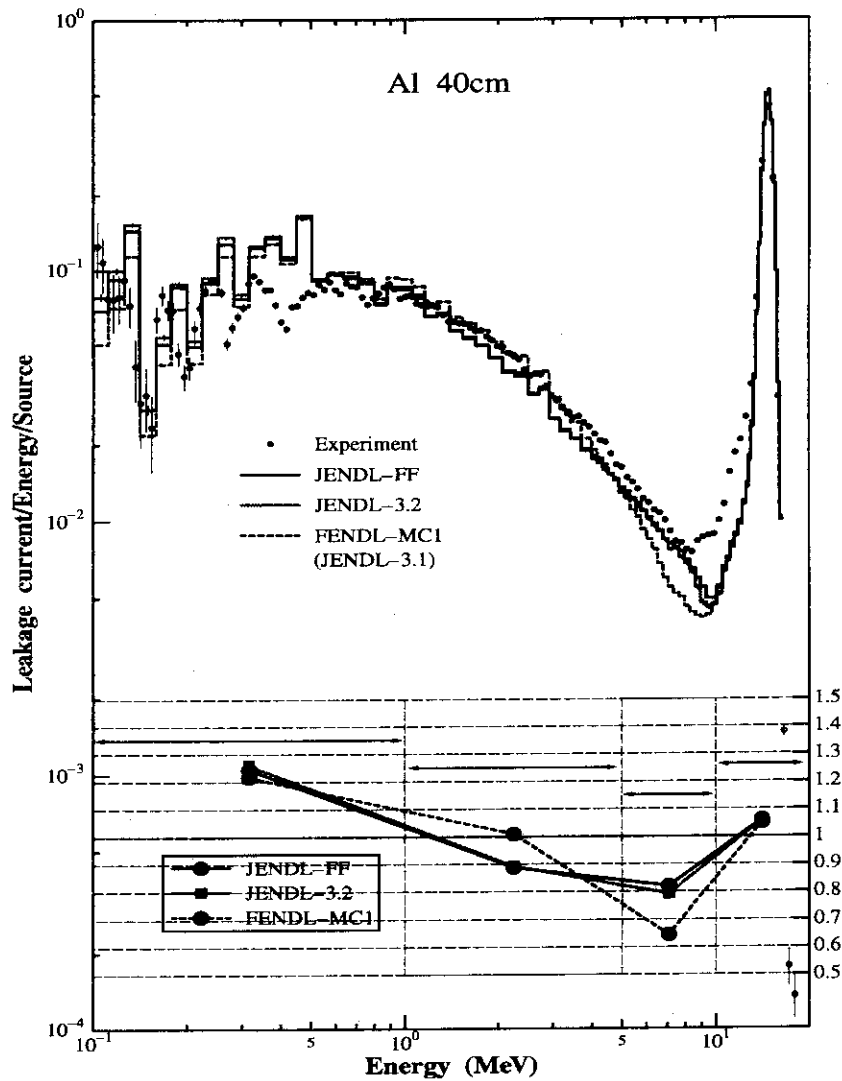
Figure 10: Experimental and calculated spectrum from Al 40 cm sphere

Both JENDL-3.2 and JENDL Fusion File give a good prediction. But for the enrgy range between 8 and 12 MeV where very few neutrons are existing and lower than 0.5 MeV where the complicated structures begin to appear, the C/E ratio differ from unity by about 20%. The prediction of FENDL-MC1 is generally as good as other two libraries, but is worse between 5 and 10 MeV.

4.5 Si 40 cm sphere
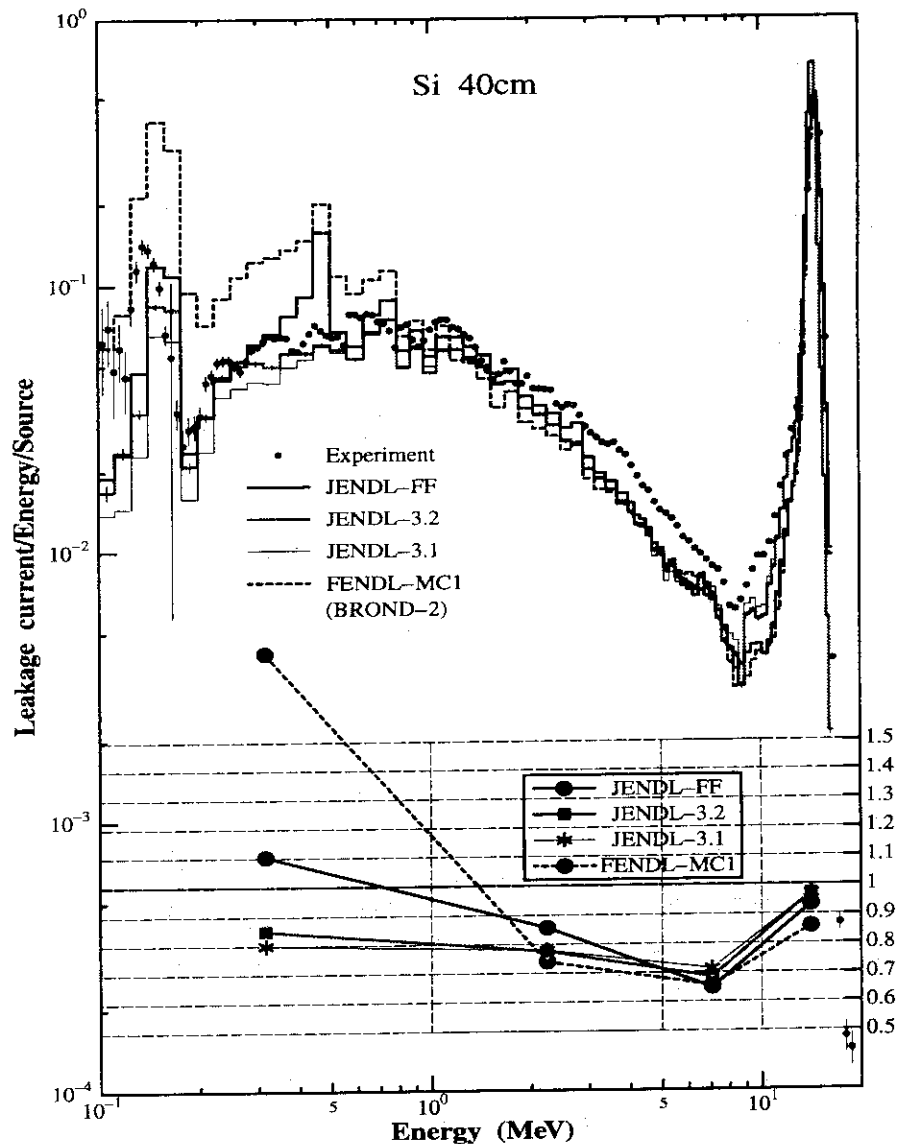
Figure 11: Experimental and calculated spectrum from Si 40 cm sphere

Though there is general resemblance in the shape of the spectra, all calculations underestimate the experiment by as much as 30 % between 1.5 MeV and 12 MeV energy range. There is severe overestimation below 1 MeV region in the calculation using FENDL-MC1, whereas other calculations give fair prediction in this enrgy range.

4.6 Si 60 cm sphere
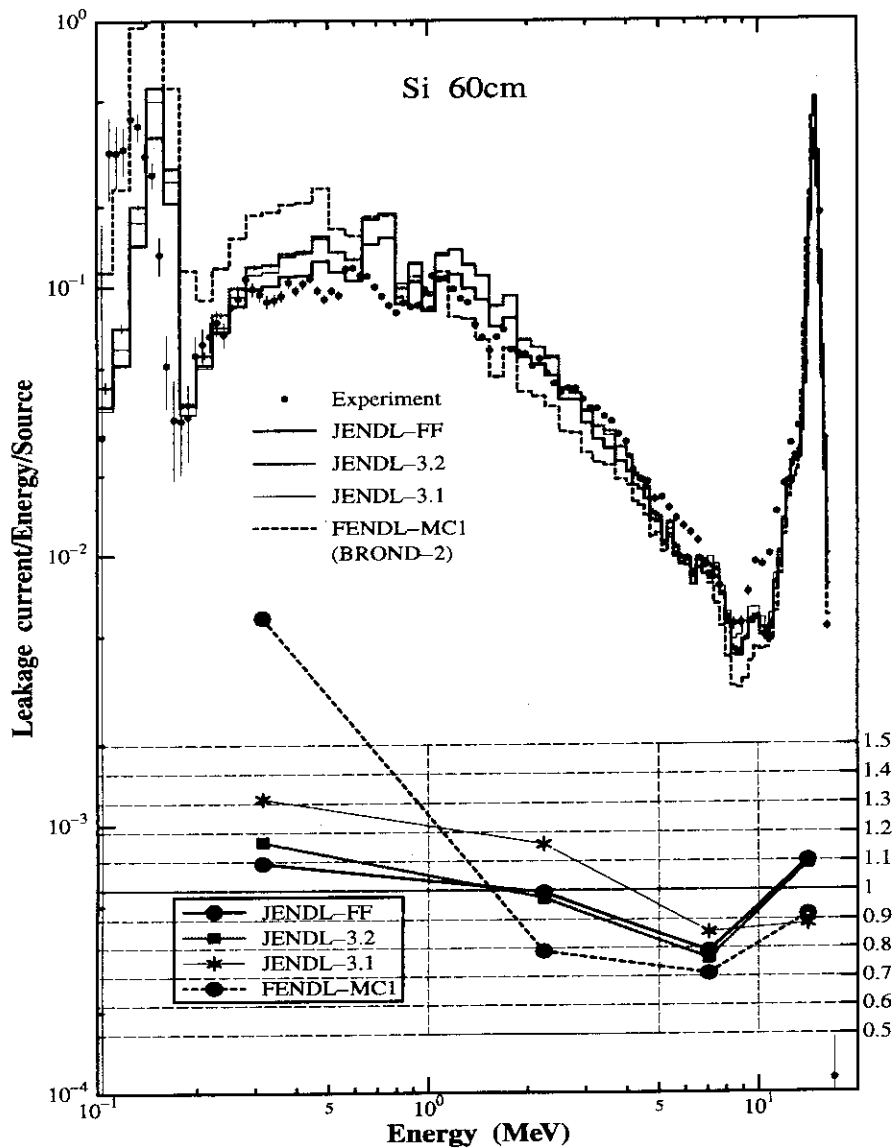
Figure 12: Experimental and calculated spectrum from Si 60 cm sphere

The underestimation appeared in the 60 cm Si sphere case is not as big as that in 40 cm Si sphere case. However, overestimation below about 1 MeV energy region is slightly larger than that of 40 cm sphere.

4.7 Ti
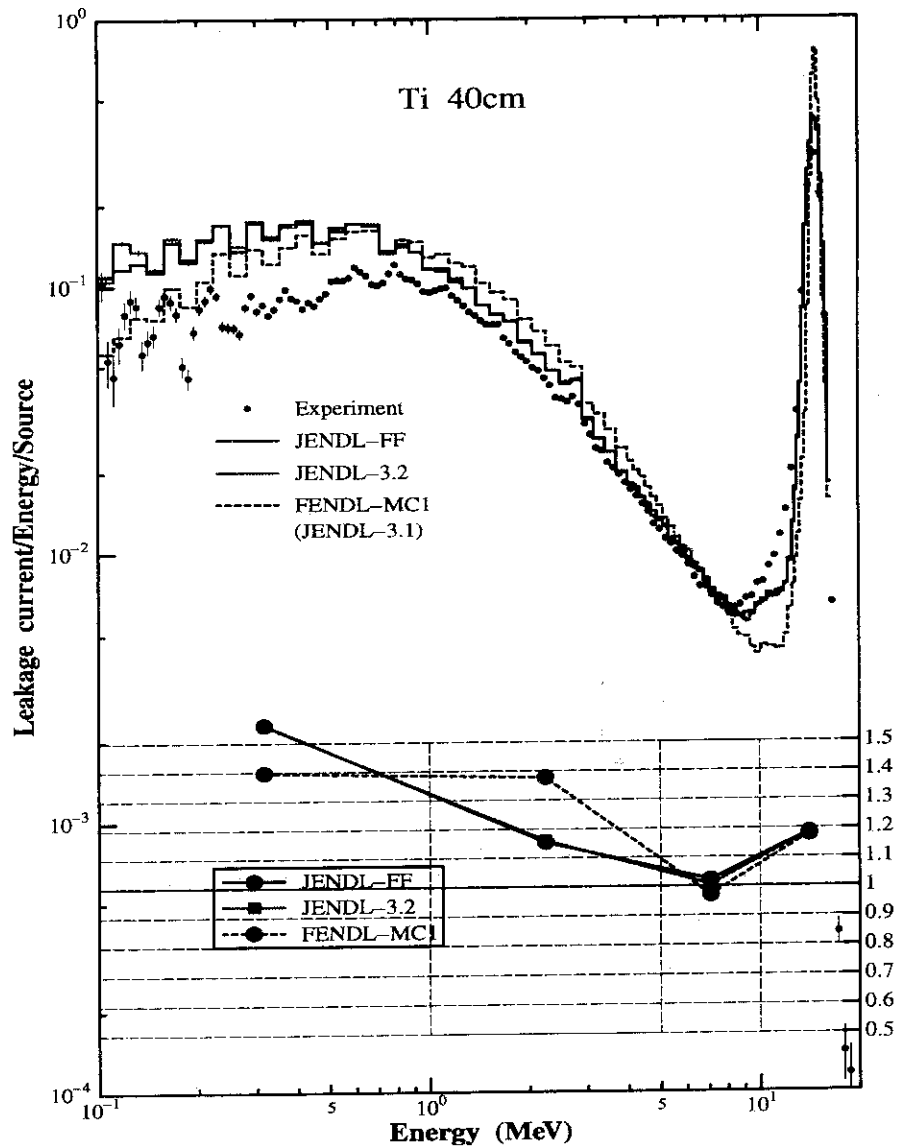
Figure 13: Experimental and calculated spectrum from Ti 40 cm sphere

All libraries give erroneous calculation resulting in 20 to 40 % discrepancy in integrated spectrum for JENDL-3.1 and 20 to 60 % for JENDL-3.2 and JENDL Fusion File.

4.8 Cr
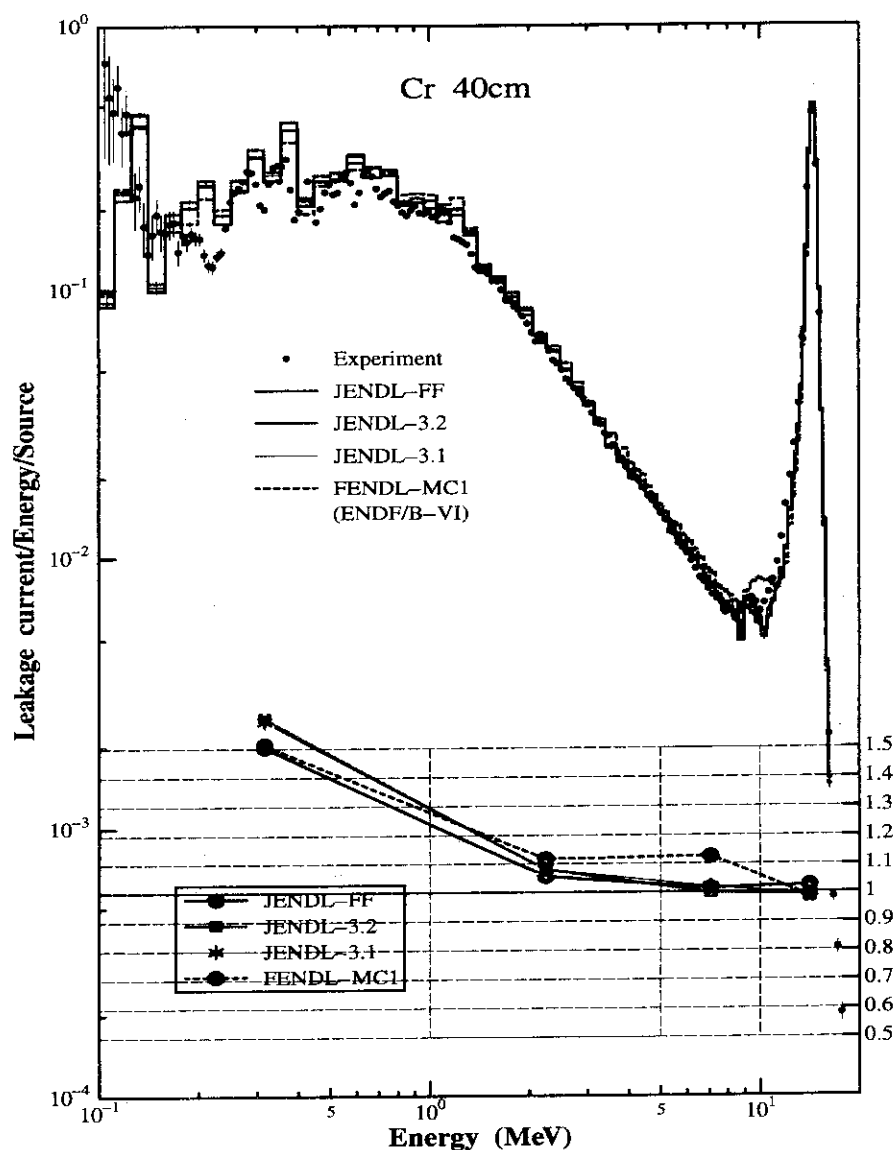
Figure 14: Experimental and calculated spectrum from Cr 40 cm sphere

Calculated spectra with all nuclear dat alibraries above 1 MeV are pretty satisfactory. Especially three JENDL based libraries give good prediction within 5 % of discrepancy from the measured values. FENDL-MC1 prediction is a little bit worse, but it is satisfactory enough. Pretty large disagreement is observed above 1 MeV where complicated structure is dominant in the spectra.

4.9 Mn
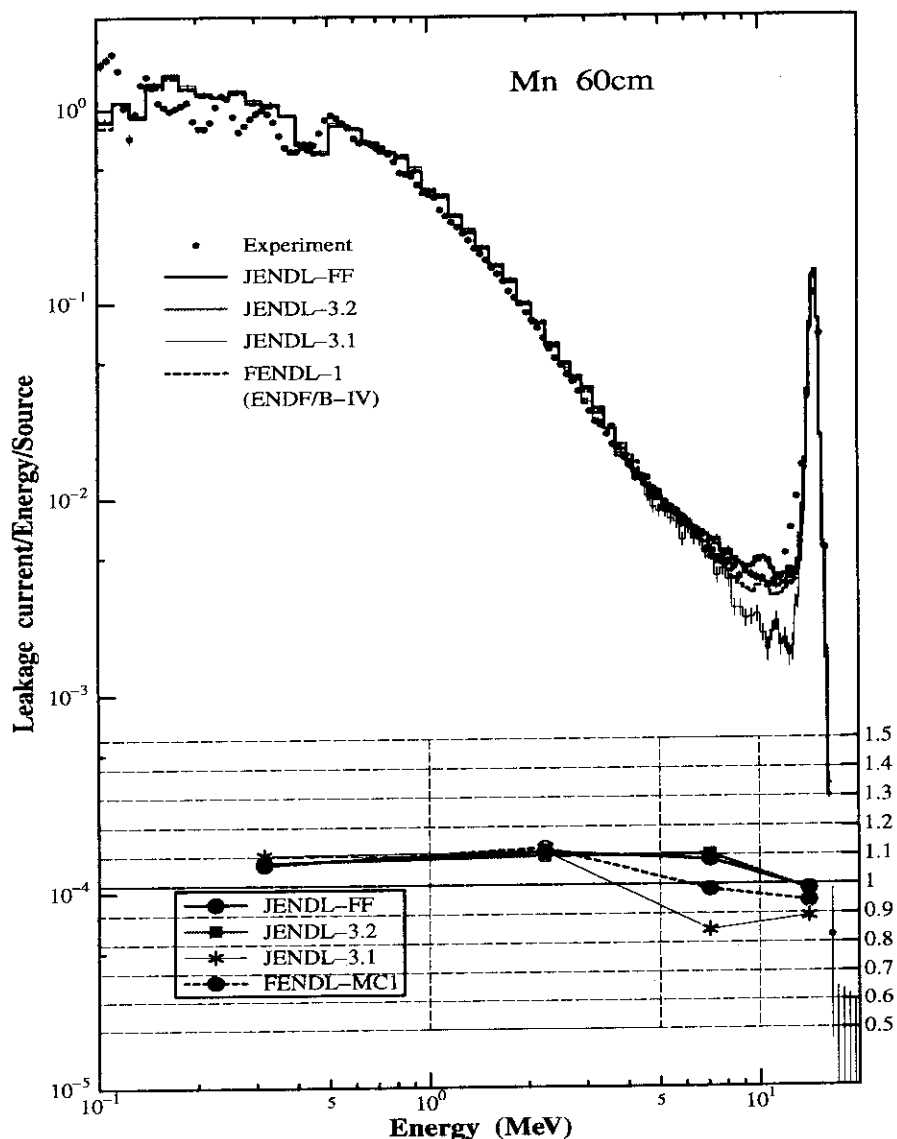
Figure 15: Experimental and calculated spectrum from Mn 61 cm sphere

JENDL-3.2 and JENDL Fusion file give similar prediction. The calculation agrees with the experiment within 10 % error. FENDL-MC1 also predicts the experiment with similar accuracy. JENDL-3.1 prediction is a little bit worse than the others in the energy region higher than 7 MeV. It can be concluded that all libraries are satisfactory above 100 keV energy region.

4.10 Co
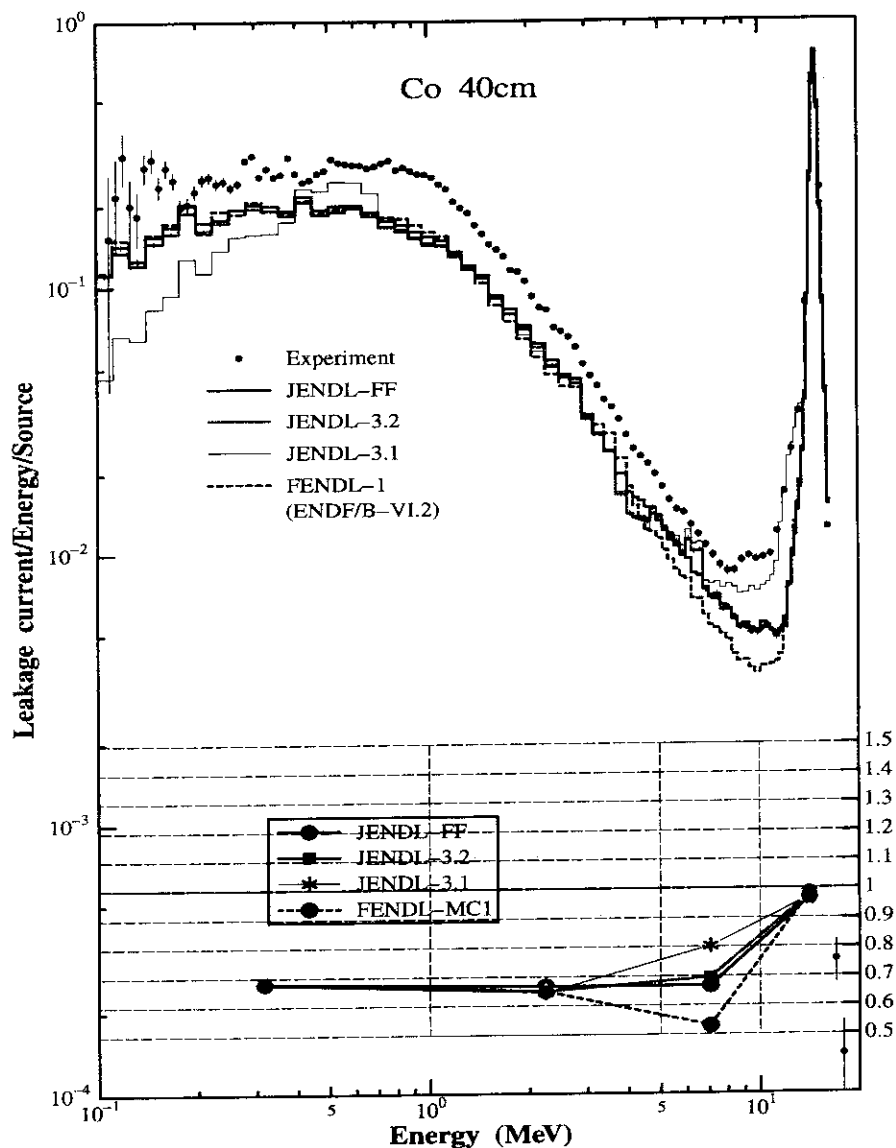
Figure 16: Experimental and calculated spectrum from Co 40 cm sphere

All calculations underestimate the experiment by more than 30 %. There is no distinct difference among different libraries. As the elastic scattering peak around 14 MeV can be predicted very well with every library, both experiment and libraries may have to be investigated further.

4.11 Cu
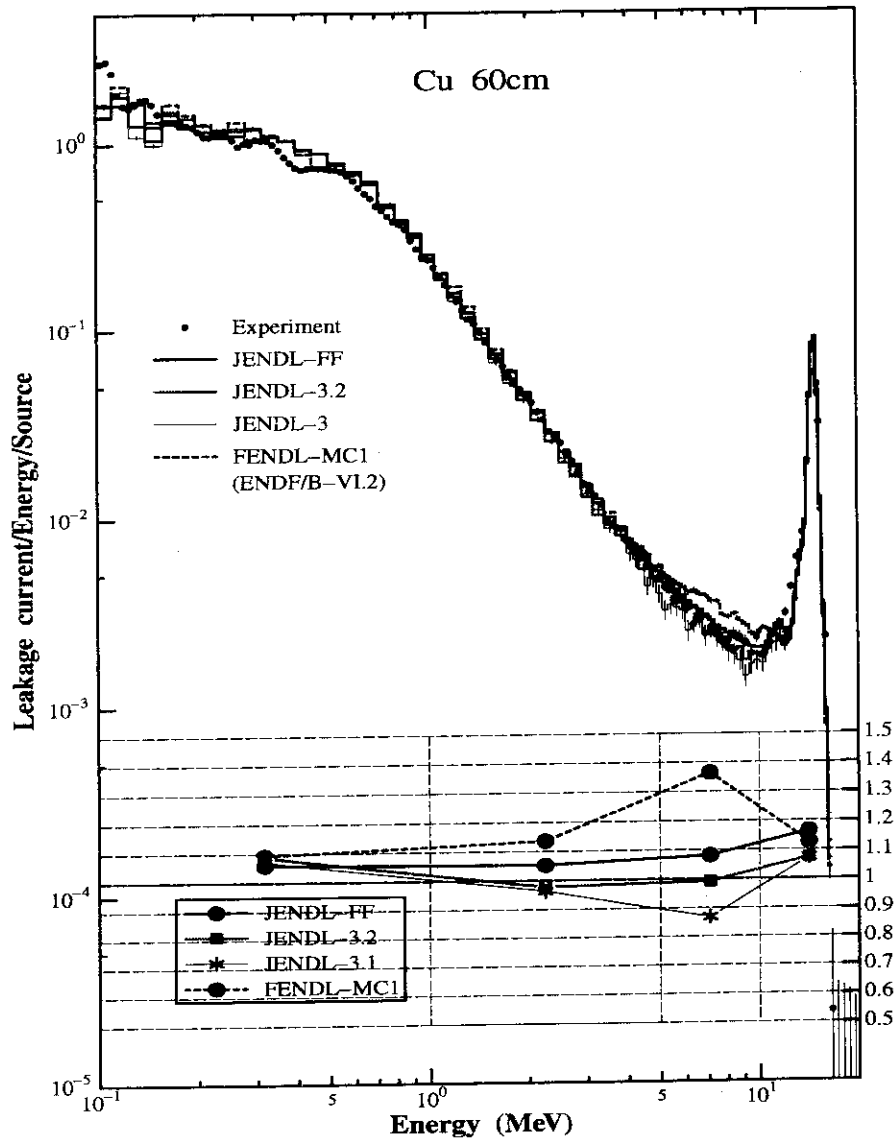
Figure 17: Experimental and calculated spectrum from Cu 61 cm sphere

JENDl-3.2 gives the prediction close to the experiment. JENDL Fusion file prediction is larger than that of JENDL-3.2 by a few % but it gives enough accurate prediction. However, FENDL-MC1 prediction gives overestimation by about 10 to 15 %.

4.12 Zr
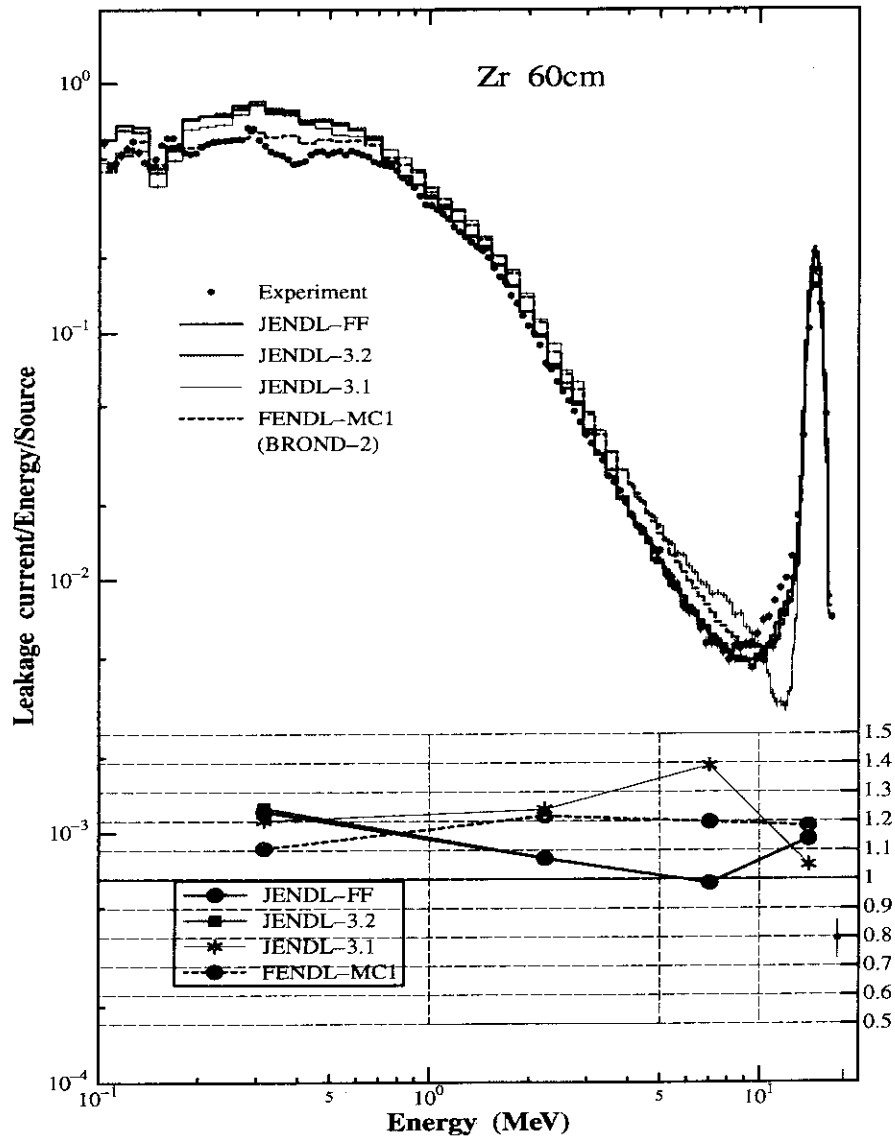
Figure 18: Experimental and calculated spectrum from Zr 61 cm sphere

JENDL-3.2 and JENDL Fusion file give the best prediction. The C/E values of the integrated flux is 10 to 15 % above unity except for the energy region below 1 MeV. FENDL-MC1 overestimates the experiment by about 20 %. JENDL-3.1 overestimates the experiment more than FENDL-MC1.

4.13 Nb
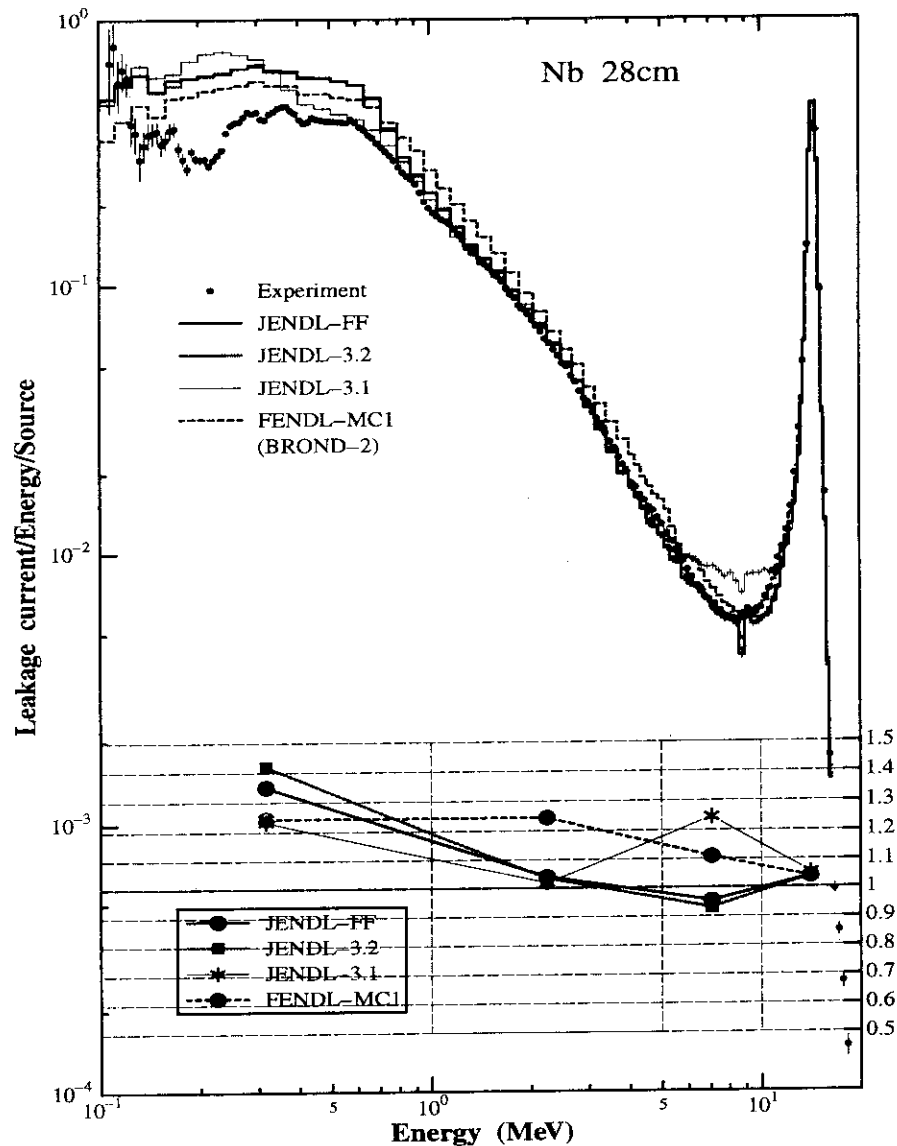
Figure 19: Experimental and calculated spectrum from Nb 28 cm sphere

JENDL-3.2 and JENDL Fusion file give pretty good prediction. The C/E values in the integrated spectra are between 5-6 %. FENDL-MC1 overestimates the experiment by 5 to 25 %.

4.14 Mo
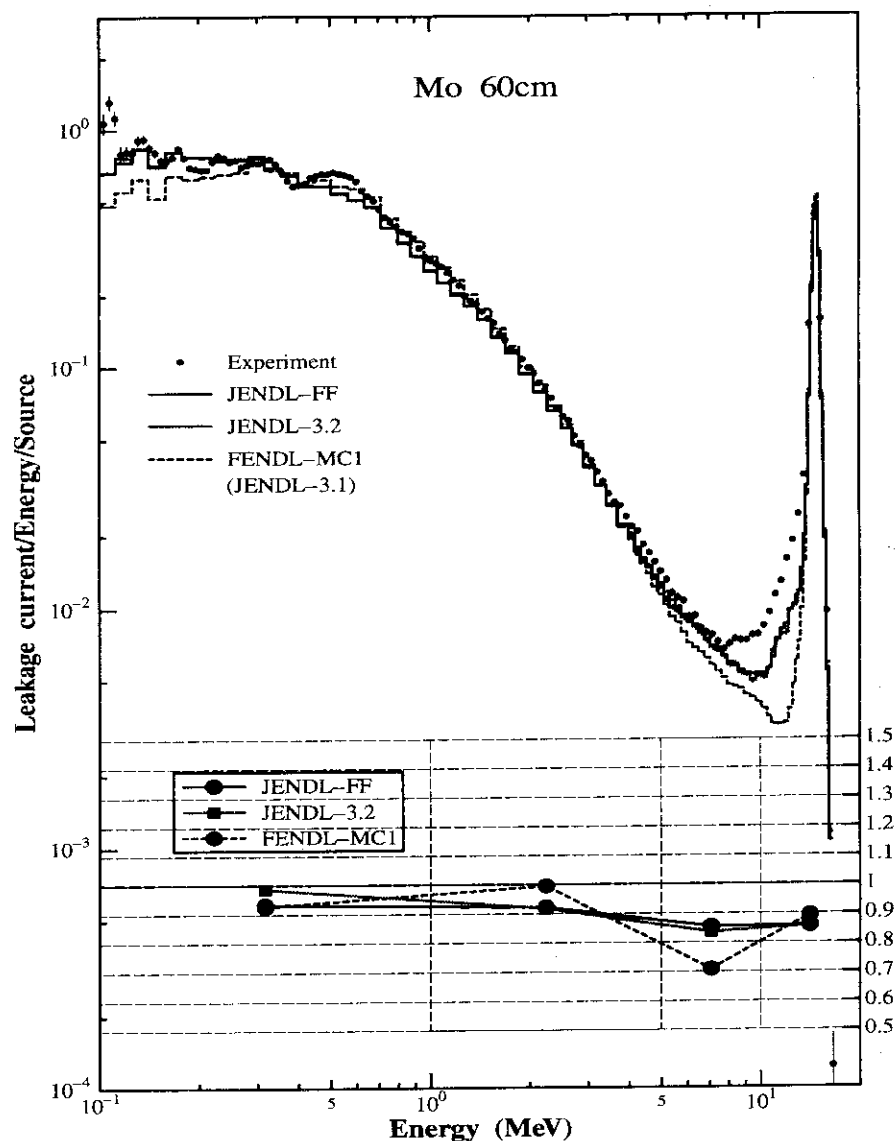
Figure 20: Experimental and calculated spectrum from Mo 61 cm sphere

JENDL-3.2 and JENDL Fusion file slightly underestimate the experiment by 8 to 14 % in whole energy range. FENDL-MC1 (JENDL-3.1) prediction is similar to the other two prediction except for the enrgy range between 5 and 12 MeV where large underestimation with FENDL-MC1 exists.

4.15 W
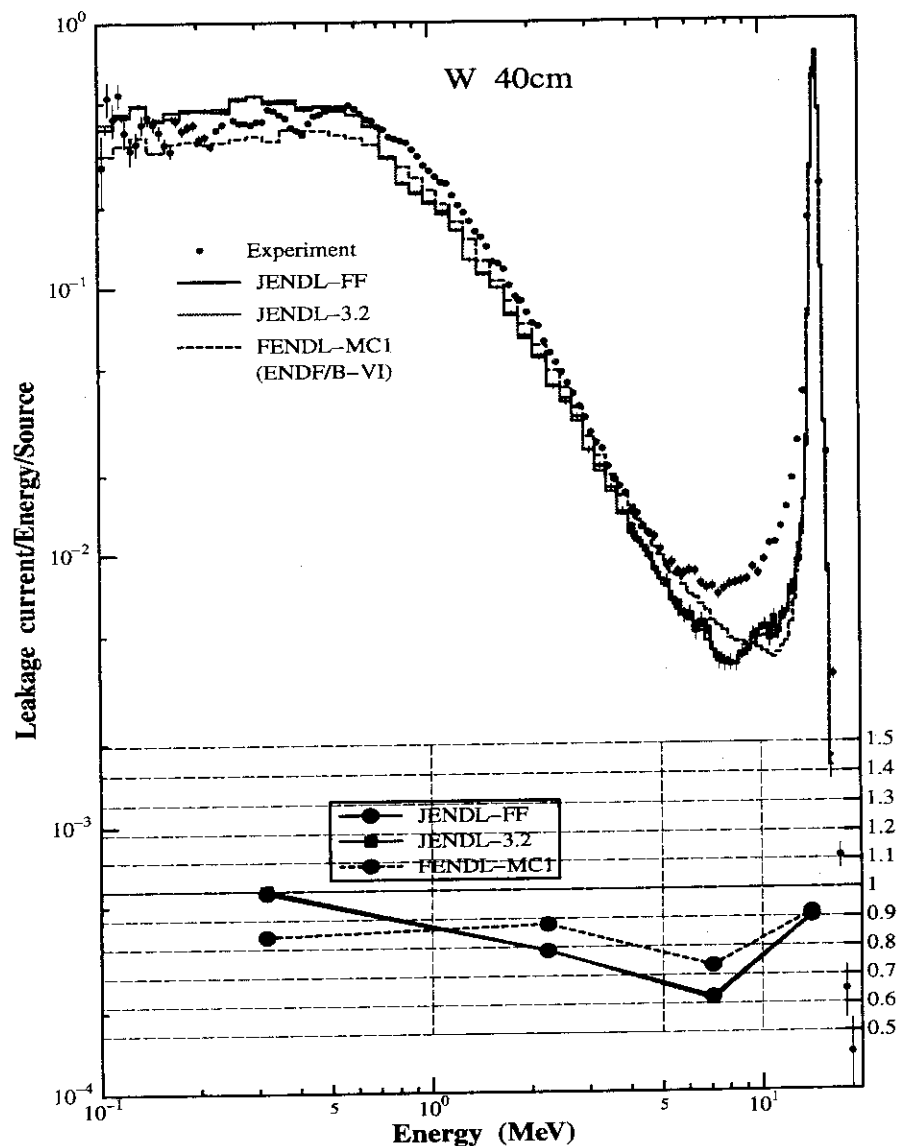
Figure 21: Experimental and calculated spectrum from W 40 cm sphere

JENDL-3.2 and JENDL Fusion file give pretty large underestimation by 10 to 40 %. FENDL-MC1 also underestimtes the experiment. However, the prediction with FENDL-MC1 is better than the prediction with JENDL-3.2 and JENDL Fusion file.by sbout 10 %.

References

[1] Pashchenko A.B., et al.: FENDL/E-1.0, IAEA-NDS-128 Rev 2., (1995).

[2] NAKAJIMA T., et al.: J. Nucl. Sci. Technol., 32[12], 1259 (1995).

[3] SHIBATA T., et al.: JAERI 1319, (1990).

[4] KOSAKO K., et al.: to be published.

[5] SUMITA K., et al.: Nucl. Sci. Eng., 106, 249 (1990).

[6] ICHIHARA C., et al.: JAERI-M 94-014, (1994).

[7] ICHIHARA C., et al.: JAERI-Conf 95-008, (1995).

[8] GANESAN S. (Compile), Improved Evaluations and Integral Data Experimental and calculated spectrum from xx xx cm sphereing for FENDL, INDC(NDS)-312/GF, (1994).

[9] BRIESMEISTER J.F. (ed.): A General Monte Carlo N-Particle Transport Code, Version 4A, LA-1265-M (1993).

[10] KOSAKO K., et al.: JAERI-M 91-187, (1991).

[11] KOSAKO K., et al.: JAERI-Data/Code 94-020, (1994).

[12] KOSAKO K., et al.: to be published.

[13] MACFARLANE R.E. et al.: FENDL/MC-1.0, Library of continuous energy cross section in ACE format for neutron-photon transport calculations with the Monte Carlo N-particle Transport Code system MCNP-4A, IAEA-NDS-169, (1995).

[14] ROSE P.F. (ed.): 4th Edition of BNL-NCS-17541, (1991).

[15] MANOKHIN V.N. et al.: IAEA-NDS-90 Rev. 8, (1994).

[16] GANESAN S.: Preparation of Fusion Benchmarks in Electronic Format for Nuclear Data Validation Studies, Summary Report of the IAEA Consultants' Meeting at IAEA Headquarters Vienna, Austria, December 13-16, 1993, INDC(NDS)-298, (1994).

The First Internet Symposium on Nuclear Data: Paper No.008

3.8 New aspects of the neutron capture in light nuclei

A. Mengoni

The Institute of Physical and Chemical Research (RIKEN)
2-1 Hirosawa, Wako, Saitama 351-01, Japan
and
ENEA, Applied Physics Section
v. Don Fiammelli 2, I-40128 Bologna. Italy
E-mail: mengoni@rikvax.riken.go.jp

Several neutron capture cross sections of light nuclei (A $\leq$ 40) for neutron energies up to the MeV region have been recently calculated. Examples are (target nuclei): ^{12}C, ^{13}C, ^{16}O and ^{10}Be. The results of these calculations will be shown together with a comparison with the most recent experimental data. In the case of $n + ^{10}$Be case, the cross section of the inverse process (Coulomb dissociation of ^{11}Be) is considered and compared with the measurement. A discussion on the relevant nuclear structure information required for the evaluation of nuclear data of light nuclei is given.

1 Introduction

Low energy neutron capture in light nuclei may have a strong contribution coming from the direct radiative capture (DRC) process. We have recently shown /1/ that, in the case in which the capture mechanism proceeds through a transition induced by incident p-wave neutrons, the capture cross section is

- insensitive to the neutron-nucleus interaction

- sensitive to the final state structure

In particular, final state wave functions with a significant component outside the nuclear surface (neutron halo) may cause a strong enhancement of the E1 transition matrix elements and therefore influence the capture cross section.

From a comparison of the experimental capture cross section with the theoretical calculations one can derive important information on the structure of nuclear bound states.

2 The DRC model

The direct capture process is alternative to the compound nucleus (CN) formation mechanism and may be described using the following definitions (details can be found in the references /1, 2/)

- Collision matrix

$$U_{i \to f} = U_{i \to f}(CN) + U_{i \to f}(DRC)$$

- Capture cross section for emission of electric dipole radiation (E1) in the transition $i \to f$

$$\sigma_{n,\gamma} = \frac{16\pi}{9\hbar} k_\gamma^3 \bar{e}^2 |Q_{i \to f}^{(1)}|^2$$

- Matrix elements for the transition

$$Q_{i \to f}^{(1)} = < \Psi_f | \hat{T}^{E1} | \Psi_i > \equiv \sqrt{S_f} \, \mathcal{I}_{i,f} \, A_{i,f}$$

with $\hat{T}^{E1} = rY^{(1)}(\theta, \phi)$, S_f : spectroscopic factor of the final state f, $\mathcal{I}_{i,f}$: radial overlap (see below) and $A_{i,f}$: angular-coupling coefficient

- Entrance channel wave function

$$\Psi_{lm}(\mathbf{r}) \equiv w_l(r) \frac{Y_{l,m}(\theta, \phi)}{r v^{1/2}}$$

where

$$w_l(r) = \frac{i\sqrt{\pi}}{k} \sqrt{2l+1} i^l [I_l - U_l O_l]$$

$$I_l \sim \exp(-ikr + \frac{1}{2} il\pi) \quad \text{and} \quad O_l \sim \exp(+ikr - \frac{1}{2} il\pi)$$

U_l is the collision matrix for the scattering process in the entrance channel, v is the incoming neutron velocity and k the corresponding wave number

- Radial matrix elements

$$\mathcal{I}_{l_i l_f} \equiv \int_0^\infty u_{l_f}(r) r w_{l_i}(r) dr$$

with $u_{l_f}(r)$: radial part of the final state wave function.

3   Examples

We have recently calculated several neutron capture cross sections for neutron energies up to the MeV region. Here we will present the results only. The details of the calculation technique and parameters used in the calculation can be found in the references /3, 4, 5, 6/.

The principal sources of experimental values are the measurements performed at the Tokyo Institute of Technology /7, 8, 9/ and at RIKEN for the inverse kinematic experiments (Coulomb dissociation) /10/.

- $n + {}^{12}C$ (Figures 1-4), $n + {}^{13}C$ (Figure 5)

- $n + {}^{16}O$ (Figure 6)

- $n + {}^{10}Be$ (Figure 7)
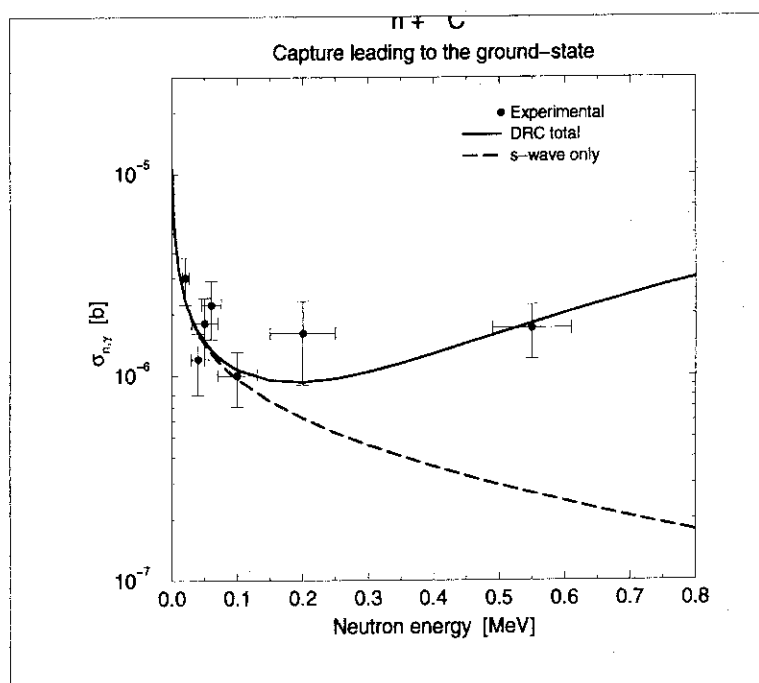
Figure 1: Capture cross section leading to the ground state of ^{13}C
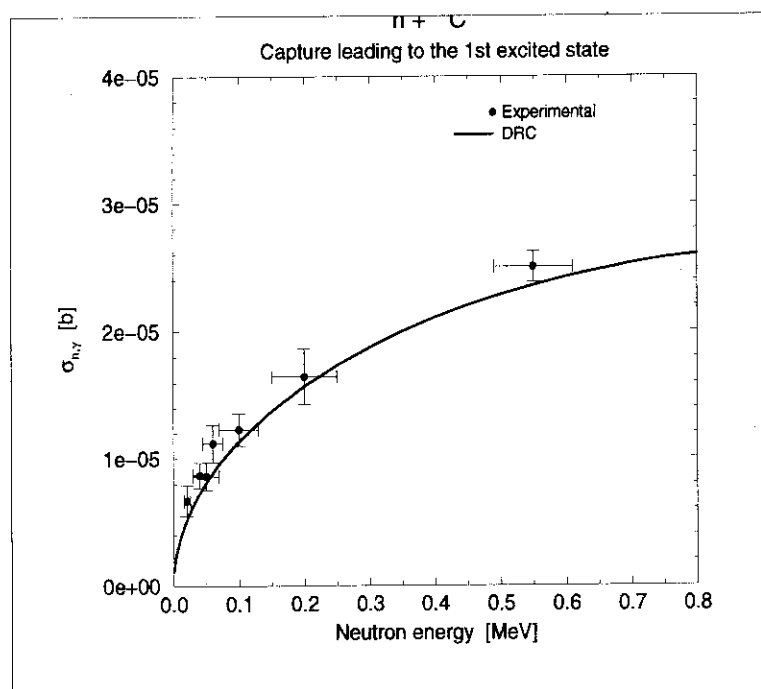
Figure 2: Capture cross section leading to the first excited state of ^{13}C
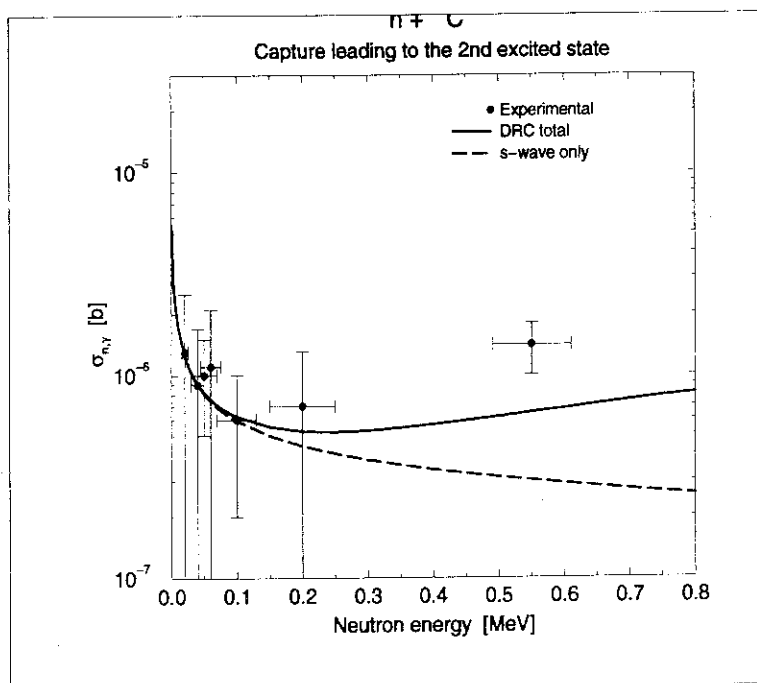
Figure 3: Capture cross section leading to the second excited state of ^{13}C
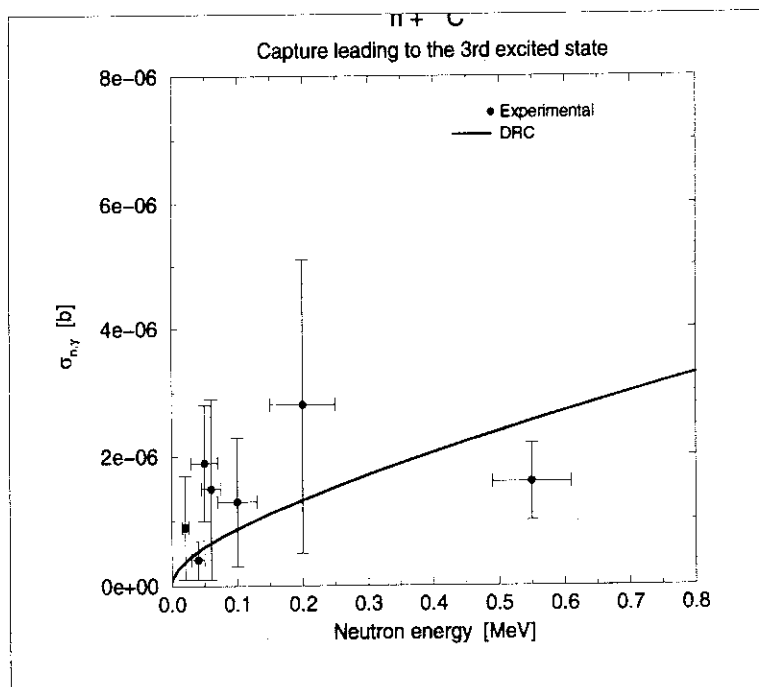
Figure 4: The capture cross section leading to the third excited state of ^{13}C
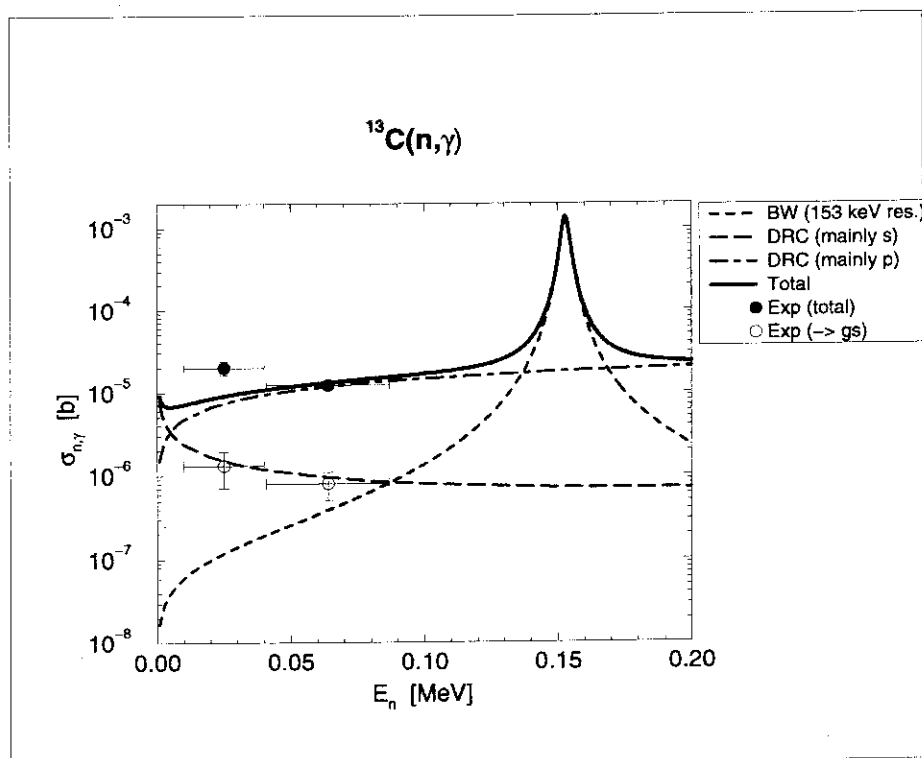
Figure 5: The capture cross section of ^{13}C

4 Capture cross section from Coulomb dissociation

The Coulomb dissociation process is the inverse process of a neutron radiative capture. Virtual photons of a field provided by a given target, interact with the incident beam. The incident nucleus can then break up into a neutron plus a residual. Measurements made using this technique have proved to be a useful tool for studying the structure as well as the reaction mechanism of nuclei far from stability. Coulomb dissociation experiments are considered to be a very promising tool to obtain neutron capture cross sections for radioactive nuclei.

The cross section obtained in a Coulomb dissociation experiment can easily be converted into a neutron capture cross section. As an example, we show here the results of the Coulomb dissociation experiment of ^{11}Be /10/, converted into the neutron capture channel.

The neutron capture cross section of ^{10}Be is shown in Figure 7. The cross section, derived from a Coulomb dissociation experiment /10/, is shown in comparison with the DRC calculations. Notice that the experimental results can only proceed through the $p \rightarrow s$ channel. In fact, the dissociation of ^{11}Be into ^{10}Be $+n$ is taking place only from the ground state of ^{11}Be.

The structure shown by the experimental results at around 1.3 MeV may be due to the 1.778 MeV level in ^{11}Be. Its effect on the neutron capture cross section is presently being investigated.
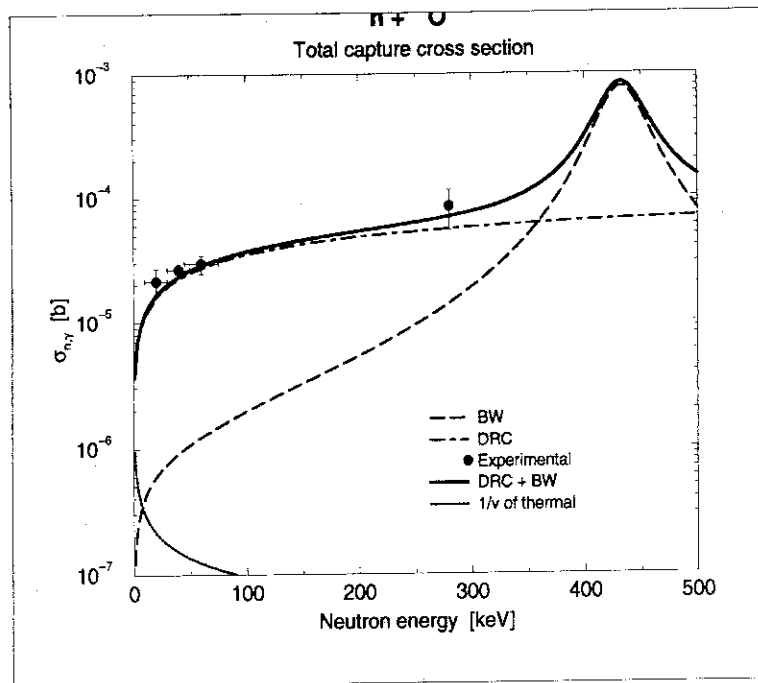
Figure 6: The capture cross section of ^{16}O

5 Comments on the results

From the results shown above, we can derive some important conclusions. Namely

- The neutron capture cross section proceeding through a DRC mechanism is insensitive to the neutron-nucleus interaction. Therefore, assuming that the correct wave function is being used for the calculation of the radial overlap, the **spectroscopic factor** S_f of the final state can be derived. In fact, S_f is the only unknown quantity in the expression for the DRC cross section.

- If the capture cross section (and/or the Coulomb dissociation cross section) is provided in an extended energy range, one can perform a Fourier-Bessel inversion of the radial overlap and obtain directly the **wave function** $u_f(r)$ of the final capturing state.

The consequences of these two results are being investigated at the moment and the outcome of this investigation will be soon reported.

6 Conclusions

We have shown here that in the situation in which the capture process is due to electric dipole (E1) $p \rightarrow s, d$ transitions, a measurement of the capture cross section may provide the spectroscopic factor of the final capturing state. Furthermore, we have shown that under certain conditions, a measurement of the (n, γ) cross section in a wide energy range may be used to derive the radial component of the final state wave function. In
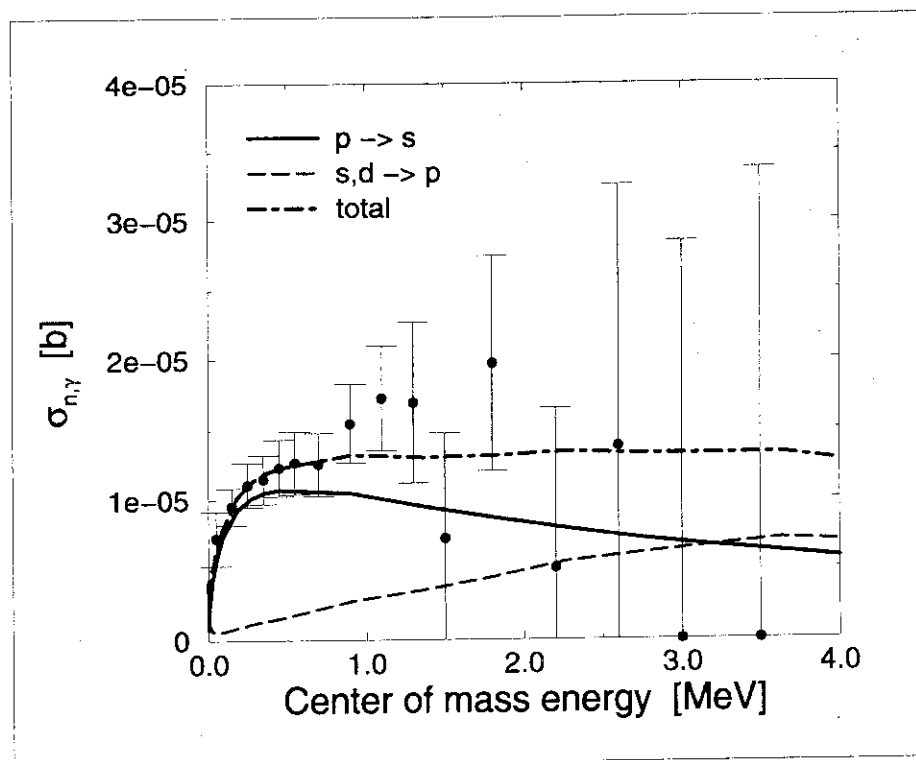
Figure 7: The capture cross sections of ^{10}Be

particular, the tail component of the bound state wave function can be derived by a Bessel-Fourier inversion of the capture cross section.

This technique can be applied in particular to detect properties of bound states dominated by a strong s-orbit configuration and low binding energy. Its natural application is therefore in detecting the halo component of wave functions of excited nuclear state of stable nuclei. Moreover, if used in conjunction with the inverse of the neutron capture process, namely the Coulomb dissociation, it may provide useful information on the halo structure of light neutron-rich unstable nuclei. These new developments have relevant consequences in astrophysical applications, in particular with reference to the estimation of neutron capture reaction rates for stellar as well as for primordial nucleosynthesis network calculations.

Acknowledgments

References

[1] A. Mengoni, T. Otsuka, and M. Ishihara, *Phys. Rev. C* **52**, (1995) 2334.

[2] T. Otsuka, M. Ishihara, N. Fukunishi, T. Nakamura and M. Yokoyama, *Phys. Rev. C* **49**, R2289 (1994).

[3] A. Mengoni, T. Otsuka and M. Ishihara, *Proceedings of the International Symposium on Origin of Matter and Evolution of Galaxies*, T. Kajino et al. Eds, World Scientific, in press (1996).

[4] A. Mengoni, *Proceedings of the RIKEN-INFN Joint Symposium, Wako, 22-27 May 1995*, T. Fukuda and A. Yoshida eds., World Scientific, in press (1996).

[5] A. Mengoni, T. Otsuka, and M. Ishihara, *3rd Symposium on Nuclear Physics with the JAERI tandem booster, Tokai-mura, 27-28 July 1995*, M. Oshima ed., in press (1996).

[6] A. Mengoni, T. Otsuka, and M. Ishihara, *Proceedings of the Workshop on Experimental Perspectives with Radioactive Nuclear Beams*, Padova, 14-17 November 1994 C. Signorini and A. R. Spalla eds., LNL-INFN(REP) 95/96.

[7] T. Ohsaki, Y. Nagai, M. Igashira, T. Shima, K. Takeda, S. Seino and T. Irie, *Ap. J.* **422**, 912 (1994).

[8] M. Igashira, Y. Nagai, K. Matsuda, T. Ohsaki and H. Kitazawa, *Ap. J.* **441**, (1995) L89.

[9] Y. Nagai and T. Shima, *Private communication* (1995).

[10] T. Nakamura *et al.*, *Phys. Lett. B* **331**, 296 (1994).

The First Internet Symposium on Nuclear Data: Paper No. 09

3.9 Systematics of Fission Cross Sections at the Intermediate Energy Region

Tokio FUKAHORI and Satoshi CHIBA

Nuclear Data Center, Japan Atomic Energy Research Institute

Tokai-mura, Naka-gun, Ibaraki-ken, 319-11 Japan

e-mail: fukahori@cracker.tokai.jaeri.go.jp, chiba@cracker.tokai.jaeri.go.jp

The systematics was obtained with fitting experimental data for proton induced fission cross sections of Ag, ^{181}Ta, ^{197}Au, ^{206,207,208}Pb, ^{209}Bi, ^{232}Th, ^{233,235,238}U, ^{237}Np and ^{239}Pu above 20 MeV. The low energy cross section of actinoid nuclei is omitted from systematics study, since the cross section has a complicated shape and strongly depends on characteristic of nucleus. The fission cross sections calculated by the systematics are in good agreement with experimental data.

1. Introduction

Evaluation of neutron, charged particles and photon nuclear data at the incident energy above 20 MeV is in progress. One of the purposes of developing evaluated intermediate energy nuclear data files is to supply basic data to waste management system, especially to accelerator-driven waste transmutation system. It is necessary to evaluate fission cross section for producing intermediate energy evaluated nuclear data file to be used for such applications, since the fission cross section is an important physical quantity in such systems and nuclei heavier than the silver also have considerable amount of fission cross sections at the intermediate energy region. As an approach to evaluate fission cross section, systematics of the cross section in the intermediate energy region is under development in JAERI to obtain the values simultaneously for various projectile-target combinations by using accumulated experimental data such as measured at Los Alamos/1/ and Gatchina/2/. As a similar approach, Simbel has been studied systematics for proton induced fission cross section as a function of incident proton energy by using a two-step model/3/. In this paper, the systematics of proton induced fission cross section is reported as an step of the total systematics study. The "fissility" was defined as ratio of fission cross section to total reaction cross section, and its dependence of excitation energy, atomic number and mass number was obtained.

2. Formulation

The systematics was obtained with fitting experimental data for proton induced fission cross sections of ^{nat}Ag, ^{181}Ta, ^{197}Au, ^{206,207,208}Pb, ^{209}Bi, ^{232}Th, ^{233,235,238}U, ^{237}Np and ^{239}Pu above 20 MeV with the following formula:

$$P_{fis}(Z, A, E) = p_1[1 - \exp\{p_3(E - p_2)\}]$$

$$p_i = A^{2/3} \exp[q_{i,1} + q_{i,2}(Z^2 / A) + q_{i,3}(Z^2 / A)^2] \qquad (i = 1,2,3)$$

where $P_{fis}(=S_{fis}/S_R)$ is defined as the fissility, S_{fis} and S_R are fission and total reaction (compound formation) cross sections, Z and A are the atomic and mass number of compound nucleus, E is

an excitation energy [MeV], $q_{i,j}$ is the parameter independent of Z and A.   It seems that the p_1, p_2 and p_3 parameters correspond to the saturation fissility, threshold energy and increasing rate, respectively.   In the case that the experimental data were only given for the fission cross section, fissility was obtained by using S_R calculated by Pearlstein's systematics/4/.   The lower energy cross sections of actinide nuclei were omitted from systematics study, since the cross section has a complicated shape and strongly depends on characteristic of nucleus.

3. Results and Discussion

The results of fissilities calculated with obtained pi parameters for ^{nat}Ag, ^{181}Ta, ^{197}Au, ^{206,207,208}Pb, ^{209}Bi, ^{232}Th, ^{233,235,238}U, ^{237}Np and ^{239}Pu are compared with experimental data in Figs. 1-13.   The Solid lines and symbols indicate calculated results and experimental data, respectively.
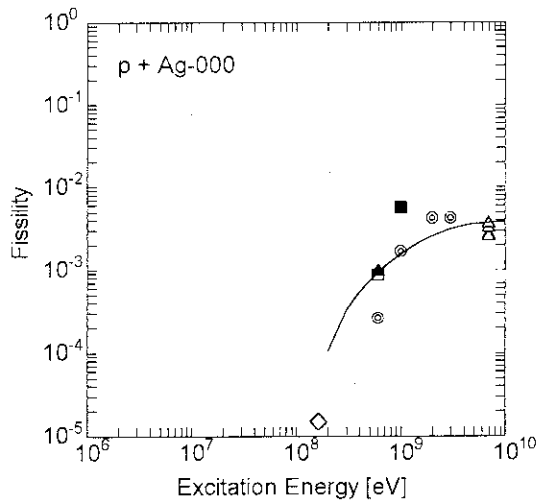
Fig.1 Fissility of ^{nat}Ag.   Solid line and
symbols indicate calculated results
and experimental data, respectively.
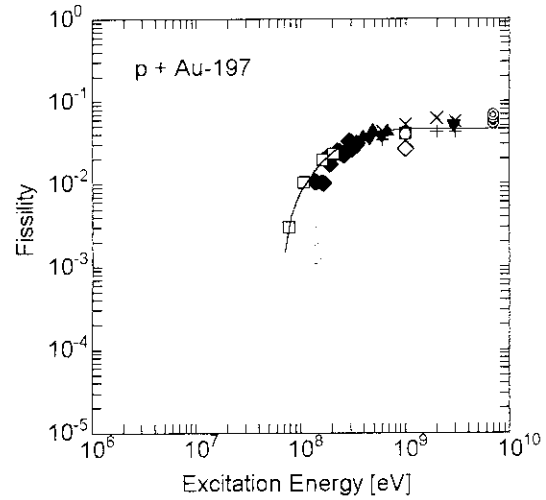
Fig.3 Fissility of ^{197}Au. Solid line and
symbols indicate calculated results
and experimental data, respectively.
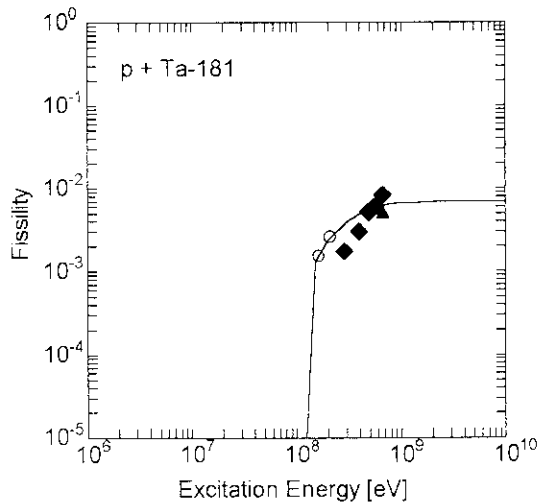
Fig.2 Fissility of ^{181}Ta. Solid line and
symbols indicate calculated results
and experimental data, respectively.
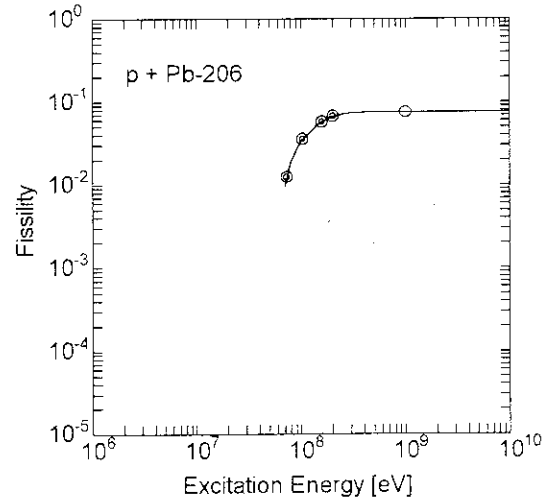
Fig.4 Fissility of ^{206}Pb. Solid line and
symbols indicate calculated results
and experimental data, respectively.
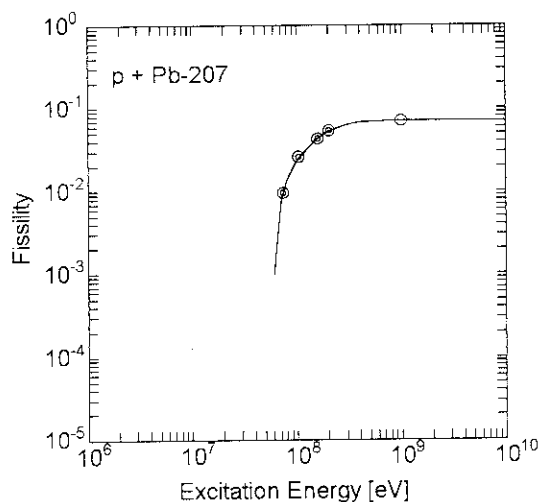
Fig.5 Fissility of ^{207}Pb. Solid line and symbols indicate calculated results and experimental data, respectively.
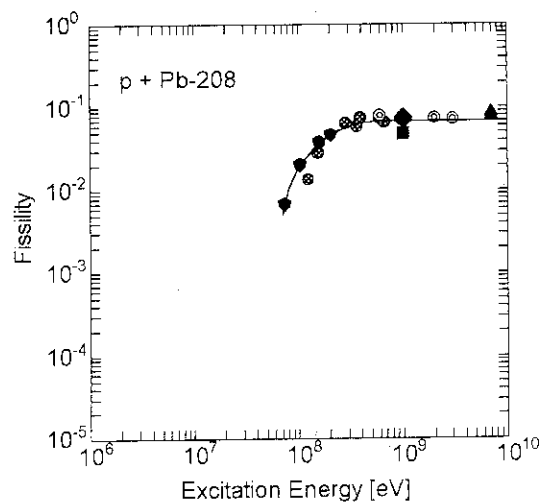
Fig.6 Fissility of ^{208}Pb. Solid line and symbols indicate calculated results and experimental data, respectively.
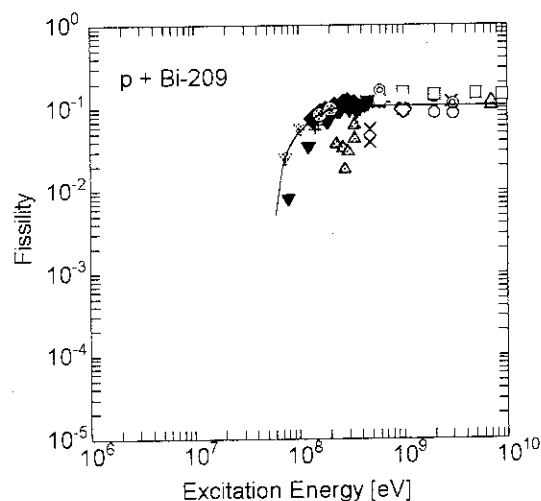
Fig.7 Fissility of ^{209}Bi. Solid line and symbols indicate calculated results and experimental data, respectively.

Though experimental data for natAg are scattered, the fitting result almost reproduce the experimental tendency (Fig.1). From Figs.2-7, the calculated results are in good agreement with the experimental data. It is noticed that the fissilities for non-actinide nuclei have similar shape as an exponential-type function with excitation energy.
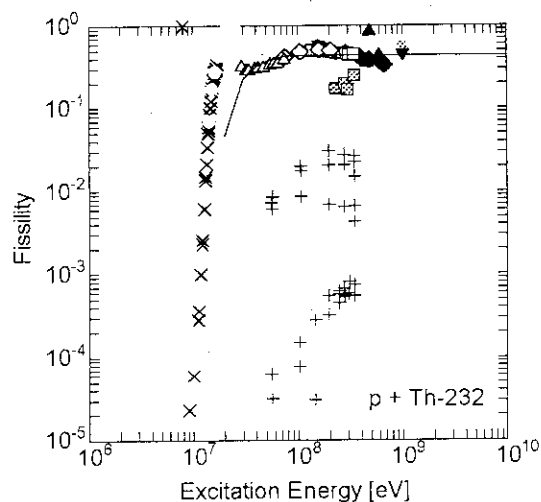
Fig.8 Fissility of ^{232}Th. Solid line and
symbols indicate calculated results
and experimental data, respectively.
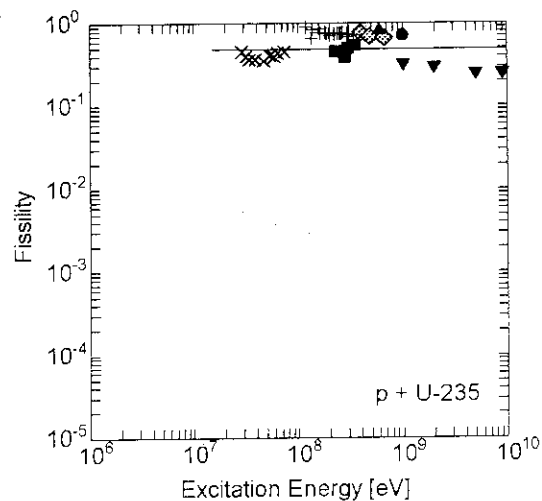
Fig.10 Fissility of ^{235}U. Solid line and
symbols indicate calculated results
and experimental data, respectively.
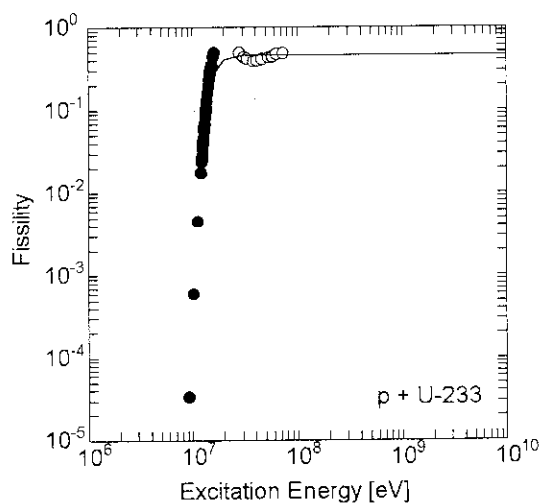
Fig.9 Fissility of ^{233}U. Solid line and symbols
indicate calculated results
and experimental data, respectively.
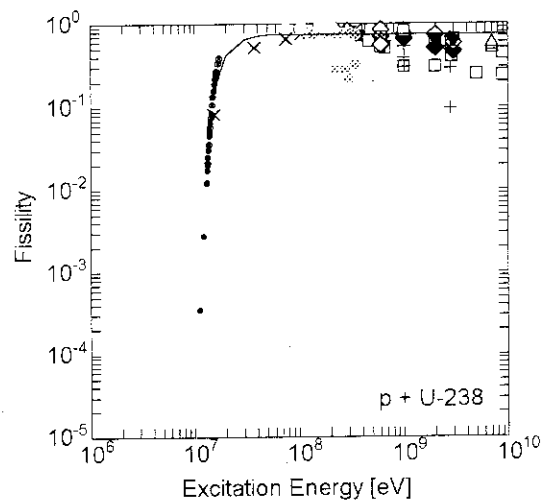
Fig.11 Fissility of ^{238}U. Solid line and
symbols indicate calculated results
and experimental data, respectively.
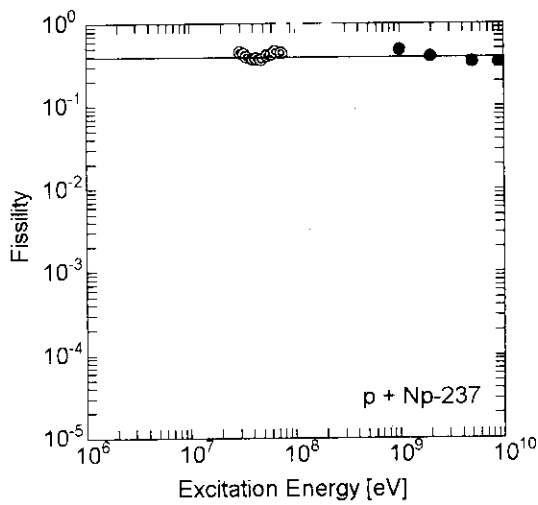
Fig.12 Fissility of ^{237}Np. Solid line and
symbols indicate calculated results
and experimental data, respectively.
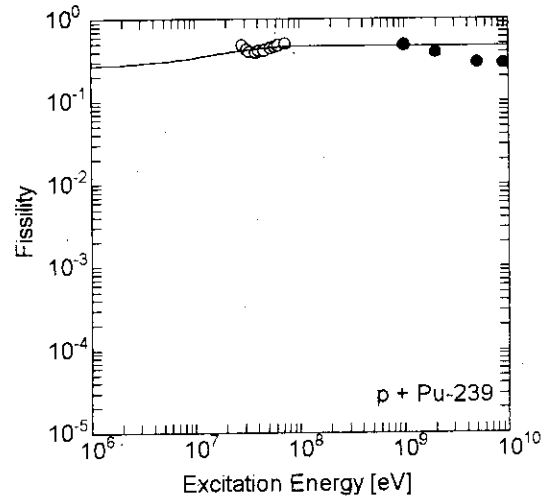
Fig.13 Fissility of ^{239}Pu. Solid line and
symbols indicate calculated results
and experimental data, respectively.

For actinide nuclei, the fissility is much closer to 100% and saturates at lower energy. The calculated results well reproduce saturated fissilities of experimental data at the intermediate energy region.

The fitting results of the p parameters and systematics are shown in Figs. 14-16. Dots are fitting results, and lines are the obtained systematics. The numerical result of systematics is summarized in Table 1.
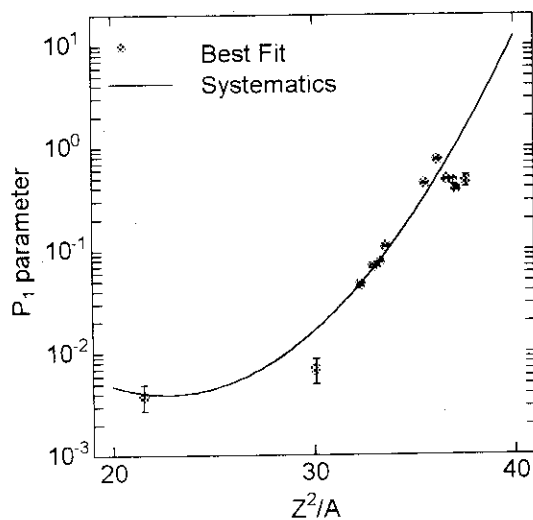
Fig.14 Z^2/A dependence of p_1 parameter of
fissility systematics.
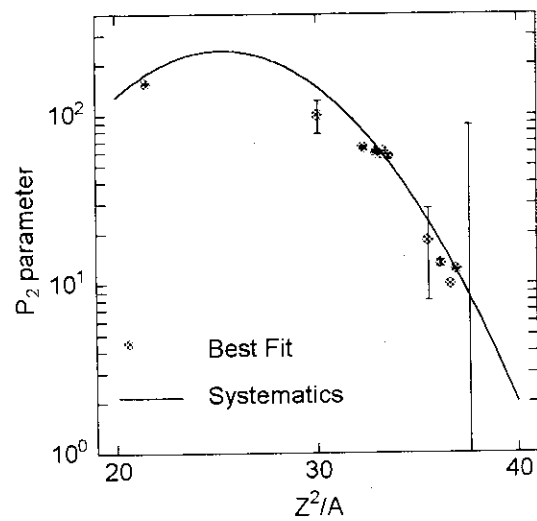
Fig.15 Z^2/A dependence of p_2 parameter of
fissility systematics.
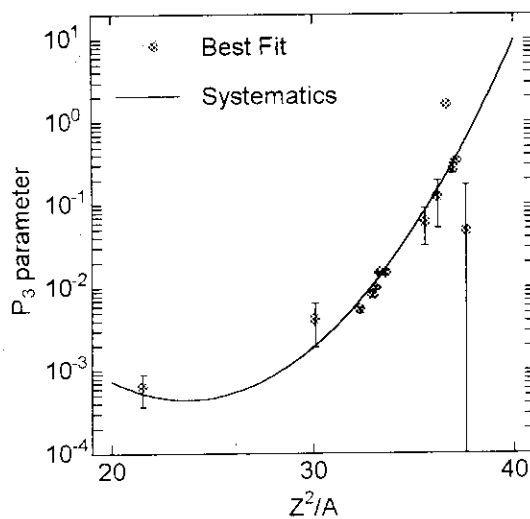
Fig. 16 Z^2/A dependence of p_3 parameter of fissility systematics.

Table 1 The result of systematics for proton induced fission cross section

	result	error(%)	Correlation Matrix		
p1 parameter					
q1,1	6.01	4.7	1	-0.99	0.97
q1,2	-1.27	1.4	-0.99	1	-0.99
q1,3	0.0274	1.1	0.97	-0.99	1
p2 parameter					
q2,1	-11.2	0.8	1	-0.99	0.97
q2,2	1.08	0.6	-0.99	1	-0.99
q2,3	-0.0219	0.4	0.97	-0.99	1
p3 parameter					
q3,1	11.2	29.4	1	-0.99	0.97
q3,2	-1.84	11.0	-0.99	1	-0.99
q3,3	0.0382	8.3	0.97	-0.99	1

The p_1 and p_3 parameter increase as a function of Z^2/A. This fact is seemed to be correct from physical consideration, since the p_1 and p_3 parameters have meanings of saturation fissility and increasing rate of fissility. On the other hand, the p_2 parameter decreases, since it represent the quantity like threshold energy. From above discussions, it is concluded that the systematics reproduces experimental data well and can be used to estimate fissility for nucleus which has no experimental data.

4. Summary

The systematics of proton induced fission cross section in the intermediate energy region was described. The shape of excited function was obtained for mass range above 180 and energy range from several tens MeV to 10 GeV by the systematics of fissility. It is

applicable to estimate fission cross section for nuclides which have no experimental data. In the future work, fission cross section induced by neutron, deuteron, alpha, photon, etc. will be included to the systematics. The fragment mass distribution and neutron energy spectrum should be also considered.

References

[1] for example, Lisowski, et al.: "Fission Cross Sections in the Intermediate Energy Region", Proc. a Specialists' Meeting on Neutron Cross Section Standards for the Energy Region above 20 MeV, May 21-23, 1991, Uppsala, Sweden, NEANDC-305'U' (1991) p.177.

[2] for example, Shcherbakov O.A.: "Experimental Investigations of the (n,f) Reaction", Sov. J. Part. Nucl., 21(2), 177 (1990).

[3] Simbel M.H.: "Phenomenological Analysis of Fission Induced by High-Energy Protons", Z. Phys., A333, 177 (1989).

[4] Pearlstein S.: "Systematics of Neutron Emission Spectra from High-Energy Proton Bombardment", Nucl. Sci. Eng., 95, 116 (1987).

The First Internet Symposium on Nuclear Data: Paper No. p010

3.10 Calculation and evaluation of cross-sections and kerma factors for neutrons up to 100 MeV on ^{16}O and ^{14}N

M. B. Chadwick[1,2] and P.G. Young[2]

[1] *University of California, Nuclear Data Group,*
Lawrence Livermore National Laboratory, Livermore, CA 94550
[2] *University of California, Theoretical Division,*
Los Alamos National Laboratory, Los Alamos, NM 87545

We present evaluations of the interaction of neutrons with energies between 20 and 100 MeV with oxygen and nitrogen nuclei, which follows on from our previous work on carbon [1]. Our aim is to accurately represent integrated cross sections, inclusive emission spectra, and kerma factors, in a data library which can be used in radiation transport calculations. We apply the FKK-GNASH nuclear model code, which includes Hauser-Feshbach, preequilibrium, and direct reaction mechanisms, and use experimental measurements to optimize the calculations. We determine total, elastic, and nonelastic cross sections, angle-energy correlated emission spectra for light ejectiles with A≤4 and gamma-rays, and average energy depositions. Our results for charged-particle emission spectra agree well with the measurements of Subramanian *et al.* [2]. We compare kerma factors derived from our evaluated cross sections with experimental data, providing an integral benchmarking of our work.

I. INTRODUCTION

A number of new applications, such as radiation transport simulations of fast neutron and proton cancer radiotherapy and the accelerator-driven transmutation of waste, require evaluated nuclear data libraries when modeling the interaction of neutrons above 20 MeV. In a previous paper [1] we described the calculation and evaluation of neutron cross sections on carbon up to 100 MeV. The present work, for oxygen and nitrogen, uses the same evaluation techniques as described in our carbon paper. We therefore provide here only a summary of the methods employed, and refer the reader to Ref. [1] for full details.

When calculating absorbed dose in the body from a fast-neutron radiotherapy beam, the most important energy-deposition mechanisms are nuclear reactions with hydrogen, oxygen, carbon and nitrogen nuclei, since these elements account (by mass) for 10%, 65%, 18%, and 3% of the body, respectively. Neutrons, being uncharged, deposit energy in matter by first

undergoing nuclear interactions which result in secondary charged nuclear ejectiles. These ejectiles then deposit their kinetic energy via electromagnetic interactions. In the case of hydrogen, it is elastic neutron-proton collisions that result in a substantial energy transfer from the incident neutrons to recoil protons. The higher mass of carbon, nitrogen and oxygen nuclei results in elastic scattering being a less important mechanism for energy deposition than for hydrogen. However, these nuclei may undergo inelastic scattering processes where nuclear fragmentation occurs. Indeed, for neutrons above approximately 70 – 80 MeV, the relatively large abundance of oxygen results in neutron-oxygen reactions giving the dominant contribution to absorbed dose in tissue.

Since only a limited number of experiments for neutron reactions on nitrogen and oxygen have been performed for energies between 20 and 100 MeV, we have based our evaluations mainly on the results of nuclear model calculations, benchmarked to the measurements where they exist. These calculations include direct, preequilibrium, and compound nucleus decay using Hauser-Feshbach theory. Our theoretical efforts, described in Sec. III and in more detail in Ref. [1], have concentrated on improvements to the modeling of reaction processes that become important at higher energies, particularly in preequilibrium emission and level densities. The light mass of oxygen and nitrogen, and consequently the relatively wide-spacing of their nuclear levels, presents a particular challenge to model calculations which rely on statistical assumptions in their derivations. However, our calculations in most cases provide a good description of the experimental data because our implementation of Hauser-Feshbach theory uses experimental nuclear level schemes for low excitation energies where a statistical level-density model is not applicable. Also, even in these light nuclei the density of nuclear states above about 10 MeV excitation energy becomes large enough for non-statistical effects to become less important.

These evaluations are available as electronic databases in the Lawrence Livermore National Laboratory (LLNL) Evaluated Nuclear Data Library (ENDL) format, and we plan to translate the library into the ENDF format. They can be used together with existing evaluations for neutrons below 20 MeV, such as the ENDL evaluation by Howerton [4] or the ENDF/B-VI evaluation by Hale et al. [5] for oxygen and by Young et al. [6] for nitrogen. Table I contains a summary of the quantities evaluated.

In Sec. II we describe our evaluation methods and compare them to those of previous analyses. Section. III describes the nuclear theory and models we use. In Sec. IV we give a detailed description of our results compared with experimental cross sections, and in Sec. V we compare kerma factors derived from our evaluated cross sections with measurements, and with other calculations. A summary and a description of directions and needs for future work are given in Sec. VI.

II. EVALUATION METHODS

The evaluation represents inclusive emission spectra of the secondary particles which need to be transported in radiation transport calculations (neutrons, gammas, and light charged particles with $A \leq 4$), as well as the total kinetic energy given to heavier charged particles, which is assumed to be deposited locally. This representation of the data is adequate for calculations of transport and absorbed dose. The libraries are fully angle-energy correlated, and describe the emission spectra at various angles, all in the laboratory frame of reference.

We have omitted triton and helium-3 emission reactions since measurements [2] show these cross sections to be small. Also, INC calculations indicate that these cross sections are small. For example, Brenner and Prael [3] calculate that 60 MeV neutrons incident on oxygen produce a yield of 15 mb tritons and 7 mb helium-3, which are small in comparison with the yields of the other light ejectiles (see our results in Table V).

The evaluations are based mainly on model calculations using the FKK-GNASH code system [7], benchmarked to available experimental data. But other reaction model codes were also used in this work: spherical optical model calculations were performed with the SCAT2 code [8]; and when evaluating preequilibrium cross sections we also considered hybrid model results from the ALICE code [9] and exciton model results from the GNASH code [7]. There are a number of advantages to using nuclear theory and model calculations to produce evaluated cross section libraries. The model input parameters can be adjusted (within the uncertainty ranges to which they are known) to optimize agreement with experimental data at incident energies where measurements have been made. The calculations then provide a useful way to interpolate and extrapolate to other energies. Also, model calculations enable evaluated libraries to be generated for all reaction products in a fully consistent way, automatically conserving energy, unitarity, spin, and parity.

Table II summarizes the experimental data used in the evaluations, in some cases pointing to other places in this paper where the data are shown in more detail. We show these various experimental data sets compared with our evaluations in Sec. IV. Some of the major steps involved in this evaluation are: (1) Optical model analyses for n, p, d, α particles to generate elastic and nonelastic cross sections, and transmission coefficients; (2) Build a database of low-lying nuclear levels for all product nuclides for use in Hauser-Feshbach and preequilibrium calculations. (3) Match a statistical level density on to the experimental low-lying levels; (4) Perform preequilibrium calculations using Feshbach-Kerman-Koonin (FKK) [10,11] quantum multistep theory, exciton, and hybrid models for comparison purposes. On the basis of these calculations, and measured cross sections, evaluate the primary preequilibrium spectra; (5) Use the FKK-GNASH code to generate inclusive cross sections based on primary and multiple preequilibrium emission, equilibrium decay, and direct reactions; (6) Use the Kalbach systematics [12] to give continuum angular distributions, and transform the double-differential cross sections to the laboratory frame assuming 2-body kinematics; and (7) Generate ENDL-format library files.

It is useful to compare the calculation methods used here with those of previous works. In addition to the present work, Refs. [13–16] used preequilibrium models with Hauser-Feshbach compound nucleus decay to study neutron reactions on biologically-important nuclei. Dimbylow [14] used an early version of the GNASH code, and his model calculations were compared against the UC-Davis cross section and kerma measurements. Even though details of the preequilibrium spectral shapes were not described very well (since early preequilibrium algorithms were utilized) the resulting kerma factors accounted for the data fairly accurately.

Intranuclear cascade (INC) calculations with either evaporation or a Fermi break-up compound nucleus decay have been described in Refs. [3,17–21]. While the physical assumptions made in these models do not hold well below 100 MeV, some analyses [3] have shown that they can provide a reasonable description of experimental measurements at these energies. It is only the comprehensive work by Brenner and Prael [3] which makes comparisons with

experimental charged-particle spectra. Brenner and Prael did not include elastic or inelastic coupled-channels scattering in their analyses, and did not present results for gamma-ray production. A failing of many INC-type calculations for reactions on biologically-important nuclei is that they do not account for the large numbers of high-energy preequilibrium deuterons, and they largely underpredict the production of alpha particles [21,22].

Finally, Caswell *et al.* [23] extended the evaluated ENDF libraries from 20 MeV to 30 MeV, using optical model results to obtain the total, elastic, and reaction cross sections. But extrapolations of partial cross sections beyond 20 MeV with this method are not always reliable. More recently, the latest ENDF/B-VI evaluation for nitrogen was extended to 40 MeV [6]. However, this evaluation was intended primarily for use in neutron transport calculations, and not all charged-particle decay channels are explicitly described. The present evaluation is unique in that experimental measurements have been utilized to optimize the model calculations, and extensive comparisons with experimental data have been made to validate our results.

III. NUCLEAR THEORY AND MODELS

We determine total, elastic, and nonelastic scattering cross sections using optical model analyses, which are also needed for generating transmission coefficients and wavefunctions in the equilibrium and preequilibrium calculations. Our work implements the spherical optical potential developed by Islam and Finlay of Ohio University [24], from 20 to 50 MeV (to 60 MeV for nitrogen). Above this energy we use the global potential developed by Madland [25], based on the earlier work of Schwandt *et al.* [26], and below 20 we use the Los Alamos spherical potential [27]. In addition to neutrons, optical potentials are also needed for the other ejectiles for calculating transmission coefficients for their decay. Proton potentials were obtained from the neutron potentials using the Lane model isospin transformation, namely $(N - Z)/A \rightarrow -(N - Z)/A$, with a Coulomb correction to the real central potential of $0.4Z/A^{1/3}$. Potentials for deuterons and alphas up to high energies were obtained using the method of Watanabe, as implemented by Madland [25].

Preequilibrium nucleon emission was obtained mainly from the FKK quantum mechanical theory, and preequilibrium deuteron and alpha clusters were obtained from the semiclassical model of Kalbach [28]. In some cases we modified the calculations to agree better with experimental measurements where they exist. Preequilibrium gamma-ray emission through the Giant Resonance is modeled using a semiclassical exciton model [7]. Contributions from multiple preequilibrium emission (MPE) processes (where more than one particle is emitted through a preequilibrium mechanism) were included using the theory of Ref. [29]. Full details of these theories are given in Ref. [1].

We use Hauser-Feshbach theory to calculate equilibrium emission of particles and gamma rays, conserving angular momentum and parity in an open-ended sequence of decay chains. We performed trial calculations to determine the most important reaction pathways and ignore paths that contain < 1 mb of cross section. Gamma, neutron, proton, deuteron, and alpha particle decay channels were included. Transmission coefficients for equilibrium particle decay were obtained using the optical potentials described above, and gamma-ray transmission coefficients were obtained from the generalized Lorentzian model of Kopecky and Uhl [30]

Nuclear level densities were determined using the Ignatyuk model [31], as implemented by Arthur *et al.* [15]. Pairing energies were obtained from the Cook systematics with the Los Alamos extensions to light nuclei from Ref. [27]. This continuum level density formulation is matched continuously onto discrete low-lying levels at the lower excitation energies. Discrete level information (energy, spin, parity, gamma-ray branching ratios) is tabulated for each nuclide in an input file, which is based on the Ajzenberg-Selove compilations [32]. For each nucleus we performed a level-density analysis and determined the excitation energy at which we judged the level data complete. Table III below lists the number of discrete levels used, and the matching energy, for the residual nuclides that can be produced (many of which are unstable). As an example of our results, in Fig. 1 we show the experimental cumulative number of levels matched on to our continuum statistical description for ^{15}N. We show this example since this nucleus is produced following high-energy deuteron emission in the ^{16}O(n, xd) reaction, and our evaluated spectra show structure corresponding to the gap of over 5 MeV between the ground and first excited states.

IV. RESULTS AND COMPARISONS WITH EXPERIMENTS

A. Total, Elastic, and Reaction Cross Sections

Table IV shows the evaluated total, elastic, and reaction (nonelastic) cross sections for oxygen and nitrogen, based on our optical model calculations. Between 20 and 100 MeV, the optical models we use provide a reasonably good description of measured reaction cross section data (see the dashed lines in Figs. 2 and 3). But since an accurate description of the reaction cross section is important for determining secondary particle spectra, we slightly modify the calculated results to better describe the experimental data to give the full lines shown in Fig. 2 and 3, and renormalize the calculated transmission coefficients accordingly. No measurements for the neutron reaction cross section on oxygen or nitrogen exist above about 50 MeV. However, systematics have been determined from a number of target elements at 95 MeV by DeJuren [33], and for 100 MeV protons by Kirby and Link [34] (at this energy the proton and neutron reaction cross sections would be expected to be very similar). We have, therefore, used these systematics to guide our evaluated reaction cross sections. Additionally, below 50 MeV we have also been guided by the proton-induced reaction cross sections of Carlson *et al.* [35]. The data points of Islam *et al.*, Olsson *et al.*, and Petler *et al.* shown in Figs 2. and 3 were obtained by subtracting their angle-integrated elastic data from the evaluated total cross sections (see below).

The evaluated total cross section was obtained by slightly modifying the optical model results to agree with data, principally the new high-accuracy results of Finlay *et al.* [36]. The results are shown in Figs. 4 and 5 compared with measurements taken from the Brookhaven National Nuclear Data Center CSISRS file [37]. In the case of nitrogen, we use the ENDF/B-VI total cross section below 40 MeV [6].

The elastic scattering cross sections were obtained from our optical model calculations, renormalized to the difference between evaluated total and reaction cross sections. The results are compared against experimental total elastic scattering data in Fig. 6. The angle-integrated data from Olsson *et al.* were taken from Ref. [38]. A legendre-fit to the Petler *et al.* nitrogen data [39] yielded elastic cross sections of 1020 ± 19 mb and 1062 ± 9

mb at 20 and 25 MeV, respectively. Measured angle-integrated elastic cross sections on oxygen between 18 and 28 MeV were obtained from the legendre fits of Islam *et al.* [40]. As an illustrative example of the differential elastic scattering, we show in Fig. 7 the elastic angular distributions at 20 and 26 MeV, compared with the differential cross section data of Islam *et al.* [24] in the center-of-mass frame.

Since direct inelastic neutron scattering to low-lying levels in oxygen has been shown to be important [40], we use the DWBA results from Ref. [40] for neutron scattering to the 3^- (6.13 MeV), 2^+ (6.92 MeV), and 1^- (7.12 MeV) states in ^{16}O. No such direct DWBA contributions were included for nitrogen.

B. Inclusive production cross sections and spectra

Table V shows the calculated production cross sections and average kinetic energies for the light ejectiles. In Figs. 8 and 9 we show the variation of these cross sections as a function of incident neutron energy. The tight binding of alpha particles along with the high probability of alpha clustering in light nuclei results in the alpha production cross section being large. Even though the multiplicities for particle production increase with increasing energy, the production cross sections do not generally show a large increase with energy because the nonelastic cross sections fall by about a factor of two between 20 and 100 MeV for oxygen and nitrogen.

An important test of the accuracy of the data libraries is that the evaluated emission spectra of light particles ($A \leq 4$) should be consistent with the measurements by Subramanian *et al.* [2] of UC-Davis. Figs. 10 and 11 show our calculated (lab frame) angle-integrated emission spectra of protons, deuterons, and alphas, compared with these measurements for oxygen and nitrogen. The structure seen at high emission energies is due to the inclusion of discrete nuclear levels in our calculations. Noteworthy features of the emission spectra seen in Fig. 10 and 11 are: (1) preequilibrium fast particle emission is particularly important and, except for alpha-emission, is large in magnitude compared to equilibrium decay (unlike reactions on heavier nuclei [43]); (2) preequilibrium deuteron emission is significant; and (3) alpha production cross sections at low emission energies are large. In general our calculations and those of Brenner and Prael [3], shown by the dashed line in Fig. 10, account for these features equally well, except for deuteron emission where our results describe the measurements more accurately.

For the UC-Davis data at 60 MeV, we have performed a new angle-integration of their double-differential data, and show our results in Fig. 10. The original UC-Davis angle-integrated results were kindly provided us by Dr. Romero who used them to obtain kerma factors [41,42]. However, the partial kerma from proton emission [42] appeared too high to us, suggesting that the angle-integrated proton spectrum may have been overestimated. For oxygen and nitrogen the measurements were only made at angles forward of 65-degrees, and consequently there are uncertainties in deriving angle-integrated spectra. The original approach of Subramanian *et al.* was to assume a constant cross section from 65-degrees back to 180-degrees. However, this overestimates the angle-integrated cross section since continuum angular distributions decrease significantly at back-angles. Our procedure instead was to use the shape of our calculated angular distribution to extrapolate the data from 65-degrees to 180-degrees. As can be seen in Fig. 10, this resulted in a significantly lower

experimental angle-integrated spectrum for proton emission, in better agreement with the model calculations. The experimental 60 MeV angle-integrated $^{14}N(n, xp)$ cross section in Fig. 11 is also probably overestimated due to the angle-integration procedure employed, as described above. Thus, we expect that much of the discrepancy seen between calculation and experiment here will vanish when a more accurate angle-integration technique is used, and we plan to check this in the future.

Figure 12 compares our calculated double-differential alpha, proton, and deuteron emission spectra against the UC-Davis measurements at 60 MeV. A dramatic example of the influence of nuclear structure is seen in the $^{16}O(n, xd)$ spectra, where the first excited ^{15}N state lies at 5.27 MeV (see Fig. 1). Our calculations account for the angular variations seen in the data, showing that the phenomenological systematics of Kalbach provide a good representation of angular distributions. At the higher emission energies the spectra show a dramatic forward peaking, typical of preequilibrium and direct reactions, since the incident projectile's direction of motion is partially preserved. At the lowest energies, the particles are emitted from compound nucleus reactions. In the center-of-mass these are emitted with angular distributions symmetric about 90-degrees (and almost isotropic), but in the laboratory some forward-peaking remains. Our calculations also clearly show how discrete structure effects in the spectra track with emission angle and energy due to kinematics.

C. Neutron Emission Compared With (p,xp) Data

There are no measurements of (n, xn) emission spectra with which we can compare our calculations. However, Bertrand and Peelle have measured $^{16}O(p, xp)$ cross sections at 40 and 60 MeV [43]. It would be expected that $^{16}O(p, xp)$ and $^{16}O(n, xn)$ spectra should be similar, particularly for the higher emission energies where Coulomb effects are negligible. Some differences would be expected due, for instance, to different Q-values in the competing channels in the two cases, but we expect such effects to have a small impact. Therefore we have used the Bertrand and Peelle measurements to benchmark our neutron emission calculations, as shown in Fig. 13, where we compare our results against the 40 and 60 MeV data. At 40 MeV the calculated emission spectrum agrees with data except at the lowest energies, where it lies below the measurements. At 60 MeV the calculations underpredict the data by about 15% between emission energies of 20 and 40 MeV. Our calculations agree better with these data than those of Brenner and Prael [3], which are also shown for comparison. Our evaluated (n, xn) spectra are approximately a factor of two larger than the (n, xp) spectra in the preequilibrium region, which is consistent with the systematics observed by Kalend *et al.* [44].

D. Comparison with exclusive measurements

Although our evaluation represents inclusive, and not exclusive, cross sections it is useful to compare our calculated excitation functions against exclusive measurements where they exist, as a further check on the evaluations.

The partial cross sections for the $(n, 2n)$ reactions on nitrogen and oxygen are shown in Fig. 14, compared with the measurements by Brill [45]. Our calculations are seen to agree

reasonably well with these data. At the higher energies the calculated $(n, 2n)$ cross section does not become very small because of the presence of multiple preequilibrium processes which provide a mechanism for the emission of two high-energy particles.

Although experimental data for the $^{16}O(n, p)$ and $^{14}N(n, p)$ reactions do not exist above 20 MeV, measurements have been made at lower energies. In Fig. 15 we show our calculations together with these data. The trends of the calculated excitation functions above 20 MeV are consistent with the lower-energy measurements. Likewise, the variation of our calculated $(n, d) + (n, np)$ cross section on oxygen above 20 MeV is consistent with the experimental point at 14 MeV, as seen in Fig. 16.

Our results for the (exclusive) partial cross sections at 20 MeV are generally in reasonable agreement with those in the existing ENDL and ENDF/B-VI evaluations, though there are some differences. The existing evaluations below 20 MeV are expected to be accurate at 14 MeV, where many experimental measurements exist. Thus, a possible way to merge our new $(E_{inc} > 20$ MeV) evaluations with lower energy evaluations would be to interpolate between the cross sections in the existing evaluations at 14 MeV to our new results at 20 MeV.

V. KERMA FACTORS

Kerma is an acronym for the kinetic energy released in matter, and is used in dosimetry for describing the indirectly ionizing radiation from neutrons. The kerma is defined as the expectation value of the kinetic energy transferred to the charged particles per unit mass at a point of interest in matter, whereas the kerma factor refers to the kerma per unit neutron fluence. Since the absorbed dose is defined as the energy imparted to matter per unit mass at a point, in general it differs from kerma because of radiation transport effects (the finite range of the secondary charged particles). Despite the fact that absorbed dose and kerma are not identical they are closely related, and if the microscopic cross sections give a kerma factor which is in agreement with experimental measurements, one can have some confidence in the absorbed dose predictions by a transport code which uses these microscopic cross sections.

We partition the calculated kerma factors into contributions from light charged particle ejectiles with $A \leq 4$ (obtained from lab-frame emission spectra), elastic recoils (obtained from elastic scattering angular distributions), and non-elastic heavy recoils (from the calculated recoil production cross sections along with energy-balance). Full details of the methods we use are given in Ref. [1].

The partial kerma factor for a certain secondary charged-particle type is obtained from the product of the cross section (in b) and the average energy (in MeV), in units of b.MeV/atom. To convert to the SI unit of Gy.m^2 (where 1 gray (Gy) = 1J/1Kg) we multiply by 0.603225 $\times10^{-15}$ for oxygen and 0.689045 $\times10^{-15}$ for nitrogen, which are the product of three factors: the number of atoms per Kg (6.0221367 / M_A) $\times 10^{26}$ (where M_A=15.994915 for oxygen, 14.003074 for nitrogen); J/MeV (1.60217733 $\times10^{-13}$); and m^2/b (10^{-28}).

A. Oxygen

In Table VI we show our calculated partial and total kerma factors based on our evaluated cross section libraries. At the lowest energies, the total kerma factor is dominated

by the alpha contribution, due to the large production cross section for alpha particles at these energies. The increasing proton and deuteron partial kerma factors are due to the importance of preequilibrium emission with increasing incident energy. The elastic recoil kerma factor, on the other hand, decreases with increasing incident energy because the elastic angular distributions become increasingly forward-peaked, resulting in a reduced recoil kinetic energy.

In Fig. 17 we show our evaluated total kerma factor from 20-100 MeV, derived from our microscopic cross section libraries, compared with experimental measurements [14,42,46,48], and we compare our result with other calculations and evaluations in Fig. 18. Below 20 MeV the histogram line shows the Howerton [4] result for the total kerma factor from the Livermore ENDL database. Our calculated kerma factor is consistent with the measurements, which provides an important benchmark for our cross sections. However, the variation seen among the experimental measurements requires some comments.

Direct kerma measurements have been recently reported by Schrewe *et al.* [48], for incident energies between 30 and 70 MeV. However, there are some uncertainties involved in obtaining kerma factors from these proportional-counter measurements due to uncertainties in gas-to-wall absorbed dose conversion factors. Kerma factors derived from measured cross sections have been presented by the UC-Davis group [41,42]. To obtain total kerma factors from their data, angle-integrated spectra need to be inferred from the double-differential measurements, the cross sections have to be extrapolated from the threshold emission energy measured to zero energy, elastic recoil kerma have to be added; and the (unmeasured) contributions from nonelastic recoil fragments have to be estimated. A range of total kerma factors based upon the UC-Davis measurements have been reported in the literature (see Fig. 17 and Refs. [14,41,42]). As discussed earlier, we had an expectation that the UC-Davis kerma factors reported at 60 MeV were too high, due primarily to an overestimate of the angle-integrated proton emission spectrum. Therefore we repeated the angle-integration of the UC-Davis data using our calculated angular distribution shapes to extrapolate the measurements from 65-degrees to backward angles (see our results in Fig. 10). In addition, we added low-emission energy threshold contributions, and elastic and non-elastic recoil contributions, from our calculations. This yielded a total experimental kerma factor at 60 MeV of 4.31 ± 0.70 f Gy m^2, which is significantly smaller than previous estimates, but in good agreement with our evaluation and with the Schrewe data. This resolves, in part at least, the discrepancy noted by Schrewe *et al.* in Ref. [48] between their latest oxygen measurements and the UC-Davis data at 60 MeV.

B. Nitrogen

Figure 19 shows our evaluated total kerma factor from 20-100 MeV compared with UC-Davis experimental measurements [14]. Our results are seen to agree well with these data. Because of the uncertainties in angle-integrating the UC-Davis double-differential cross sections, as discussed above, we believe that the experimental data point at 60.7 MeV is too high. Our results are compared with other calculations and evaluations in Fig. 20. It is evident that there is a considerable variation in the predictions of different calculations.

In the absence of detailed nuclear structure effects, the total kerma factor for elements with similar Coulomb barriers (such as nitrogen and oxygen) would be expected to vary

approximately as $A^{-1/3}$ ($1/A$ from the normalization constant in the kerma definition, and $A^{2/3}$ from the non-elastic cross section), which gives a ratio of 1.05 for nitrogen to oxygen. However, the total kerma factor above 20 MeV for nitrogen exceeds that for oxygen by a larger amount due to differences in the detailed nuclear structure of these elements and the residual nuclei produced. One such example is the large differences in Q-values for proton emission, +0.63 MeV for nitrogen, -9.64 MeV for oxygen, which leads to higher partial proton kerma factors for nitrogen.

VI. CONCLUSIONS

We have produced evaluated nuclear data bases for neutrons incident on nitrogen and oxygen. The preequilibrium model calculations were optimized to account for experimental measurements, particularly those of Subramanian *et al.*, and this technique results in evaluated emission spectra which generally account for the experimental data well. Compared to Brenner and Prael's model calculations, which represent the most detailed and well-benchmarked calculations prior to the present work, our results are more accurate for deuteron emission and the quality is comparable for proton and alpha emission. Furthermore, total kerma factors derived from our calculations describe the experimental measurements well. We found that a new angle-integration of the UC-Davis oxygen data at 60 MeV, using our model calculations to extrapolated to unmeasured angles, resulted in a lower experimental total kerma factor than originally reported. We plan to repeat this analysis for the other energies and other target nuclei measured at UC-Davis. A high priority for a future experiment is one which measures the secondary charged particles from neutron reactions on oxygen over a wide angular range.

These evaluated data, together with our result for carbon [1], can be used in radiation transport calculations of absorbed dose in fast neutron and proton radiotherapy. The libraries can be updated when new experimental measurements, such as the 60 MeV $^{16}O+n$ data currently being analyzed at Louvain-la-Neuve [51], become available. Further details of this evaluation, including tabulations and figures of the data, are given in Ref. [52].

VII. ACKNOWLEDGMENTS

REFERENCES

[1] M.B. Chadwick, M. Blann, L.J. Cox, P.G. Young, and A.S. Meigooni, accepted for publication by Nuclear Science and Engineering (1995); M.B. Chadwick, M. Blann, L.J. Cox, P.G. Young, and A.S. Meigooni, Lawrence Livermore National Laboratory report UCRL-ID-120829 (1995).

[2] T.S. Subramanian, J.L. Romero, F.P. Brady, D.H. Fitzgerald, R. Garrett, G.A. Needham, J.L. Ullmann, J.W. Watson, C.I. Zanelli, D.J. Brenner, and R.E. Prael, Phys. Rev. C **34**, 1580 (1986); J.L. Romero, private communication to MBC (1994).

[3] D.G. Brenner and R.E. Prael, At. Data and Nucl. Data Tables **41**, 71 (1989).

[4] R.J. Howerton, Lawrence Livermore National Laboratory document UCRL-50400 **27** (1986)*revised*.

[5] G.M. Hale, P.G. Young, M.B. Chadwick, and Z.P. Chen, in *Proceedings of the International Conference on Nuclear Data for Science and Technology*, Julich, Germany, 13-17 May 1991, edited by S.M. Qaim (Springer Verlag, 1992) p. 921; Brookhaven National Nuclear Data Center ENDF/B-VI evaluation.

[6] G.M. Hale, P.G. Young, M.B. Chadwick, in *Proceedings of the International Conference on Nuclear Data for Science and Technology*, Gatlinburg, Tennessee, May 9-13 1994, edited by K. Dickens (American Nuclear Society, 1994) p. 607; Brookhaven National Nuclear Data Center ENDF/B-VI ^{14}N, Rev. 3, evaluation.

[7] P.G. Young, E.D. Arthur, and M.B. Chadwick, Los Alamos National Laboratory document LA-MS-12343 (1992); M.B. Chadwick and P.G. Young, Phys. Rev. C **47**, 2255 (1993).

[8] O. Bersillon, Bruyeres-le-Chatel progress report CEA-N-2037, p. 111 (1978).

[9] M. Blann, Lawrence Livermore National Laboratory document UCRL-JC-109052 (1991).

[10] H. Feshbach, A. Kerman, and S. Koonin, Ann. Phys. (N.Y.) **125**, 429 (1980).

[11] P.E. Hodgson and M.B. Chadwick, invited paper to the *International Conference on Nuclear Data for Science and Technology*, Gatlinburg, Tennessee, May 9-13 1994, edited by K. Dickens (American Nuclear Society, 1994) p. 519.

[12] C. Kalbach, Phys. Rev. C **37**, 2350 (1988).

[13] M.B. Chadwick, M. Blann, P.G. Young, and G. Reffo, in *Proceedings of the International Conference on Nuclear Data for Science and Technology*, Gatlinburg, Tennessee, May 9-13 1994, edited by K. Dickens (American Nuclear Society, 1994) p. 658.

[14] P.J. Dimbylow, Phys. Med. Biol. **27**, 989 (1982).

[15] P.G. Young, E.D. Arthur, M. Bozoian, T.R. England, G.M. Hale, R.J. LaBauve, R.C. Little, R.E. MacFarlane, D.G. Madland, R.T. Perry, and W.B. Wilson, Los Alamos National Laboratory document LA-11753-MS (1990).

[16] G.H. Herling, R.H. Bassel, J.H. Adams, and W.A. Frazer, Naval Research Report 8441, Washington, D.C., (1981).

[17] R.G. Alsmiller Jr., and J. Barish, Health Physics **33**, 98 (1977).

[18] M.A. Behrooz and D.E. Watt, in *Proc. 4th Symp. on Neutron Dosimetry*, EUR-7448 (Luxembourg, CEC) 353-360 (1981).

[19] K. Morstin, A. Dydejczyk, and J. Booz, Rad. Prot. Dos. **23**, 35 (1988).

[20] A.H. Wells, Radiat. Res. **80**, 1 (1979).

[21] S. Mashnik, private communication to MBC (1995).

[22] K. Morstin, A. Dydejczyk, J. Booz, in *Nuclear and Atomic Data for Radiotherapy and Related Radiobiology*, International Atomic Energy Agency report STI/PUB/741 (IAEA, Vienna, 1987).

[23] R.S. Caswell, J.J. Coyne, M.L. Randolph, Radiat. Res. **83**, 217 (1980).

[24] M.S. Islam, R.W. Finlay, J.S. Petler, J. Rapaport, R. Alarcon, and J. Wierzbicki, Phys. Med. Biol. **33**, 315 (1988).

[25] D.G. Madland, in *Proceedings of a Specialists' Meeting on Preequilibrium Reactions*, Semmering, Austria, 10-12 Feb. 1988, edited by B. Strohmaier (NEA Report NEANDC-245, 1988) p. 103.

[26] P. Schwandt, *et al.* Phys. Rev. C **26**, 55 (1982).

[27] E.D. Arthur, Los Alamos National Laboratory progress report LA-9841-PR (1983).

[28] C. Kalbach, Z. Phys. A **283**, 401 (1977).

[29] M.B. Chadwick, P.G. Young, D.C. George, and Y. Watanabe, Phys. Rev. C **50**, 996 (1994).

[30] J. Kopecky and M. Uhl, Phys. Rev. C **41**, 1941 (1990).

[31] A.V. Ignatyuk, G.N. Smirenkin, and A.S. Tishin, Sov. J. Nucl. Phys. **21**, 255 (1975).

[32] F. Ajzenberg-Selove, Nucl. Phys. **A449**, 1 (1986); Nucl. Phys. **A375**, 1 (1982); Nucl. Phys. **A392**, 1 (1983); Nucl. Phys. **A413**, 1 (1984); Nucl. Phys. **A433**, 1 (1985).

[33] J. Dejuren and N. Knable, Phys. Rev. **77**, 606 (1950).

[34] P. Kirby and W.T. Link, Can. J. Phys. **44**, 1847 (1966).

[35] R.F. Carlson, A.J. Cox, T.N. Nasr, M.S. De Jong, D.L. Ginther, D.K. Hasell, A.M. Sourkes, W.T.H. Van Oers, and D.J. Margaziotis, Nucl. Phys. **A445**, 57 (1985); R.F. Carlson, A.J. Cox, J.R. Nimmo, N.E. Davidson, S.A. Elbakr, J.L. Horton, A. Houdayer, A.M. Sourkes, W.T.H. Van Oers, and D.J. Margaziotis, Phys. Rev. C **12**, 1167 (1975).

[36] R.W. Finlay, W.P. Abfalterer, G. Fink, E. Montei, T. Adami, P.W. Lisowski, G.L. Morgan, and R.C. Haight, Phys. Rev. C **47**, 237 (1993).

[37] National Nuclear Data Center (NNDC), Brookhaven National Laboratory, Upton, NY 11973; electronic mail: NNDC@BNL.GOV.

[38] N. Olsson, E. Ramstrom, and B. Trostell, Phys. Med. Biol. **35**, 1255 (1990).

[39] J.S. Petler, M.S. Islam, R.W. Finlay, and F.S. Dietrich, **32**, 673 (1985).

[40] M.S. Islam and R.W. Finlay, Nuclear Data and Atomic Data Tables **58**, 245 (1994).

[41] F.P. Brady and J.L. Romero, *Final Report to the National Cancer Institute*, University of California, Davis, (1979).

[42] J.L. Romero, F.P. Brady, and T.S. Subramanian, in *Nuclear Data for Basic and Applied Sciences*, Santa Fe, New Mexico, 13-17 May, 1985, edited by P.G. Young (Gordon and Breach, 1986) p. 687.

[43] F.E. Bertrand and R.W. Peelle, Phys. Rev. C **8**, 1045 (1973).

[44] A.M. Kalend *et al.*, Phys. Rev. C **28**, 105 (1983).

[45] O.D. Brill, N.A. Vlasov, S.P. Kalinin, L.S. Sokolov, Sov. Phys. Dokl. **6**, 24 (1961).

[46] C.L. Hartmann, P.M. DeLuca Jr., and D.W. Pearson, Radiat. Prot. Dosim. **44**, 25 (1992).

[47] P.M. DeLuca Jr., H.H. Barschall, Y. Sun, and R.C. Haight, Rad. Prot. Dosim. **23**, 27 (1988).

[48] U.J. Schrewe, W.D. Newhauser, H. J. Brede, V. Dangendorf, P.M. DeLuca, Jr., S. Gerdung, R. Nolte, P. Schmelzbach, H. Schuhmacher, and T. Lim, in Chalk River

Conference, 1994, to be published in Rad. Prot. Dos. (1995); private communication to M.B. Chadwick (1995).

[49] D.G. Brenner and R.E. Prael, in *Nuclear and Atomic Data for Radiotherapy and Related Radiobiology*, ed. K. Okamoto (IAEA, Vienna, 1985) p. 205.

[50] R.M. White *et al.*, invited paper to the *Seventh Symposium on Neutron Dosimetry*, Berlin, Germany, October 14-18 (1992); Rad. Prot. Dos. **44**, 11 (1992).

[51] S. Benck, V. Corcalciuc, and J.P. Meulders, private communication to MBC (1995).

[52] M.B. Chadwick and P.G. Young, Lawrence Livermore National Laboratory report UCRL-ID-122436 (1995).

TABLES

Reaction type	Cross section	Angle-energy correlated lab spectra	Average lab energy deposition
n,total	√	–	–
n,nonelastic	√	–	–
n,elastic	√	(c.m. angular distributions)	√
n,xn	√	√	√
n,xp	√	√	√
n,xd	√	√	√
n,xα	√	√	√
n,xγ	√	(isotropic)	√
n,nonelastic recoils	–	–	√

TABLE I. Contents of the Evaluated Data Libraries.

Reaction type	Citation to experimental measurement
Nonelastic	See Figs. 2 and 3
Total	See Figs. 4 and 5
Elastic	See Figs. 6 and 7
Inelastic neutron scattering	See Islam and Finlay [40]
p, d, α production	27, 40, 61 MeV, Subramanian et $al.$ [2], see Figs. 10-12
$(n, 2n)$	Brill (1961), see Fig. 14
(n, p)	Martin (1954) and Dejuren (1962), and Felber (1976), see Fig. 15
(n, d)	Lillie (1952), see Fig. 16
(p, xp)	Bertrand and Peelle [43], see Fig. 13 (guide for $^{16}O(n, xn)$ calcs.)

TABLE II. Summary of experimental cross section data guiding these evaluations

Nucleus (1000Z+A)	Number of levels	Matching energy	Nucleus (1000Z+A)	Number of levels	Matching energy
9017	20	7.479	7016	18	5.255
9016	10	5.104	7015	22	10.855
9015	2	1.950	7014	9	6.565
9014	1	0.000	7013	13	10.637
9013	1	0.000	7012	7	3.740
9012	1	0.000	7011	1	0.000
9011	1	0.000	7010	1	0.000
8017	45	10.026	6015	16	7.479
8016	24	13.327	6014	18	11.762
8015	13	9.741	6013	10	9.190
8014	6	6.890	6012	8	12.162
8013	4	6.925	6011	12	8.724
8012	1	0.000	6010	5	7.180
8011	1	0.000	6009	2	3.330

TABLE III. The number of low-lying discrete levels included, along with the matching excitation energy (in MeV) above which we used the Ignatyuk continuum level density description. For nuclides with $Z \leq 6$, see Table III in Ref. [1].

Energy (MeV)	^{16}O+n			^{14}N+n		
	Total	Elastic	Nonelastic	Total	Elastic	Nonelastic
20	1640	1020	620	1550	1019	531
23	1646	1054	592	1465	961	504
27	1594	1071	523	1436	954	482
30	1559	1059	500	1394	929	465
35	1479	1012	467	1321	884	437
40	1402	967	435	1249	839	410
50	1211	815	396	1067	702	365
60	1050	680	370	924	597	327
70	912	573	339	788	490	298
80	807	489	318	693	410	283
90	721	421	300	611	340	271
100	637	340	297	550	288	262

TABLE IV. Evaluated total, elastic, and nonelastic (reaction) cross sections (in mb) for n+^{16}O and ^{14}N, for various laboratory neutron energies.

^{16}O+n									
Energy	$\sigma(n)$	$E_{av}(n)$	$\sigma(p)$	$E_{av}(p)$	$\sigma(d)$	$E_{av}(d)$	$\sigma(\alpha)$	$E_{av}(\alpha)$	$\sigma(\gamma)$	$E_{av}(\gamma)$
20	558	6.5	54	5.2	25	5.2	403	5.1	402	4.5
23	512	7.8	70	5.9	35	6.1	397	5.6	361	4.7
27	480	8.8	122	6.8	50	7.4	389	4.5	322	4.8
30	460	10.0	129	7.7	55	9.6	415	4.4	308	4.9
35	437	11.8	150	9.2	57	13.3	424	4.4	287	4.9
40	413	13.4	162	10.5	61	16.5	392	4.8	264	4.9
50	403	17.3	192	13.0	67	20.2	290	5.3	253	4.8
60	407	19.7	223	15.8	66	22.2	249	6.0	231	4.7
70	396	22.3	227	18.4	68	25.4	228	6.5	207	4.6
80	395	24.8	231	19.7	68	27.7	219	6.9	187	4.5
90	400	26.6	242	21.7	68	27.8	219	7.3	165	4.5
100	419	28.7	256	23.2	72	28.3	221	7.6	158	4.5

^{14}N+n									
Energy	$\sigma(n)$	$E_{av}(n)$	$\sigma(p)$	$E_{av}(p)$	$\sigma(d)$	$E_{av}(d)$	$\sigma(\alpha)$	$E_{av}(\alpha)$	$\sigma(\gamma)$	$E_{av}(\gamma)$
20	424	6.6	209	4.0	45	6.5	214	5.3	320	3.6
23	448	7.2	210	4.8	54	7.5	213	6.3	296	3.3
27	511	7.5	232	5.6	68	8.6	228	5.0	249	3.0
30	520	8.3	234	6.3	73	10.1	262	4.9	230	3.0
35	507	9.2	232	7.9	80	12.5	329	4.6	194	3.1
40	498	10.4	231	9.0	86	15.2	369	4.6	169	3.1
50	475	13.2	235	11.9	84	19.5	382	4.6	134	3.2
60	450	16.0	237	14.9	74	23.0	358	5.0	120	3.3
70	419	18.4	228	17.6	69	26.5	336	5.8	102	3.3
80	425	20.0	242	18.9	70	28.7	336	6.1	90	3.3
90	429	21.9	251	20.4	69	30.2	319	6.5	84	3.3
100	430	23.7	258	21.5	71	30.5	310	6.8	74	3.3

TABLE V. Evaluated production cross sections (in mb) and average energies (in MeV) in the n+^{16}O and ^{14}N reactions, for various laboratory neutron energies (in MeV).

E_n	^{16}O+n						^{14}N+n					
	p	d	α	non. rec.	elas. rec.	Total	p	d	α	non. rec.	elas. rec.	Total
20	0.17	0.08	1.24	0.22	0.28	1.99	0.58	0.20	0.79	0.44	0.41	2.42
23	0.25	0.13	1.33	0.29	0.27	2.27	0.70	0.28	0.92	0.47	0.37	2.74
27	0.50	0.22	1.06	0.36	0.27	2.41	0.89	0.41	0.79	0.47	0.35	2.90
30	0.60	0.32	1.10	0.39	0.26	2.67	1.02	0.51	0.88	0.47	0.33	3.21
35	0.84	0.45	1.13	0.39	0.24	3.05	1.27	0.69	1.04	0.42	0.30	3.72
40	1.02	0.61	1.13	0.37	0.23	3.36	1.44	0.90	1.18	0.41	0.28	4.21
50	1.51	0.82	0.94	0.33	0.19	3.78	1.93	1.13	1.21	0.40	0.23	4.90
60	2.12	0.89	0.90	0.30	0.15	4.35	2.43	1.17	1.24	0.40	0.20	5.45
70	2.52	1.03	0.89	0.29	0.12	4.86	2.75	1.27	1.33	0.37	0.14	5.87
80	2.74	1.14	0.91	0.27	0.10	5.17	3.15	1.39	1.42	0.34	0.12	6.41
90	3.17	1.14	0.96	0.26	0.09	5.63	3.54	1.43	1.44	0.31	0.09	6.80
100	3.58	1.23	1.01	0.25	0.07	6.14	3.82	1.49	1.46	0.28	0.08	7.13

TABLE VI. Evaluated partial and total kerma factors (in units of f Gy m^2) for oxygen and nitrogen, for various laboratory neutron energies (in MeV). Contributions from protons, deuterons, alphas, non-elastic recoils, and elastic recoils, are given.

FIGURES
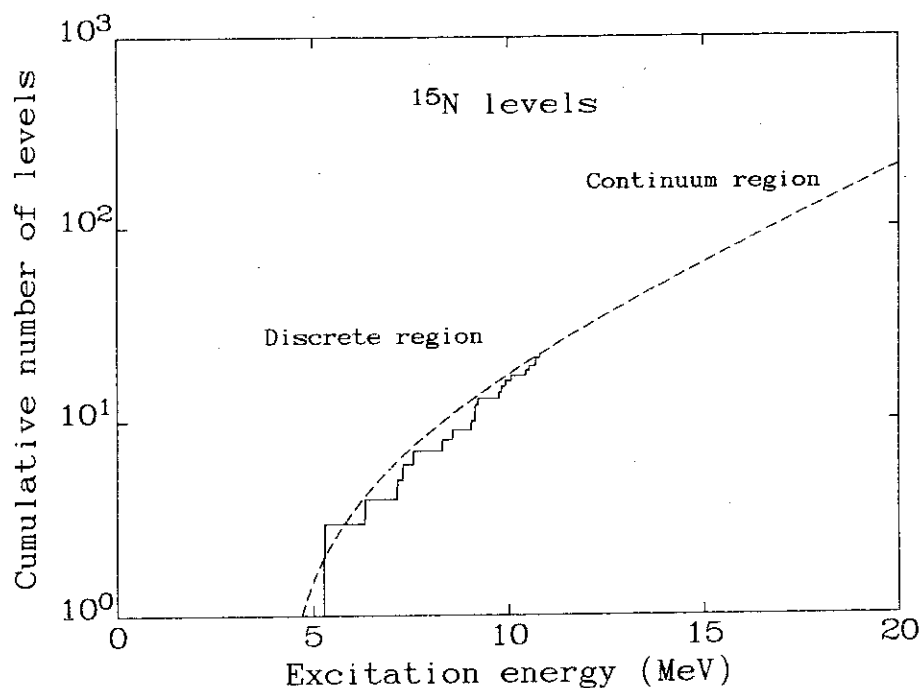
Fig. 1. An illustrative example of a level density analysis, for ^{15}N. Below 10.8 MeV experimental levels are used, and above this energy we use a statistical description, given by the dashed line.
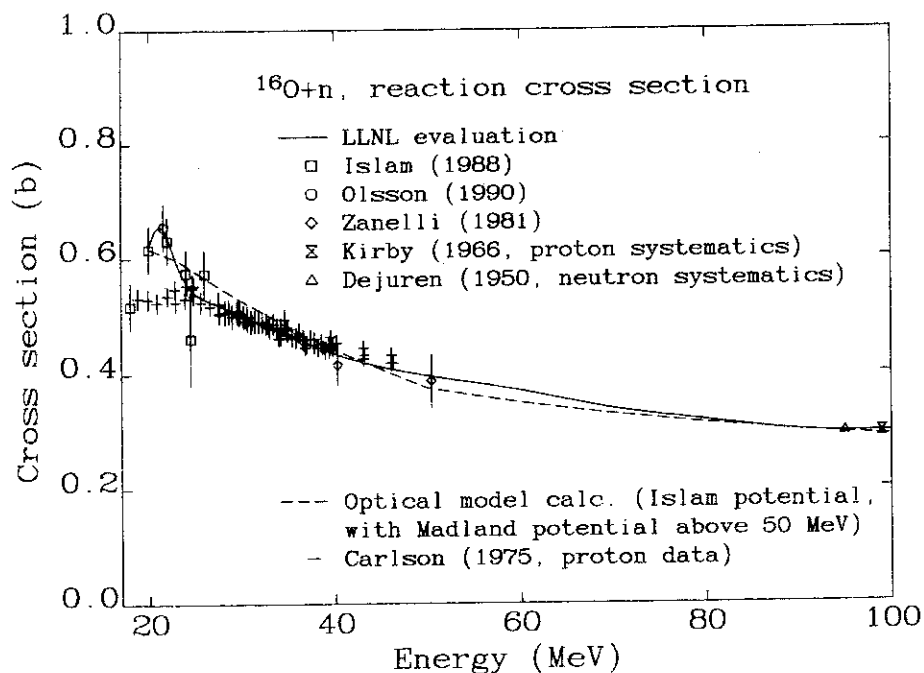
Fig. 2. Nonelastic cross section for neutrons on oxygen. The experimental data were taken from the Brookhaven NNDC CSISRS file [37].
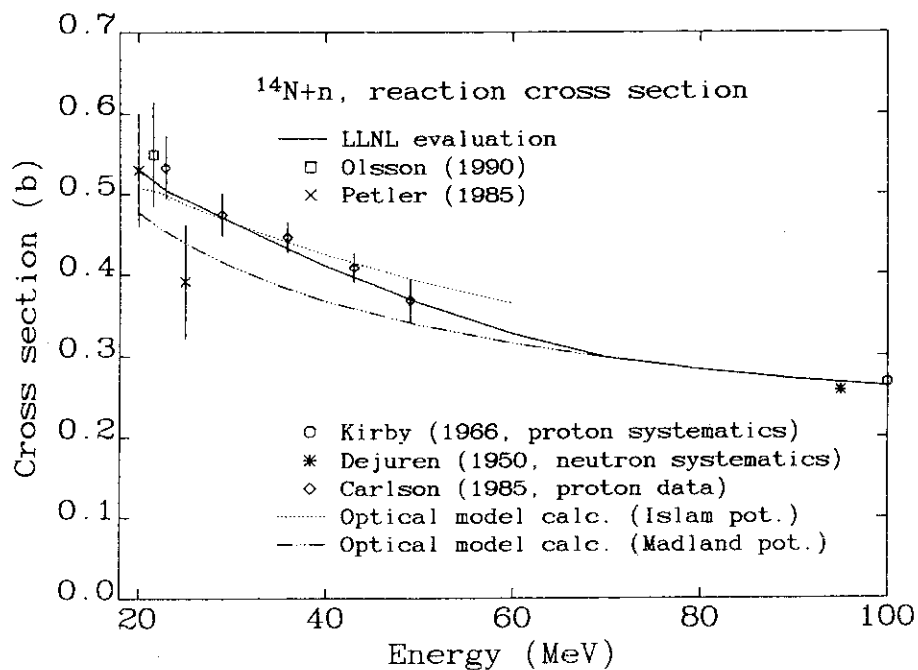
Fig. 3. Nonelastic cross section for neutrons on nitrogen. The experimental data were taken from the Brookhaven NNDC CSISRS file [37].
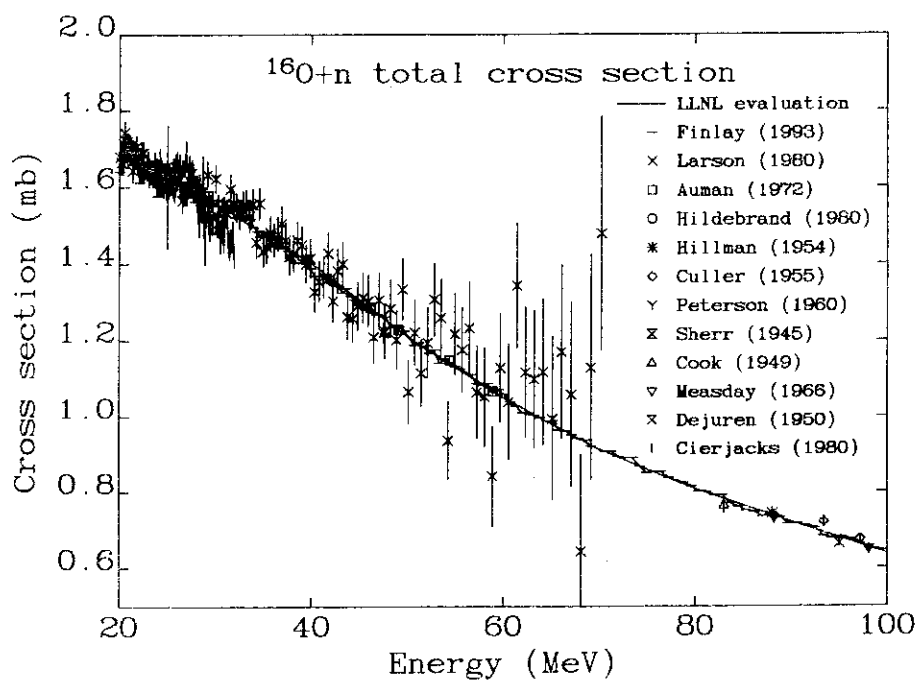
Fig. 4. Total cross section for neutrons on oxygen. The experimental data were taken from the Brookhaven NNDC CSISRS file [37]. .
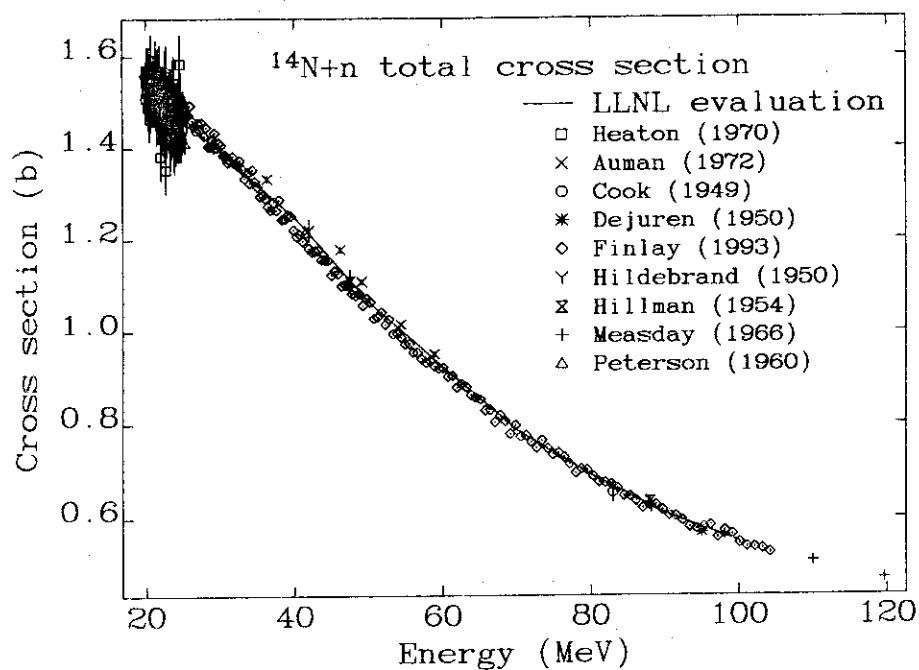
Fig. 5. Total cross section for neutrons on nitrogen. The experimental data were taken from the Brookhaven NNDC CSISRS file [37].
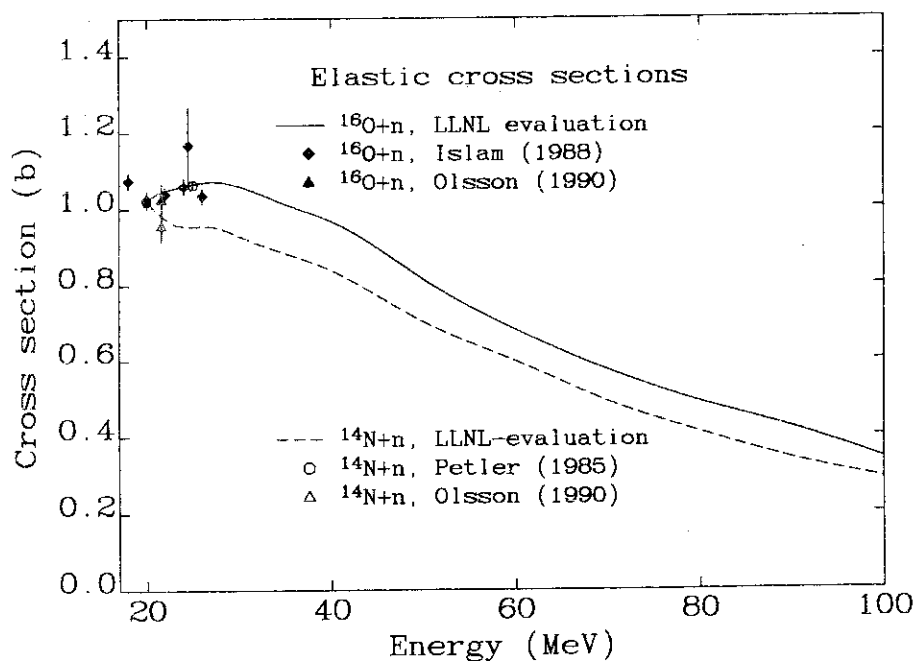
Fig. 6. Elastic cross section for neutrons on oxygen and nitrogen. The experimental data were taken from the Brookhaven NNDC CSISRS file [37].
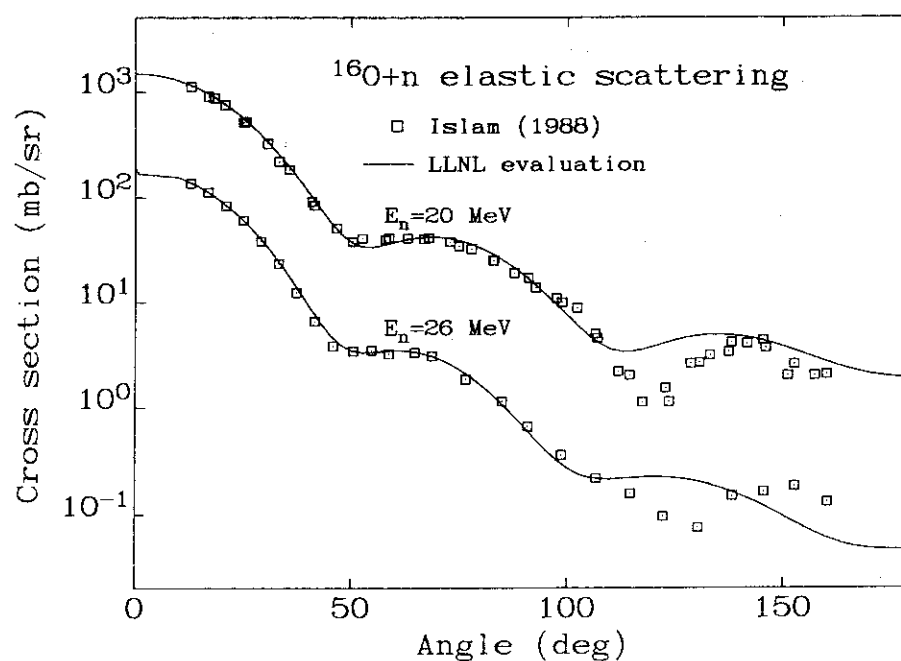
Fig. 7. Elastic angular distributions for neutrons on oxygen, compared with data of Islam *et al.* [24].
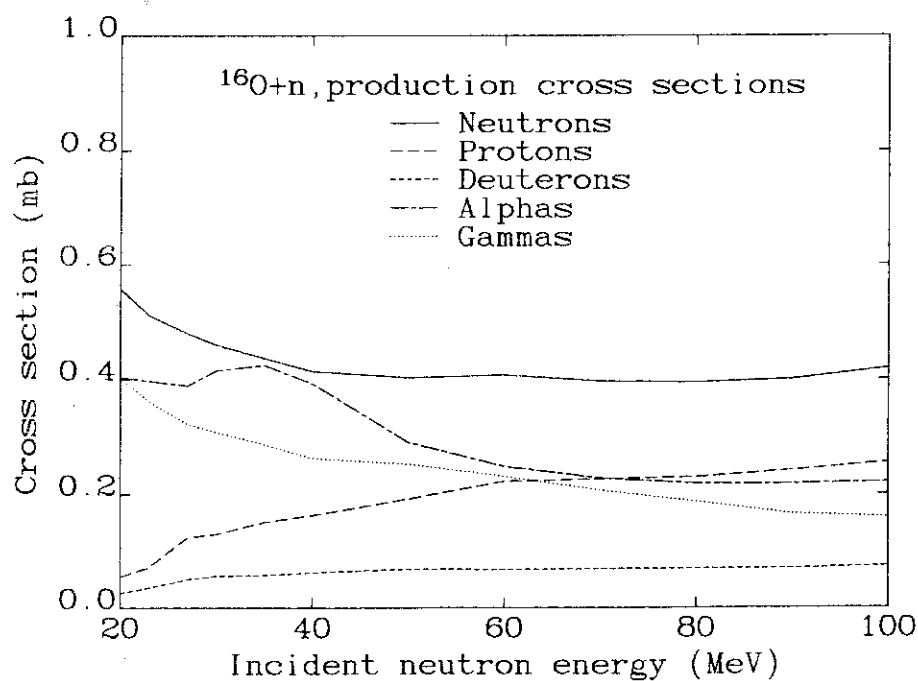
Fig. 8. Production cross sections of secondary particles with $A \leq 4$ for neutrons on oxygen.
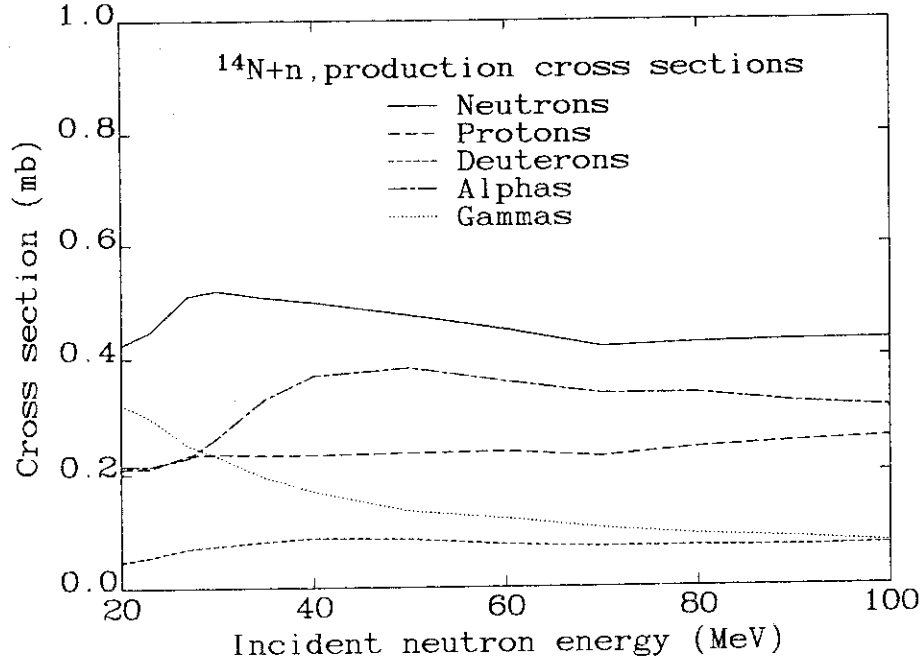
Fig. 9. Production cross sections of secondary particles with $A \leq 4$ for neutrons on nitrogen.
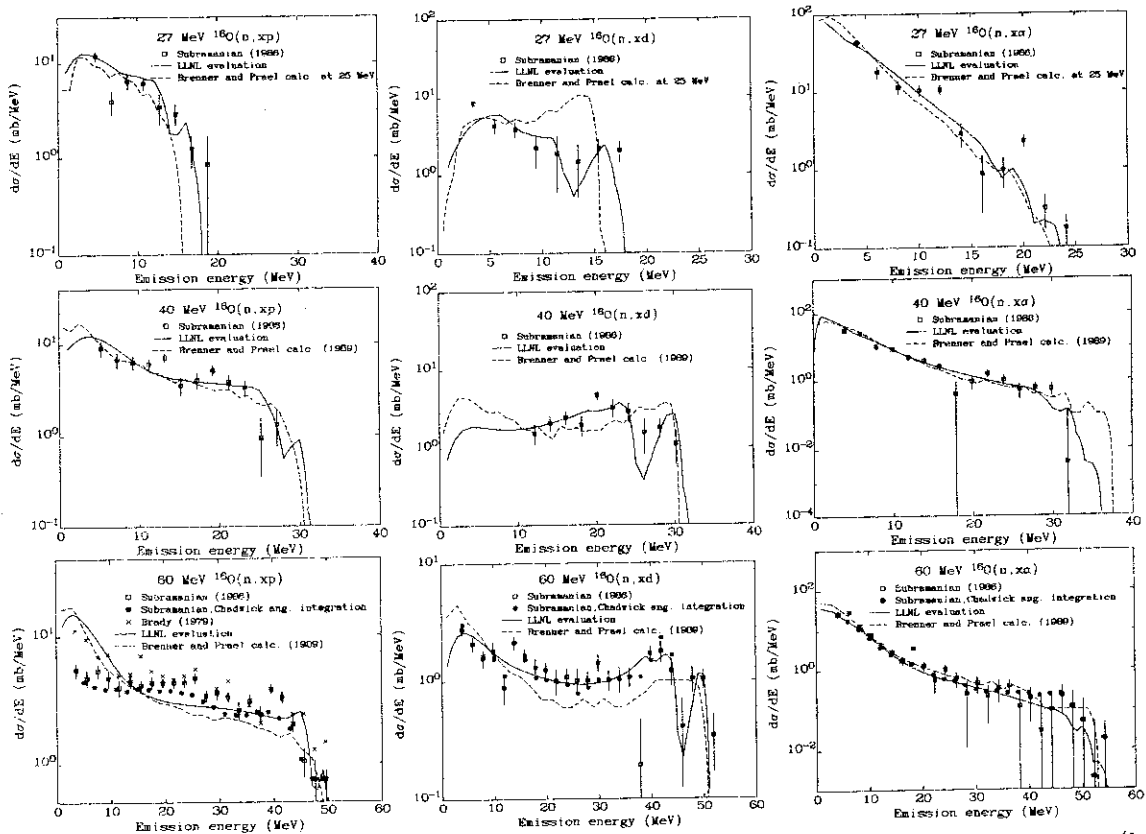
Fig. 10. Calculated angle-integrated proton, deuteron, and alpha emission spectra (lab frame) for neutrons on oxygen, compared with the data of Subramanian *et al.* [2]. Model calculations of Brenner and Prael [3] are also shown for comparison.
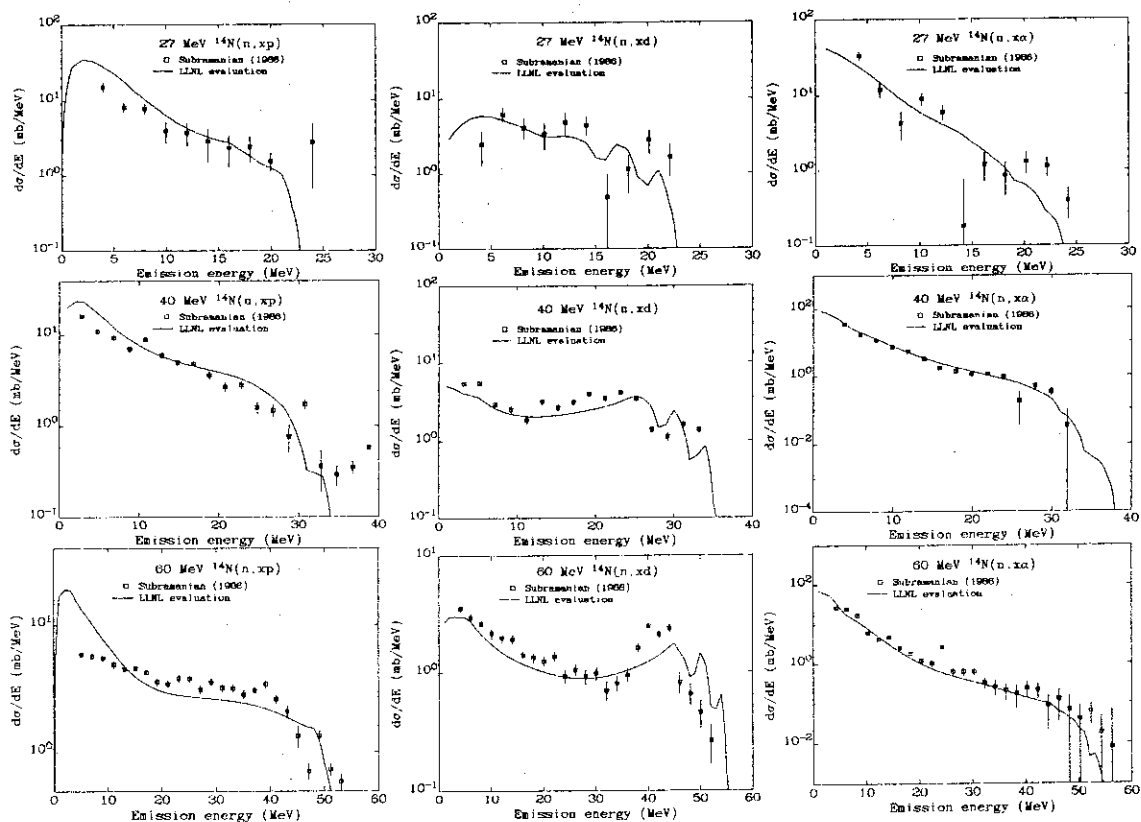
Fig. 11. Calculated angle-integrated proton, deuteron, and alpha emission spectra (lab frame) for neutrons on nitrogen, compared with the data of Subramanian *et al.* [2].
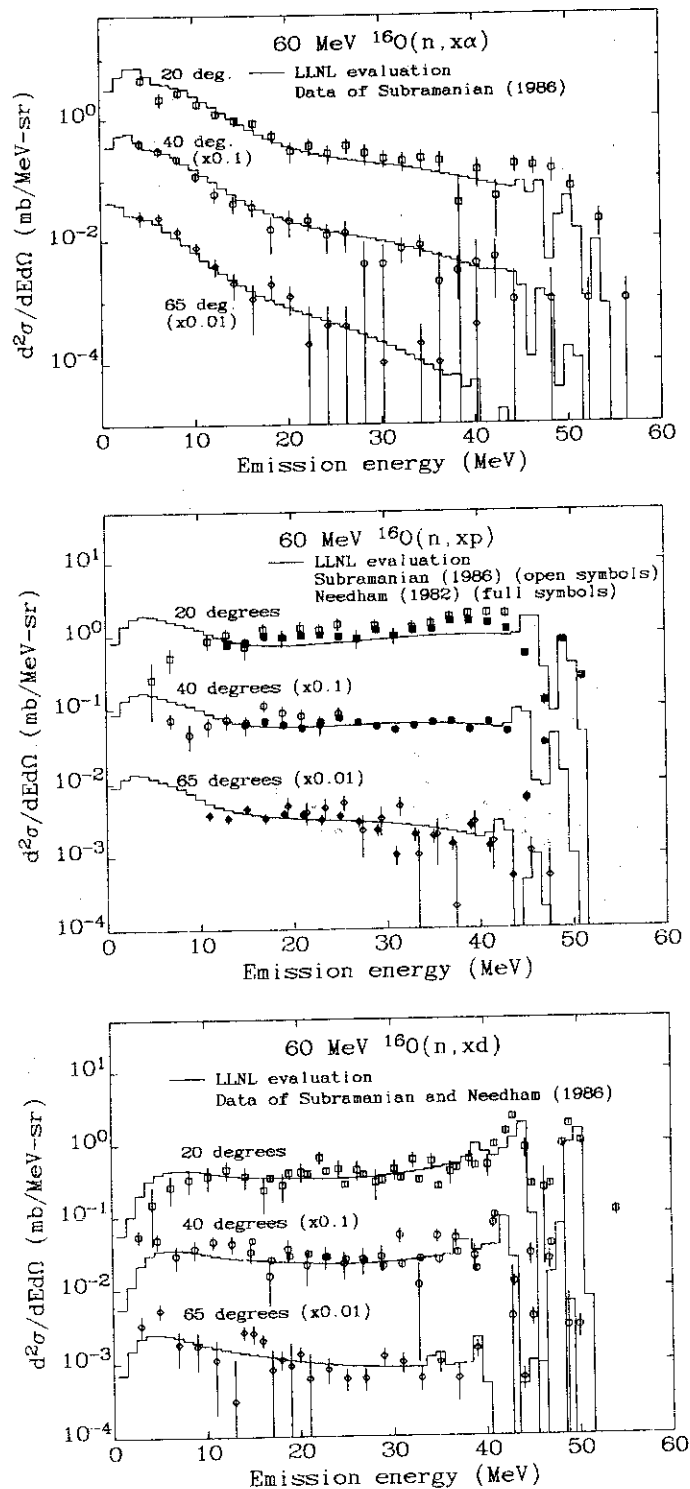
Fig. 12. Calculated double-differential spectra (lab frame) for alphas, protons, and deuterons following 60 MeV neutrons on oxygen, compared with the data of Subramanian et al. [2].
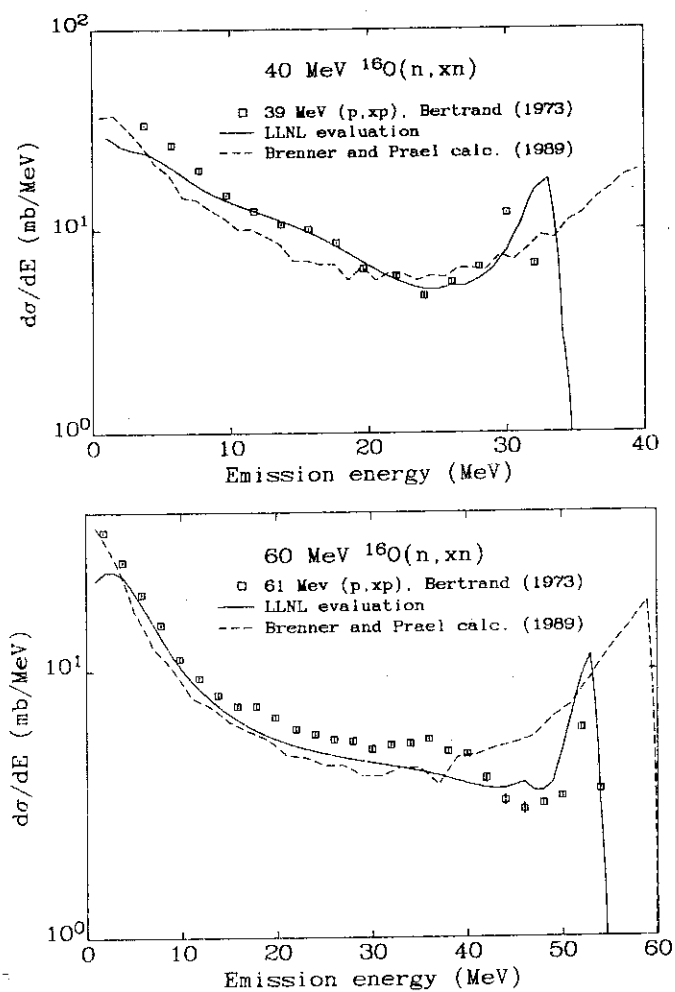
Fig. 13. Calculated $^{16}O(n,xn)$ angle-integrated spectra (lab frame) at 40 and 60 MeV compared with the Bertrand and Peelle $^{16}O(p,xp)$ measurements [43]. Brenner and Prael $^{16}O(n,xn)$ calculations are also shown for comparison [3].
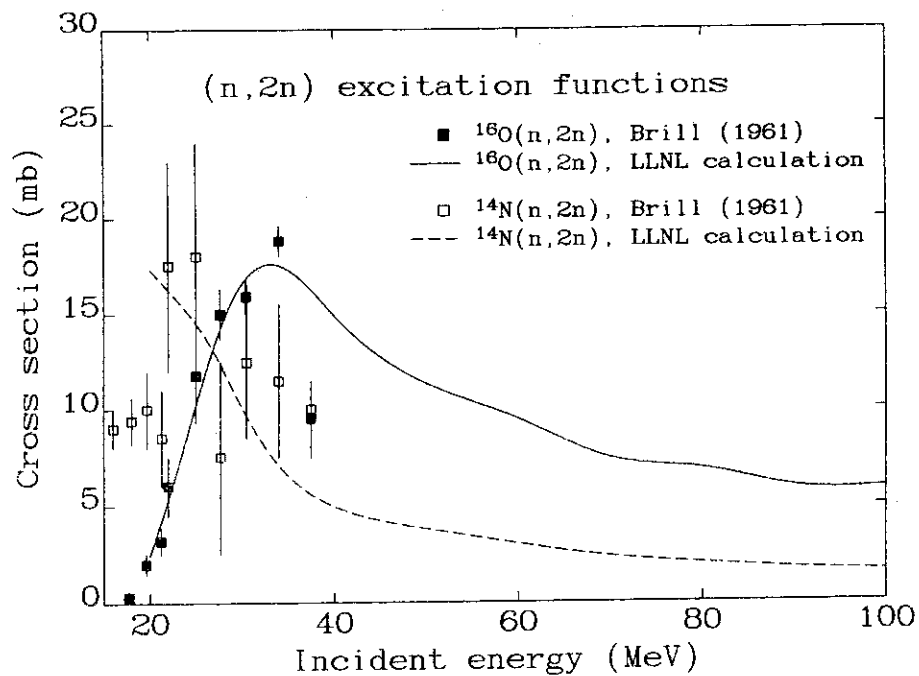
Fig. 14. The $^{16}O(n, 2n)^{15}O$ and $^{14}N(n, 2n)^{13}N$ calculated excitation functions compared with data of Brill et $al.$ [45].
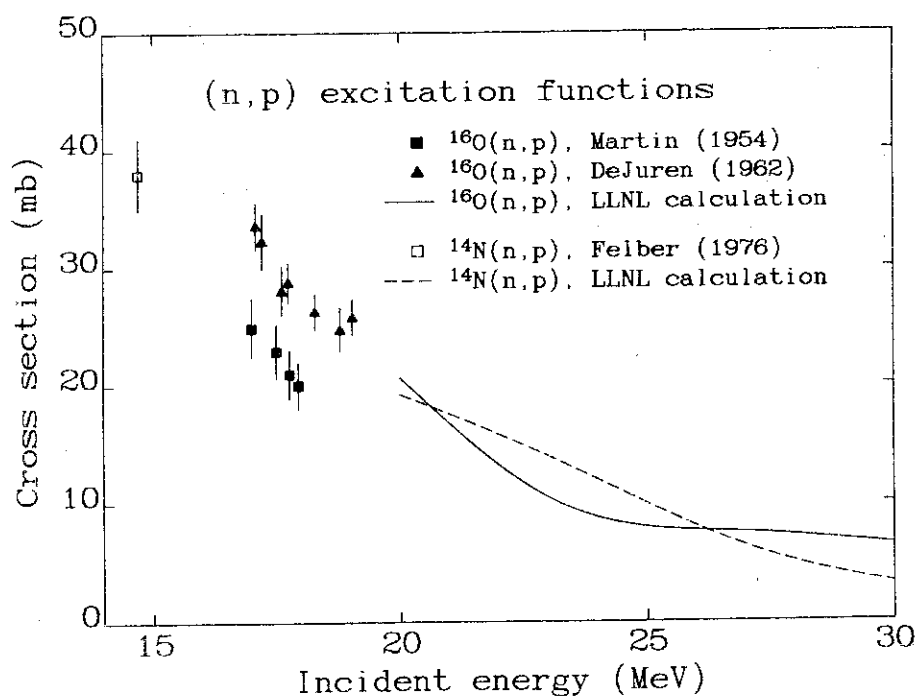
Fig. 15. The calculated $^{16}O(n, p)^{16}N$ excitation function compared with experimental data taken from the Brookhaven NNDC CSISRS file [37].
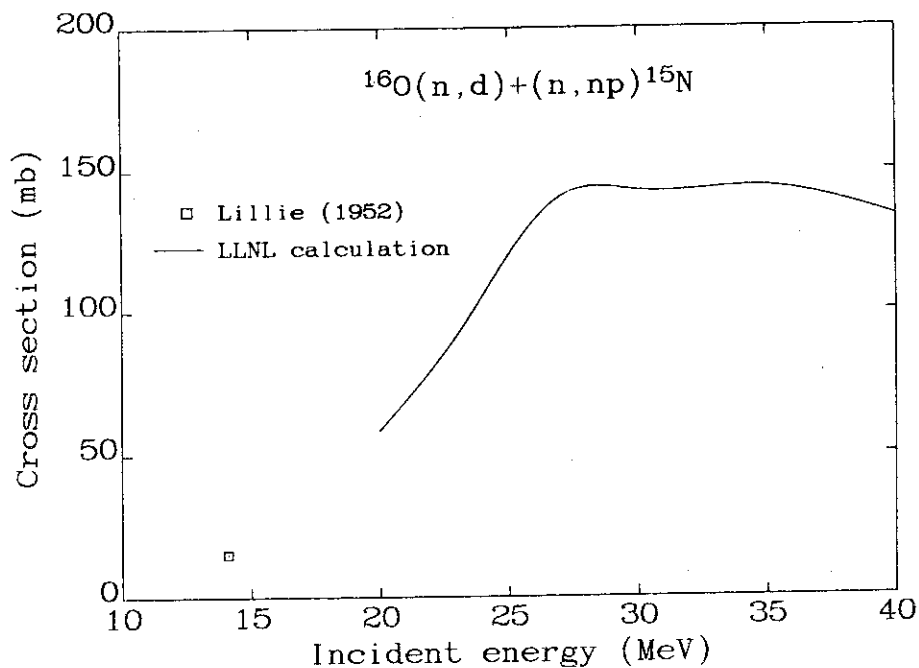
Fig. 16. The $^{16}O(n,d) + (n,np)^{15}N$ calculated excitation function compared with data of Lillie *et al.* taken from the Brookhaven NNDC CSISRS file [37].
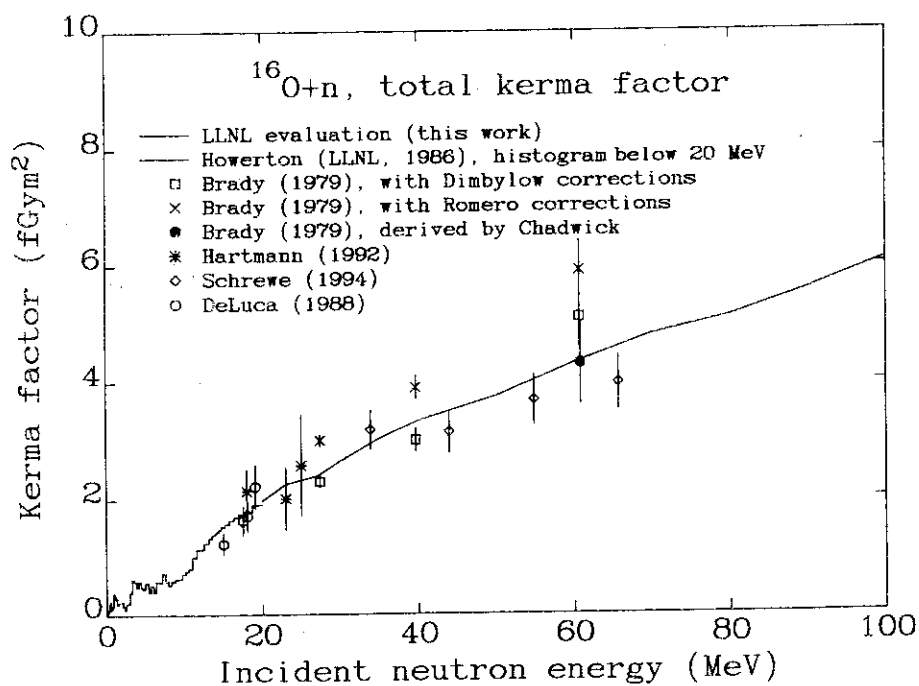
Fig. 17. Total calculated kerma factor for neutrons on oxygen compared with experimental measurements [14,42,46–48].
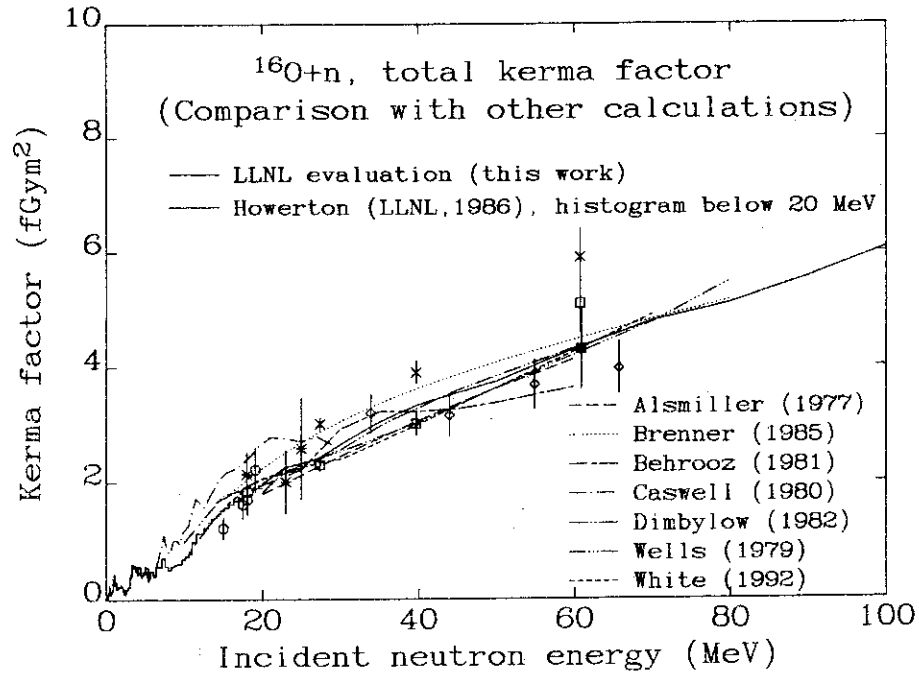
Fig. 18. Total calculated kerma factor for neutrons on oxygen compared with other calculations and evaluations [17,49,18,23,14,4,20,?]. For key to experimental points, see Fig. 17.
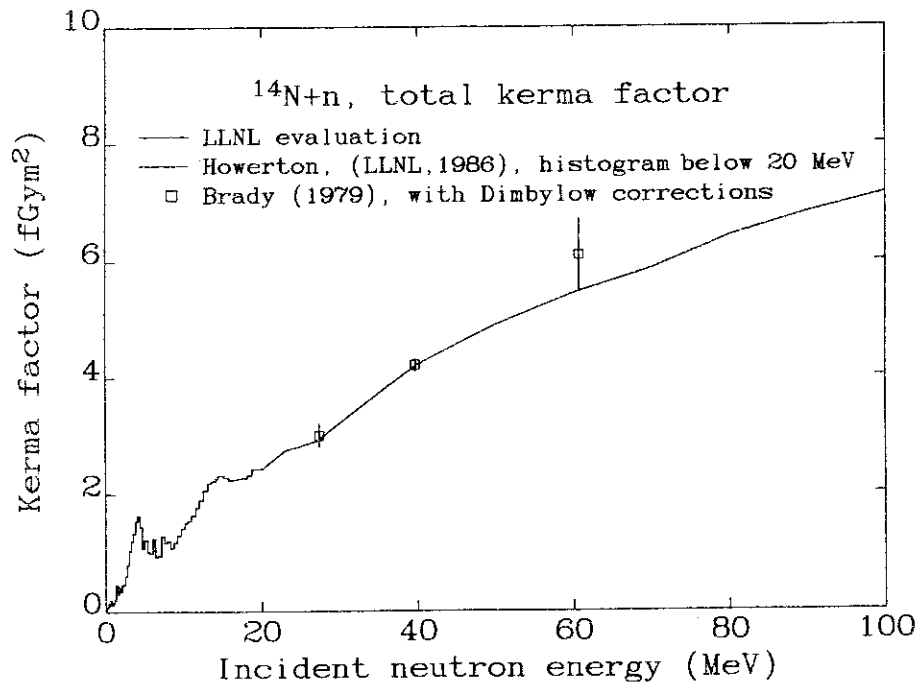
Fig. 19. Total calculated kerma factor for neutrons on nitrogen compared with experimental measurements of Brady et al. [14].
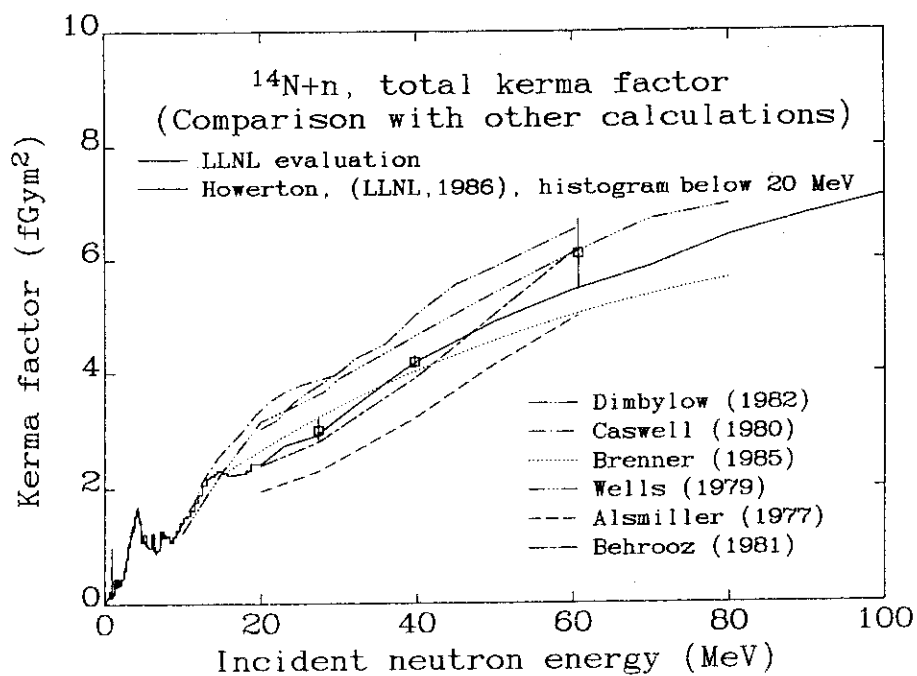
Fig. 20. Total calculated kerma factor for neutrons on nitrogen compared with other calculations and evaluations [17,49,18,23,14,4,20]. For key to experimental points, see Fig. 19.

3.11 Experimental Studies of keV Energy Neutron-Induced Reactions Relevant to Astrophysics and Nuclear Physics

T. Shima, T. Kii, T. Kikuchi, F. Okazaki, T. Kobayashi, T. Baba, Y. Nagai
and
M. Igashira*

*Department of Applied Physics, Tokyo Institute of Technology
and
* Research Laboratory for Nuclear Reactors, Tokyo Institute of Technology
2-12-1 O-okayama, Meguro, Tokyo 152, Japan
E-mail address : shima@nagai.ap.titech.ac.jp*

Nuclear reactions induced by keV energy neutrons provide a plenty of informations for studies of both astrophysics and nuclear physics. In this paper we will show our experimental studies of neutron- induced reactions of light nuclei in the keV energy region by means of a pulsed keV neutron beam and high-sensitivity detectors. Also we will discuss astrophysical and nuclear-physical consequences by using the obtained results.

1. Introduction

Origin of the elements is one of the most fundamental questions of nature. In the current astrophysics, it is considered that elements are produced by processes of nucleosynthesis occurring in the early universe and in stars. Neutron-induced reactions of light nuclei play quite important roles in nucleosynthesis in both sites. In the primordial nucleosynthesis, the standard big bang scenario/1,2/ predicts only negligible amounts of nuclei other than ^{2}H, ^{3}He, ^{4}He and ^{7}Li were produced because of the gaps at mass numbers of $A = 5$ and 8. However, if the QCD phase transition takes place by first-order, a fluctuation of the baryon density is formed, and the space is separated into two zones of the proton-rich one and the neutron-rich one. This is so-called the inhomogeneous big bang model/3/. In this model nucleosynthesis can proceed beyond the above mass gaps/4-6/, and in the neutron rich zone heavier nuclei can be produced via reaction chains such as ^{1}H(n,γ)^{2}H(n,γ)^{3}H(d,n)^{4}He(t,γ)^{7}Li (n,γ)^{8}Li(α,n)^{11}B(n,γ)^{12}B(e$^-$ ν_e) ^{12}C(n,γ)^{13}C(n,γ)^{14}C(n,γ)^{15}C ..... and so on. Since these reaction chains include many neutron-induced reactions of light nuclei, the efficiency of nucleosynthesis strongly depends on the cross sections of these reactions. Here the neutron energy range of interest is from a few to a few hundred keV, corresponding to the temperature of the universe in the era of the primodial nucleosynthesis. Therefore the keV neutron-induced reaction cross sections of light nuclei are important. On the other hand, nuclei heavier than ^{56}Fe are considered to be produced by neutron capture processes of stellar nucleosynthesis. There are two kinds of neutron capture processes. One is slow neutron capture (s-) process, and another is rapid neutron capture (r-) process. They are considered to be occurring in helium burning zones of evolved stars and in super novae, respectively. Neutrons for the s-process are supposed to be provided from the ^{13}C(α,n)^{16}O reaction in low and intermediate mass stars and the ^{22}Ne(α,n)^{25}Mg reaction in stars heavier than ten solar mass/7,8/. However, helium rich zones usually contain large quantities of light nuclei such as ^{12}C, ^{14}N, ^{16}O etc., s-process may be hindered if the neutron-induced cross sections of those light nuclei are too large. Such light nuclei are called 'neutron poisons'/9/. So the cross sections of light nuclei are crucial also in stellar s-process.

From the view point of nuclear physics, neutron capture reactions of light nuclei are

quite useful to study capture mechanisms, properties of the excited states of the produced nucleus, and so on/10,11/.

So far we have measured (n,γ) cross sections of ^{1}H, ^{7}Li, ^{12}C, ^{13}C and ^{16}O and an (n,p) cross section of ^{14}N. In the following we would like to demonstrate outlines of the ^{12}C$(n,\gamma)^{13}$C and^{14}N$(n,p)^{14}$C experiments as examples. Also we will show astrophysical and nuclear-physical consequences.

2. Measurement of the ^{12}C$(n,\gamma)^{13}$C reaction

2.1 Experimental method

The experiment was carried out at the Research Laboratory for Nuclear Reactors (RLNR) in Tokyo Institute of Technology/12/. We employed a 1.5 ns pulsed neutron beam and a method of the prompt γ-ray detection. The pulsed neutron beam was generated by using the ^{7}Li$(p,n)^7$Be reaction ($Q = -1.64$ MeV). The proton energies were adjusted to 1.955, 2.13 and 2.48 MeV in order to produce neutrons in the energy ranges from 10 to 75 keV, from 30 to 250 keV and from 450 to 600 keV, respectively. The energy distribution and the intensity of the neutron beam was monitored with a ^{6}Li glass scintillation counter during the experiment. Fig. 1 shows an example of the neutron energy spectrum with the average enregy of between 10 and 75 keV.
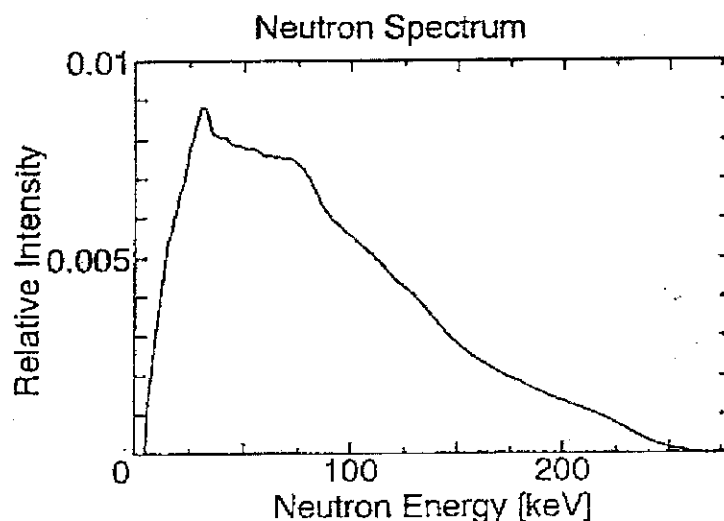
Figure 1. A neutron energy spectrum observed with a gold sample.

The neutron beam irradiated a natural carbon sample made of graphite of the reactor grade. The thickness, the diameter, and the density were 24.8 mm, 60.2 mm and 1.66 g/cc, respectively, and the number density of ^{12}C nuclei was 0.2041 atoms/b. Prompt γ-rays from the produced nuclei were detected with a high-sensitivity γ-ray spectrometer. Fig. 2 shows a schematic drawing of the spectrometer. The spectrometer consists of a central NaI(Tl) scintillation counter with a diameter of 7.6 cm and a length of 15.2 cm, a cylindrical one with a diameter of 25.4 cm and a length of 28.0 cm. The latter is used as a Compton suppressor and a veto counter for charged cosmic rays and background γ-rays from surroundings. We used a shielding made of 20 cm thick borated paraffin and a shielding made of 10 cm thick lead, in order to reduce backgrounds due to neutrons and neutron-induced γ-rays, respectively.
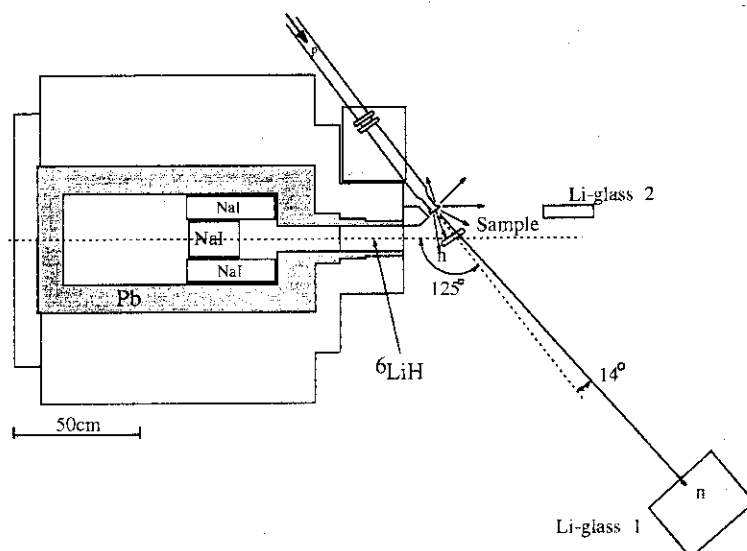
Figure 2. A schematic drawing of the cross section of the γ-ray spectrometer.

The spectrometer was set at the angle of 125° with respect to the neutron beam axis. Since we can safely assume the γ transitions are dominated by dipole ones in the keV energy region, the second Legendre polynomial vanishes at this angle, and we can obtain the angle-integrated γ-ray intensities. In this measurement we made three kinds of runs with the carbon sample, the gold sample, and without any sample. Since the cross section of the $^{197}Au(n,\gamma)^{198}Au$ reaction is known with accuracy of better than about 3% up to a few hundred keV/13/, we could use it as a normalization of the measurement. The run with no sample was done to measure the energy spectrum of the incident neutron without disturbance due to the neutron scattering in samples. These three kinds of runs were carried out cyclically in order to remove the effect of the time dependences of the conditions of the apparatuses and the neutron beam.

2.2 Data analysis

Fig. 3 shows a neutron TOF spectra measured with the γ-ray spectrometer.
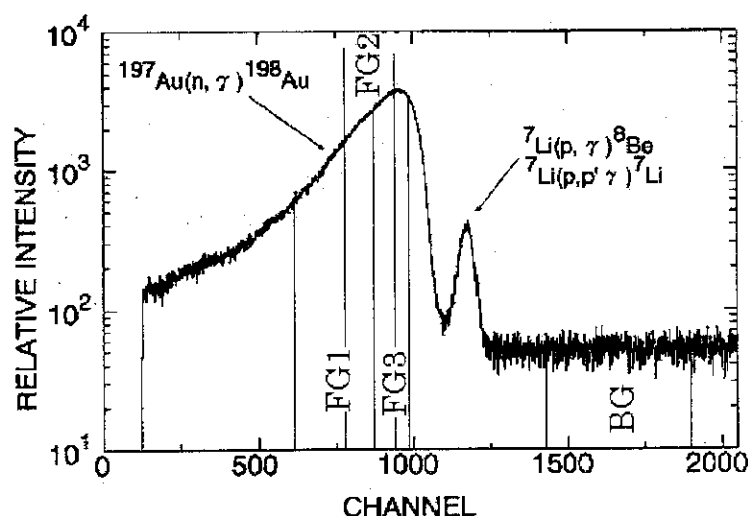
Figure 3. A neutron TOF spectrum for the gold sample measured with the γ-ray spectrometer.

In this spectrum, TOF is plotted against the abscissa, namely it is decreasing as the channel number increases on the horizontal axis. A sharp peak at 1170 channel is

due to the |gamma-rays from the ^{7}Li(p,γ)^{8}Be and ^{7}Li(p,p' γ)^{7}Li reactions. A broad peak distributed between 100 and 1100 channels corresponds to the ^{197}Au(n,γ)^{198}Au reaction events. In order to obtain the cross sections for different neutron energies, we set several gates on the TOF spectrum as shown in Fig. 3. FGs are the gates for the foreground events, and BG is the one for the background events including the events due to thermal neutrons, cosmic rays, γ-rays from surroundings, and so on. Net spectra of the γ-ray pulse heights for each gates are obtained by subtracting the spectrum for BG from the ones for each FGs.
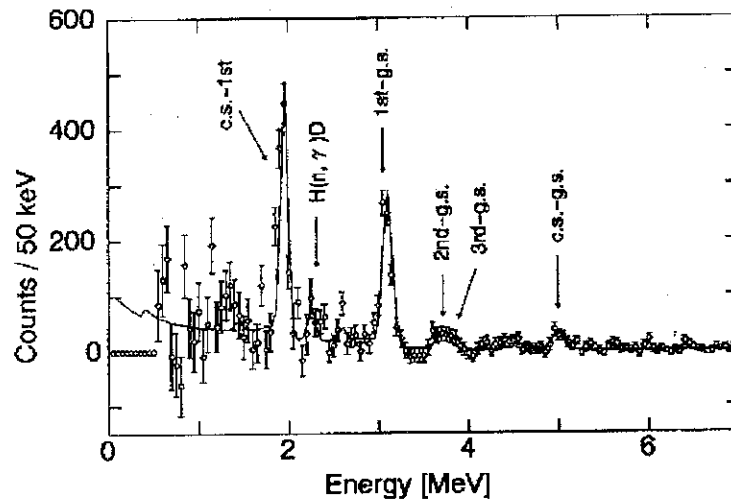
Figure 4. A net spectrum measured with the ^{13}C sample.

Fig. 4 shows an example of the net spectra obtained for the gate FG3. In Fig. 4, we can find several peaks due to the γ-rays emitted from the transitions of the produced ^{13}C nuclei. An intensity of each γ-rays was obtained by fitting the peak with the response function of the γ-ray spectrometer. The partial cross section σ_i from the captured state to a low-lying i-th state is obtained by using the corresponding transition intensity I_i as follows :

$$\sigma_i = C \times \frac{(\Omega \times N \times \phi)_{Au} \times I_{Au}}{(\Omega \times N \times \phi)_{^{12}C} \times I_i}, \tag{1}$$

where Ω, N, and ϕ denote the solid angles of the samples to the ^{7}Li neutron source, the thicknesses of the samples, and the neutron intensities in the measurements, respectively. I_{Au} stands for the transition intensity of the ^{197}Au(n,γ)^{198}Au reaction. A coefficient C is a correction factor for the multiple scattering effect and the absorption of the incoming neutrons in each samples. The correction factor was calculated by using a Monte Carlo cord TIME-MULTI developed by Senoo et al./14/.

2.3 Results

The partial cross sections were obtained as listed in Table 1.

E_n	$\overline{E_n}$	Partial (μb)				Total (μb)
		c.s.→gnd	c.s.→1st	c.s.→2nd	c.s.→3rd	
12~26	21	3.0±0.8	6.7±1.2	1.3±1.3	0.9±0.9	11.9±2.2
30~50	40	1.2±0.4	8.7±1.0	0.9±1.2	0.4±0.5	11.2±1.7
30~70	50	1.8±0.6	8.6±1.1	1.0±0.5	1.9±0.9	13.1±1.6
30~75	60	2.2±0.7	11.2±1.5	1.1±1.0	1.5±2.8	15.9±3.4
70~130	97	1.0±0.3	12.3±1.3	0.6±0.4	1.3±1.0	15.2±1.7
160~250	199	1.6±0.7	16.5±2.2	0.7±0.7	2.8±3.4	21.6±4.1

Table 1. Summary of the ^{12}C(n,γ)^{13}C cross sections.

2.4 Discussions

The presently obtained $^{12}C(n,\gamma)^{13}C$ total cross section is about ten times larger than the values obtained from the thermal capture cross section with 1/v extrapolation, which has been used in previous calculations of nucleosynthesis. This result indicates that heavy element production can be more efficient than previously expected in the inhomogeneous big bang nucleosynthesis. On the other hand, stellar heavy element synthesis will be hindered due to consumption of neutrons by the $^{12}C(n,\gamma)^{13}C$ reaction. Especially, the effect of ^{12}C will be more important in low metalicity stars, because the neutron capture by heavier nuclei become negligible.

As for the reason why the cross section becomes much larger than the 1/v extrapolated value, the energy dependences of the partial cross sections give us hints. We can find the total capture cross section is dominated by the partial one for the transition from the captured state to the first 2s1/2 state. This transition is likely to be occuring by E1 transition in the energy range of the present concerns, and therefore the initial ^{12}C 0^+ state has to absorb the p-wave compornent of the incident neutrons. And if we can assume that the state of the core ^{12}C nucleus is not changed in the case of the p-wave neutron capture, the cross section becomes proportional to the velocity of the neutron, or the square root of the neutron energy equivalently. Consequently, the total cross section becomes much larger than the 1/v extrapolated value. This implies that the $^{12}C(n,\gamma)^{13}C$ reaction occurs with the direct capture mechanism, and the 2s1/2 state of ^{13}C has a strong single-particle character. A theoretical discussion is made by Mengoni in his contribution to this symposium.

2.5 Preliminary results for the other reactions

Recently we studied two reactions of $^7Li(n,\gamma)^8Li$ and $^{13}C(n,\gamma)^{14}C$, and preliminary results were obtained as shown below.

2.5.1 $^7Li(n,\gamma)^8Li$

This reaction is important in the inhomogeneous big bang nucleosynthesis, because they are included in the reaction chain shown in Sec. 1. And it is also important concerning the solar neutrino problem. Namely, the discrepancy between the theoretically predicted solar neutrino flux and the experimentally measured one has been a long-standing serious problem/15/. One of the solutions to the problem is that in the theoretical prediction the neutrino flux from the ^8B beta decay may be overestimated by using a too-large value of the cross section of the $^7Be(p,\gamma)^8B$ reaction, which is a part of the CNO cycle of the hydrogen burning in the sun. In reality, the cross section at the temperature of the solar center is far smaller than the limit of the experimental sensitivity at present. So the cross section has been estimated by extrapolating the experimental data at higher energies, and it cannot be avoided that a no small systematic error is introduced with the extrapolation. Here the study of the $^7Li(n,\gamma)^8Li$ reaction may provide informations with which we can verify the estimated value of the $^7Be(p,\gamma)^8B$ reaction cross section. This is because the $^7Li(n,\gamma)^8Li$ reaction is a mirror reaction of $^7Be(p,\gamma)^8B$, and the $^7Li(n,\gamma)^8Li$ cross section is expected to be convertible into the $^7Be(p,\gamma)^8B$ one by taking into account the effects of the electromagnetic interaction properly. And in the real experiment it is much easier to measure the $^7Li(n,\gamma)^8Li$ reaction, since the $^7Li(n,\gamma)^8Li$ reaction is not hindered by the Coulomb barrier in contrast with the $^7Be(p,\gamma)^8B$ reaction.

In the $^7Li(n,\gamma)^8Li$ experiment we used the procedure similar to that for the $^{12}C(n,\gamma)^{13}C$ experiment, except for the γ-ray detector and the (n,γ) sample. In this experiment we employed a new γ-ray detector, consisting of four NaI(Tl) crystals with a diameter of 22.9 cm and a length of 20.3 cm. As for the ^7Li sample we used a disk made of Li_2O with a diameter of 64 mm, in which ^7Li was enriched to 99.94was 0.101 atoms/b. As the prelimiary results, 52.3±3.3 μb and 32.1±2.0 μb were obtained as the total cross section at the average neutron energies of 24.9 keV and 50.7 keV, respectively. This result seems to support the relatively smaller value of the $^7Be(p,\gamma)^8B$ cross section estimated by Barker/16/, and it can partly reduce the discrepancy between the predicted ^8B solar neutrino flux and the measured one.

2.5.2 $^{13}C(n,\gamma)^{14}C$

The contribution of the $^{13}C(n,\gamma)^{14}C$ reaction in the inhomogeneous big bang nucleosynthesis is important as well as the above discussed reactions. In addition, the reaction may be one of the strong neutron poisons for the s-process operating with the $^{13}C(\alpha,n)^{16}O$ neutron source, because it can absorb not only the produced neutrons but also the ^{13}C seed nucleus.

The measurement of the $^{13}C(n,\gamma)^{14}C$ reaction cross section was carried out with the same experimental procedure and the same γ-ray spectrometer as the $^{12}C(n,\gamma)^{13}C$ measurement. We used a sample of 99.9% enriched ^{13}C packed in a container made of natural carbon. The thickness of the sample was 0.0459 atoms/b. The obtained results are listed in Table 2.

		Partial (μb)			Total (μb)
E_n	$\overline{E_n}$	c.s.$\rightarrow$g.s.	1st$\rightarrow$g.s.	5th$\rightarrow$g.s.	
10~40	25.7	1.3±0.6	12.2±2.6	6.3±2.5	19.8±3.7
41~87	61.1	0.8±0.3	9.8±1.3	1.6±1.1	12.2±1.7

Table 2. Summary of the $^{13}C(n,\gamma)^{14}C$ cross sections

3. Measurement of the $^{14}N(n,p)^{14}C$ reaction

^{14}N is produced efficiently by the CNO hydrogen burning, and thus it is the secondary abundant nuclide in the helium burning zones. The mass fraction of ^{14}N in the helium burning zones is typically of the order of 10^{-4}/17/. When the helium burning is operating, ^{14}N can be converted through the reaction chain $^{14}N(\alpha,\gamma)^{18}F(\beta^+)^{18}O$ $(\alpha,\gamma)^{22}Ne$ into ^{22}Ne, which is one of the candidates of the neutron sources for s-process. ^{14}N, however, may also act as a strong neutron poison for s-process, because the $^{14}N(n,p)^{14}C$ reaction cross section is very large compared to the neutron-induced reaction cross sections of other nuclei at stellar temperature. Therefore the effect of ^{14}N on the s-process is very crucial. Nevertheless the effect is still uncertain. This is mainly due to large discrepancies between the data of the $^{14}N(n,p)^{14}C$ cross section in the keV region, which were obtained by previous experiments. For example, Brehm et al. obtained 0.81±0.05 mb and 0.52±0.06 mb at $kT = 25.0$ keV and 52.4 keV, respectively/18/. These values are factors of 2~3 smaller than the evaluated ones by Fowler et al./19/ by using the data of reverse reactions/20/, which were used in previous calculations of the s-process nucleosynthesis. On the other hand, Koehler and O'Brien measured the cross section in the neutron energies of between 61 meV and 34.6 keV/21/, and the obtained values are consistent with the estimation. If the cross section is smaller than about a few hundred μb at $kT = 25.0$ keV, the effect of ^{14}N as a neutron poison becomes less important, since the neutrons are absorbed mainly by not ^{14}N but heavier nuclei. But if the cross section of ^{14}N is as large as a few mb, the effect of ^{14}N cannot be neglected. Therefore it is needed to obtain a reliable cross section of the $^{14}N(n,p)^{14}C$ reaction in order to investigate the effect of ^{14}N as well as the heavy element synthesis by the s-process.

3.1 Experimental method

In the experiment we used a keV energy pulsed neutron beam at RLNR, which is the same as the one used in our (n,γ) measurements. We employed a detector called Gas Scintillation Drift Chamber (GSDC)/22/. The GSDC is a hybrid of a gas scintillation counter and a time projection chamber. Since it is filled with a mixture of He and N_2, it serves as an active gas target. Therefore a detection efficiency of nearly 100% and a solid angle of 4π are obtained. Fig. 5 shows a schematic drawing of the experimental setup.

The neutron beam was introduced into the GSDC through a neutron collimater made of borated paraffin and a γ-ray shield made of 10 cm lead bricks. We used two kinds of gas samples, a mixture of 80% natural He and 20% N_2 (hereafter "natural sample"), and a mixture containing 0.31% ^3He in addition to the natural sample (hereafter "enriched sample"). Since the cross section of the $^3He(n,p)^3H$ reaction is well known in the keV

energy region/23/, it can be used for calibrating the detection efficiency of the GSDC. Pressures of the sample gases were kept at 600 Torr.
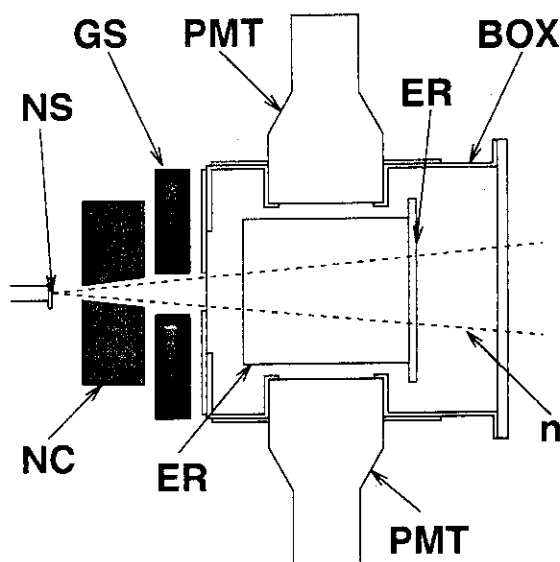
Figure 5. The experimental setup in the ^{14}N(n,p)^{14}C measurement.
NS: ^{7}Li neutron source, NC: neutron collimeter, GS: γ-ray shield,
n: neutron beam, ER: effective region, BOX: gas-tight box,
PMT: photomultiplier tubes.

When an incoming neutron causes an (n,p) reaction event in the active region of the GSDC, an emitted proton moves in the gas by producing both ionized electrons and excited gas atoms. The ionized electrons are detected by sense wires of the GSDC, and the signals provide informations about the shape of the track and the energy of the proton. With these informations, the (n,p) reaction events can be separated from the background ones with a high selectivity. The excited atoms produce prompt scintillation photons with a life time of a few nsec. By detecting these photons, we could obtain signals of the (n,p) reaction time, which was used as both the time signal of the time-of-flight (TOF) measurement and the trigger signal of the GSDC. The TOF measurement was carried out not only to measure neutron energies but also to reject the contribution of the thermal neutrons. Since they have no time-correlation with the incident neutron pulse, they produce a constant background component in the TOF spectrum. So we can subtract the thermal background by setting appropriate gates in the TOF spectrum as follows.

3.2 Data analysis

In Fig. 6 histograms (a) and (b) show the neutron TOF spectra obtained for the measurements with the enriched sample and the natural one, respectively. Here, in the histogram (b), the values five times as much as the real observed counting rates.

Here sharp peaks around 0 channel are due to the signals of the γ-rays from the ^{7}Li(p,γ)^{8}Be reaction events occuring at the ^{7}Li neutron source. Broad humps between 14 and 50 channel consist of two components, the (n,p) reaction events by the keV neutrons, and the ones by the thermal neutrons. In order to obtain net (n,p) counting rates, we set three gates of FG1, FG2, and BG, corresponding to the foreground events due to higher energy neutrons, the one due to lower energy neutrons, and the background events mainly due to thermal neutrons, respectively.

Fig. 7 is an example of net spectra of protons, obtained with the gate FG1 for the enriched sample gas. A broad peak around 80 channel is due to the protons which have complete trajectories in the effective region of the GSDC. A net counting rate $R_{FG1}(enr.)$ for the gate FG1 was given as an area of the spectrum above the discrimination level indicated in Fig. 7.
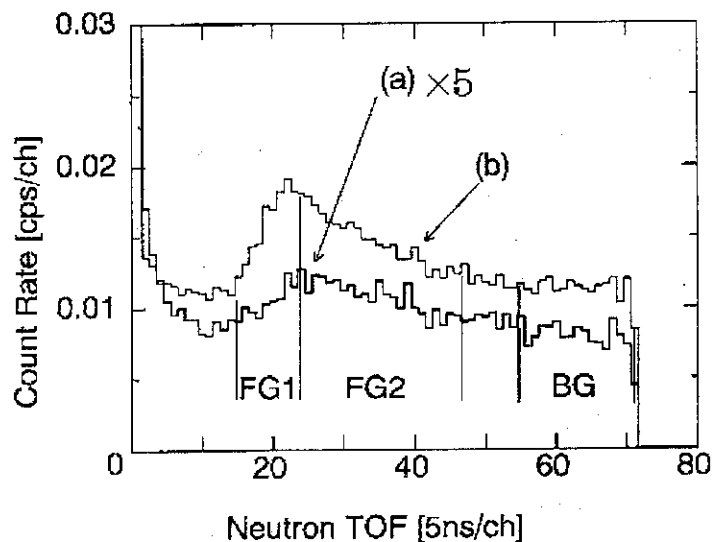
Figure 6. Neutron TOF spectra for the enriched (a) and the natural (b) samples.
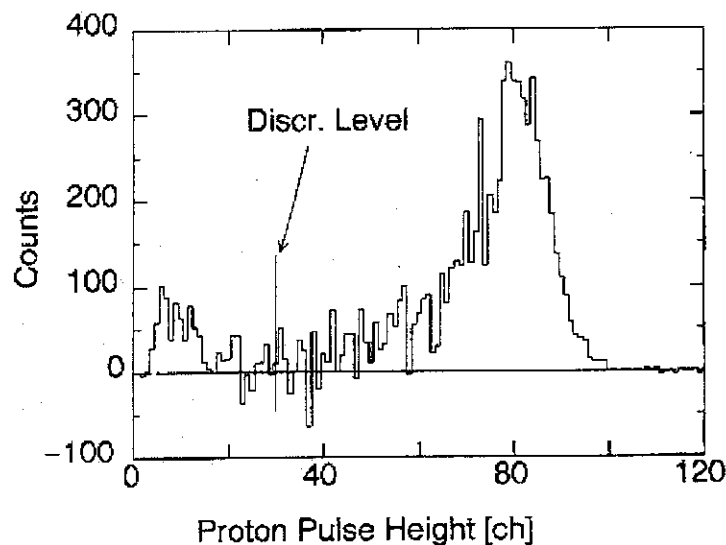
Figure 7. A net spectrum of the protons in the measurement of the enriched sample.

Net counting rates $R_{FG2}(enr.)$, $R_{BG}(enr.)$, $R_{FG1}(nat.)$, $R_{FG2}(nat.)$, and $R_{BG}(nat.)$ were obtained by the same procedure for the enriched sample and the natural sample. Here "enr." and "nat." denote the types of the sample gases used to measure respective Rs.

The cross section of the $^{14}N(n,p)^{14}C$ reaction is given as follows :

$$\sigma(^{14}N) = \frac{R(^{14}N)}{R(^3He)} \times \frac{\varepsilon(^3He)}{\varepsilon(^{14}N)} \times \frac{N(^3He)}{N(^{14}N)} \times \frac{\phi(^3He)}{\phi(^{14}N)} \times \sigma(^3He), \tag{3}$$

where σ, ε, N, and ϕ stand for the (n,p) cross sections, the detection efficiencies for the emitted protons, the surface densities of the (n,p) sample nuclei, and the neutron intensities, for the measurements with the samples denoted by the indices, respectively.

3.3 Results and discussions

The ^{14}N(n,p)^{14}C reaction cross sections were obtained as 1.67±0.33(stat.)±0.13(sys.) mb and 1.19±0.14(stat.)±0.10(sys.) mb at the average neutron energies of 35.8 keV (FG1) and 67.1 keV (FG2), respectively. The present result seems to be consistent with the data given by Koehler and O'Brien/21/, and the one by Gledenov et al./24/. These are supporting the evaluated values in ENDF/B-VI/25/. This implies ^{14}N is potentially a neutron poison for the s-process nucleosynthesis. The effect of ^{14}N on stellar s-process nucleosynthesis was studied by simulating nuclear reactions occuring at helium burning shells. We used a calculation cord ZNT471 (Hashimoto et al./26/), and used a model of a star with the following assumptions :

i) the temperature T and the total mass density D of the helium shell are fixed at
$T = 2.5 \times 10^8$ K and $D = 1.4 \times 10^4$ g/cm^3,
ii) the effects of the convection of the zone and the rotation of the star are negligible, and
iii) the initial mass fractions of ^{1}H, ^{4}He and ^{14}N are 18.1%, 20.0% and 0.0984%, respectively, and others are the same as the solar abundances.

Fig. 8 shows the results of the calculations with different values of the ^{14}N(n,p)^{14}C cross section. The solid curve indicates the time dependence of the neutron density in the helium burning zones obtained by the calculation with the 'normal value' of the cross section evaluated by Fowler et al., which is generally used in calculations of nucleosynthesis by s-process. The long-dashed and short-dashed curves were obtained with the double and half values of the normal cross section, respectively. This result indicates that the neutron density in the helium burning zones strongly depends on the ^{14}N(n,p)^{14}C cross section.
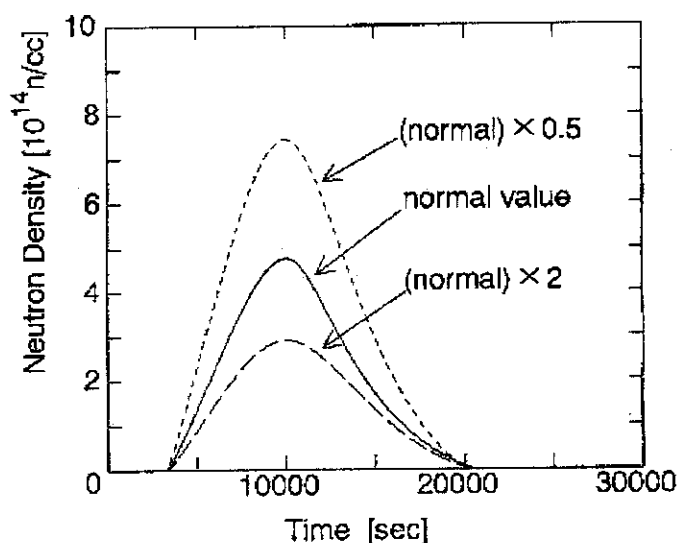
Figure 8. Calculated neutron densities in the helium burning zones with different values of the ^{14}N(n,p)^{14}C cross section.

4. Summary

The nuclear data of the keV neutron induced reactions of light nuclei are indispensable to study nucleosynthesis occuring in both stars and the early universe, and also useful to investigate the mechanism of the neutron capture process in the keV energy region, the properties of the excited states of the produced nucleus, and so on. For further researches of these subjects, the followings are to be studied :

i) neutron-induced reactions of the rare isotopes such as ^{18}O, ^{22}Ne, ^{36}Ar, etc., which are important in stellar nucleosynthesis,
ii) neutron-induced reactions with cross sections smaller than a few microb,

iii) (n,γ) reactions in the neutron energy range up to a few MeV, which are required in studying the neutron capture process,

and so on. For this purpose improvement of detectors and development of an MeV neutron source are now in progress.

References :

[1] R.V. Wagoner, W.A. Fowler and F. Hoyle, *Astrophys. J.* **148** (1967) 3
[2] R.V. Wagoner, *Astrophys. J.* **179** (1973) 343
[3] J.H. Applegate and C.J. Hogan, *Phys. Rev.* **D31** (1985) 3037
[4] J.H. Applegate, C.J. Hogan and R.J. Scherrer, *Phys. Rev.* **D35** (1987) 1151
[5] T. Kajino, G.J. Mathews and G.M. Fuller, *Astrophys. J.* **364** (1990) 7
[6] L.H. Kawano et al., *Astrophys. J.* **372** (1991) 1
[7] A.G.W. Cameron, *Phys. Rev.* **93** (1954) 932
[8] I. Iben Jr., *Astrophys. J.* **196** (1975) 525, 549
[9] I. Iben Jr., and A. Renzini, *Astrophys. J. Lett.* **263** (1982) L23
[10] T. Ohtsuka et al., *Phys. Rev.* **C49** (1994) R2289
[11] A. Mengoni, T. Ohtsuka and M. Ishihara, *Phys. Rev.* **C52** (1995) 2334
[12] T. Ohsaki et al., *Astrophys. J.* **422** (1994) 912
[13] ENDF/B-VI, data file for ^{197}Au, 1991, evaluated by P.G. Young
[14] K. Senoo et al., *Nucl. Instr. and Meth.* **A339** (1994) 556
[15] J.N. Bahcall, *Neutrino Astrophysics* (Cambridge Univ. Press, Cambridge, 1989)
[16] F.C. Barker, *Nucl. Phys.* **A588** (1995) 693
[17] I. Iben Jr., *Phys. Rep.* **250** (1995) 1
[18] K. Brehm et al., *Z. Phys.* **A330** (1988) 167
[19] W.A. Fowler et al., *Annu. Rev. Astron. Astrophys.* **13** (1975) 69
[20] M. Sanders, *Phys. Rev.* **104** (1956) 1434
[21] P.E. Koehler and H.A. O'Brien, *Phys. Rev.* **C39** (1989) 1655
[22] T. Shima et al., *Nucl. Instr. and Meth.* **A356** (1995) 347
[23] ENDF/B-VI, data file for ^3He, 1990, evaluated by G. Hale et al.
[24] Yu.M. Gledenov et al., *Z. Phys.* **A348** (1994) 199
[25] ENDF/B-VI, data file for ^{14}N, 1994, evaluated by P. Young et al.
[26] M. Hashimoto and K. Arai, *Phys. Rep. of the Kumamoto Univ.,* **7** (1985) 47

The First Internet Symposium on Nuclear Data: Paper No. 12

3.12 Uncertainties in fission-product decay-heat calculations

K. Oyamatsu, H. Ohta, T. Miyazono and K.Tasaka*

Department of Energy Engineering and Science, Nagoya University

Furo-cho , Chikusa-ku , Nagoya , 464-01 JAPAN

e-mail: oyak@luna.nucl.nagoya-u.ac.jp

The present precision of the aggregate decay heat calculations is studied quantitatively for 50 fissioning systems. In this evaluation, nuclear data and their uncertainty data are taken from ENDF/B-VI nuclear data library and those which are not available in this library are supplemented by a theoretical consideration. An approximate method is proposed to simplify the evaluation of the uncertainties in the aggregate decay heat calculations so that we can point out easily nuclei which cause large uncertainties in the calculated decay heat values. In this paper, we attempt to clarify the justification of the approximation which was not very clear at the early stage of the study. We find that the aggregate decay heat uncertainties for minor actinides such as Am and Cm isotopes are 3-5 times as large as those for ^{235}U and ^{239}Pu. The recommended values by Atomic Energy Society of Japan (AESJ) were given for 3 major fissioning systems, ^{235}U(t), ^{239}Pu(t) and ^{238}U(f). The present results are consistent with the AESJ values for these systems although the two evaluations used different nuclear data libraries and approximations. Therefore, the present results can also be considered to supplement the uncertainty values for the remaining 17 fissioning systems in JNDC2, which were not treated in the AESJ evaluation. Furthermore, we attempt to list nuclear data which cause large uncertainties in decay heat calculations for the future revision of decay and yield data libraries.

1. Introduction

The precise determination of the production and decay of fission product nuclei is necessary from the viewpoints of not only their decay heat release but also their activities emitted for a long time. The knowledge of fission product properties serves as a basis in designing a heat removal system of a reactor, a spent fuel reprocessing plant and a final processing plant for radioactive wastes.

Thanks to the accumulation of the measured and properly estimated decay data

for about two decades, the decay heat summation calculations for major fissioning systems, such as ^{235}U and ^{239}Pu, have come to give good agreement with the measured values within a typical error of 5%. However, this agreement does not guarantee the precision of the whole nuclear data or the prediction power for other fissioning systems. A higher burnup fuel in light water reactors, and transmutations of actinides and long-lived fission products require more precise knowledge of the properties of fission products from minor actinides, such as Cm and Am, which have not been considered well so far. In spite of their increasing importance, the nuclear data for these minor actinides seem to be still less accurate compared with those for major actinides.

The purpose of this study is to evaluate the uncertainties in the decay heat summation calculations for these minor actinide fissioning systems and to point out fission product nuclides whose yields, decay constants or decay energies need to have better precision. This work is also intended to be our first step for the precise determination of properties of fission product nuclei.

In this paper, we intend to make clear the justification of our approximation used in the uncertainty calculations. Some small errors found in the preliminary calculations [1] are also fixed in this paper.

2. An approximate summation calculation

Uncertainty caluculations require derivatives of the decay heat power with respect to decay constants, fission yields, and decay energies. Consequently, the exact calculations are too complicated. In this paper we use an approximate method to calculate decay heat power. The approximate method has the following advantages:

(1) able to obtain the analytic solution easily,
(2) easier to calculate the derivative values analytically,
(3) easier to point out nuclear data to cause large uncertainties in the decay heat power.

The number of atoms of nuclide i, $N_i(t)$ is calculated with the following simplified decay chain which consists of at most only three nuclides.

exact decay chain

decay constant $\quad \lambda_1 \quad \lambda_2 \quad \lambda_3 \quad \lambda_{i-3} \quad \lambda_{i-2} \quad \lambda_{i-1} \quad \lambda_i$

nuclide $\qquad X_1 \rightarrow X_2 \rightarrow X_3 \rightarrow \cdots \rightarrow X_{i-2} \rightarrow X_{i-1} \rightarrow X_i \rightarrow \cdots$

initial value $\quad y_1 \quad y_2 \quad y_3 \qquad\qquad y_{i-2} \quad y_{i-1} \quad y_i$

approximate decay chains

(1) For X_1, X_2 and X_3, the numbers of the atoms are calculated exactly.

decay constant $\quad \lambda_1 \quad \lambda_2 \quad \lambda_3$

nuclide $\qquad X_1 \rightarrow X_2 \rightarrow X_3 \rightarrow \cdots$

initial value $\quad y_1 \quad y_2 \quad y_3$

(2) For X_i (i>3), the number of atoms is calculated only with its mother (X_{i-1}) and grandmother (X_{i-2}) nuclides. The initial value for the number of atoms of the grandmother nuclide is taken to be its cumulative yield in order to take into account decays of the upper stream nuclides.

decay constant $\quad \lambda_2 \quad \lambda_3 \quad \lambda_4$

nuclide $\qquad X_2 \rightarrow X_3 \rightarrow X_4 \rightarrow \cdots$

initial value $\quad Y_2 \quad y_3 \quad y_4 \qquad \left(Y_2 = y_1 + y_2\right)$

....

decay constant $\quad \lambda_{i-2} \quad \lambda_{i-1} \quad \lambda_i$

nuclide $\qquad X_{i-2} \rightarrow X_{i-1} \rightarrow X_i \rightarrow \cdots$

initial value $\quad Y_{i-2} \quad y_{i-1} \quad y_i$

$$\left(Y_{i-2} = y_1 + y_2 + \cdots + y_{i-2}\right)$$

assumption

The difference between the exact and approximate values which is propotinal to λ_i / λ_3 is sufficiently small.

The present approximation is not affected much by even-odd effects which are relatively significant in the neighborhood of the stable nuclides. Actually, the decay heat power calculated in this approximation is found to be in excellent agreement with the exact value at cooling times less than 10^{10} (s) as shown in Fig. 1.
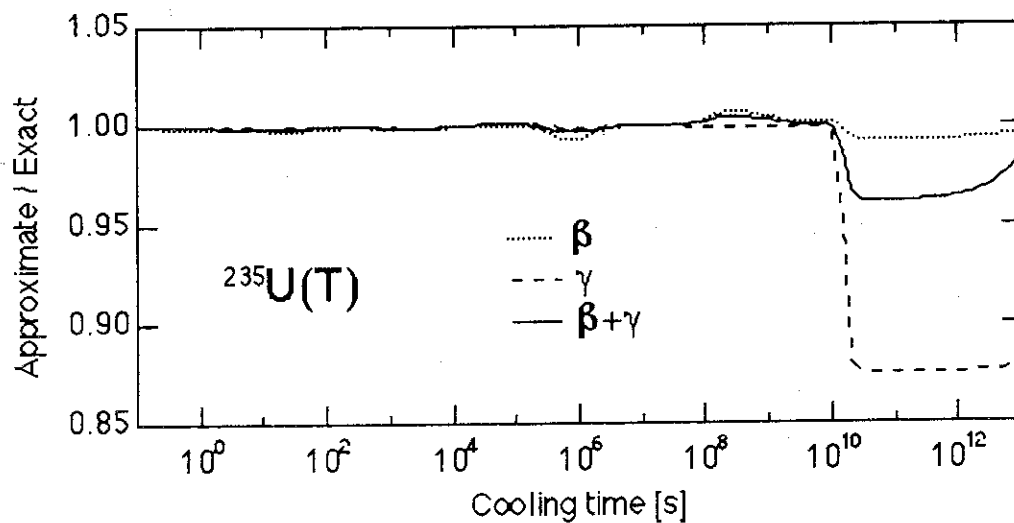
Fig. 1. The comparison between the approximate and exact decay heat power in the case of thermal fission of ^{235}U.
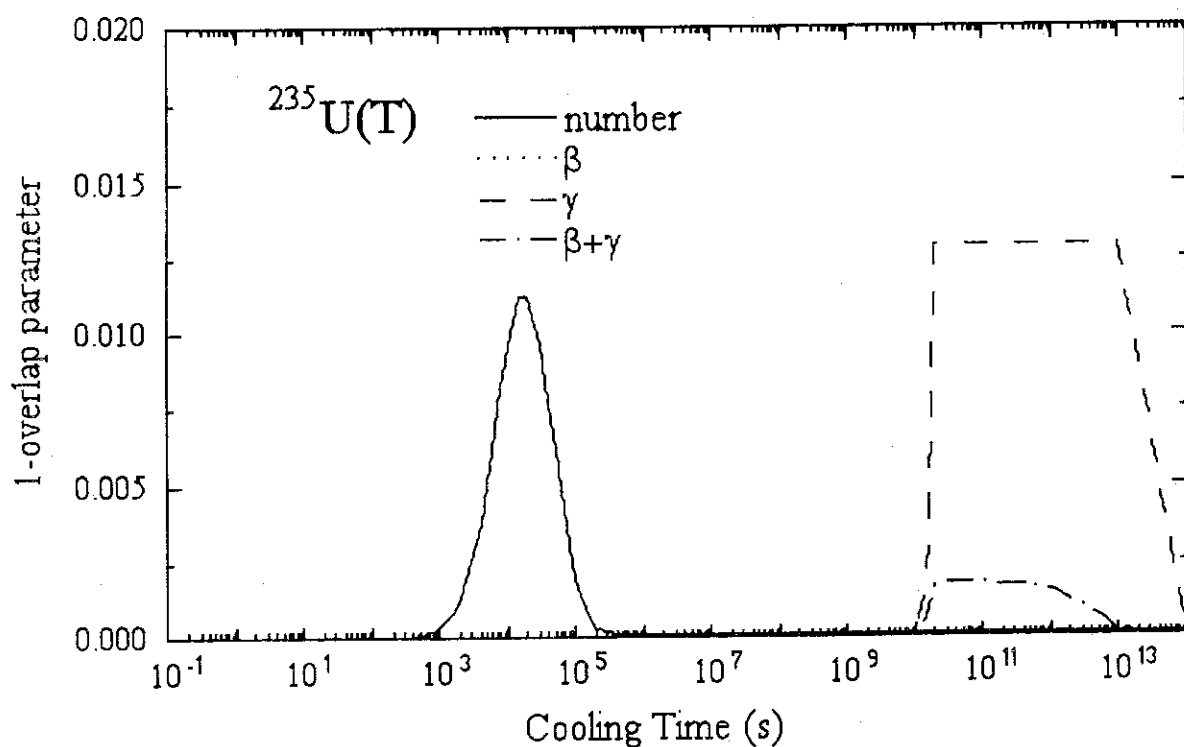
Fig. 2. The overlap of the contributions from indivisual nuclides between the approximate and exact decay heat power in the case of thermal fission of ^{235}U.

Furthermore, with the method in paper 023 in this symposium, we confirm that this approximation gives accurate decay heat powers from indivisual nuclides and the number of atoms of each nuclides. Figure 2 shows the overlap μ which is a measure of the difference between exact and approximate calculations. When the result of the two calculations are equal, the overlap μ is equal to unity. We see that, for both atom numbers and decay energies, the contributions from the indivisual nuclides agrees very well at $t < 10^{10}$ (s) except for a peak at 10^4 (s) for atom numbers. This peak has no significance because the difference is due only to the number of atoms of the **stable** ^{97}Mo. Therefore, the decay heat power is not affected at all.

Therefore, we perform the uncertainty evaluation in the decay heat summation calculation in the approximate method at cooling times less than 10^{10} (s) in the case of instantaneous irradiation in the following. The uncertainty in the decay heat power in out approximation is given by

$$\left(\delta P(t)\right)^2 = \sum_i \left[\left(\frac{\partial P}{\partial E_i}\right)^2 (\delta E_i)^2 + \left(\frac{\partial P}{\partial \lambda_i}\right)^2 (\delta \lambda_i)^2 + \left(\frac{\partial P}{\partial y_i}\right)^2 (\delta y_i)^2 + \left(\frac{\partial P}{\partial Y_i}\right)^2 (\delta Y_i)^2 \right]$$

It should be noted that this equation includes terms with the cumulative yields because we use the approximate decay chains instead of the exact ones. The uncertainty value calculated in our approximate method is considered to be close to the exact one because the decay heat and the number of atoms of each nuclide are sufficiently in good agreement with the exact ones. Furthermore, although the introduction of the cumulative yields makes it impossible to point out the causal decay constant or independent yield values at long cooling times, our approximate method is still useful for finding out key nuclides which give substantial contributions to the total decay heat power. The correlation effects among uncertainty values of independent yields are also taken into account in the present uncertainty evaluation as in Refs. [2,3]. Therefore, the final formula for the uncertainty is more complicated than the above equation.

3. Nuclear data and their uncertainty values

Values of fission yields, decay constants, average decay energies and their uncertainties are taken from ENDF/B-VI. Unfortunately, this nuclear data library does not provide us with uncertainty values for decay constants and/or decay energies that were theoretically (or empirically) estimated. Therefore we supplement uncertainty values of these decay energies in a similar way to the one in Ref. [4]. As for the uncertainties in the estimated decay constants, we assume $\delta \lambda_i = \lambda_i$ because the

estimated decay constants often differ from the measured ones by an order of magnitude.

4. Results and discussion

We have calculated uncertainties in summation calculations of the beta, gamma and total decay heat for 50 fissioning systems. As an example, Fig. 3 depicts the cooling time dependence of the uncertainty in the gamma decay heat power for thermal fission of ^{235}U. We find similar cooling time dependence of the beta, gamma and total decay heat power for all fissioning systems. Namely, the uncertainty is relatively small in the range of cooling times between 10^4 and 10^7 (s) but large at shorter and longer cooling times. The large uncertainty at short cooling times reflects large uncertainties in nuclear data of nuclides with short half lives. The large uncertainty at long cooling times may imply the need for more precise knowledge of nuclear level structures. On the other hand, we see from Table 1 that the magnitude of the uncertainty value does depend on the fissioning system. The uncertainties for minor actinides are larger by a factor of 3-5 than those for major actinides. Typical examples of the uncertainty values are 1-6% for ^{235}U(T), 2-7% for ^{239}Pu(T), 4-12% for ^{241}Am(F) and 5-3% for ^{244}Cm(F).

Table 1. Uncertainties in decay heat summation calculations.

fissile	β (%)	γ (%)	β+γ (%)
^{235}U(T)	1~6	1~6	1~6
^{238}U(F)	1~5	2~5	2~4
^{239}Pu(T)	2~12	2~13	2~7
^{237}Np(F)	3~12	3~9	3~9
^{241}Am(F)	4~13	4~20	4~13
^{243}Am(F)	5-13	5-16	4~12
^{244}Cm(F)	4~13	5~20	5~13
^{246}Cm(F)	5~14	6~17	5~12
^{248}Cm(F)	5~15	6~15	5~12
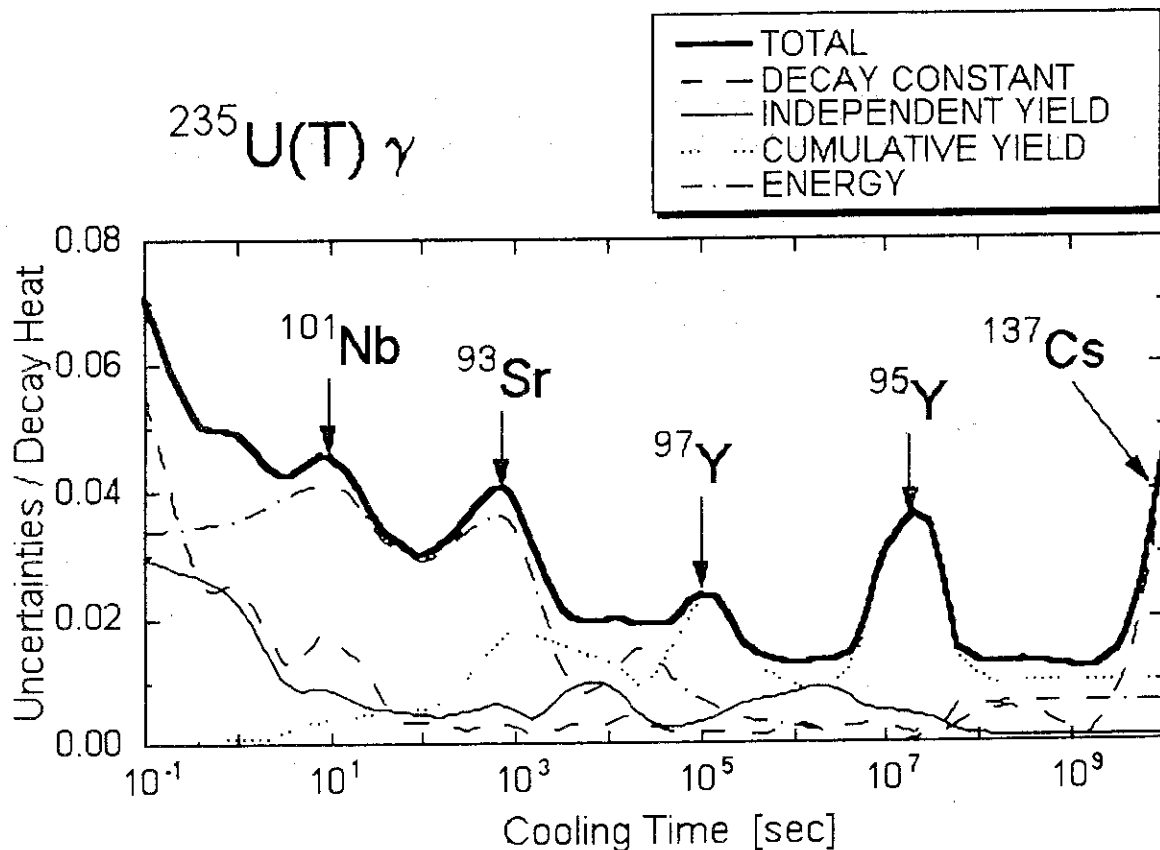
Fig. 3. Uncertainties in the gamma decay heat calculation for thermal fission of ^{235}U. Also shown with arrows are the main causal nuclides for the large uncertainty values.

It should be noted that, as for ^{235}U(T), ^{239}Pu(T) and ^{238}U(F) studied in Ref. [4], the present results are consistent with Ref. [4] (AESJ recomendation values) in spite of differences in the nuclear libraries and approximations.

Furthermore, we find that each peak in Fig. 3 is caused by nuclear data of a few nuclides, and point out the main causal nuclides, some of which are shown with arrows.The more precise determination of these nuclear data will substantially reduce the uncertainties in the decay heat summation calculations.

We are now preparing to publish the complete list of these causal nuclides together with tables and figures of the uncertainty values in the decay heat calculations for all fissioning systems in order to serve as a guidance for tuning up the present nuclear data library.

References

1) Ohta, H., Oyamatsu, K.and Tasaka, K.:"A Simple Method for Evaluation of Uncertainties in Fission Product Decay Heat Summation Calculations", JAERI Conf96-008.

2) F. SCHMITTROTH, Nucl. Sci. and Eng., 59, 117-139 (1976).

3) B. I. SPINRAD, Nucl. Sci. and Eng., 62, 35-44 (1977).

4) J. KATAKURA and S. IIJIMA, J. Nucl. Sci. Technol., 29[1], 11 (1992).

----

* Deceased, Feb. 14, 1995.

The First Internet Symposium on Nuclear Data: Paper No. 13

3.13 Systematic study of even-even nuclei with Hartree-Fock+BCS method using Skyrme SIII force

Naoki Tajima, Satoshi Takahara, and Naoki Onishi
Institute of Physics, University of Tokyo
Komaba 3-8-1, Meguro-ku, Tokyo, 153, Japan
Email : tajima@nt1.c.u-tokyo.ac.jp, staka@hep1.c.u-tokyo.ac.jp

We have applied the Hartree-Fock+BCS method with Skyrme SIII force formulated in a three-dimensional Cartesian-mesh representation to even-even nuclei with $2 \leq Z \leq 114$. We discuss the results concerning the atomic masses, the quadrupole ($m=0$, 2) and hexadecapole ($m=0$, 2, 4) deformations, the skin thicknesses, and the halo radii. We also discuss the energy difference between oblate and prolate solutions and the shape difference between protons and neutrons.

1 Introduction

Among theoretical attempts which aim at treating all the nuclides in a single framework, the simplest category seems to be the mass formula. Hence, let us focus the discussion in this section on the nuclear masses, although the purpose of our calculation is not restricted to the masses. The most familiar mass formula may be that of Bethe and Weizsaecker /1, 2/, which expresses the nuclear masses as a function of the number of neutrons (N) and that of protons (Z) as,

$$E(N,Z) = a_V A + a_S A^{2/3} + a_I(N - Z)^2 A^{-1} + a_C Z^2 A^{-1/3}, \qquad (1)$$

where $A = N + Z$. By changing the values of four coefficients, the r.m.s. error from experimental data /3/ of even-even nuclei can be decreased down to 3.5 MeV. The form of this formula originates in the liquid drop picture of the atomic nucleus together with a parabolic approximation to the dependence on the total isospin. The first step to decrease the error is to take into account the shell effect.

Taking into account the shell effect, the TUYY mass formula /4/, for example, achieved an r.m.s. mass error of as small as 538 keV. The number of fitting parameters are 6 for the gross part (corresponding to the parameters of the Bethe-Weizsaecker formula) while that for the shell part is as many as 269: There is one parameter for each value of Z in an interval $1 \leq Z \leq 112$ and one for each value of N in $1 \leq N \leq 157$. It is not at all our intention to question the quality of the predictions of the TUYY mass formula in particular, and indeed its stability for extrapolations has been already demonstrated by the developpers of the formula, but generally speaking, less number of

parameters are preferable for the reliability of the extrapolation to nuclei not synthesized yet[1]. One usually switches to less phenomenological models in order to reduce the number of parameters.

The most elaborate one among such models seems to be the finite-range droplet model with a microscopic shell correction (FRDM), whose latest update was done by Möller et al. /5/. Another extensive calculation was carried out by Aboussir et al. /6/ in the extended Thomas-Fermi plus Strutinsky integral method (ETFSI).

The former as well as the latter methods can be regarded as approximations to the Hartree-Fock (HF) equation. The straight-forward solutions of the equation including deformation require long computation time for global calculations even with present computers. Such global results are not yet available to the public as far as we know. This is the reason why we have embarked on an extensive HF+BCS calculation.

In this paper, we utilize a widely used force of the Skyrme SIII to examine what predictions it makes for a large number of nuclei, rather than aiming at the determination of the parameters of the force through calculations requiring by two orders of magnitude as long computation time as the calculations for this paper.

2   Set up of the calculation

For the mean-field part of the interaction, we adopt the Skyrme force. The Skyrme force is an effective interaction widely used in mean-field calculations. It is essentially a zero-range force but modified with the lowest order momentum dependences to emulate the finite-range effects, a density dependence to reproduce the saturation, and a spin-orbit coupling term.

The relation between the Skyrme-HF model and the relativistic mean-field model /7/ has been discussed by many authors (see, e.g., Ref. /8/), which has invoked arguments on the density dependence (the ratio of the isoscalar to the isovector density dependences) of the spin-orbit term /9, 10, 11, 12/. However, as these arguments are not yet conclusive, we rather like to use the old but well-examined standard form of the Skyrme force in this paper.

Among the many parameter sets proposed for the Skyrme force, we choose the SIII /13/. Its validity has been examined in many nuclear structure calculations. In particular, it produces single-particle spectra in good agreement with experiment. It also reproduces fairly well the $N - Z$ dependence of the binding energy /14/ compared with other widely-used parameter sets of SGII /15/ and SkM* /16/. Although its incompressibility is said to be too large, it is not a serious drawback because elaborate fittings of the parameters of the Skyrme force /12/ and the FRDM /5/ have shown that different assumptions for the incompressibility lead to practically the same quality of fittings to nuclear masses.

The force SkSC4 /6/ was determined through the most extensive fitting to nuclear mass data among the Skyrme forces. It is not our intention to criticize the force, but it should be noticed that the fitting was done in the ETFSI scheme, which produces unnegligibly different energy from that of the HF method. Because of this disadvantage,

---

[1]Here, again, we are not talking of the TUYY mass formula in particular, because the TUYY mass formula features the relatively small number of parameters as a mass formula expressing the masses as a simple and explicit functions of N and Z. Other formulae contain about 500 parameters, because they have one parameter for each value of A in addition to N and Z.

we do not choose the force SkSC4 in this paper. In future calculations, this force is certainly one of the important forces to be tried.

For the pairing channel of the intercation, we used the seniority force. The seniority force is a most commonly used force for the description of the pairing correlation. Its pair-scattering matrix elements are usually defined as a constant. We multiply them with cutoff factors depending on the single-particle energy. For the form of the cutoff function, see Ref. /17/. This cutoff function is very important because in the BCS treatment of nuclei far from the β-stability line, one has to take care so that the continuum states are not occupied, which give rise to unphysical nucleon gas extending over the entire box.

In order to treat a wide range of nuclei on a single footing, we need a prescription to determine the strength of the pairing interaction for each nucleus. For this purpose, we have developed a method based on the continuous spectrum approximation which uses the semiclassical single-particle level density obtained in the Thomas-Fermi approximation. We replace the strength with 0.6 MeV when it exceeds 0.6 MeV.

It should be kept in mind that a more accurate treatment of the pairing is necessary for deformed and/or near-drip-line nuclei than for spherical stable nuclei. One should not underestimate the importance of the pairing from one's experience with stable and spherical nuclei. The pairing correlation influences on the deformation as well as on the location of the neutron drip line. For example, one can see in Ref. /14/ that the potential energy curve of ^{186}Pb is substantially changed when the pairing interaction strength is slightly reduced. Similar example of ^{80}Zr is discussed in Ref. /17/.

We use a HF+BCS code EV8 /18/, in which the single-particle wavefunctions are expressed in a three-dimensional Cartesian-mesh representation, while most of the other methods for deformed nuclei express the single-particle wavefunctions by the expansion in a harmonic oscillator basis. Let us mention three advantages of the mesh representation. First, it is capable of treating nucleon skins and halos. In contrast, they cannot be described efficiently in the oscillator-basis expansion because the asymptotic form of wavefunctions far from the nuclear surface is determined by the basis. Second, one can treat exotic (e.g., high-multipole) shapes and large (e.g., super and hyper) deformations without preparing a basis specific to each shape. Third, the saturation property of density makes the atomic nucleus a very suitable object to the mesh representation.

In the three-dimensional Cartesian-mesh representation, each single-particle wavefunction $\psi(x, y, z)$ is defined in a rectangular box $(-\frac{1}{2}L_x \le x \le \frac{1}{2}L_x, -\frac{1}{2}L_y \le y \le \frac{1}{2}L_y, -\frac{1}{2}L_z \le z \le \frac{1}{2}L_z)$ with its values ψ_{ijk} at cubic mesh points, $(x_i, y_j, z_k) = (i - \frac{1}{2}, j - \frac{1}{2}, k - \frac{1}{2})a$, where i, j, and k take on integers. In this study, the mesh size a is set to 1 fm, while the size of the box is $L_x = L_y = 26$ fm, $L_z = 28$ fm for $Z < 82$ and $L_x = L_y = 28$ fm, $L_z = 30$ fm for $Z \ge 82$. The nucleus is placed at the center of the box.

We impose a symmetry with respect to reflections in x-y, y-z, and z-x planes (the point group D_{2h}). This symmetry allows triaxial solutions, although all of our solutions have eventually turned out axial and stable against γ-deformation. On the other hand, the symmetry prohibits odd-multipole deformations, which may not be negligible in some actinide nuclei. According to the calculations with the FRDM /5/, the nucleus ^{222}Ra has the largest octupole deformation ($\beta_3 = 0.15$, the energy gain due to the octupole deformation is -1.4 MeV), while except in the neighborhood of this nucleus the octupole deformation occurs only in odd-A and odd-odd nuclei.

One might wonder that a mesh size of 1 fm were too large to describe the abrupt change of density at nuclear surface. It was demonstrated in Ref. /18/, however, that the mesh size can produce enough accurate results for several spherical nuclei with mass

below ^{208}Pb. We did a similar test of accuracy for a deformed actinide nucleus ^{240}Pu and found that the relative errors of the quadrupole moment and the total energy are 0.4% and 0.5%, respectively. (The method of the extrapolation to $a \rightarrow 0$ is explained in Ref. /17/.) This order of accuracy is higher than necessary for the quadrupole moment, while it is not for the energy to make comparison with experiments. Considering that the r.m.s. deviation of the atomic masses of recent mass formulae is ~ 0.5 MeV, the desirable precision is of the order of 0.1 MeV, which is only 0.005 % of the total binding energy of ^{240}Pu. Therefore, the binding energy, but not the other quantities, has to be corrected for the effect of the finite mesh size.

The origin of this unexpectedly high accuracy with apparently coarse meshes has been explained by Baye and Heenen /19/. The equation to determine { ψ_{ijk} } is usually derived through a discrete approximation to the Schroedinger equation. They presented an alternative point of view, in which they introduced a set of orthogonal basis functions $f_{ijk}(x, y, z)$ such that { ψ_{ijk} } are the coefficients to expand $\psi(x, y, z)$ in this basis. (In this point of view, the equation for { ψ_{ijk} } is determined uniquely from the variational principle.) This basis can be unitary-transformed to plane-wave basis with $|k_\kappa| < \pi/a$ ($\kappa = x, y, z$), which suggests that the atomic nucleus is a very suitable physical object to apply the mesh representation because the saturation property of nuclear matter guarantees the suppression of large-momentum components in wavefunctions from the view point of the Thomas-Fermi approximation.

To enjoy this high accuracy, the method to determine { ψ_{ijk} } must be in accordance with the view point of Baye and Heenen. Exact variational treatment with the plane-wave basis requires, however, long computation time and diminish the simplicity of the Cartesian-mesh representation. The code EV8 is designed to emulate the plane-wave expansion method, though it is based on the discrete approximations, by choosing the appropriate orders of approximation formulae for derivatives (the 7- and 9-point formulae for the first and second derivatives, respectively) and integrals (the mid-point formula).

The calculation has been done for N ranging from outside the proton drip line to beyond the experimental frontier in the neutron-rich side. This paper is mainly concerned with the proton-rich nuclei than the neutron-rich ones. We thoroughly explore the proton-rich side, even to beyond the proton drip line by several neutrons, while restricting the investigations in the neutron-rich side within the experimental frontier plus a few neutrons. This is because the HF+BCS method used in this paper cannot correctly include the coupling in the pairing channel with the continuum, which can be influential in nuclei near the neutron drip line /20, 21/. The HF+BCS method including the coupling with the continuum gives rise to unphysical neutron gas surrounding the nucleus. The solution of this problem requires the Hartree-Fock-Bogolyubov method, with which ordinary and pair densities are spatially localized when the Fermi level is at a negative energy /20/. On the other hand, for nuclei near the proton drip line, the HF+BCS method is still applicable in practice to obtain localized solutions because the Coulomb barrier confines the wavefunctions of low-and-positive as well as negative energy levels.

We obtained spatially localized solutions for 1029 nuclei, together with the second minima for 758 nuclei. The other details of the method of the calculations are described in Refs. /17, 22/.

3 Results of the calculation

The results of our HF+BCS calculations with Skyrme SIII force are available as data tables. The data are given not only for the ground states but also for the lowest exited local minima of the HF+BCS equation. The latter represent shape isomers. The tabulated quantities are the atomic masses, nuclear binding energies, Fermi levels, pairing gaps, r.m.s. radii, quadrupole moments, deformation parameters, skin thicknesses, halo radii, kinetic energy, spin-orbit energy, pairing energy, and the direct part of the Coulomb energy. Moments and deformation parameters are given for protons, for neutrons, and for the mass.

In this paper, we define the deformation parameters as those of a sharp-surface uniform-density liquid drop which has the same moments as the HF+BCS solution has.

3.1 nuclear mass

The calculated masses have been corrected for the inaccuracy due to the finite mesh size of $a=1$ fm /17/. This kind of correction is necessary only for the masses, because their relative errors have to be by far smaller than those of other quantities in order to compare with experimental data.

¿From the calculated masses, we found regions of enhanced stability around double-magic nuclei with $(N, Z) = (50,50)$, $(82,50)$, and $(126,82)$. Another double-magic nucleus $(82,82)$ is outside the two-proton drip line. The super-heavy double-magic nucleus $(184,114)$ does not look like a local minimum of nuclear mass in our result.

The two-proton drip line of the HF+BCS with SIII and that of the FRDM are overlapping in most places. The distance between them is $\Delta Z=4$ for $N=40$, $\Delta N=4$ for $Z=42$ and 78, and $\Delta Z \leq 2$ and $\Delta N \leq 2$ for the other isotope and isotone chains.

The two-neutron drip lines of the two theoretical approaches are also close to each other. The difference looks of the same size as that between the FRDM and the TUYY mass formula /4/, both of which are models whose parameters were determined through extensive fittings to the mass data. This fact indicates the quantitative appropriateness of the macroscopic isospin dependence of the SIII force.

The calculated masses tend to be overbinding for $Z=8$ and 20 isotopes, and $N=50$, 82, and 126 isotones. Unlike spherical nuclei including these semi-magic isotopes and isotones, deformed nuclei have positive errors, which are about 3 MeV rather independently of the size of deformation.

The largest underbinding (about 7 MeV) occurs in ^{8}Be, which is the most strongly deformed nuclei among the 1029 nuclei. An additional binding is expected to arise from the angular momentum projection effect.

Table 1: R.m.s. mass differences (MeV)

	AW'93		TUYY		FRDM		ETFSI		EV8C	
TUYY	0.52	(480)								
FRDM	0.68	(462)	4.31	(1521)						
ETFSI	0.74	(430)	4.27	(1472)	2.74	(1742)				
EV8C	2.22	(480)	2.59	(977)	2.50	(958)	2.26	(940)		
MACRO	3.55	(480)	17.25	(2228)	16.07	(2246)	8.29	(1895)	5.71	(1029)

In Table 1, we show the r.m.s. differences of the masses of even-even nuclei between theoretical models as well as between the experiments and the models. In the table, AW'93 represents the experimental atomic mass table by Audi and Wapstra (their best recommended values excluding those estimated from systematic trends) /3/, TUYY the mass formula of Tachibana et al. /4/, FRDM the finite-range droplet model /5/, ETFSI the extended Thomas-Fermi Strutinsky integral method with the SkSC4 force /6/, EV8C the HF+BCS results using the Skyrme SIII force with the correction, and MACRO the Bethe-Weizsaecker type function fitted to AW'93. In parentheses are the number of nuclei to calculate the difference. The r.m.s. deviation from AW'93 is 2.2 MeV for EV8C, which is 3-4 times as large as that of 0.52 MeV for TUYY, 0.68 MeV for FRDM, and 0.74 MeV for ETFSI. It should be noticed, however, that the parameters of FRDM, TUYY, and ETFSI were fitted to all the available recent experimental mass data while the parameters of the SIII force were determined by fitting to the masses and charge radii of only seven spherical nuclei. In addition, the number of the fitting parameters is 275 in TUYY, 19 in FRDM, and 8 in ETFSI, while it is only 6 in the SIII force.

3.2   quadrupole moment

We compare the calculated quadrupole moment with the intrinsic quadrupole moment Q_0 deduced from the experimental $B(E2; 0^+ \rightarrow 2^+)$ values (given in Ref. /23/ for 289 even-even nuclei ranging over $4 \leq Z \leq 98$). The deduction was done assuming a rigid rotor model.

For nuclei with $|Q_0| < 3.5$ b, the agreement with experiment is mostly excellent. For nuclei with smaller $|Q_0|$, however, it often occurs that the HF+BCS solution has a spherical shape when the experimental $B(E2)$ is not necessarily very small. This may be explained by attributing the enhanced $B(E2)$ not only to static deformations but also to the collective shape oscillation around the spherical equilibrium. It may also be related to the complicated landscapes of the potential energy curves of nuclei with $A=50$-100.

The largest discrepancy is found in ^{222}Th, whose experimental Q_0 is 5.5 b while the HF+BCS solution is spherical.

The even-even nuclei having the largest intrinsic quadrupole moment is ^{252}Cf in the experimental table, while it is ^{244}Rf among the 1029 HF+BCS solutions ($Q_0=16.6$ b).

3.3   quadrupole deformation

We found that nuclei at major-shell closures are spherical except for some N=28 isotones, while the deformation develops between the major-shell closures. Such pattern of the development of deformation looks regular for mass less than one hundred, while it is not so regular for mass greater than one hundred, i.e., the change of deformation along isotope or isotone chains is not always smooth. In addition, oblate ground states are embedded here and there in light-mass region while for heavier-mass nuclei they are found only exceptionally in regions near major-shell closures.

Our calculations tend to predict smaller deformations than the FRDM for nuclei in $28 < Z, N < 50$. These discrepancies in deformation often occur in a manner that our model gives a spherical shape while the FRDM predicts $\delta \sim 0.4$. These are originated in shape coexistence, i.e., the potential energy curve has more than one minimum which are energetically competing within 1 MeV or so.

The largest deviation from the experimental a_{20} deduced from $B(E2; 0^+ \rightarrow 2^+)$ was found in ^{12}C. The largest deformation among the 1029 even-even nuclei which we calculated occurs in ^8Be ($a_{20}=0.62$).

3.4 hexadecapole deformation

The axial hexadecapole deformation parameter a_{40} of the ground-state solutions becomes sizable for $Z > 50$. The sign is positive in the first half of the major shells and negative in the second half. This behavior is in agreement with the results of the FRDM /5/ as well as with a naive expectation from the density profile of pure-j single-particle wavefunctions. The largest value of $|a_{40}|$ is about 0.1 both for positive and negative signs.

3.5 axial asymmetric deformation

Non-axial deformation parameters have turned out very small.

Deformations with the magnetic quantum number $m=2$ (i.e., triaxial deformations) are almost vanishing for all the nuclei we calculated: The magnitudes of $|a_{22}|$ and $|a_{42}|$ are smaller than 10^{-4}.

The deformation with $m=4$ (a_{44}) is larger than those with $m=2$. Its typical size is of the order of 10^{-3}. However, these small non-axial deformations cannot affect any observables in experimentally detectable ways. Incidentally, it is an interesting problem how a_{44} develops as the angular momentum increases /24/.

There is a supplementary comment on the $m=4$ deformations: For $m=2$ deformations, the Cartesian-mesh basis has the corresponding symmetry, i.e., it is invariant for the interchange of the x- and the y-axes. On the other hand, for $m=4$ deformations, the corresponding symmetry is not exactly conserved by the Cartesian mesh because it is not equivalent between the direction along the x-axis and the direction in a line $x=y$. This anisotropy of the basis may affect the value of a_{44}. Incidentally, the sign of a_{44} does not have a meaning when $m=2$ deformations are vanishing: A shape with a_{44} and a shape with $-a_{44}$ should be equivalent when a_{22} and a_{42} are zero.

3.6 shape difference between protons and neutrons

One of the advantages of mean-field methods over shell-correction schemes is that the protons and the neutrons do not have to possess the same radius and deformation. It is also an advantage of the Cartesian-mesh representation over the expansion in harmonic-oscillator bases. In order to make the best use of this advantage, we have calculated the liquid-drop shape parameters separately for protons and neutrons as for 1029 ground and 758 first-excited solutions.

The result shows that the largest differences occur in the lightest nuclei. In general, however, the shapes of proton and neutron density distributions are not remarkably different from each other. Off cource we do not exclude the possibility of larger proton-neutron shape difference in nuclei near the neutron drip line because our calculation does not reach the drip line except in light mass region.

3.7 energy difference between oblate and prolate solutions

We investigated the systematics of the excitation energy between the oblate and the prolate solutions. The energy difference is small near major-shell closures but large in the middle of the major shells. Apart from this shell fluctuation, we found an overall trend that, as the nucleus becomes heavier, the energy difference increases while the size of deformation decreases. We also noticed a clear difference between below and above the $N = 50$ magic. For nuclei with $N < 50$, the changes along isotope chains are not so regular as in heavier nuclei and the oblate solutions often have lower energies than prolate ones. For nuclei with $N > 50$, oblate ground states are very rare and found only in nuclei very close to shell magics. The dominance of prolate deformations for $N > 50$ may be attributed to the change of the nature of the major shells from the harmonic-oscillator shell to the Mayer-Jensen shell.

3.8 skins and halos

The greatest advantage of the mesh representation for this paper is that it is fit to describe skins and halos. Our results show that the skin grows monotonously and regularly as nucleons are added to the nucleus. On the other hand, the halo grows very slowly except near the drip lines, where it changes the behavior completely and expands very rapidly. We also found that the neutron skin tends to make the density distribution more spherical.

4 Concluding remarks

Among the future problems for the extensive mean-field calculations of the nuclear ground-states properties are the improvements of the method to determine the pairing force strengths and the extension of the calculation to the neutron drip line by incorporating the coupling to the continuum in the pairing channel. Our final goal is the comparison of various Skyrme forces in their ability to reproduce the nuclear ground-state properties globally in the nuclear chart, and possibly the improvements of the force parameters.

As a next step, we are now investigating the deformations of light nuclei ($N, Z < 50$) and their dependence on the Skyrme force parameter sets, since this paper has shown that the deformations of heavy nuclei are reproduced excellently with the Skyrme SIII force while those of light nuclei are not always reproduced so well.

We are also doing an extensive investigation of zero-spin super deformation states using the same cartesian-mesh HF+BCS code.

The hyper-text version of this paper as well as the tables containing the results of our calculations can be obtained at **ftp://nt1.c.u-tokyo.ac.jp/isnd/isnd.html.**

References

[1] C.F. von Weizsaecker, Z. Phys. **96** (1935) 431.

[2] H.A. Bethe and R.F. Bacher, Rev. Mod. Phys. **8** (1936) 82.

[3] G. Audi and A.H. Wapstra, Nucl. Phys. **A565** (1993) 1.

[4] T. Tachibana, M. Uno, M. Yamada, and S. Yamada, Atomic Data Nucl. Data Tables **39** (1988) 251.

[5] P. Möller, J.R. Nix, W.D. Myers, and W.J. Swiatecki, Atom. Dat. Nucl. Dat. Tab. **59** (1995) 185.

[6] Y. Aboussir, J.M. Pearson, A.K. Dutta, and F. Tondeur, Nucl. Phys. **A549** (1992) 155; Atom. Dat. Nucl. Dat. Tab. **61** (1995) 127.

[7] P.-G. Reinhard, Rep. Prog. Phys. **52** (1989) 439.

[8] K. Sumiyoshi, D. Hirata, H. Toki, and H. Sagawa, Nucl. Phys. **A552** (1993) 437.

[9] M.M. Sharma, G.A. Lalazissis, W. Hillebrandt, and P. Ring, Phys. Rev. Lett. **72** (1994) 1431.

[10] J. Dobaczewski and W. Nazarewicz, Phys. Rev. Lett. **73** (1994) 1869.

[11] J.M. Pearson and M. Farine, Phys. Rev. **C50** (1994) 185.

[12] P.-G. Reinhard and H. Flocard, Nucl. Phys. **A584** (1995) 467.

[13] M. Beiner, H. Flocard, Nguyen van Giai, and P. Quentin, Nucl. Phys. **A238** (1975) 29.

[14] N. Tajima, P. Bonche, H. Flocard, P.-H. Heenen, and M.S. Weiss, Nucl. Phys. **A551** (1993) 434.

[15] Nguyen van Giai and H. Sagawa, Phys. Lett. **B106** (1981) 379.

[16] J. Bartel, P. Quentin, M. Brack, C. Guet, and H.-B. Hakansson, Nucl. Phys. **A386** (1982) 79.

[17] N. Tajima, S. Takahara, and N. Onishi, to be published in Nucl. Phys. **A**; preprint UT-Komaba 96-9; e-print nucl-th/9604037.

[18] P. Bonche, H. Flocard, P.-H. Heenen, S.J. Krieger, and M.S. Weiss, Nucl. Phys. **A443** (1985) 39.

[19] D. Baye and P.-H. Heenen, J. Phys. **A19** (1986) 2041.

[20] J. Dobaczewski, H. Flocard, and J. Treiner, Nucl.Phys. **A422** (1984) 103.

[21] J. Dobaczewski, I. Hamamoto, W. Nazarewicz, and J.A. Sheikh, Phys. Rev. Lett. **72** (1994) 981.

[22] N. Tajima, N. Onishi, S. Takahara, Nucl. Phys. **A588** (1995) 215c-220c.

[23] S. Raman, C.H. Malarkey, W.T. Milner, C.W. Nestor, JR., and P.H. Stelson, Atomic Data Nucl. Data Tables **36** (1987) 1.

[24] I. Hamamoto and B. Mottelson, Phys. Lett. **B333** (1994) 294.

3.14 **Refinement of the gross theory of nuclear β-decay, and hindrance of the first-forbidden transition of rank 1**

Hidehiko Nakata, Takahiro Tachibana* and Masami Yamada*
Department of Physics and Applied Physics, Waseda University, 3-4-1 Okubo, Shinjuku-ku,
Tokyo 169, Japan
e-mail:69315093@cfi.waseda.ac.jp

*Advanced Research Center for Science and Engineering, Waseda University, 3-4-1 Okubo,
Shinjuku-ku, Tokyo 169, Japan
e-mail:tachiban@cfi.waseda.ac.jp
e-mail:myamada@cfi.waseda.ac.jp

Recently the gross theory of nuclear β-decay was refined for odd-odd nuclei. In this refinement, the effect of the selection rule of β-transitions from the ground states of odd-odd nuclei to those of even-even nuclei was taken into account based on a statistical consideration. The transitions to the first 2^+ excited states in even-even nuclei were also taken into account according to the selection rule approximately. In that study, it was found that the transitions between 1^- ground states of the odd-odd nuclei and 0^+ ground states of even-even nuclei, belonging to the first-forbidden transitions of rank 1, are strongly hindered. A reduction factor was introduced for the transitions to the ground states of even-even nuclei to take into account this hindrance. It was also found that the strength functions of the Gamow-Teller transitions obtained from the conventional gross theory are underestimated by a factor of about 3. In order to improve this underestimation, the Lorentz-type function was adopted for the one-particle strength function in the model instead of the hyperbolic-secant-type function. In the present study we have newly analyzed the experimental ft-values of odd-A nuclei, and found that the first-forbidden transitions of rank 1 are also considerably hindered between the ground states. Following the above refinement we have calculated the β-ray spectra of some odd-odd short-lived fission products with the use of the refined gross theory. These results are compared not only with the experiments by Rudstam et al. but also with the conventional gross theory.

1. Introduction

The gross theory of nuclear β-decay has been successful in describing gross properties of β-decay. It is a certain average theory which does not take into account characteristics of individual nuclei except for their Q-values. In the decays of odd-odd nuclei, the experimental half-lives strongly depend on the spin-parities of the parent nuclei. Then the gross theory gives rather poor agreement with experimental data in the calculation of the half-lives of odd-odd nuclei unless the Q-values are very large. Recently, we have refined the gross theory for odd-odd nuclei on the supposition that the spin-parity of the parent nucleus can be determined.

On the way of the above refinement, it was found that the first-forbidden transition of

rank 1 between the ground states are strongly hindered in the decays of even-A nuclei. Then it is natural to examine whether a similar hindrance exists in the transitions between the ground states of odd-A nuclei.

Besides the half-life, the β-ray spectrum is an important property giving information on the β-strength function. Since the refined gross theory for odd-odd nuclei gives much better agreement with experimental half-lives than the conventional gross theory does, we expect that it also gives better agreement with experimental β-ray spectra.

In Section 2, we give a brief survey of the gross theory, and in Section 3 give a short explanation of the refinement of the theory for the decays of odd-odd nuclei. In Section 4, we show that the hindrance of the first-forbidden transition of rank 1 between the ground states, which was confirmed in the decays of even-A nuclei, are also seen in the decays of odd-A nuclei. In Section 5, we show some results of the β-ray spectra calculated by the refined gross theory. Finally, we give conclusions in Section 6.

2. Brief survey of the gross theory

The gross theory of nuclear β-decay is a theory which treats the β-decay strength to all the final nuclear levels as an averaged function based on sum rules of the β-decay strengths. In this theory, it is assumed that the strength function is given by an integral of one-particle strength function $D_\Omega(E, \varepsilon)$ as follows:

$$\left| M_\Omega(E) \right|^2 = \int_{\varepsilon_{min}}^{\varepsilon_{max}} D_\Omega(E, \varepsilon) W(E, \varepsilon) \frac{dn_1}{d\varepsilon} d\varepsilon \ . \tag{1}$$

Here, Ω denotes the type of the β-decay operator (in the gross theory, allowed and first-forbidden transitions are taken into account), E represents the energy of the final nuclear state measured from the initial state, ε is the one-particle energy of the decaying nucleon, $dn_1/d\varepsilon$ represents the one-particle energy distribution of decaying nucleon, and, finally, $W(E, \varepsilon)$ is a weight function to take into account the Pauli exclusion principle.

In the gross theory, a few one-particle levels near the Fermi surface are treated as discrete levels in order to take into account the pairing effect. The other parts of the levels are treated as continuous levels approximated by a Fermi gas model.

3. Refinement of the gross theory for the decays of odd-odd nuclei

In the β-decay of an odd-odd nucleus, the daughter nucleus has the ground state with spin-parity 0^+ and the first excited state usually with 2^+. Therefore, if we can determine the spin-parity of the parent nucleus, we know which selection rules apply to the transitions to the ground and first excited states. We refined the gross theory for odd-odd nuclei to take into account these selection rules. In the following we briefly give the procedure for this refinement.

(a) In the ground-state transition, the strength caused by the transition type satisfying the selection rule is enhanced by a statistical factor k, and the other strengths are put equal to zero. Since the conventional gross theory should give the average strength, this factor is expressed as

$$k(Z, N) = \frac{\langle 2j_n + 1 \rangle_s \langle 2j_p + 1 \rangle_s}{2J + 1},$$ (2)

where j_n and j_p are the angular momenta of the odd neutron and odd proton respectively, and J is the spin of the parent nucleus. In Eq. (2), the numerator represents the degeneracy in the "ground" state of the odd-odd nuclei in the model of the conventional gross theory, while the denominator is the actual degeneracy. The brackets in the numerator mean a smooth function of N or Z representing a local average of the degeneracy calculated by a single-particle shell model.

(b) The first-forbidden transitions of rank 1 to the grounds states are strongly hindered. In order to take into account this hindrance, the ground-state strengths caused by the first-forbidden transition of rank 1 are multiplied by a hindrance factor 0.06.

(c) In order to satisfy the sum rules for the whole nucleus, which are observed to some extent in the conventional gross theory, we make the following adjustment. If the strength to the ground state is cancelled, the amount of the cancelled strength is added to the strengths to excited states. On the other hand, if the strength to the ground state is enhanced, the amount of the enhanced strength is subtracted from the strengths to excited states.

(d) In the case where the transitions to the first excited 2^+ states predominate over the transitions to the ground states because of selection rules, we take into account the effect of the transitions to 2^+ state. However, the first excited 2^+ state is not explicitly represented in the conventional gross theory. Therefore, we share part of the ground-state strength to the first excited state in a phenomenological way as follows. First, the ground-state strengths are calculated by the procedures (a) and (b) according to the selection rules for the 2^+ state. We further multiply these strengths by a factor 0.1. The procedure (c) is also followed in order to observe the sum rule. Finally, we shift the above strengths up to the level of the first 2^+ state, whose excitation energies are inferred from experimental data by a systematic way.

In the study of ref. 1, it was also found that the Gamow-Teller strengths calculated by the conventional gross theory /2/ are underestimated by a factor of about 3 on the average. Then, recently, we improved the one-particle strength functions of the gross theory to give an average strength /3/. We adopt this improved one-particle strength function in the calculation of the β-ray spectra as explained in Section 5.

4. Hindrance of the first-forbidden transition of rank 1

As mentioned in Section 3, we found, in the study of the refinement of the gross theory for odd-odd nuclei /1/, that the transition between 1^- ground states of odd-odd nucleus and 0^+ ground states of even-even nuclei are strongly hindered.

We have examined whether there is a similar hindrance in the transitions between ground states of odd-A nuclei. In Fig. 1, we show experimental log ft values taken from ENSDF (Evaluated Nuclear Structure Data File) /4/ with a correction term, which is introduced to recover the symmetry between the initial and final states. The values for the transitions
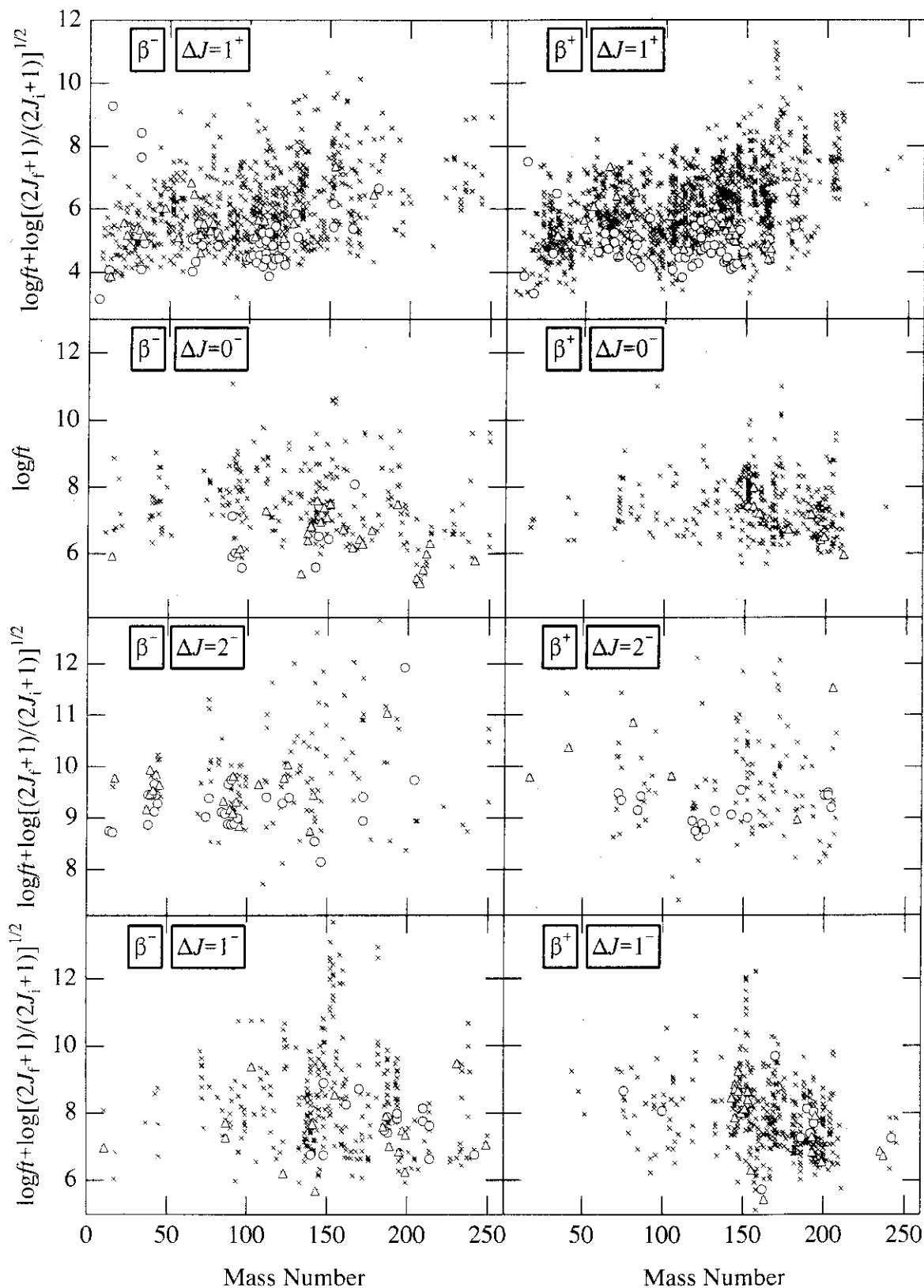
Fig. 1. Experimental log *ft* values /4/ supplemented by a correction term. Circles are for the transitions between ground states of even-*A* nuclei, triangles are for the transitions between ground states of odd-*A* nuclei, and crosses are for the others.

between ground states of odd-A nuclei are shown by triangles, while circles are for the transitions between ground states of even-A nuclei and crosses are for the others.

It is a normal trend that the log ft values for the transitions to ground states are smaller than the ones to the excited states on the average, since the level density of the final states increases rapidly with the excitation energy and the β-strengths are shared among many excited states. This trend is clearly seen in Fig. 1 in the cases where the plot is made for transitions with spin change 1 and no parity change (the Gamow-Teller transition) and for those with spin change 0 and parity change (the first-forbidden transitions of rank 0 and rank 1 are dominant). In the case of the unique first-forbidden transition ($\Delta J = 2^-$), the trend looks somewhat weaker. However, if we take into account the strong possibility that many unique first-forbidden transitions to excited states escaped observation due to their too small branching ratios, we can admit that the trend is also strong in this case. On the other hand, this trend can not be seen in the case where the plot is made for transitions with spin change 1 and parity change (the first-forbidden transition of rank 1 is dominant). This is an evidence for the hindrance of the first-forbidden transition of rank 1 between ground states. By the way, the log ft values for the transitions between ground states of odd-A nuclei are somewhat larger than the ones in even-A nuclei on the average. This tendency can be understood by the gross theory refined for odd-odd nuclei /1/, in which the ground-state strength in the decay of an odd-odd nucleus is multiplied by a statistical factor.

In the case of odd-odd nuclei, the hindrance factor for the first-forbidden transition of rank 1 between the ground states was estimated to be 0.06 in ref. 1. A quantitative study is now in progress for the hindrance of the transitions between ground states of odd-A nuclei. At the present stage, we estimate the hindrance factor to be about 0.2. We suspect that, in both even-A and odd-A nuclei, the reason for the hindrance is the fact that the operator of the first-forbidden transition of rank 1 transfers the 0^+ nucleon pair states to states with more repulsive relative motions than the other β-decay operators do. The hindrance factor in odd-A nuclei is not so small as the one in even-A nuclei. This is consistent with our suspicion, since, in odd-A nuclei, there are less 0^+ pair states to be transferred by the β-decay operator than in even-A nucleus.

5. Calculations of β-ray spectra

In the study of nuclear β-decay, it goes without saying that the β-ray spectrum gives useful information on the strength function. It is worth while for a theoretical model to be examined whether the estimated β-ray spectra agree well with the experiment. In this section, we show some results of the calculated β-ray spectra by using the refined model mentioned in the previous sections.

The β-ray spectrum $P(E_e)$ is calculated with the use of the strength functions as

$$
P(E_e) = T \int_0^{Q-E_e} \left[\sum_{\Omega} S_{\Omega}(E_{exc}) F(Z, E_e) \zeta_{\Omega}(Z, E_e, Q - E_{exc}) \right.
$$
$$
\left. \times (Q - E_{exc} - E_e)^2 (E_e^2 - m^2 c^4)^{1/2} E_e \right] dE_{exc}. \tag{3}
$$

Here, S_{Ω} is the strength function including the coupling constant ($S_{\Omega}(E_{exc}) \propto |M_{\Omega}(E_{exc} - Q)|^2$), $F(Z, E_e)$ the Fermi function, ζ_{Ω} the shape factor, T the calculated β-decay half-life, Q the β-decay Q-value, E_e the β-ray energy, E_{exc} the excitation energy in the daughter nucleus, m the electron rest mass, and c the speed of light in vacuum. Rudstam et al. carried out an

experiment on the β-ray spectra for many short-lived fission products. /5/ In this experiment, the β-ray spectra were measured for 94 nuclides, of which 27 nuclides are odd-odd ones. According to the ENSDF, /4/ the ground states of 19 nuclides among these odd-odd ones are assigned spin-parities from experiments. They are ^{80}As[1($^+$)], ^{82}As[(1$^+$)], ^{84}As[0$^-$, 1($^-$), 2$^-$], ^{84}Br[2$^-$], ^{86}Br[(2$^-$)], ^{88}Br[1, 2$^-$], ^{90}Rb[0$^-$], ^{92}Rb[0$^-$], ^{94}Rb[3($^-$)], ^{96}Rb[2$^-$], ^{96}Y[0$^-$], ^{98}Y[(0)$^-$], ^{134}Sb[(0$^-$), (7$^-$)], ^{136}I[1$^-$], ^{138}I[(2$^-$)], ^{140}Cs[1$^-$], ^{142}Cs[0$^-$], ^{146}Cs[1$^-$], and ^{146}La[2$^-$]. Here, uncertain spin-parities are given in parentheses. We calculate the β-ray spectra of these 19 nuclides by using the refined model, and compare them with the experiment /5/ as well as with those calculated by the second-generation model of the conventional gross theory, the GT2 model. /2/ In the calculations, the Q-values are taken from ref. 6. The effects of the refinement appear in the spectra near the ground states of daughter nuclei, that is to say in the regions of large β-ray energies.

For example, in Fig. 2, we show the β-ray spectra of 6 nuclides calculated by using the refined model and the GT2 model /2/ together with the experimental data. /5/ The calculated β-ray spectra of ^{92}Rb and ^{94}Rb by using the refined model show better agreement with the experiment than those by the GT2 model do. In the case of ^{92}Rb, the ground state spin-parity is assigned 0$^-$, and only the first-forbidden transition of rank 0 occurs to the ground state of the daughter nucleus, which has spin-parity 0$^+$ because of the even-even nucleus. According to the refinement mentioned in Section 3, the first-forbidden transition of rank 0 is multiplied by the factor k, and all the other transitions are cancelled between the ground states. The effects of the factor k makes the spectrum of ^{92}Rb large in the region of E_e=5-6 MeV. In the case of ^{94}Rb, the ground state spin-parity is assigned 3($^-$), and the transition between the ground states of the parent and daughter nuclei is considered to be a third-forbidden transition. Then all the transitions between the ground states are cancelled in the calculations, because only the allowed and first-forbidden transitions are taken into account in the gross theory. The transition to the first 2$^+$ state in the daughter nucleus is included in the calculation, but this strength is rather weak. As can be seen in figure for ^{94}Rb, the cancel of the strengths between the ground states brings good agreement with the experiment. Nuclei ^{84}Br, ^{88}Br, ^{90}Rb and ^{142}Cs show similar tendencies. In the case of ^{88}Br, the ground-state spin-parity is not uniquely determined but both the calculated spectra with spin-parities 1$^-$ and 2$^-$ are almost the same. Although the β-ray spectrum of ^{90}Rb obtained by using the refined model shows good agreement with the experiment, the GT2 model can also give almost the same result for this nucleus.

On the other hand, the agreement of the spectra of ^{138}I with the experiment in Fig. 2 is not so good after the refinement. In this case, the value of the factor k given in Eq.(2) does not seem to be suitable for this nucleus. The situation of ^{146}La has the same tendency as ^{138}I. It is expected that, if we could obtain a suitable value of k for each nucleus, the results would be in better agreement with the experiment.

For nuclei ^{80}As, ^{84}As, ^{86}Br, ^{96}Rb, ^{96}Y, ^{98}Y, ^{134}Sb, ^{136}I ^{140}Cs and ^{146}Cs, the β-ray spectra obtained by using the present model are improved in some energy regions, but not in other energy regions in comparison with the experiments. We should note that the experimental errors are very large for some of these nuclei. In the data file ENSDF, more than one spin-parities [0$^-$, 1($^-$), 2$^-$] are assigned for ^{84}As. Although the experimental β-ray spectrum has large errors, the calculated spectrum with the spin-parity 1$^-$ or 2$^-$ shows better agreement with the experiment than that with the spin-parity 0$^-$ does. This observation suggests that the
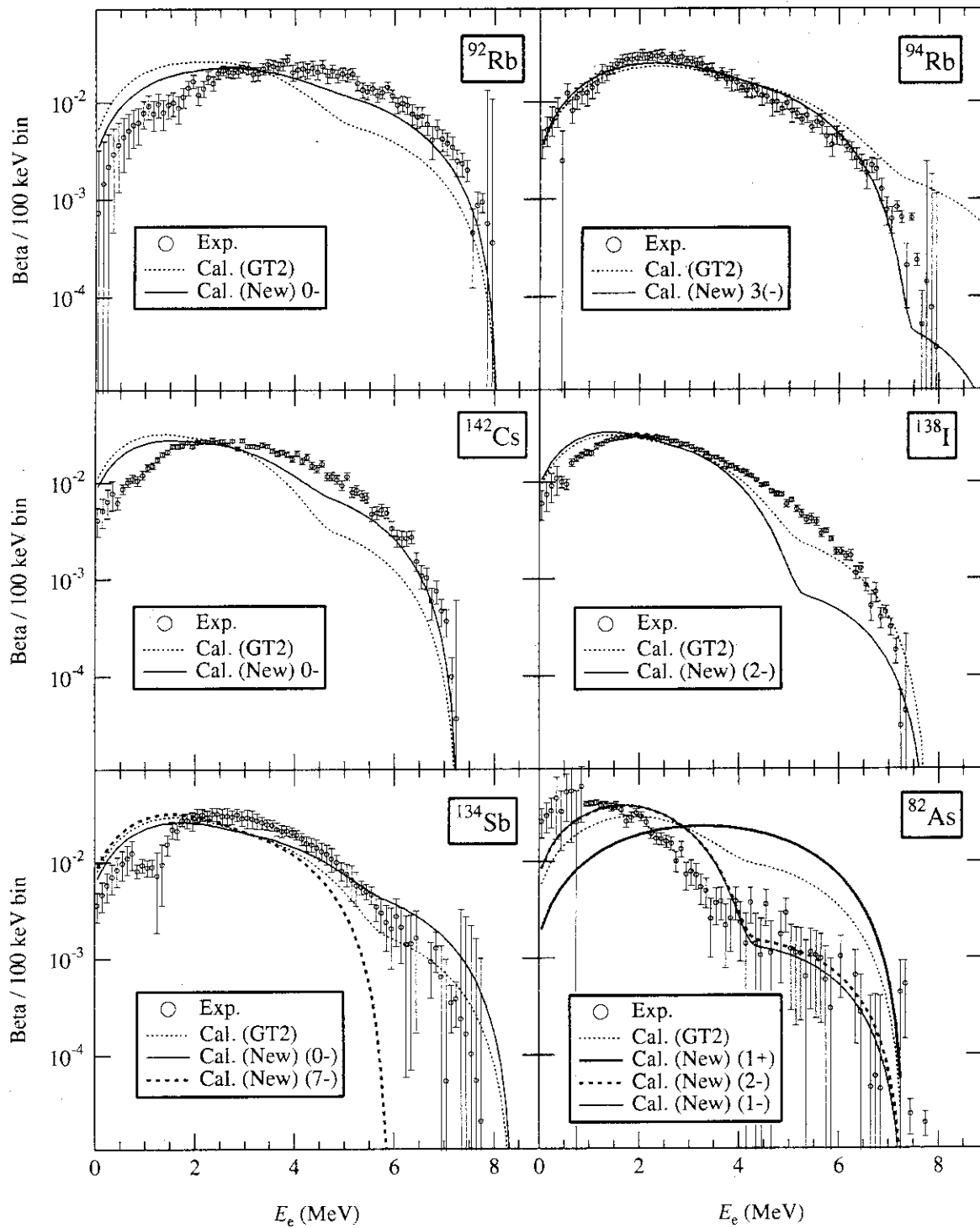
Fig. 2. Calculated and experimental β-ray spectra of ^{92}Rb, ^{94}Rb, ^{142}Cs, ^{138}I, ^{134}Sb and ^{82}As. 'Cal. (GT2)' means the 2nd version of gross theory /2/ and 'Cal. (New)' the present calculation. The experimental data are taken from ref. 5. The abscissa is the transition energy and the ordinate means number of β-particles / 100 keV interval / decay

ground state spin-parity of ^{84}As is 1$^-$ or 2$^-$, and not 0$^-$. In the case of ^{134}Sb, the calculated spectra suggest that the ground state spin-parity is likely to be 0$^-$ and not 7$^-$ (see Fig.2).

Finally we should make some comments on the nucleus ^{82}As. While an uncertain spin-parity (1$^+$) is given to this nucleus, the calculated spectrum with this spin-parity 1$^+$ shows large discrepancies with the experiment. If we adopt the other spin-parity 1$^-$ or 2$^-$, results are much better than that in the case of 1$^+$. The log ft value of the transition between the ground states of ^{82}As and ^{82}Se is estimated to be 6.2 by experiment. (This means log $f^{1u}t$=8.3 for the unique first-forbidden transition.) This log ft is somewhat larger than the average log ft for the Gamow-teller (1$^+$ → 0$^+$) transition in this nuclidic region, but is in an admissible range. On the other hand, it is somewhat smaller than expected for the first-forbidden transitions either unique or nonunique, but again this possibility cannot be definitely excluded. Anyhow this β-decay need to be investigated further.

6. Conclusions

In this study we have obtained some success in refining the gross theory by taking into account the effect of the selection rules and the hindrance of the rank-1 first-forbidden transitions in the ground-state transitions The increase of the tail part of the Gamow-Teller strength function by a factor of about 3 has also been suggested. Although the selection rules reflect the nuclear shell structure, there remain much shell effect not taken into account in the gross theory. Therefore, we are now developing "semi gross" theory, in which the shell effects of parent nuclei are taken into account. At the present stage, it includes only the Fermi and Gamow-Teller transitions but the first-forbidden transition will be taken into account in the near future.

References

[1] H. Nakata, T. Tachibana and M. Yamada, Nucl. Phys. **A594** (1995) 27.

[2] T. Tachibana, M. Yamada and Y. Yoshida, Prog. Theor. Phys. **84** (1990) 641, and references therein.

[3] T. Tachibana and M. Yamada, Proc. Int. Conf. 'ENAM' (1995), to be published

[4] Evaluated Nuclear Structure Data File (ENSDF) 1995, communicated through Nuclear Data Center, Japan Atomic Energy Research Institute.

[5] G. Rudstam et al., Atomic Data and Nuclear Data Tables **45**, 239 (1990).

[6] G. Audi and A. H. Wapstra, Nucl. Phys. **A595**, 409 (1995); **A565**, 1 (1993).

The First Internet Symposium on Nuclear Data: Paper No. p015

3.15 Radiochemical determination of the neutron capture cross sections of ^{241}Am irradiated in the JMTR reactor

N. Shinohara, Y. Hatsukawa, K. Hata, and N. Kohno

Japan Atomic Energy Research Institute

Tokai-mura, Naka-gun, Ibaraki-ken 319-11, Japan

Email : hata@popsvr.tokai.jaeri.go.jp

The thermal neutron capture cross section σ_0 and Resonance integral I_0 of ^{241}Am leading to the production of ^{242m}Am and ^{242g}Am were measured by radiochemical method. The cross sections obtained in this study are σ_0=60.9 $\pm$ 2.6 barn, I_0=213 $\pm$ 13 barn for ^{241}Am(n,γ)^{242m}Am and σ_0=736 $\pm$ 31 barn, I_0=1684 $\pm$ 92 barn for ^{241}Am(n,γ)^{242g}Am.

1 Introduction

Minor actinides produced by neutron capture and successive beta-decay are accumulated in a high burnup reactor. The actinide isotopes produced together with the fission products cause severe problems in waste management. One of the important reactions in the buildup of the minor actinides is the neutron capture of ^{241}Am. Isomeric ^{242m}Am produced by the ^{241}Am(n,γ) reaction is very significant because the isomer has a very large capture cross section at thermal energies and consequently can be transmuted into higher americium isotopes. The relatively short-lived isotope of ^{242}Cm is also formed via ^{241}Am(n,γ)^{242g}Am reaction, and its contribution to the decay heat causes severe problems in spent-fuel handling. However, there is still discrepancy for the absorption cross sections of ^{241}Am leading to the production of ^{242m}Am and ^{242g}Am. The accurate data on the capture cross section of ^{241}Am have been required to be with accuracy of 5%, as registered in the World Request List for Nuclear Data WRENDA 91/92 . In this study, highly-purified ^{241}Am targets were irradiated in JMTR (Japan Material Testing Reactor). The thermal neutron capture cross section and the resonance integral of ^{241}Am and the isomeric ratios have been radiochemically measured. The obtained data are compared with evaluated values.

2 Experimental

2.1 Principle for determination of the capture cross sections and the resonance integrals

For the purpose of measuring the capture cross section of 2200-m/sec neutrons and the resonance integral, this experiment was carried out by the Cd-ratio method [3]: a

Cd-covered target and another without Cd-cover are irradiated together with neutron flux monitors. In the convention by Westcott et al. [4], the effective cross section for Maxwellian neutrons, $\hat{\sigma}$ is defined by

$$R = n v_0 \hat{\sigma} \qquad (1)$$

where R is the reaction rate per atom in the case of the irradiation without Cd shield, n the neutron density including both thermal and epithermal neutrons, and $v_o = 2200$ m/sec. The quantity $n v_0$ plays the role of the "flux." The cross section $\hat{\sigma}$ is also given by

$$\hat{\sigma} = \sigma_0 [g G_{th} + r \sqrt{T/T_0} s_0 G_{epi}] \qquad (2)$$

where s_o is the reaction cross section for 2200-m/sec neutrons, and g the measure of the cross section deviation from the $1/v$ law in the thermal energy region. The $r\sqrt{T/To}$ gives the fraction of epithermal neutrons in the neutron spectrum, and s_o is defined by

$$s_o = \frac{2}{\sqrt{\pi}} \frac{I_0'}{\sigma_0} \qquad (3)$$

where I_0' is the resonance integral after subtracting the $1/v$ component. The G_{th} and G_{epi} denote self-shielding coefficients for thermal and epithermal neutrons, respectively. From Eqs. (1) and (2), the next equation is deduced,

$$R/\sigma_0 = n v_0 + n v_0 r \sqrt{T/T_0} s_0 G_{epi} \qquad (4)$$

$$= \phi_1 + \phi_2 s_0 G_{epi} \qquad (5)$$

In the case of the irradiation with Cd shield, similar equations are derived as follows,

$$R'/\sigma_0 = n v_0 r \sqrt{T/T_0} (1/K + s_0 G_{epi}) \qquad (6)$$

$$= n' v_0 + n v_0 r \sqrt{T/T_0} s_0 G_{epi} \qquad (7)$$

$$= \phi_1' + \phi_2' s_0 G_{epi} \qquad (8)$$

where the term including $1/K$ in Eq.(6) denotes the contribution of the $1/v$ component above Cd cut-off energy. The values of ϕ_1, ϕ_2, ϕ_1', and ϕ_2' can be obtained from the irradiation of flux monitors (two sets of Co and Au wires in this study) put near the target. From Eqs.(5) and (8),

$$s_0 G_{epi} = -\frac{\phi_1 - \phi_1'(R/R')}{\phi_2 - \phi_2'(R/R')} \qquad (9)$$

and then

$$\sigma_0 = \frac{R}{\phi_1 + \phi_2 s_0 G_{epi}} \qquad (10)$$

are obtained, where the quantity σ_0 is the value to be measured first in this study. Since the G_{epi} is reasonably assumed to be unity because of the thickness of the [241]Am

target prepared in this work, the quantity I_0' can be obtained using Eq. (3). The $1/v$ contribution to the resonance integral for a Cd cut-off energy of 0.5 eV is given by

$$I_0 = I_0' + 0.45\sigma_0 \tag{11}$$

where I_0 is the resonance integral to be also determined [5].

3 Radiochemical procedure

3.1 Target

Americium targets (>99.99% purity of ^{241}Am) were purified by ion-exchange method and prepared on aluminum disks by electrodeposition method [6]. Weighed 0.504%-Co/Al and 0.061%-Au/Al alloy wires were used for monitoring the neutron fluxes at the target positions.

3.2 Irradiation

Two sets of the ^{241}Am target with the Co- and Au-flux wires were irradiated in JMTR for 4 days by using a hydraulic type capsule.

3.3 Chemical separation

The americium samples and radiometric sources for α-particle measurements were purified chromatographically by anion exchange with nitric acid and methyl alcohol at room temperature [7]. Chemical recovery of the americium after the ion exchange is more than 99.9%.

3.4 Radioactivity measurements

γ-ray activities from ^{60}Co and ^{198}Au (neutron flux monitors) were measured with a coaxial HPGe detector. The ^{241}Am targets before and after the irradiation were measured with a silicon surface barrier detector. Figure 1 gives α-particle spectra of the target measured in this study.

4 Results and discussion

4.1 Neutron flux

The reaction rates, R, of ^{60}Co and ^{198}Au (neutron flux monitors) were obtained from the absolute activities measured by γ-ray spectrometry, and the values of R/σ_0 in Eqs.(5) and (8) were computed by using the data σ_0's listed in Table 1. The obtained R/σ_0's were plotted as a function of the parameter $S_0 G_{epi}$, where the other parameters used are also given in Table 1. By least squares fitting of Eq. (5) or (8) to the data, the neutron fluxes ϕ_1, ϕ_2, ϕ_1', and ϕ_2' were determined as shown in Table 2. The ratios of ϕ_1/ϕ_1' and ϕ_2/ϕ_2' are 0.003 and 1.1, respectively.

5 Analyses of the decay and growth curves of the activity ratio ^{242}Cm/^{241}Am

The growth and decay behaviors on the α-activity ratios of ^{242}Cm/^{241}Am have been precisely observed by the radiochemical method. Figure 2 is the decay and growth curves of the ratio in the irradiated ^{241}Am sample. By analyzing the curves in detail, atom ratios of ^{242m}Am/^{241}Am and ^{242g}Am/^{241}Am can be computed as follows:

5.1 Decay of the activity ratios of ^{242}Cm/^{241}Am

When the numbers of atoms after EOB (end of the bombardment) are N_0, N_1, N_2, N_3 and N_4 for ^{241}Am, ^{242m}Am, ^{242g}Am, ^{242}Cm and ^{238}Pu, respectively, the activity ratio, A_{mes}, of ^{242}Cm/^{241}Am measured in this study before chemical separation (strictly speaking, the measured ratio is expressed by ^{242}Cm/(^{241}Am+^{238}Pu) because the same α-particles with 5.5 MeV is released from target ^{241}Am and decay product ^{241}Pu) is expressed by

$$A_{mes} = \frac{dN_3/dt}{dN_0/dt + dN_4/dt} \tag{12}$$

$$= \frac{\lambda_3 \frac{N_3^0}{N_0^0} e^{-\lambda_3 t}}{\lambda_0 e^{-\lambda_0 t} + \frac{\lambda_3 \lambda_4}{\lambda_3 - \lambda_4} \frac{N_3^0}{N_0^0} (e^{-\lambda_4 t} - e^{-\lambda_3 t})} \tag{13}$$

where N_0 means the number of atoms at EOB. By least squares fitting of Eq. (13) to the decay curve (see Fig. 2), the atom ratios of ^{242}Cm/^{241}Am at EOB were determined.

5.2 Growth of the activity ratios of ^{242}Cm/^{241}Am

When the atom numbers after the chemical separation are, respectively, N_{0c}, N_{1c}, N_{2c}, N_{3c} and N_{4c} for ^{241}Am, ^{242m}Am, ^{242g}Am, ^{242}Cm and ^{238}Pu, the growth of the activity ratio of ^{242}Cm/^{241}Am (see Fig. 2) can be expressed by

$$\frac{dN_{3c}/dt}{dN_{0c}/dt} = \frac{k_1 \lambda_1 \lambda_2 \lambda_3}{\lambda_0 (\lambda_2 - \lambda_1)(\lambda_3 - \lambda_1)} \frac{N_{1c}^0}{N_{0c}^0} e^{-(\lambda_1 - \lambda_0)t}$$

$$+ \left(\frac{k_1 \lambda_1 \lambda_2 \lambda_3}{\lambda_0 (\lambda_1 - \lambda_2)(\lambda_3 - \lambda_2)} \frac{N_{1c}^0}{N_{0c}^0} + \frac{k_2 \lambda_2 \lambda_3}{\lambda_0 (\lambda_3 - \lambda_2)} \frac{N_{2c}^0}{N_{0c}^0} \right) e^{-(\lambda_2 - \lambda_0)t}$$

$$+ \left(\frac{k_1 \lambda_1 \lambda_2 \lambda_3}{\lambda_0 (\lambda_1 - \lambda_3)(\lambda_2 - \lambda_3)} \frac{N_{1c}^0}{N_{0c}^0} + \frac{k_2 \lambda_2 \lambda_3}{\lambda_0 (\lambda_2 - \lambda_3)} \frac{N_{2c}^0}{N_{0c}^0} \right) e^{-(\lambda_3 - \lambda_0)t} \tag{14}$$

where N^0 means the number of atoms at the chemical separation (180 days after EOB). The value k_1 and k_2 are the correction factors for branching yields of IT of ^{242m}Am (0.99524) and β-decay of ^{242g}Am (0.827) respectively. By least squares fitting of this formula to the growth curve (see Fig. 2), the atom ratios of ^{242m}Am/^{241}Am at EOB were determined.

6 Formation cross sections of ^{242m}Am and ^{242g}Am

The reaction rate of ^{242m}Am by thermal or epithermal neutrons is

$$R = \frac{N_3}{N_0} \times \frac{\lambda_3}{1 - e^{-\lambda_3 t}} \tag{15}$$

The formation cross section of ^{242m}Am for 2200 m/sec neutrons, so, was obtained from Eqs. (9) and (10) and the calculated ratio R/R' using Eq. (22), while the resonance integral, I_0, was computed from Eqs (3) and (11). Table 3 shows the cross sections obtained by this method. By the similar procedure as mentioned above, the formation cross sections of ^{242}Cm were determined, where the contibution of the decay product ^{242}Cm of ^{242m}Am to the reaction product ^{242}Cm was corrected by the ^{242m}Am data mentioned above, but is negligible small. The ^{242}Cm cross sections were converted to those of ^{242g}Am by correcting the β-decay branching of ^{242g}Am to ^{242}Cm. The results are also given in Table 4, together with the isomeric ratios.

7 Comparison with evaluated values

The thermal cross section and the resonance integral evaluated by Mughabghab [8] and the total absorption cross section by JENDL-3.2 [9] are listed in Table 3. The $\sigma_{n,\gamma}$ value obtained in this work are larger than the evaluated ones (10-40 % in difference) . Our method for the cross-section determination is not affected by the accuracy of the ^{241}Am amount on the targets, because the cross sections can be derived from the relative atom ratios of ^{242}Cm to ^{241}Am measured with precision of 0.2-1.1 %. Moreover, because the highly-purified ^{241}Am targets were used in this work and then there is no influence from impurity, our results could be reliable with acuuracy of 4-6 %. Isomeric ratios, i. e. relative population of the ground state to the total capture cross section (g/(m+g)) are also given in Table 3. The ratio measured in thermal neutron energy (0.92) agrees excellently with the evaluated value by Mughabghab [8] and the previous data measured by Wisshak et al. [10], as seen in Table 3. However, the isomeric ratio in epithermal region (0.89) is not consistent with the Wisshak's value (27 % in difference). It seems that this discrepancy is due to the difference between this integral measurements performed in reactor neutron spectra and the quasi-monoenergetic experiment with 30-keV neutrons.

References

[1] Z. Delin, et al.: *CNIC-00690*, 97 (1992).

[2] N. Kocherov and P. K. McLaughlin (eds.): *INDC(SEC)-104* (1993).

[3] T. Sekine, Y. Hatsukawa, K. Kobayashi, H. Harada, H. Watanabe, and T. Katoh: *J. Nucl. Sci. Tech.* **30** 1099 (1993).

[4] C. H. Westcott, W. H. Walker and T.K. Alexander: *2nd Int. Conf. on the Peaceful Uses of Atomic Energy*, Vol. 16, p. 70, IAEA, Geneva (1958)

[5] S. F. Mughabghab and D. I. Garber: *BNL 325, 3rd ed.,* Vol.1 (1973).

[6] N. Shinohara and N. Kohno: *Appl. Radiat. Isot.* **40** 41 (1989).

[7] S. Usuda and N. Kohno: *Sep. Sci. Technol.* **23** 1119 (1988).

[8] S. F. Mughabghab: *BNL 325, 4th ed.*, Vol.2 (1988).

Table 1. Nuclear data used for the neutron-flux monitoring and the cross-section determination

nuclide	σ_0 (b)	I_0 (b)	s_0	G_{epi}
^{59}Co	37.18 ± 0.06	74 ± 2	1.83	0.995
^{197}Au	98.65 ± 0.09	1550 ± 28	17.02	0.993

nuclide	half-life	decay (branching %)
^{241}Am	432.0 ± 0.2 y	α (100)
^{242m}Am	152 ± 7 y	IT (99.524)
^{242g}Am	16.01 ± 0.02 h	β (82.7)
^{242}Cm	162.76 ± 0.04 d	α (100)
^{238}Pu	87.71 ± 0.03 y	α (100)

σ_0: cross section for 2200 m/sec neutrons,

I_0: resonance integral,

$s_0 = (2\pi^{-1/2})(I_0'/\sigma_0)$, where I_0' is the resonance integral after subtracting the $1/v$ component,

G_{epi}: self-shielding coefficient for epithermal neutrons.

Table 2. Neutron flux determined by the flux monitors

sample	ϕ_1 or $\phi_1'(n/cm^2 \cdot s)$	ϕ_2 or $\phi_2'(n/cm^2 \cdot s)$
no Cd shield	$(1.06 \pm 0.05) \times 10^{14}$	$(5.99 \pm 0.34) \times 10^{12}$
with Cd shield	$(2.78 \pm 0.11) \times 10^{11}$	$(6.50 \pm 0.09) \times 10^{12}$

Table 3. Cross sections and isomeric yield ratios of ^{242}Am produced by the ^{241}Am(n,γ) reaction

Reaction	σ_0 (b)	I_0 (b)	Ref.
^{241}Am(n,γ)^{242m}Am	60.9 $\pm$ 2.6	213 $\pm$ 13	this work
	54 $\pm$ 5	195 $\pm$ 20	Mughabghab [8]
^{241}Am(n,γ)^{242g}Am	736 $\pm$ 31	1684 $\pm$ 92	this work
	533 $\pm$ 13	1230 $\pm$ 100	Mughabghab [8]
total	797 $\pm$ 31	1897 $\pm$ 93	this work
	587 $\pm$ 12	1425 $\pm$ 100	Mughabghab [8]
	600.4	1305	JENDL-3.2 [9]

Neutron energy	Isomeric ratio g/(g+m)	Ref.
thermal	0.92 $\pm$ 0.05	this work
	0.91 $\pm$ 0.02	Mughabghab [8]
	0.92 $\pm$ 0.06*	Wisshak et al.[10]
epithermal	0.89 $\pm$ 0.07	this work
	0.86 $\pm$ 0.09	Mughabghab [8]
	0.65 $\pm$ 0.05**	Wisshak et al.[10]

*value at 14.75-MeV neutron

**at 30-keV neutron

Table 4. Final result on cross sections and isomeric yield ratios

Reaction	σ_0 (b)	I_0 (b)
^{241}Am(n,γ)^{242m}Am	60.9 $\pm$ 2.6	213 $\pm$ 13
^{241}Am(n,γ)^{242g}Am	736 $\pm$ 31	1684 $\pm$ 92

Neutron energy	m/g ratio
thermal	0.0827 $\pm$ 0.049
epithermal	0.126 $\pm$ 0.010
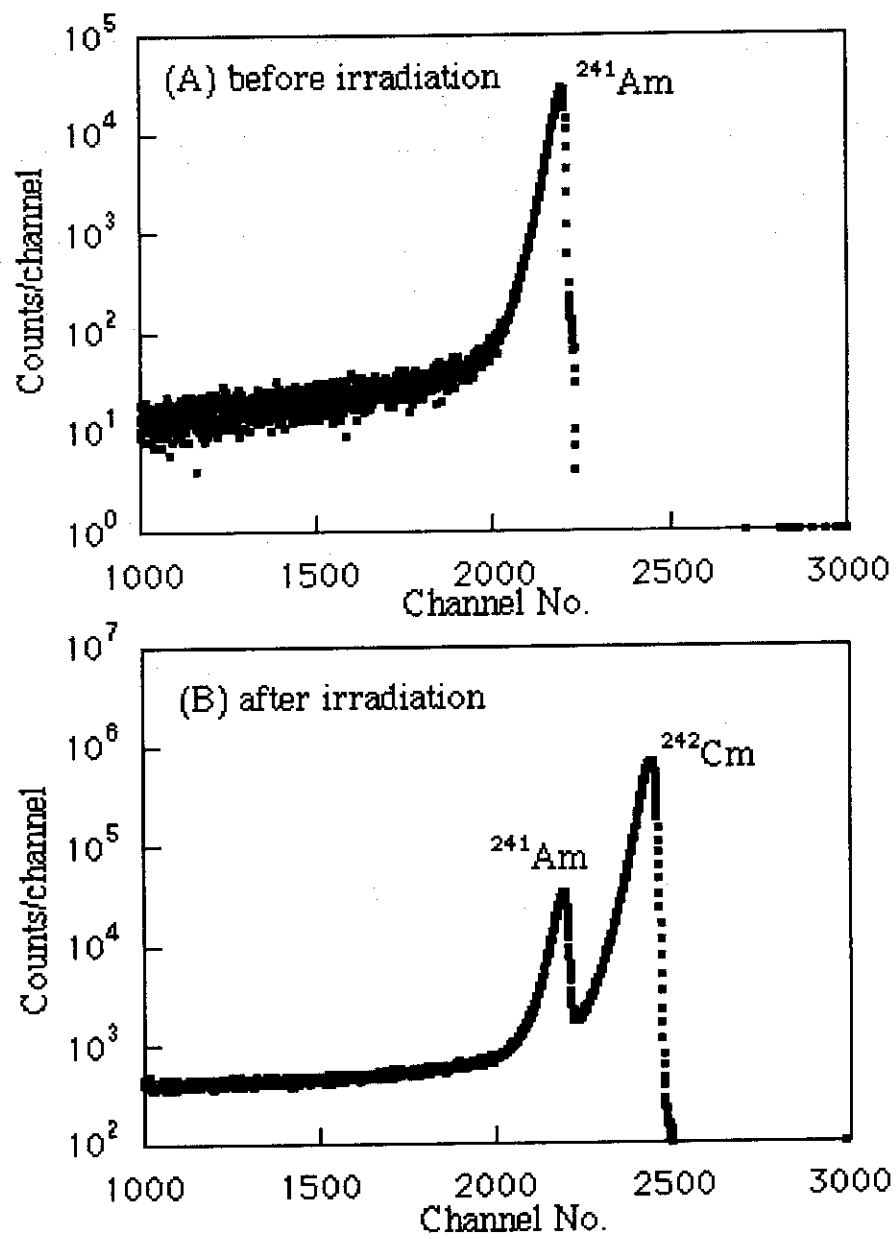
Figure 1: Alpha-particle spectra of the ^{241}Am target.
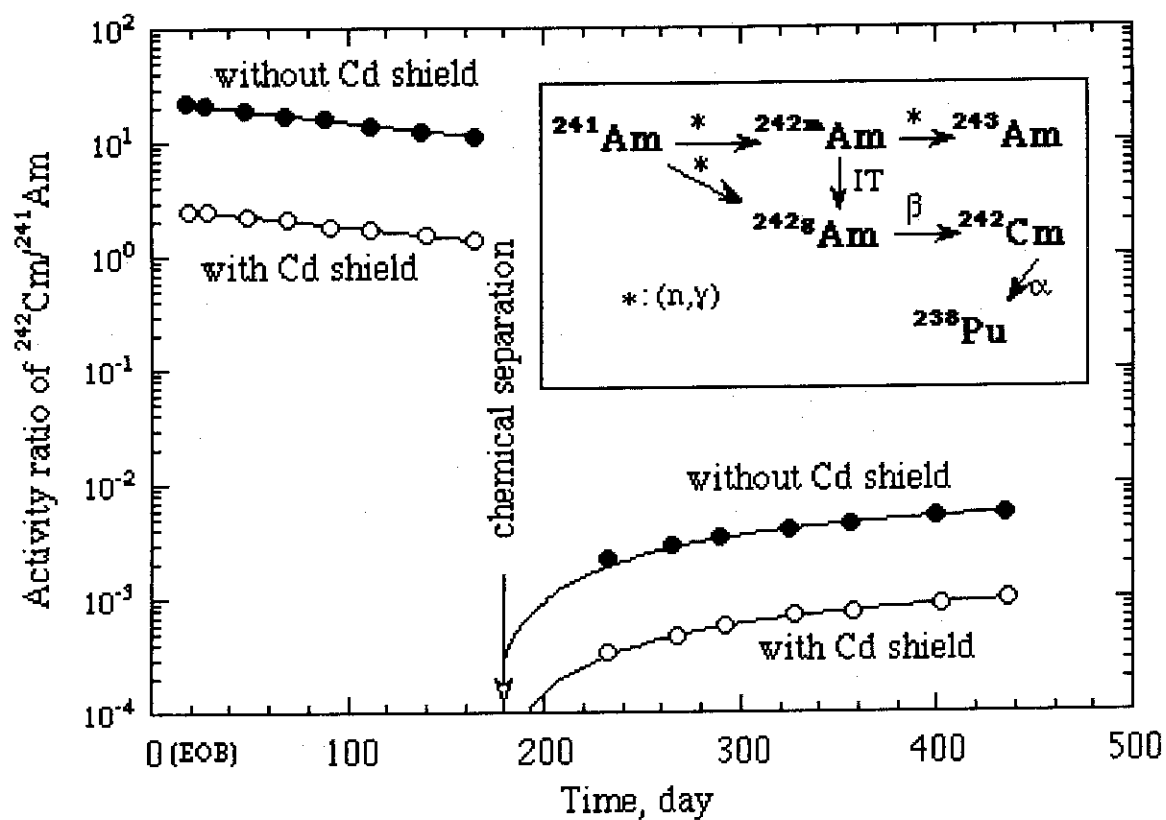
Figure 2: Decay and growth of ^{242}Cm in the irradiated ^{241}Am target.

3.16 Measurement of 14 MeV Neutron Cross Section of ^{129}I with Foil Activation Method

Isao Murata, Daisuke Nakano and Akito Takahashi

Department of Nuclear Engineering, Osaka University

Yamada-oka, 2-1, Suita 565 Japan

Email:murata@nucl.eng.osaka-u.ac.jp

The ^{129}I, which is one of the most famous fission products (FPs), is of very important concern from the standpoint of waste transmutation due to its extremely long half life. The accurate reaction cross section data of ^{129}I induced by 14 MeV neutrons are indispensable when evaluating the performance to transmute it in a fusion reactor. However, there was no available experimental data reported until now. We measured 14 MeV neutron induced reaction cross sections of ^{129}I to give the reference cross section data for evaluation of transmutation performance and nuclear data, using OKTAVIAN facility of Osaka university, Japan.

Since the available amount of ^{129}I as a sample is quite small, probably less than 1 mg, the foil activation method was adopted in the measurement. The sample was a sealed source of ^{129}I and the γ-rays from the irradiated sample were measured with a Hp-Ge detector. Several γ-rays peaks which could be expected to be caused by two nuclear reactions of $^{129}I(n,2n)$ and $^{129}I(n,\gamma)$ were observed. We confirmed that these peaks corresponded to those of ^{128}I and ^{130}I through ascertaining each energy and half life. From the measurement, the cross section of $^{129}I(n,2n)$ and the effective production cross section of ^{130}I produced by the $^{129}I(n,\gamma)^{130}I$ reaction including the contribution of $^{129}I(n,\gamma)^{130m}I$ reaction, that were estimated to be 1.1±0.1 b and 0.032±0.003 b, respectively at 14.8 MeV, were obtained with an acceptable accuracy of about 10 %,though the errors caused by the uncertainty of γ decay scheme data still existed. The measured cross sections were compared with the evaluated nuclear data of JENDL-3.2 and ENDF/B-VI. For the $^{129}I(n,2n)$ reaction,the evaluations overestimate the cross section by 30~40 %, while for the $^{129}I(n,\gamma)$ reaction,the evaluations underestimate by at least one order of magnitude.

1 Introduction

Recently, the possibility transmutation of nuclear wastes, i.e., minor actinide (MA) and fission product (FP), has been investigated energetically[1]. As practical methods of

transmutation, applications of fission reactor, proton accelerator and fusion reactor and so on have been taken into consideration. The basic scenario of the transmutation is proposed as follows: Transmuting MAs directly or converting MAs into FPs by spallating them, then the residual FPs will be transmuted or converted into benign nuclides for geological site burial. As for the transmutation of FPs, use of (n, γ) reactions are promising because of their large cross section for thermal neutrons by a fission reactor. While the threshold reactions by fusion neutrons (14 MeV neutrons produced by DT(deuterium-tritium) reactions), represented by the $(n, 2n)$ reaction, are also applicable for the transmutation. Though there exist several measurements of (n, γ) reaction cross sections[2, 3, 4] with thermal neutrons, measurement with 14 MeV neutrons has not been conducted. At present, therefore, accurate estimation of transmutation performance with 14 MeV neutrons is difficult because uncertainties in the evaluated nuclear data of target FPs are not clear, or maybe very large. This fact suggests that the measurement of reaction cross section of FPs with 14 MeV neutrons is very important for both nuclear physics, models which are means of nuclear data evaluations, and nuclear engineering, works for estimating the transmutation performance with a fusion reactor.

In this study, ^{129}I, which is one of the most famous fission products (FPs) from the standpoint of waste transmutation due to its extremely long half life, is the target, because this nuclide has various advantages for foil activation method as shown later. The accurate reaction cross section data of ^{129}I induced by 14 MeV neutrons are indispensable when evaluating the performance to transmute it in a fusion reactor. However, there was no available experimental data reported until now. We, therefore, measured the 14 MeV neutron induced reaction cross sections of ^{129}I to give the reference cross section data for evaluation of nuclear data and transmutation performance by 14 MeV neutrons, using OKTAVIAN facility of Osaka university, Japan. The experimental results were compared with the evaluated nuclear data of JENDL-3.2 and ENDF/B-VI.

2 Experiment

2.1 Sample for irradiation

The FPs which are recognized as target nuclides of transmutation are listed in Table1. Because they are radioactive, a massive sample cannot be utilized. Therefore, it is almost impossible to obtain the reaction cross sections of them by analyzing emitted secondary particles. We, for this reason, adopted the foil activation method, with which we can obtain the information of reaction products after neutron irradiation through emitted

Table 1: Main transmutation target FPs

	E_γ (KeV)	$\tau_{1/2}$ (Year)	Key issue
^{90}Sr	-	28.8	Heat source
^{137}Cs	662	30.17	
^{99}Tc	-	2.1×10^5	Inherent risk
^{129}I	39.6	1.6×10^7	
^{135}Cs	-	3.0×10^6	

OKTAVIAN D.C. line
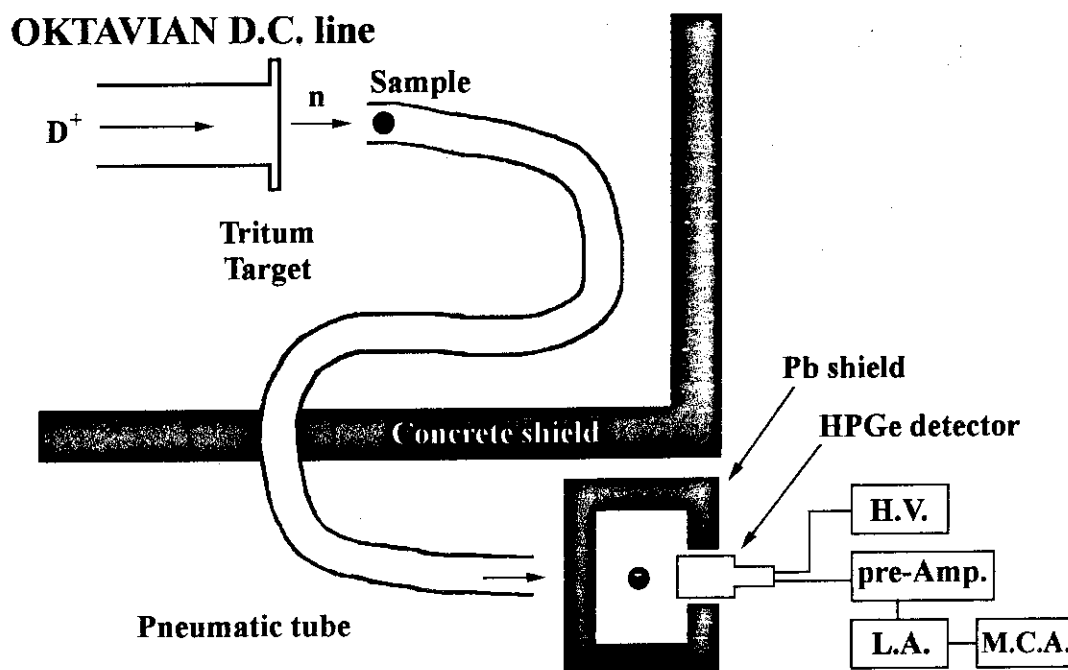
Figure 1: The experiment system configuration of the activation method

γ-ray measurement, even if the amount of the sample is quite small. However, as shown in Table1, some FPs decay through β-ray emission following some γ-rays emission; which means the sample activity itself may become a background in the γ-ray measurement. While the alternative is separation of the nuclides after neutron irradiation. However, since the main target reaction is $(n, 2n)$ at about 14 MeV, the separation technique becomes very difficult because they are isotopes. Table1 also shows there are two kinds of transmutation targets; namely one is short half-life nuclide regarded as heat source, and the other is very long half-life nuclide retaining inherent risk for an extremely long period. For the foil activation method, long half-life FPs have very much an advantage because the number of nuclides per unit radioactivity is several orders of magnitude larger than that of short half-life one. Also it is indispensable that the target FP creates radioactive nuclides having appropriate long half lives by neutron irradiation. From the above discussions, we selected the ^{129}I as a target sample. Because, first of all, this is one of the most important FP from the standpoint of transmutation of radioactive waste, and the half life of ^{129}I is quite long, 1.7×10^7 years. Also the energy of γ-ray associated with the β decay is so low that the γ-ray cannot transmit the detector window and the radioactive nuclides in the irradiated ^{129}I sample have appropriate long half lives of 20 minutes to 30 days.

The sample is a sealed source of 3.7 kBq, in which about 10^{18} nuclei are contained. Therefore, reaction cross sections as low as 10 mb could be measured, though depending on the half life of reaction product. Practically, the background caused by irradiating the casing used to seal the sample, disturbs the measurement especially for short half life nuclides.
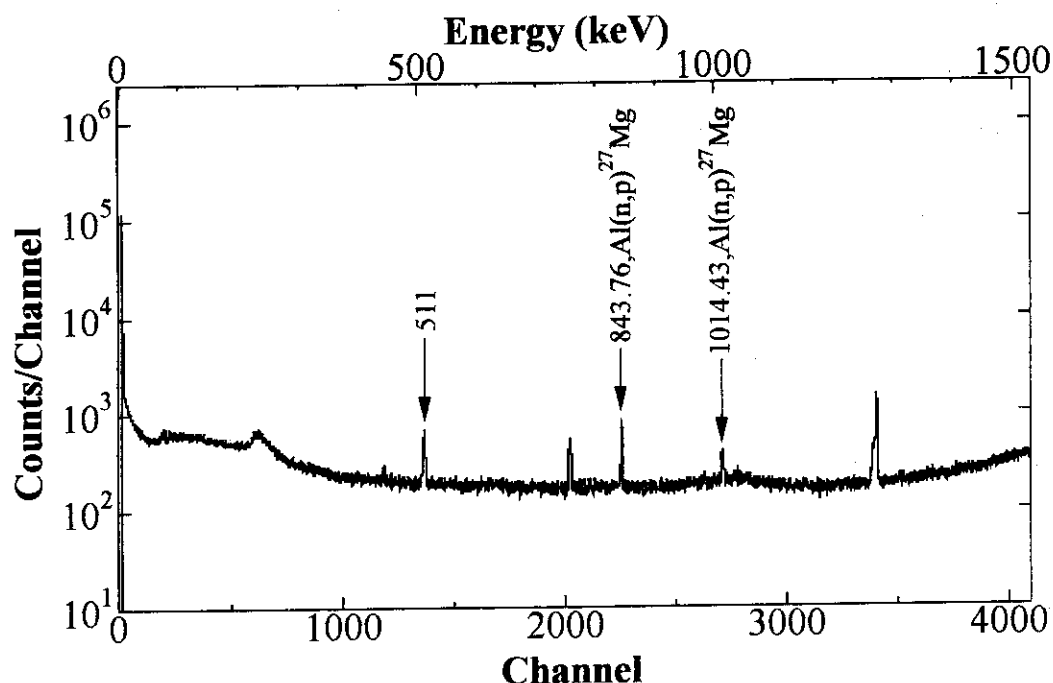
Figure 2: Pulse height spectrum of γ-rays from ^{129}I irradiated by 14 MeV neutrons(Just after irradiation)

2.2 Neutron source

The measurement was carried out using a continuous DT neutron source of the DC line of OKTAVIAN facility, Osaka university, Japan. Since the sample was arranged on the front surface of the rotating target assembly along the D^+ beam line, the neutron energy was empirically estimated to be about 14.8 MeV. There exist low energy neutron contribution (thermal $\sim$ several MeV) of about 20 % in the incident neutron spectrum at the sample position. The accurate effective energy is to be determined by experiment with the Zr/Nb ratio method. The obtained neutron flux was about 10^9 n/cm^2/sec on the same position. The relative neutron fluence was measured with a BF_3 proportional counter to take into account the time variation of neutron flux measured with a MCS system. The absolute neutron fluence was determined with the activities of Al and Nb foils which are irradiated at the same position. The schematic experimental arrangement is illustrated in Fig.1. Because the spatial dose equivalent rate is still very high in the heavy irradiation room of OKTAVIAN DC line target, one cannot enter the room just after irradiation. Therefore, by using a pneumatic tube as shown in the figure, retrieving the irradiated sample immediately after irradiation, the measurement with a Hp-Ge system can be started. With this system, the cross section of a reaction, the daughter nuclides of which even have long half lives of more than several seconds, can be measured: Practically we obtained the γ-ray spectrum from ^{16}N, having a half life of about 7 seconds, which was produced by irradiating water sample using this system.

2.3 Irradiation and activity measurement

The irradiation was planned focusing on two cases; one is for the short half life of 25 minutes of ^{128}I produced by $^{129}I(n, 2n)$ reaction and the other is for the longer half

lives of more than 12 hours. Therefore, to prevent the production of longer half-life background nuclides, two patterns of irradiation, namely, one hour irradiation and several days irradiation, which were determined by considering the half life of the target nuclide, were performed. After retrieving the sample by the pneumatic tube, the γ-rays from the irradiated sample were measured with a Hp-Ge detector. The absolute efficiency of the detector is about 0.3 % for 1 MeV γ-ray at 5 cm distance from the detector front window. Fig.2 shows an example of pulse height spectrum of the irradiated sample just after irradiation. The ^{129}I itself has no background γ-ray in this energy range as described earlier. However, high background counts were observed in the figure, because this is due to activation of the casing material. The contribution of many short half-life background nuclides as well as ^{27}Mg from $^{27}Al(n,p)$ reaction were observed. γ-rays from the target reaction were, therefore, surely detected, but not seen in the spectrum. Also the count rate for Fig. 2 was extremely high so that the dead time exceeds 10 %, which, as a result, requires a proper cooling to reduce background activity. Fortunately, most activities resulting in the high count rates, which have relatively short half lives less than 10 minutes, in which the longest one is ^{27}Mg, decay in several minutes. The dead time was reduced to negligible level in about 20 minutes. We started measuring the target γ-rays after cooling the background.

2.4 Error estimation

The following errors were taken into account in deriving the cross section:(1)Absolute intensity and half life of the sample and standard sources, (2)Position of the sample and activation foil arranged and (3)Statistical error of counting. The errors induced by these effects are listed in Table 2. From the Table, it was found before counting that the summation of the errors except statistical one was over several percentages. Therefore, the counting time was determined such that the cumulative error does not exceeds 10 %. The evaluated total error was about 9 % although errors with respect to transition probability between nuclear levels quoted from Ref.[5] in this study were not considered.

Table 2: Estimated errors in the derivation of the cross section

Item		Error(%)
Sample	Activity	6
	Half life	2.6
	Measurement	3.7
Position of the sample and foil		5
Activation foil	Weight	0.8
	Measurement	1.1
Standard source	Activity	5
	Half life	negligible
Total evaluated error		<9

Periods of irradiating,cooling and counting are 70m, 45m and 25m, respectively
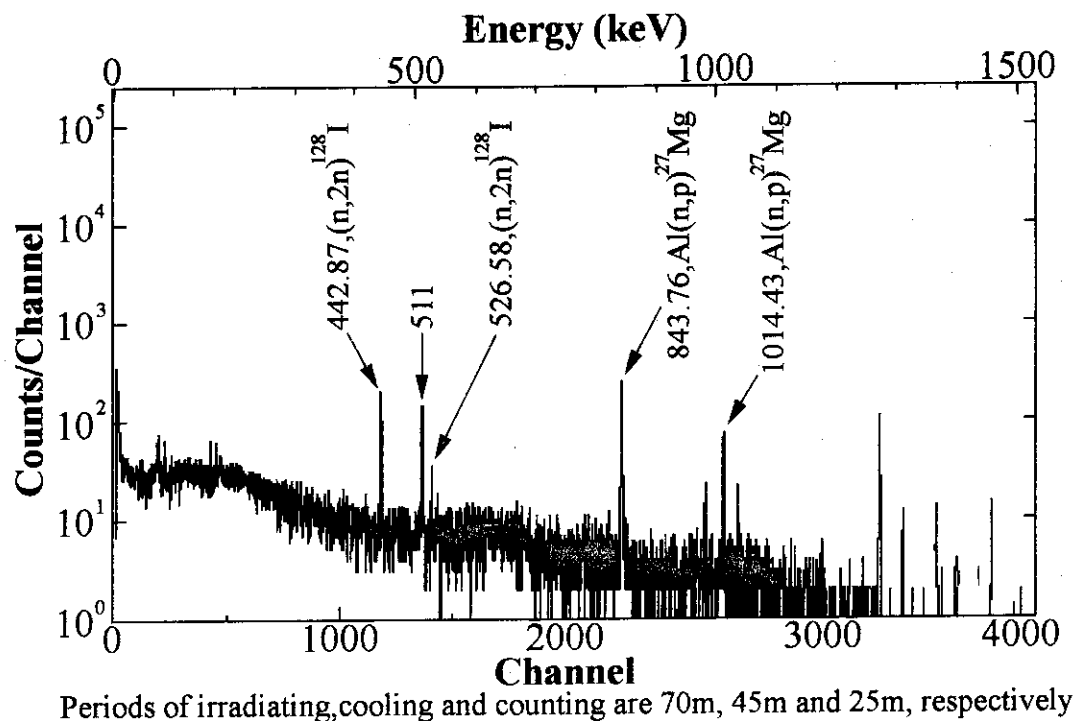
Figure 3: Pulse height spectrum of γ-rays from ^{129}I irradiated by 14 MeV neutrons(Peaks associated with ^{128}I are observed)

Periods of irradiating, cooloing and counting are 1d, 1d 2d, respectively
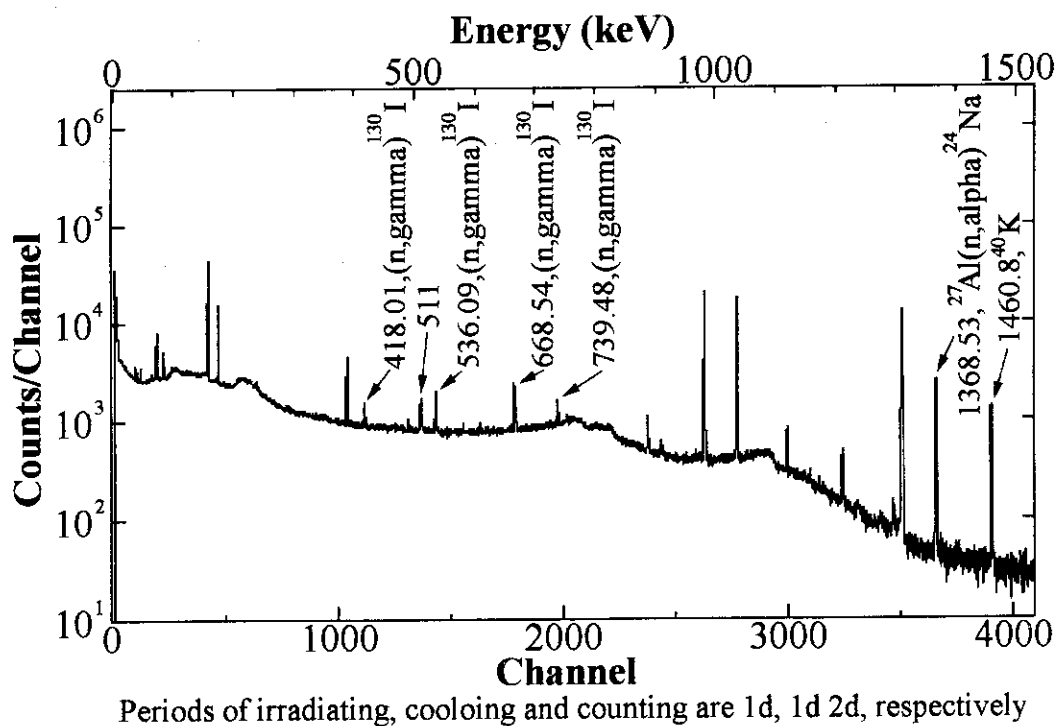
Figure 4: Pulse height spectrum of γ-rays from ^{129}I irradiated by 14 MeV neutrons(Peaks associated with ^{130}I are observed)

3   Results and Discussion

The measured pulse height spectra were shown in Fig.3 and Fig.4, the conditions of which are 70 minutes of irradiation, 45 minutes of cooling and 25 minutes of counting and 1 day irradiation, 1 day cooling and 2 days counting, respectively. To reduce background of short half life nuclides, the former employed the cooling time of 45 minutes. For the cross section evaluation, another spectrum, which was measured for a longer time, was used. The irradiation and cooling periods of the latter were determined considering the target nuclide half life of 12 hours.

From the spectra obtained, several γ-rays which could be expected to be caused by two nuclear reactions of $^{129}I(n, 2n)$ and $^{129}I(n, \gamma)$ were observed. We confirmed that these peaks corresponded to those of ^{128}I and ^{130}I through ascertaining each energy and half life. From the prediction with the evaluated nuclear data, it was expected that some other reactions could be observed. However, nothing but the two reactions was found. we, therefore, presume that especially for the reactions of (n, p) and (n, α), the evaluation may underestimate their cross sections.

3.1 $^{129}I(n, 2n)$ reaction cross section

Figure 5 shows the simplified decay scheme of ^{128}I. In the measured spectrum in Fig.3, γ-rays of 443 keV and 527 keV were observed associated with the transition from the first excited state, $2^+(443\ \text{keV})$ of ^{128}I to the ground state and the transition from the second excited state of $2^+(969\ \text{keV})$ to the first excited state, respectively. The half life of the measured γ-ray was measured from the change in counting rate, to confirm the identification of the measured and expected γ-ray. The time dependence of the neutron flux was strictly considered in the derivation of the cross section. The measured cross section of $^{129}I(n, 2n)$ reaction at 14.8 MeV is 1.1 ± 0.1 b as shown in Table 3. From the comparison with the evaluated nuclear data of JENDL-3.2 and ENDF/B-VI, the two evaluations overestimate the experimental results by 40 % and 30 %, respectively.

3.2   Effective cross section of $^{129}I(n, \gamma)$ reaction

Figure 6 shows the simplified decay scheme of ^{130}I. The ^{130}I has the isomeric state of $2^+(48\ \text{keV}$ higher than $^{130}I)$, the half life of which is 9.2 minutes. By the reaction of ^{129}I with DT neutrons, ^{130}I and ^{130m}I can be yielded with a certain rate. To estimate the rate precisely, thirty-minute-counting just after irradiation was very important and indispensable because 17 % of the isomeric state decay through β-ray emission resulting

Table 3: Measured cross sections compared with the evaluations

	Cross section at 14.8 MeV (barn)		
	Experiment	JENDL-3.2	ENDF/B-VI[*1]
$^{129}\text{I}(n, 2n)^{128}\text{I}$	1.1 ± 0.1	1.52	1.46
$^{129}\text{I}(n, \gamma)^{130}\text{I}$	0.032 ± 0.003[*2]	1.00×10^{-3}	1.83×10^{-3}

*1 Evaluated at 15 MeV

*2 Effective production cross section
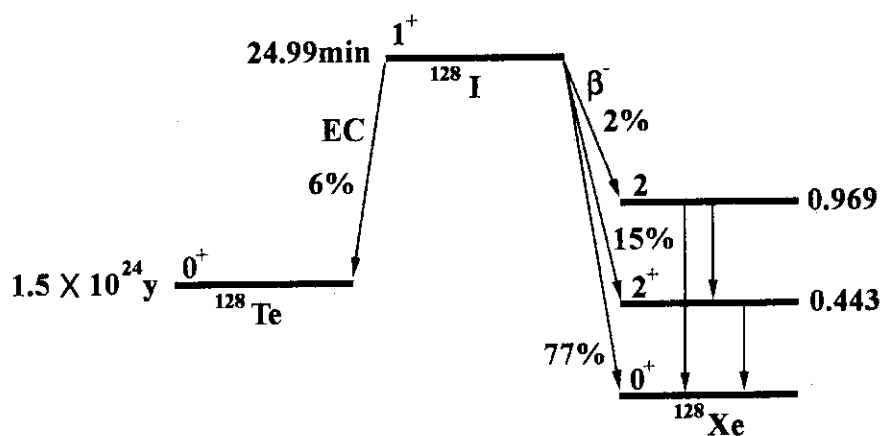
Figure 5: Simplified decay scheme of ^{128}I
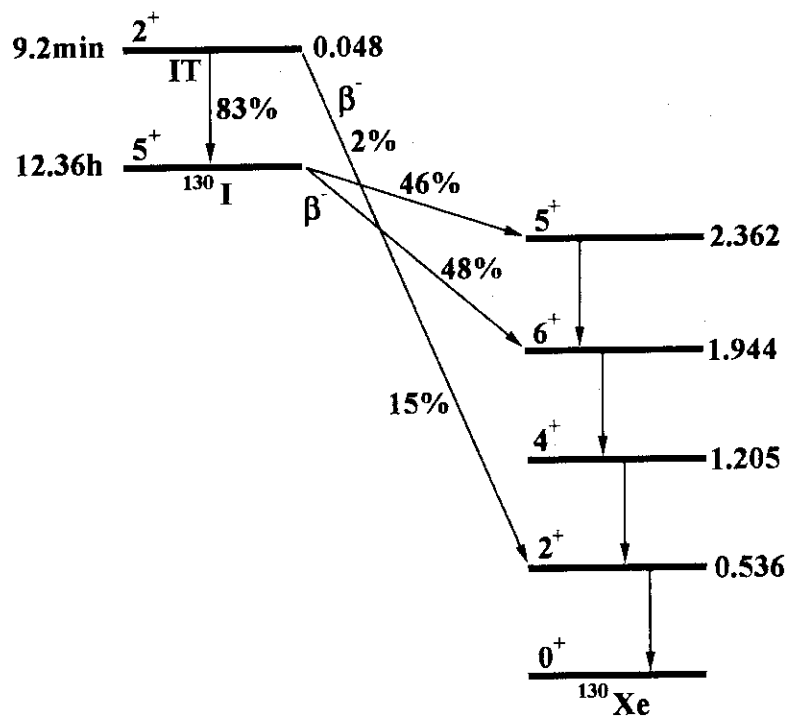
Figure 6: Simplified decay scheme of ^{130}I

in transition to the first excited state, $2^+(0.536$ MeV$)$, of ^{130}Xe mainly, that is also the path of transition after β decay of ^{130}I. In this experiment, the background was dominant for about 30 minutes after irradiation. Therefore, the contribution to pulse height spectrum due to decay of the isomeric state could not be identified accurately. We, thus, evaluated the newly defined effective production cross section of ^{130}I from the measured result by assuming that 83 % of produced ^{130m}I had already decayed by isomeric transition just after irradiation. This value can describe time dependent decay behavior of ^{130}I accurately after ^{130m}I decays completely. The pulse height spectrum of γ-rays associated with their decays mainly consist of four peaks, which correspond to the energies of 418 keV, 739 keV, 669 keV and 536 keV due to the transitions from $5^+(2.36$ MeV$)$, through $6^+(1.94$ MeV$),4^+(1.20$ MeV$)$ and $2^+(0.536$ MeV$)$, to the ground state, respectively. The target γ-rays were confirmed through the measurement of their half lives. From the result, the effective production cross section of ^{130}I was 0.032 ± 0.003 b as shown in Table 3. We cannot evaluate the difference of the cross section directly compared with the present result and the evaluation. However, considering the fact that the summation of $^{129}I(n,\gamma)^{130}I$ and $^{129}I(n,\gamma)^{130m}I$ reaction cross sections clearly exceeds the effective production cross section of ^{130}I, the both evaluations of JENDL-3.2 and ENDF/B-VI underestimate the cross section by at least one order of magnitude. However, taking into account the shape of the energy differential cross section of $^{129}I(n,\gamma)$ and existence of low energy neutron contribution, it is noticed that the experimental value may, include the low energy cross section contribution. Therefore, we are planning the following analysis and experiment to examine the low energy contribution, that are the calculation of the neutron spectrum in the heavy irradiation room and the irradiation experiment using thermal neutron absorber.

4   Conclusion

This paper reports the first results of 14 MeV neutron induced reaction cross section measurements of ^{129}I, which is very important from the standpoint of waste transmutation due to its extremely long half life. From the measurement, the cross section of $^{129}I(n,2n)$ and the effective production cross section of ^{130}I produced by the $^{129}I(n,\gamma)^{130}I$ reaction, including the contribution of $^{129}I(n,\gamma)^{130m}I$ reaction were obtained with foil activation method, that is evaluated as 1.1 ± 0.1 b and 0.032 ± 0.003 b, respectively at 14.8 MeV, though the errors caused by the uncertainty of γ decay scheme data still existed. The measured cross sections were compared with the evaluated nuclear data of JENDL.-3.2 and ENDF/B-VI. For the $^{129}I(n,2n)$ reaction, the evaluations overestimate the cross section by $30 \sim 40$ %, while for the $^{129}I(n,\gamma)$ reaction, the evaluations underestimate by at least one order of magnitude. Also nothing but the above two reactions was found in this measurement, we, therefore, presume that especially for the reactions of (n,p) and (n,α), the evaluation may underestimate their cross sections.

References

[1] H.Sekimoto and T.Osawa(Ed.), *J.At.Energy Soc.Japan* 37[3], 159(1995)

[2] T.Sekine,et al., *J.Nucl.Sci.Technol.*, 30[11], 1099(1993)

[3] H.Harada,et al., ibid., 31[3], 173(1994)

[4] T.Katoh,et al., *Proc.Int.Conf.on Nuclear Data for Science and Technology*, Gatlinburg,230(1994),ORNL

[5] C.M.Lederer and V.S.Shirley(Ed.), *"Table of Isotopers, Seventh Edition"*, John Wiley & Sons, Inc.,New York(1978)

The First Internet Symposium on Nuclear Data: Paper No. 017

3.17 A systematic study of even-even nuclei in the nuclear chart by the relativistic mean field theory

K. Sumiyoshi[1], D. Hirata[2], I. Tanihata, Y. Sugahara and H. Toki[3]
The Institute of Physical and Chemical Research (RIKEN)
Hirosawa, Wako, Saitama 351-01, Japan
E-mail : sumi@postman.riken.go.jp

We study systematically the properties of nuclei in the whole mass range up to the drip lines by the relativistic mean field (RMF) theory with deformations as a microscopic framework to provide the data of nuclear structure in the nuclear chart. The RMF theory is a phenomenological many-body framework, in which the self-consistent equations for nucleons and mesons are solved with arbitrary deformation, and has a potential ability to provide all the essential information of nuclear structure such as masses, radii and deformations together with single particle states and wave functions from the effective lagrangian containing nuclear interaction.

As a first step toward the whole project, we study the ground state properties of even-even nuclei ranging from Z=8 to Z=120 up to the proton and neutron drip lines in the RMF theory. We adopt the parameter set TMA, which has been determined by the experimental masses and charge radii in a wide mass range, for the effective lagrangian of the RMF theory. We take into account the axially symmetric deformation using the constrained method on the quadrupole moment. We provide the properties of all even-even nuclei with all the possible ground state deformations extracted from the deformation energy curves by the constrained calculations. By studying the calculated ground state properties systematically, we aim to explore the general trend of masses, radii and deformations in the whole region of the nuclear chart. We discuss the agreement with experimental data and the predictions such as magicness and triaxial deformations beyond the experimental frontier.

1 Introduction

The recent advance at the radioactive nuclear beam facilities such as the one in RIKEN provides us with an increasing number of information on unstable nuclei far away from the stability line. We are having the experimental data such as masses, radii and deformations of unstable nuclei in a wider region of the nuclear chart than before. The studies

---

[1]Also: Max-Planck-Institut für Astrophysik (MPA), Karl-Schwarzschild-Str. 1, 85740 Garching, Germany

[2]Also: Japan Synchrotron Radiation Research Institute (JASRI) - SPring-8, Kamigori, Hyogo, 678-12, Japan

[3]Also: Research Center for Nuclear Physics (RCNP), Osaka University, Mihogaoka, Ibaraki, Osaka 567, Japan

of exotic nuclei with those data have revealed the novel phenomena such as neutron halos /1/ and neutron skins /2/ and bring new findings in nuclear physics /3//4/. Having experimental efforts toward the drip lines in the nuclear chart, it is extremely interesting to exploit the general feature of the nuclear properties in the whole region of the nuclear chart starting from a reliable many body framework.

Recently, there has been a great progress in the relativistic many body framework /5/. Among them, the relativistic mean field (RMF) theory, which is a phenomenological model based on the recent success of the relativistic Brueckner Hartree Fock theory /6/, has been successfully applied to the description of various ground state properties of nuclei. It has been shown that the RMF theory reproduces the properties of stable nuclei in a wide mass range of the periodic table /7//8/. It is also remarkable that the RMF theory reproduces the properties of unstable nuclei far away from stability as well as stable ones /9//10//11/. The RMF theory has been also applied successfully to the description of the deformation properties as well as other properties both for stable and unstable nuclei /12/. The equilibrium shapes of unstable nuclei are investigated through the comparisons with the experimental information on deformations and the shape coexistence is predicted for some nuclei and the change of shapes between prolate and oblate ones along isotopes is explored /13/.

Unfortunately, most of the RMF studies on deformed nuclei so far have been made for a limited region of nuclides in the nuclear chart such as a series of isotopes due to the lack of the experimental data and the computational power. In order to clarify the systematics of the shape coexistence and the shape transition of nuclei together with the behavior of other properties such as masses, charge radii and neutron skins, fully systematic study of deformed nuclei in the RMF theory is clearly required for nuclides in the whole region of the nuclear chart, especially for unstable nuclei away from stability. Having this aim of understanding the general trend of nuclear properties in the nuclear chart, we study the ground state properties of about 2000 even-even nuclei up to the drip lines in the relativistic mean field (RMF) theory with axial deformation. We perform constrained calculations of ground state deformations for all the even-even nuclei from oxygen isotopes to superheavy isotopes up to the proton and neutron drip lines using the supercomputer VPP500 at RIKEN. We tabulate the nuclear properties for all the possible ground state deformations extracted by the constrained calculations of all nuclei.

2 The relativistic mean field theory

In the RMF theory, the system of nucleons is described by the fields of mesons and nucleons under the mean field approximation /5/. Strong interaction between nucleons is mediated by the mesons, which are created in turn by the existence of nucleons. We start with the effective lagrangian, which is relativistically covariant, composed of meson and nucleon fields. We adopt the lagrangian with the non-linear σ and ω terms based on the relativistic Brueckner Hartree Fork theory /11/ as follows,

$$
\begin{aligned}
\mathcal{L} =\ & \overline{\psi}[i\gamma^{\mu}\partial_{\mu} - M]\psi + \frac{1}{2}\partial_{\mu}\sigma\partial^{\mu}\sigma - \frac{1}{2}m_{\sigma}^{2}\sigma^{2} - \frac{1}{3}g_{3}\sigma^{3} - \frac{1}{4}g_{4}\sigma^{4} - g_{\sigma}\overline{\psi}\psi\sigma \\
& -\frac{1}{4}H_{\mu\nu}H^{\mu\nu} + \frac{1}{2}m_{\omega}^{2}\omega_{\mu}\omega^{\mu} + \frac{1}{4}c_{3}(\omega_{\mu}\omega^{\mu})^{2} - g_{\omega}\overline{\psi}\gamma_{\mu}\psi\omega^{\mu} \\
& -\frac{1}{4}G_{\mu\nu}^{a}G^{a\mu\nu} + \frac{1}{2}m_{\rho}^{2}\rho_{\mu}^{a}\rho^{a\mu} - g_{\rho}\overline{\psi}\gamma_{\mu}\tau^{a}\psi\rho^{a\mu}
\end{aligned}
$$

$$-\frac{1}{4}F_{\mu\nu}F^{\mu\nu} - e\overline{\psi}\gamma_\mu\frac{(1-\tau^3)}{2}\psi A^\mu,$$

where the notation follows the standard one. Deriving the Euler-Lagrange equations from the lagrangian under the mean field approximation, we get a set of the Dirac equation for nucleons and the Klein-Gordon equations for mesons. We solve self-consistently the Dirac equations and the Klein-Gordon equations by expanding the fields in terms of the harmonic oscillator wave functions.

The RMF theory contains the meson masses, the meson-nucleon coupling constants and the meson self-coupling constants as parameters. We adopt the parameter set TMA, which was determined by fitting the experimental data of masses and charge radii in a wide mass range /14/. A novel feature of this parameter set is the mass dependence so as to reproduce nuclear properties quantitatively from the light mass region to the superheavy region. In order to take into account the axially symmetric deformation, we expand the fields in terms of the eigenfunctions of a deformed axially symmetric harmonic oscillator potential. We perform the constrained calculations on the quadrupole moment of the nucleon distribution to survey the coexistence of multiple shapes /15/. We use the quadratic constraint to get full curves of the energy surface due to the axial deformation.

Since it turns out that many nuclides have several solutions with different equilibrium deformations and similar binding energies, it is hard to choose the ground state configuration uniquely and it is rather interesting to explore the shape coexistence and the indication of other type of deformation. We extract all the possible equilibrium deformations from the energy curves obtained by the constrained calculations. We then perform non-constrained calculations starting from the deformation parameter of all the selected minima as an initial guess and obtain the physical quantities as final values. We tabulate the quantities thus obtained for all the minima for all nuclide. In order to explore the general trend of the table of nuclear properties and to compare them with the experimental data, we need to choose a solution from multiple solutions. In the following analysis, we select a solution which has the absolute minimum among the multiple solutions whenever they are available. The analysis on the systematics of multiple solutions without doing any selection of minima is currently being made /16/.

3 Calculated nuclear properties

The rms deviation of the masses from experimental data turns out to be within 3 MeV. The agreement with experimental data is fairly good taking account of the fact that the nuclear masses are calculated by the self-consitent many body framework starting from the effective lagrangian. We note that the number of free parameters in the present framework is 14. It is also worth mentioning that the present calculation with the parameter set TMA reproduces the binding energy of Fe, which is the most bound nuclide and has not been reproduced in the previous RMF calculations.

We show in Figure 1 the deformation parameter of the proton distribution in the nuclear chart. Patterns of prolate and oblate region can be seen generally. The characteristic of the neutron magic number is preserved having spherical shapes except for the neutron rich nuclei with N=20, 28, 50 where the deformed shapes appear. The proton magic numbers Z=50, 82 lose their characteristic in the regions away from the neutron magic numbers. Several lines along N=70 close to the neutron drip line, N=138, 184, 198 around Z=82, and Z=58, 92 around N=82, 126, 184 can be seen suggesting magicness.
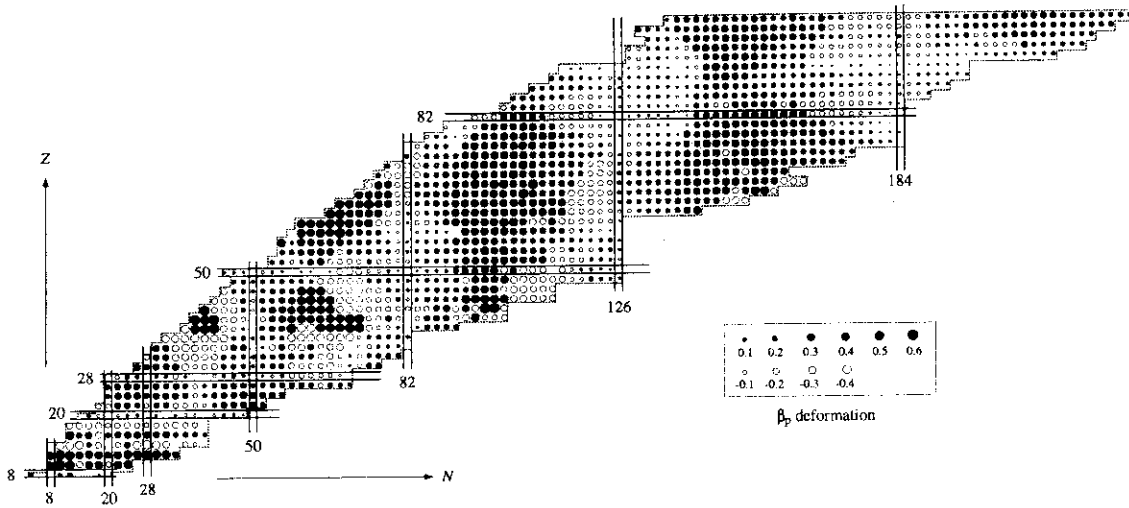
Figure 1: *The deformation in the N-Z plane. The prolate and oblate shapes are denoted by closed and open circles, respectively, in the scale shown in the legend.*

For lighter mass region, the shape tends to change depending on the proton number. For heavier mass region, the prolate shape dominates the region away from the magic numbers. The oblate shape tends to appear the left side of the neutron magic numbers and in some regions close to the neutron drip line. It is interesting to see that there is a strong deformed region around $Z=38$, 40, 42 with $N=38$, 60, which are suggested to be deformed magic numbers by the experiments /4/.

Figure 2 shows the thickness of neutron (proton) skin defined as the difference between the root-mean-square radii of neutron and proton distributions in the nuclear chart. The thick neutron skin is seen generally for nuclei in the neutron rich region away from the stability. The thickness can be as large as 1 fm for very neutron rich nuclei close to the neutron drip line. The proton skin can be found only for proton rich nuclei around the proton drip line in the light mass region.

Detailed analysis on the systematics of the present tabulation and more extensive comparisons with the experimental data and the other theoretical mass tables will be published elsewhere /16/. Possible triaxial deformations are also being studied in the triaxial RMF code in the cases of the coexistence of prolate and oblate deformations observed in the present study /13/. It is to be noted that the calculated mass table covering the nuclear chart in the present study has a profound implication to astrophysical problems such as the determination of the nuclides in the outer crust of neutron stars and the path of r-process nucleosynthesis. These astrophysical applications are currently being made /17/.

4 Summary

We have done the calculation of the ground state properties of about 2000 even-even nuclei ranging from $Z=8$ to $Z=120$ up to the proton and neutron drip lines in the relativistic mean field (RMF) theory. As far as we know, the present work is the first microscopic and selfconsistent calculation covering all the even-even nuclides up to both
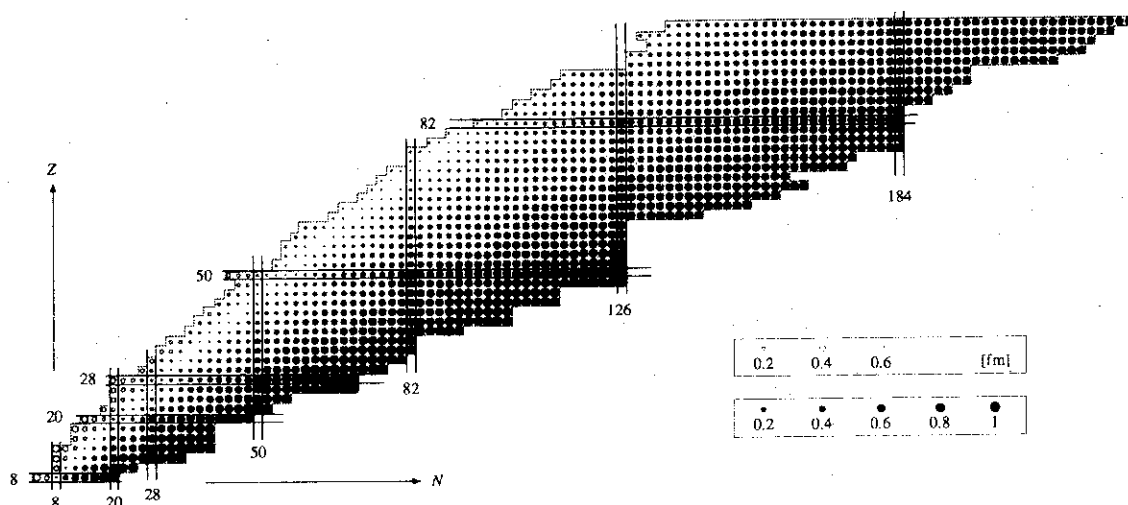
Figure 2: *The difference between the rms radii of neutron and proton distributions in the N-Z plane. The neutron and proton skins are denoted by closed and open circles, respectively, in the scale shown in the legend.*

the proton and neutron drip lines. We take into account the axially symmetric deformation using the constrained method with the deformation parameter. We extract all the possible ground state deformations from the deformation energy curves obtained by the constrained calculations. We adopt the parameter set TMA, which has been determined by the experimental masses and charge radii in a wide mass range, for the effective lagrangian of the RMF theory. We have tabulated the calculated nuclear properties for all equilibrium deformations of all even-even nuclei. We have explored the general trend of masses, radii and deformations in the whole region of the nuclear chart. We have discussed the agreement with experimental data and predictions such as magicness beyond the experimental frontier.

Acknowledgment

References

[1] I. Tanihata, H. Hamagaki, O. Hashimoto, Y. Shida, N. Yoshikawa, K. Sugimoto, O. Yamakawa, T. Kobayashi & N. Takahashi, *Phys. Rev. Lett.*, **55** (1985) 2676.

[2] I. Tanihata, D. Hirata, T. Kobayashi, S. Shimoura, K. Sugimoto & H. Toki, *Phys. Lett.*, **B289** (1992) 261.

[3] I. Tanihata, in *Treatise on Heavy Ion Science*, Plenum, New York, **8** (1989) 443.

[4] J. H. Hamilton, in *Treatise on Heavy Ion Science*, Plenum, New York, **8** (1989) 3.

[5] B. D. Serot & J. D. Walecka, *Adv. Nucl. Phys.*, **16** (1986) 1.

[6] R. Brockmann & R. Machleidt, *Phys. Rev.*, **C42** (1990) 1965.

[7] P.-G. Reinhard, M. Rufa, J. Maruhn, W. Greiner & J. Friedrich, *Z. Phys.*, **A323** (1986) 13.

[8] Y. K. Gambhir, P. Ring & A. Thimet, *Ann. of Phys.*, **198** (1990) 132.

[9] D. Hirata, H. Toki, T. Watabe, I. Tanihata, B. V. Carlson, *Phys. Rev.*, **C44** (1991) 1467.

[10] K. Sumiyoshi, D. Hirata, H. Toki & H. Sagawa, *Nucl. Phys.*, **A552** (1993) 437.

[11] Y. Sugahara & H. Toki, *Nucl. Phys.*, **A579** (1994) 557.

[12] D. Hirata, H. Toki, I. Tanihata & P. Ring, *Phys. Lett.*, **B314** (1993) 168.

[13] D. Hirata, K. Sumiyoshi, B. V. Carlson, H. Toki & I. Tanihata, submitted to *Nucl. Phys.*, **A**.

[14] Y. Sugahara, *Doctor thesis*, Tokyo Metropolitan University (1995).; Y. Sugahara & H. Toki, in preparation.

[15] H. Flocard, P. Quentin, A. K. Kerman & D. Vautherin, *Nucl. Phys.*, **A203** (1973) 433.

[16] D. Hirata, K. Sumiyoshi, Y. Sugahara, H. Toki & I. Tanihata, in preparation.

[17] K. Sumiyoshi, T. Tachibana, D. Hirata, Y. Sugahara, H. Toki & I. Tanihata, in preparation.

The First Internet Symposium on Nuclear Data: Paper No.18

3.18 Measurement of Formation Cross Sections of short-lived nuclei by 14 MeV neutron —Nd, Sm, Dy, Er, Yb—

H. Sakane, T. Iida*, A. Takahashi*, H. Yamamoto and K. Kawade
Department of Nuclear Engineering, Nagoya University,
Furo-cho, Chikusa-ku, Nagoya 464-01, Japan
*Department of Nuclear Engineering, Osaka University,
Yamadaoka, Suita-shi, Osaka 565, Japan
e-mail: h956319m@eds.ecip.nagoya-u.ac.jp

Eight neutron activation cross sections producing the nuclei with half-lives between 3 min and 24 min were obtained at the energy range between 13.4 and 14.9 MeV by activation method. The cross sections were $^{146}Nd(n,p)^{146}Pr$, $^{154}Sm(n,\alpha)^{151}Nd$, $^{162}Dy(n,p)^{162}Tb$, $^{163}Dy(n,np)^{162}Tb$, $^{163}Dy(n,p)^{163}Tb$, $^{164}Dy(n,p)^{164}Tb$, $^{170}Er(n,\alpha)^{167}Dy$, $^{174}Yb(n,p)^{170}Tm$. $^{163}Dy(n,np)^{162}Tb$ ($T_{1/2}=7.7$ min) was obtained for the first time. Present results are compared with previous results and the evaluated data of JENDL-3 and ENDF/B-VI. There are some discrepancies between present results and the JENDL-3 and ENDF/B-VI.

1 Introduction

Neutron activation cross section data around 14 MeV have become important from the view point of fusion reactor technology, especially for calculations on radiation damage, nuclear transmutation, induced activity and so on. However the cross section data have not often been measured in reasonable accuracy, or there are no available data on some reactions because of difficulty in measuring short-lived activities. As a result, the evaluated data will not be unreliable. We have been measuring activation cross sections of short-lived nuclei by 14 MeV neutron at the Intense 14 MeV Neutron Source Facility (OKTAVIAN) of Osaka University. In this work eight cross sections for the (n,p),(n,np) and (n,α) reaction leading to short-lived nuclei with half-lives between 3 min and 24 min were measured in a qualified experimental condition. [1-4]

2 Experiment

2.1 Irradiation and flux determination

The D-T neutrons were generated by bombarding Ti-^{3}T mounted in a rotating target with d$^+$ beam of 5 mA and 300 keV using the OKTAVIAN facility at Osaka University. A peneumatic sample transport system was used for the irradiation of samples. The angles of the irradiation position to the d$^+$ beam were 0°, 55°, 75°, 105°, 125° and 155°, which covered the neutron energies ranging from 14.9 to 13.7 MeV. Another peneumatic tube was also set at −105° to examine the the arrangement of peneumatic; if the pneumatic tubes were correctly set, the obtained cross sections by the irradiation at 105° and −105° show good agreement. The distance between T-target and irradiation position was 15 cm. Typical neutron fluxes at each irradiation position were 0.9-1.5 $\times 10^8 n/\text{cm}^2/\text{s}$. An additional tube at the distance of 1.5 cm from the T-target were used for making the intense activity to calibrate HPGe detectors. The ratio of neutron flux at 1.5 cm to 15 cm was about 50. The neutron flux at the sample position was measured with use of the ^{27}Al(n,p)^{27}Mg reaction. The cross section was ^{27}Al(n,p)^{27}Mg were determined by referring to the standarded ^{27}Al(n,α)^{24}Na reactions. The samples were sandwiched by two Al foils of 10 mm $\times$ 10 mm and 0.2 mm in thickness. The fluctuation of neutron flux were monitored at an intarvals of 3 s by a fission counter. The effective neutron enregy of incident neutrons at each irraadiation position was determined by the reaction ratio of ^{93}Zr(n,2n)^{92}Zr to that of ^{93}Nb(n,2n)^{92m}Nb (Nb/Zr method).

2.2 Sample preparation

Mass separated isotopes from the Oak Ridge National Laboratory and natural abundance were used as samples. Powder samples were wrapped in powder papers (each sample size: 10/$times$10 mm and about 1 mm in thickness; sample masses: 20-70 mg). The foil samples were rectangular-shaped 10×10 mm and 0.1-0.2 mm in thickness.

2.3 Activity measurement

Gamma-ray emitted from the irradiated samples and Al were measured with 12% and 16% HPGe detectors. Each detector covered with a 5 mm thick acrylic absorber in order to reduce beta-rays, and the acrylic-spacer with length at 4.5 cm were also put on the detector. We call it staderd position. The distance between the standard position and the surface of detector is 5.0 cm. The full-energy peak efficiencies at standard position were calibrated with standard sources of ^{152}Eu, ^{133}Ba, ^{60}Co, ^{24}Na, ^{56}Co. Coincidence summing effect were taken into considertion. The efficiency data between 50-340 keV were fitted with a function with 6-fitting-parameter, and those between 340-3000 keV were fitted with

a function with 7-fitting-parameter. The errror in the efficency curves are estimated to be 1.5% above 300 keV, 3% between 80 and 300 keV and 5% below 80 keV. The irradiated samples were put at close position without the acrylic spacer in order to obtain good statistics. To obtain the efficiency at close position, an extra sample with the same form as other samples was irradiated with rather strong neutron flux by using calibration pneumatic tube. This sample was used for efficiency calibration between the standard position and close position. The detector efficiency at close position are larger than that at standard position by a factor of about seven.

2.4 Decay data

In Table 1, measured reactions of associated decay data of the half-life, the γ-ray energy and the absolute intensity in photons per disintegration are listed together with Q-values.

2.5 Corrections

Corrections were made for time fluctuation of neutron flux, thickness of samples, self absorption of γ-ray, sum-peak effect of ganma-ray and contribution of low energy neutrons below 10 MeV. The total errors δ_t were described by combining the experimental errors δ_e and the errors of nuclear data δ_r in quadratic: $\delta_t^2 = \delta_e^2 + \delta_r^2$. Accuracy of the obtained cross sections were around 4.5% in case of good statistics.

3 Results and discussion

Numerical data table of cross sections are given in Table 2. The graphs are given in Figs 1'8 together with the experimental data and the evaluation data of JENDL-3 and ENDF/B-VI. The cross sections of $^{163}Dy(n,np)^{162}Tb$ were obtained for the first time. The cross sections of $^{146}Nd(n,p)^{146}Pr$, $^{154}Sm(n,\alpha)^{151}Nd$, $^{162}Dy(n,p)^{162}Tb$, $^{163}Dy(n,p)^{163}Tb$, $^{170}Er(n,\alpha)^{167}Dy$, $^{174}Yb(n,p)^{170}Tm$ were obtained at six energy points between 13.4-14.9 Mev, although the previous results had been obtained at one energy point. Present results are compared with the evaluation data of JENDL-3 and ENDF/B-VI. The evaluations of JENDL-3 for $^{162}Dy(n,p)^{162}Tb$, $^{163}Dy(n,p)^{163}Tb$, and $^{164}Dy(n,p)^{164}Tb$ agree reasonably well with experimental results. The evaluation of JENDL-3 for $^{154}Sm(n,\alpha)^{151}Nd$ is 40% larger. The JENDL-3 for $^{163}Dy(n,np)^{162}Tb$ is about 1/6 of experimental result. The slope of excitation function of JENDL-3 for $^{170}Er(n,a)^{167}Dy$ is about 1/5. The evaluation ENDF/B-VI for $^{146}Nd(n,p)^{146}Pr$ is about 1/4. The slope of ENDF/B-VI for $^{164}Dy(n,p)^{164}Tb$ is about 1/7.

4 Conclusion

Eight activation cross sections were obtained. There are some discrepancies between present results and the evaluation data of JENDL-3 and ENDF/B-VI. Re-evaluations for these reactions are needed.

5 REFERENCES

[1] T.Katoh et al. JAERI-M 89-083 (1989) (in Japanese)
[2] K.Kawade et al. JAERI-M 90-171 (1990)
[3] K.Kawade et al. JAERI-M 92-020 (1992)
[4] K.Kawade et al. JAERI-M 93-124 (1993)

Table 1: Measured reactions and decay parameters.

Reaction	$T_{1/2}$	E_γ(keV)	I_γ(%)	Q(MeV)
146Nd(n,p)146Pr	24.15(18)m	453.89	48.0(24)	-3.37
154Sm(n,α)151Nd	12.44(7)m	116.71	46.8(18)	4.14
162Dy(n,p)162Tb	7.7(2)m	260.080	79(5)	-1.75
163Dy(n,np)162Tb [a]	7.7(2)m	260.080	79(5)	-1.75 [b]
163Dy(n,p)163Tb	19.5(3)m	351.25	26(3)	-8.02
164Dy(n,p)164Tb	3.0(1)m	168.829	24.0(12)	-3.07
170Er(n,α)167Dy	6.20(8)m	569.66	48(2)	5.47
174Yb(n,p)174Tm	5.4(1)m	366.6	92(4)	-2.31
27Al(n,α)24Na [c]	14.959(4)h	1368.6	99.994(3)	-3.13
27Al(n,p)27Mg [d]	9.462(11)m	843.8	72.0(4)	-1.83

a) (n,np) means [(n,d)+(n,n'p)+(n,pn)]

b) Q(n,n'p) is given here. Q(n,d)=Q(n,n'p)+2.225MeV

c) Standard reaction (ENDF/B-V) used in this work.

d) Seceondary conventional reaction used for short-lived nuclei.

Table 2: Activation cross sections of short-lived nuclei

^{146}Nd(n,p)^{146}Pr (24.15m)					^{154}Sm(n,α)^{154}Nd(12.44m)				
En(MeV)	σ (mb)	δ e(%)	δ_r (%)	δ_t (%)	En(MeV)	σ (mb)	δ_e (%)	δ_r(%)	δ_t(%)
14.87	5.67	5.2	5.1	7.3	14.87	0.494	35	3.9	35
14.58	4.30	7.4	5.1	9.0	14.58	0.640	30	3.9	31
14.28	3.94	10	5.1	11	14.28	0.480	53	3.9	54
13.88	3.77	6.5	5.1	8.3	13.88	0.236	71	3.9	71
13.65	2.93	12	5.1	13	13.65	0.304	46	3.9	46
13.40	2.60	7.3	5.1	8.9	13.40	0.480	28	3.9	28
162Dy(n,p)162Tb(7.7m)					**163Dy(n,np)162Tb(7.7m)**				
En(MeV)	σ (mb)	δ e(%)	δ r(%)	δ t(%)	En(MeV)	σ (mb)	δ e(%)	δ r(%)	δ t(%)
14.87	4.54	4.5	6.3	7.7	14.87	0.678	14	6.3	15
14.58	3.92	4.8	6.3	7.9	14.58	0.668	15	6.3	17
14.28	3.74	6.4	6.3	8.9	14.28	0.495	22	6.3	23
13.88	3.06	5.0	6.3	8.0	13.88	0.233	38	6.3	39
13.65	2.55	5.7	6.3	8.5	13.65	0.168	55	6.3	55
13.40	2.24	6.0	6.3	8.7	13.40	0.124	66	6.3	66

163Dy(n,p)163Tb(19.5m)

En(MeV)	σ (mb)	δ e(%)	δ r(%)	δ t(%)
14.87	4.03	9.5	11.6	15
14.58	3.17	13	11.6	18
14.28	3.39	14	11.6	18
13.88	3.00	13	11.6	17
13.65	2.50	16	11.6	19
13.40	2.24	14	11.6	19

164Dy(n,p)164Tb(3.0m)

En(MeV)	σ (mb)	δ e(%)	δ r(%)	δ t(%)
14.87	2.81	24	6.0	25
14.58	2.63	30	6.0	25
14.28				
13.88				
13.65				
13.40				

^{170}Er(n,α)^{167}Dy(6.20m)

En(MeV)	σ (mb)	δ e(%)	δ r(%)	δ t(%)
14.87	1.52	18	4.2	18
14.58	1.18	21	4.2	21
14.28	1.03	36	4.2	37
13.88				
13.65	0.426	47	4.2	47
13.40	0.397	37	4.2	37

174Yb(n,p)174Tm(5.4m)

En(MeV)	σ (mb)	δ e(%)	δ r(%)	δ t(%)
14.87	3.19	5.0	4.4	6.7
14.58	2.94	5.4	4.4	7.0
14.28	2.52	7.6	4.4	8.8
13.88	2.14	6.1	4.4	7.5
13.65	1.62	8.0	4.4	9.1
13.40	1.45	7.5	4.4	8.7

Fig.1

Fig.2

^{162}Dy(n,p)^{162}Tb(7.7m)

Fig.3

^{163}Dy(n,np)^{162}Tb(7.7m)

Fig.4

^{163}DY(n,p)^{163}Tb(19.5m)

Fig.5

^{164}Dy(n,p)^{164}Tb(3.0m)
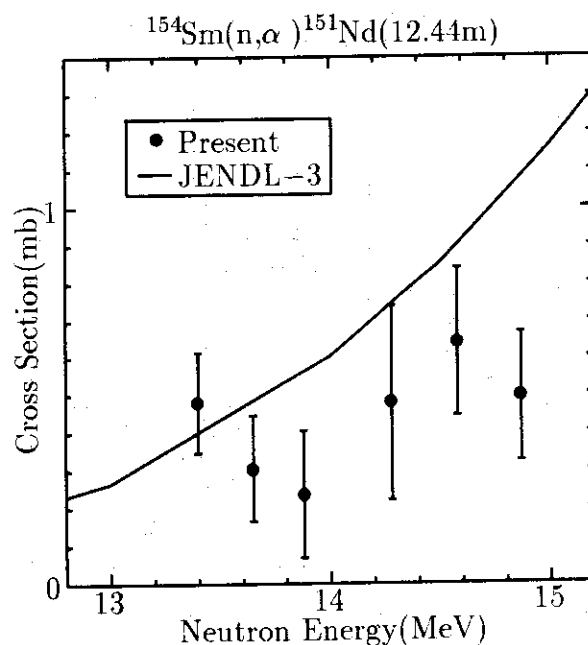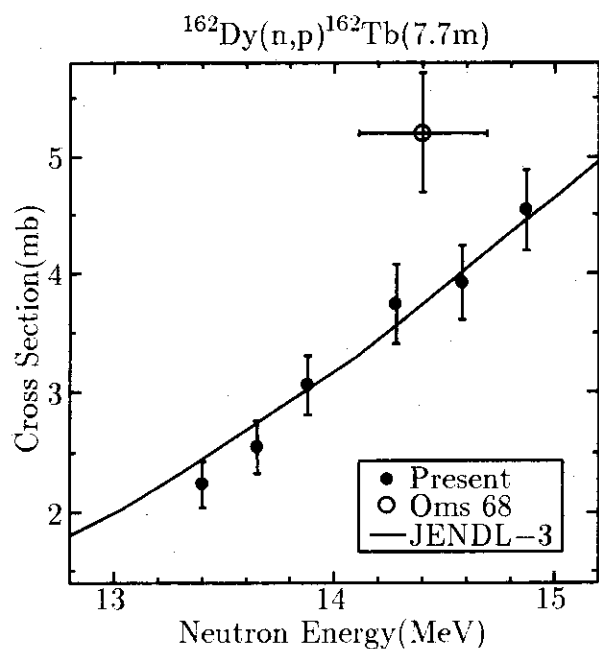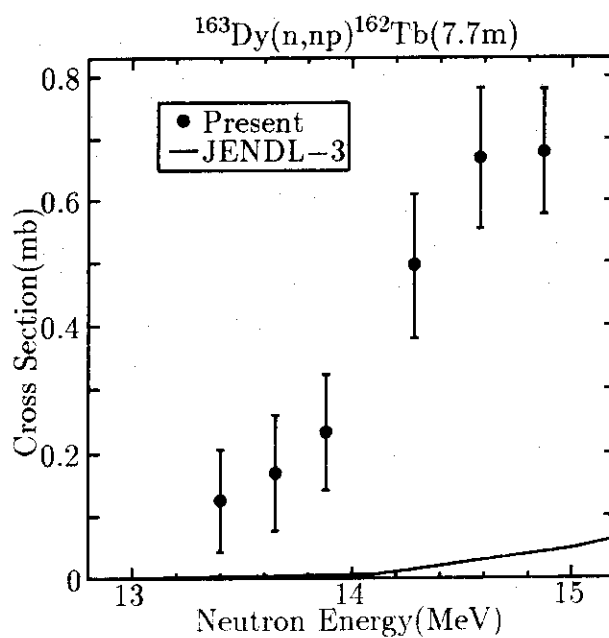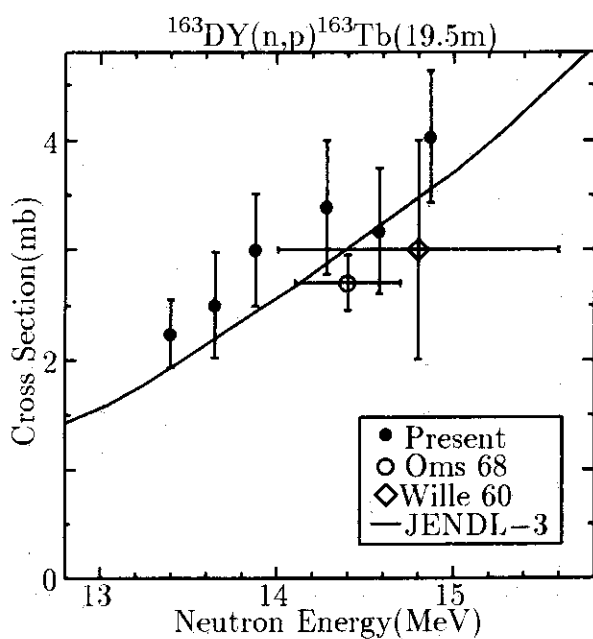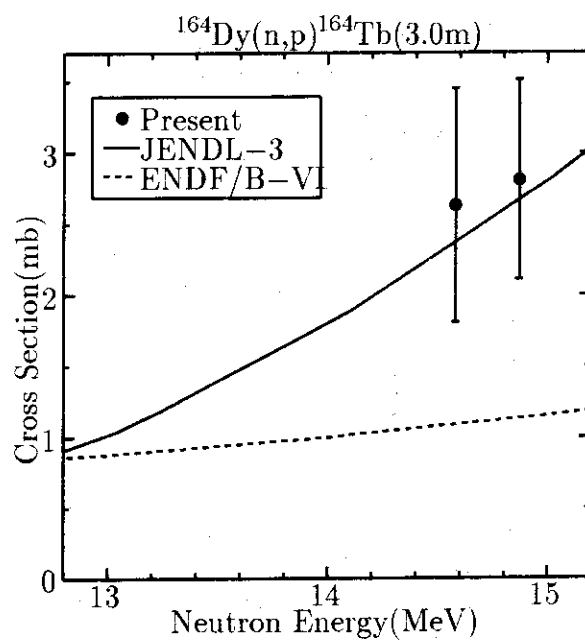
Fig.6
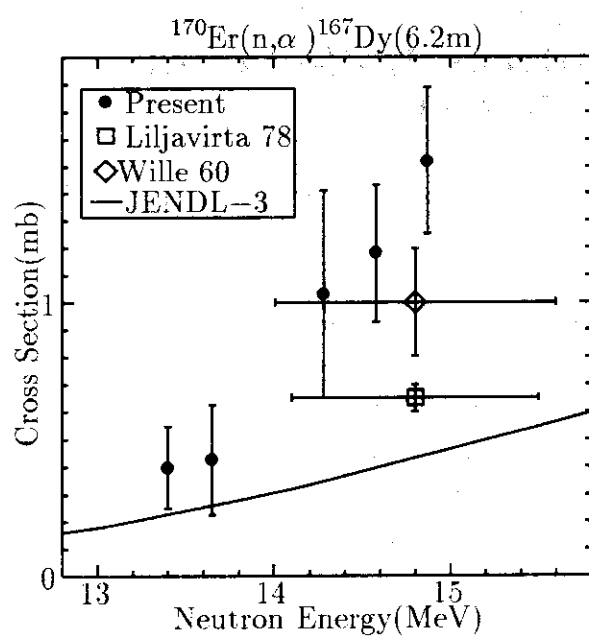
Fig.7
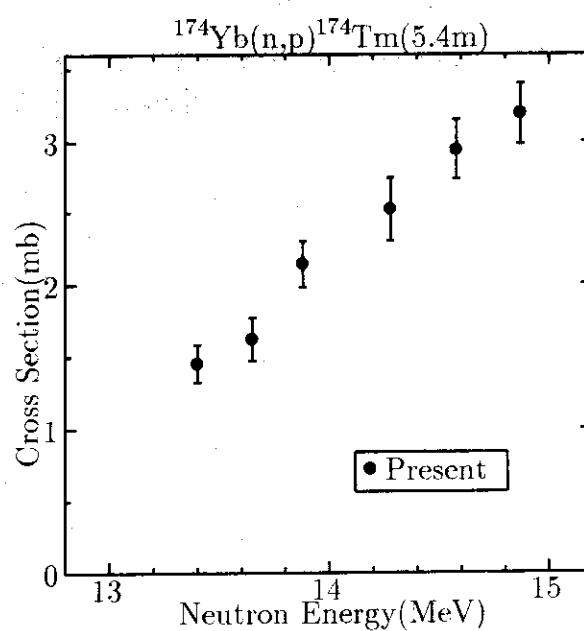
Fig.8

The First Internet Symposium on Nuclear Data: Paper No.19

3.19   Measurements of Beta-decay Half-lives of Short-lived Nuclei

T. Hirose, Y. Tsurita, H. Yamamoto, T. Iida*, A. Takahashi*, Y. Kasugai**, Y. Ikeda**
and K. Kawade

Department of Energy Engineering and Science, Nagoya University
Furo-cho, Chikusa-ku, Nagoya, 464-01, Japan
*Department of Nuclear Engineering, Osaka University
Yamadaoka, Suita-shi, Osaka, 565, Japan
**Japan Atomic Energy Research Institute
Tokai-mura, Naka-gun, Ibaraki-ken, 319-11, Japan
Email : h966425m@eds.ecip.nagoya-u.ac.jp

The β-decay half-lives of short-lived nuclei produced by 14 MeV neutron bombardments were measured with Ge detectors, a High-rate spectroscopy amplifier (EG&G ORTEC model 973) and a Spectrum multi-scaler (Laboratory equipment corporation SMS-48) in the multi-scaling mode. The adequate corrections for pile-up and dead-time losses were made by applying source and pulser methods. The half-lives of ^{53}V, ^{53g}Fe, ^{89m}Y and ^{162}Tb were determined with uncertainties of 0.13~0.65%. It has been shown that previous values shorter than 10 min were systematically longer than the present ones.

1   Introduction

The half-life is one of the most fundamental constants on radioactive isotopes. In the measurements of nuclear reaction cross sections with the activation method, the uncertainty of half-life values brings a strong effect to the results of the cross sections. However the previously published values of half-lives sometimes show the discrepancy much larger than the individual uncertainties. In order to improve the reliability of the half-lives of short-lived nuclei, the half-lives of ^{53}V, ^{53g}Fe, ^{89m}Y and ^{162}Tb with $T_{1/2}$=16 s~8.5 m were measured.

2   Experiment

Short-lived nuclei were produced by 14 MeV neutron bombardments. The 14 MeV neutrons were generated by the intense 14 MeV neutron generator of Osaka University (OKTAVIAN) and the facility of Fusion Neutronics Source (FNS) of JAERI. Fig. 1 displays a block diagram of the counting system. The γ-rays were measured with ORTEC

Ge detectors and the High-rate spectroscopy amplifier[1] to measure at high counting rate in the multi-scaling mode. In order to measure half-lives in the order of seconds (^{89m}Y), the spectrum multi-scaling was accomplished using the Spectrum multi-scaler (SMS) to reduce the data transfer time. Decay was followed for 5~10 times the half-life at equal intervals of 1/3 of the half-life.

It is necessary for precision determination of the half-lives that proper corrections for pile-up and dead-time losses are made since the counting rate greatly changes during the measuring time in the measurements of short-lived activities. A new method using reference source and constant-pulser has been developed by us[2]. The source method using reference γ-rays is reliable for corrections. Statistical fluctuations of the source, however, happen and the peak area evaluation of reference γ-rays might be effected by decaying compton backgrounds coming from short-lived nuclei of interest. On the other hand the pulser method[3] gives high degree of accuracy and no effect to γ-ray spectrum, but the peak shape of pulser is different from that of real γ-radiations and the constant-pulser produces no random pile-up pulse by itself. There might be some differences between both the methods. The variation in the peak intensity ratios of the reference source (^{60}Co) to the pulser was examined. As shown in Fig. 2, the ratios were well constant at high counting rate up to 80 kcps. It is considered that the measurement at the rate up to 80 kcps would be reliable. The decay curve was determined by the least squares fits in the range that the peak intensity ratios were constant, that is, the counting rate was less than 80 kcps.

3   Results and discussion

A γ-ray spectrum and decay curve of ^{53}V are shown in Fig. 3 and Fig. 4, respectively. The results are summarized in Table 1 together with production reactions, energy of measured γ-rays, reference sources, number of measurement and evaluation values[4]. The half-lives of ^{53}V, ^{53g}Fe, ^{89m}Y and ^{162}Tb were deduced with uncertainties of 0.13~0.65%. In Fig. 5-8, the results are compared with previous works[5, 6]. In Fig. 9, relative deviations of previous values from the present are shown. It is clearly seen that most of previous values shorter than about 10 min were longer than the present and our previous ones[2, 7-11]. Especially, the maximum of relative deviations of ^{53}V was found to be 9%. The cause might result from insufficient corrections for pile-up and dead-time losses. It is likely to start measurements at high counting rate to get good statistics during the short measuring time and the decay curve would show a longer half-life compared with the true value if the corrections are not enough.

4   Conclusion

It has been already recognized in our previous works that most of previous values shorter than 10 min were systematically longer than our measured ones. Since the

present results also showed the same tendency, it is needed to measure the half-lives of short-lived nuclei by applying adequate corrections.

References

[1] M. L. Simpson et al., IEEE Trans. Nucl. Sci. Vol. 38, No. 2, 89 (1991)

[2] M. Miyachi et al., Nucl. Data for Sci. and Tech., 897 (1988 Mito)

[3] O. U. Anders, Nucl. Instr. and Meth. 68, 205 (1969)

[4] R. B. Firestone and V. S. Shirley, Table of Isotopes 8th Ed., (1996) John Wiley & Sons, New York

[5] C. M. Lederer and V. S. Shirley, Table of Isotopes 7th Ed., (1978) John Wiley & Sons, New York

[6] Nuclear Data Sheets

[7] K. Kawade et al., JAERI-M 90-171 (1990)

[8] K. Kawade et al., JAERI-M 92-027, 364 (1992)

[9] S. Itoh et al., JAERI-M 94-019, 264 (1994)

[10] S. Itoh et al., JAERI-Conf 95-008, 185 (1995)

[11] T. Hirose et al., JAERI-Conf 96-008, 177 (1996)

Table 1: Results of half-life measurements.

Nuclide	Production Reaction	Energy (keV)	Reference Source[a]	Number of Measurement	Half-life	
					Present	Reference[b]
^{53}V	^{53}Cr(n,p)	1006.2	^{137}Cs	5	1.497(3) m	1.61(4) m
^{53g}Fe	^{54}Fe(n,2n)	377.9	^{57}Co	4	8.558(11) m	8.51(2) m
^{89m}Y	^{89}Y(n,n')	909.2	^{137}Cs	7	15.68(4) s	16.06(4) s
^{162}Tb	^{165}Ho(n,α)	260.1	^{57}Co	5	7.74(5) m	7.60(15) m

a) These sources were used for corrections of pile-up and dead-time losses.
b) Taken from ref. [4].
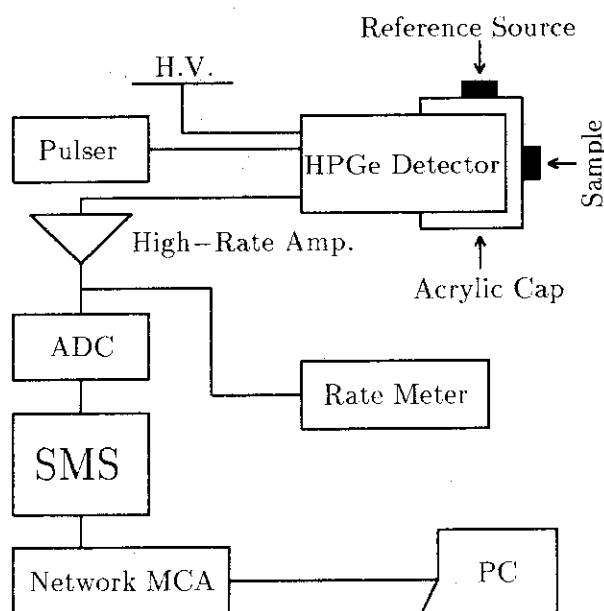
Fig. 1: Block diagram of the counting system.
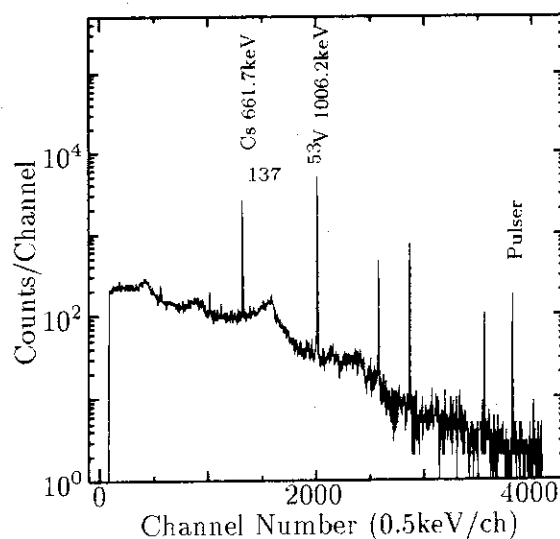
Fig. 3: Gamma-ray spectrum in the decay of ^{53}V.
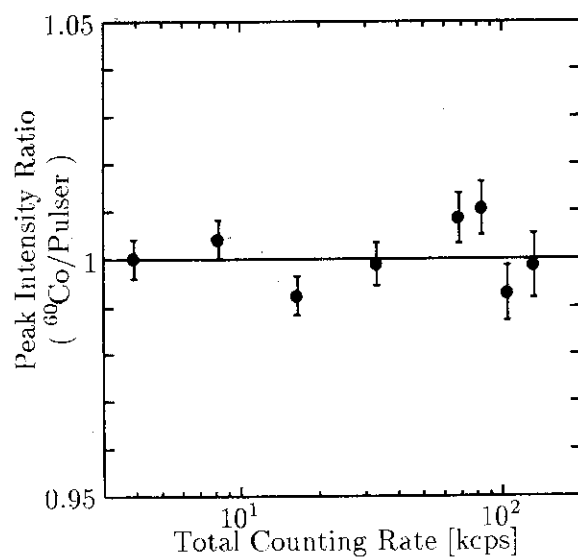
Fig. 2: Peak intensity ratios of reference source (^{60}Co) to pulser.
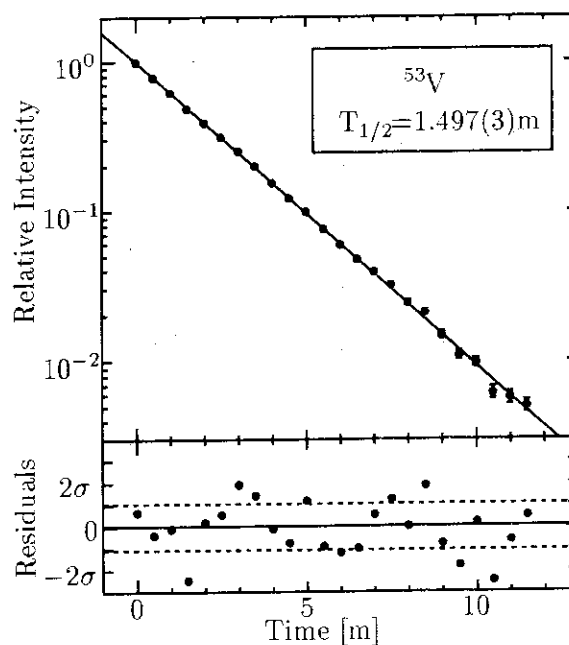
Fig. 4: Decay curve of ^{53}V and residuals from a least squares fitting analysis.
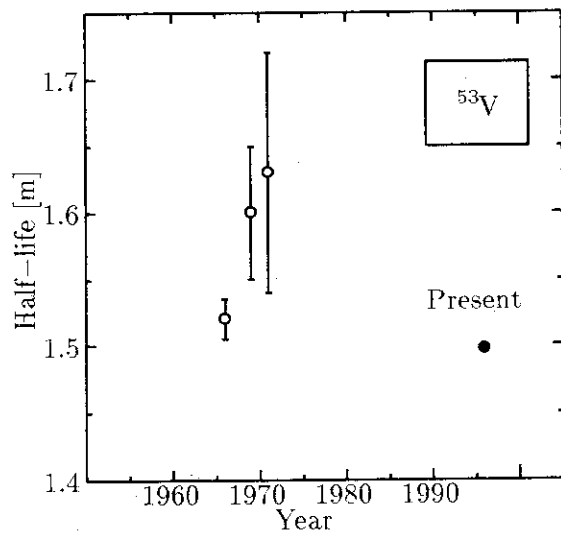
Fig. 5: Comparison with previous works taken from ref. [6].
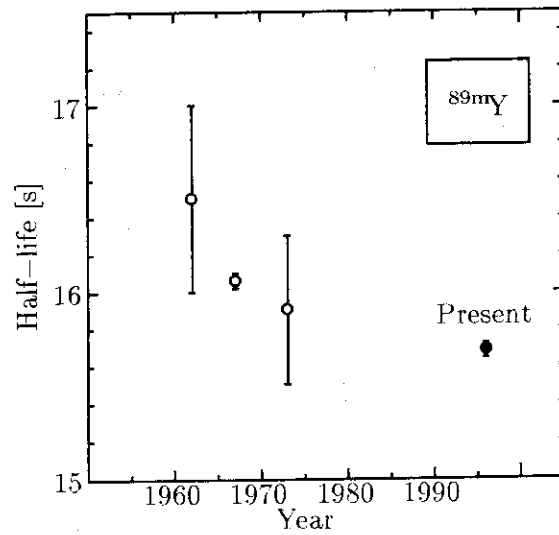
Fig. 7: Comparison with previous works taken from ref. [5].
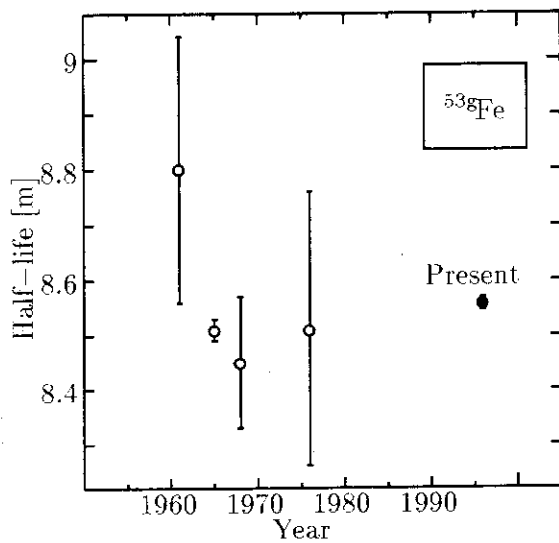
Fig. 6: Comparison with previous works taken from ref. [6].
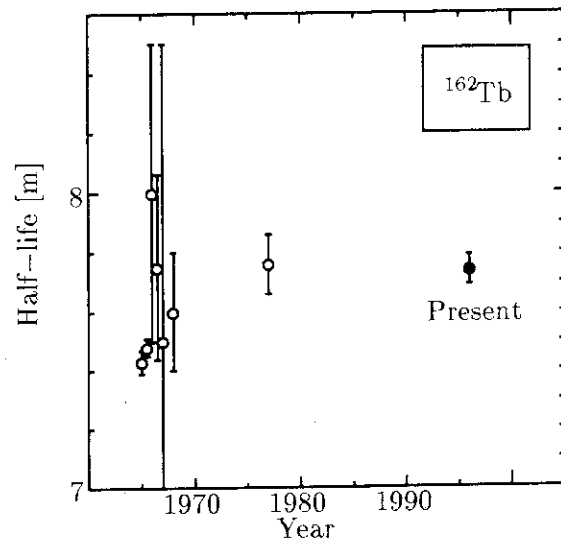
Fig. 8: Comparison with previous works taken from ref. [6].
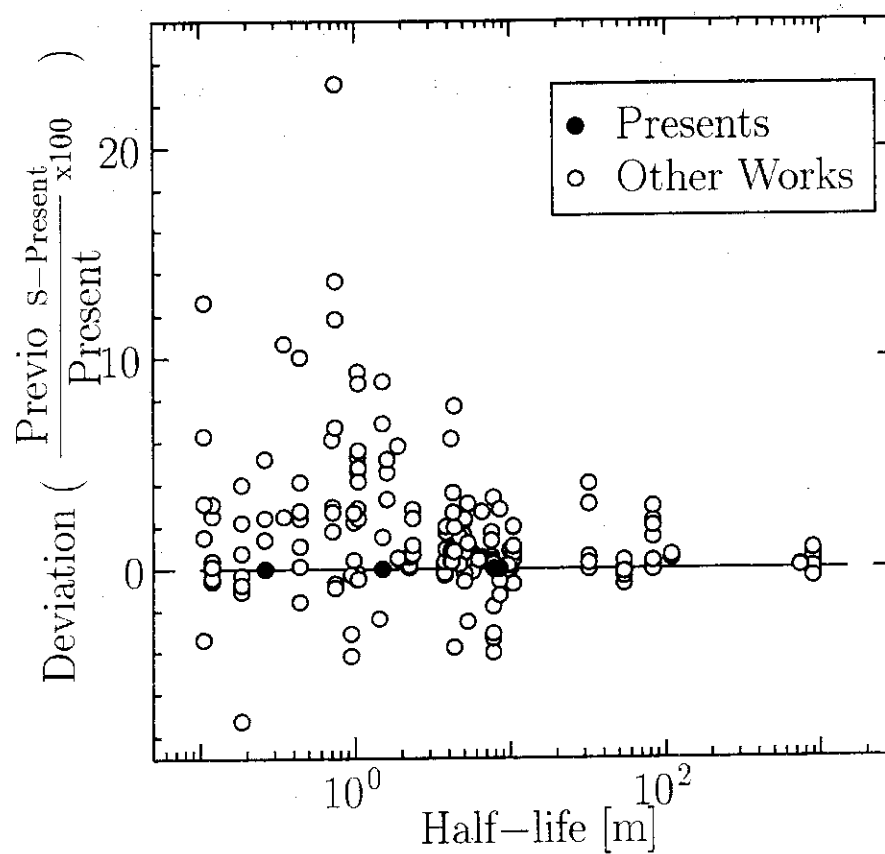
Fig. 9: Relative deviations of previous values from the present and our previous ones.

The First Internet Symposium on Nuclear Data: Paper No.020

3.20 Retrieval System of Nuclear Data for Transmutation of Nuclear Materials

Mitsutane FUJITA, Misako UTSUMI and Tetsuji NODA

National Research Institute for Metals

1-2-1, Sengen, Tsukuba, Ibaraki 305 Japan

Email : fujita@tamamo.nrim.go.jp

Abstract

A database storing the data on nuclear reaction was built to calculate for simulating transmutation behavious of materials /1/—/3/. In order to retrieve and maintain the database, the user interface for the data retrieval was developed where special knowledge on handling of the database or the machine structure is not required for end-user. It is indicated that using the database, the possibility of He formation and radioactivity in a material can be easily retrieved though the evaluation is qualitatively.

1 Introduction

In the data system for nuclear material design and selection used in various reactors, huge material databases and several kinds of tools for data analysis or simulation code of the phenomena under irradiation are required. The challenge of a computer-based simulation system for the transmutation, radio activation, decay-heat and biological hazard potential of materials is done, since the simulation of the phenomenon under neutron irradiation is important in view of alloy design and selection of materials used in various reactors. A database storing the data on nuclear reaction needs to calculate of the simulation. In the database for nuclear reaction, the data of nuclear reaction for material design is stored and we can understand qualitatively the behavior of nuclear reaction such as the transmutation or decay. The database is required for the friend user-interface for the retrieval of necessary data. In the paper, features and functions of the developed system are described and especially, examples of the easy accessible search of material properties are introduced.

2 Outline of the nuclide database for nuclear materials

2.1 Data collection

Various data, which are required for simulation on nuclear reaction, have been collected from reports as follows.

Element Table
Atomic number
Element
Number of isotopes
Atomic weight
Density

Isotope Table
Element
Atomic number
Isotope
Mass number
Number of nuclear reaction data
Abundance ratio
Judge stable or unstable
Half-life
Unit of time
Exposure rate constant
Decay constant(λ)
Permissible concentration in air
Decay heat
Judge metastable or not
Decay product
Mode of Decay
Branching ratio

Transmutation Table
Element
Isotope
Transmutation
Produced nuclide
Transmutation No
Number of data
Number of data
Number of energy group
Reference
Published year

Spontaneous Decay Table
Isotope
Decay mode
Branching ratio
Remark

Cross Section Table
Transmutation No
Level 1
Level 2
Level 3
Level 4
Level 5

γ Energy Table
Isotope
E(γ)
I(γ)
E(γ)×I(γ)/100
E(γ)×I(γ)/100×μ(E(γ))

Decay mode Table
Mass number
Number of isotopes
Number of stable isotopes
Number of metastable isotopes

β⁺,β⁻ or α Energy Table
Isotope
Decay mode
E(β⁺,β⁻or α)
I(β⁺,β⁻or α)
E(β⁺,β⁻or α)×I(β⁺,β⁻or α)/100

Figure 1: Data structure of the database for nuclear reaction.

1. Nuclear data such as neutron cross-section are collected from JAERI's CRROSLIB, ENDF/B-6, JENDL-3 and FENDL 1.1. The number of element stored in the database is 54 at present, however, this will increase to be 89 in near future.

2. The data on element and isotope are collected from

   - "Table of Radioactive Isotopes" E. Browne and R. B. Firestone,1986, LBLU of C, John Wiley & Sons,

   - "Chart of the Nuclides" compiled by Y. Yoshizaw and T. Horiguchi and M. Yamada, 1980, JNDC and NDC in JAERI.

2.2 Database system

In the nuclide database, the data of nuclear reaction for material design is stored and we can understand qualitatively the behavior of nuclear reaction such as the transmutation or decay. The database is managed by 4th Dimension where RDBMS (relational database management system) is supported on the PC (Macintosh). The RDBMS and PC were selected to be able to build the friend user-interface for the retrieval of necessary data.

2.3 Data structure

The database consists of five main tables and three supplemental tables, as shown Fig. 1. Main tables are element, isotope, spontaneous decay, transmutation and cross section
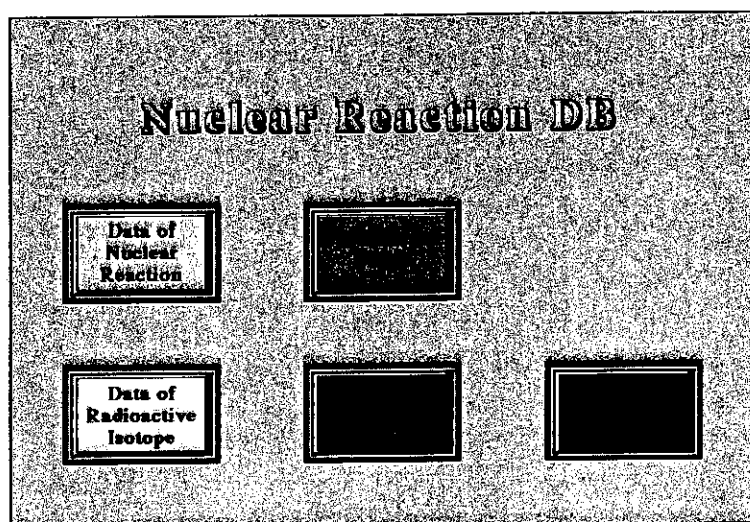
Figure 2: Opening screen of the nuclear reaction database.

table. The element table has the data such as element name, atomic weight and etc. These data are input values obtained from ordinary periodic table. The data in the isotope table consist of the natural abundance ratio, half-life data, gamma-ray or beta-ray energy and maximum permissible concentration in air (MPC), which are taken from isotope table. The spontaneous decay table has the data of decay mode and branching ratio. The transmutation table has the data of transmutation process, produced nuclide and etc.. The neutron cross-section table stores the data with 42-energy group covering from thermal neutron energy to 15MeV. The supplemental tables are three kinds of spontaneous decay, decay mode, gamma energy and beta or alpha. These tables play the roles due to aid the retrieval and the calculation of decay heat. Both tables are related by a certain unique key mutually.

3 Functions and user-interface

3.1 Functions

Fig. 2 shows opening main menu screen of the database. This database has four retrieval functions of nuclear reaction process, properties of radioactive isotope, spontaneous decay of each isotope and decay of produced nuclides after nuclear reaction. We can understand qualitatively the behavior of nuclear reaction such as the transmutation or decay.

3.2 User-interface for retrieval data

After choosing one of four functions on opening screen, various folders corresponding to the function appear as shown Fig. 3,4,5,6. Fig. 3 indicates the retrieval folders of records on nuclear reaction. List screen displays a listing of 843 records of nuclides produced by nuclear reaction in the folder, as shown Fig. 3(a) and then by pressing the button of "parent nuclides", it is possible to view the contents of a nuclear reaction process as shown Fig. 3(b). Fig. 4 indicates the retrieval folders of records on isotope

Nuclear Reaction Data 843 / 843

Element	Target nucleus	Transmutation	Num of Data	Num of Energy G	Produced nucleus	Judge stable	Reference	Published year
Ti	Ti46	NP	16	42	Sc46	U	ENDF/B-4	1974
Ti	Ti46	NG	42	42	Ti47	S	ENDF/B-4	1974
V	V51	ND	7	42	Ti50	S	ENDF/B-4	1974
V	V51	N2N	4	42	V50	S	ENDF/B-4	1974
V	V51	NNA	4	42	Sc47	U	BNL-325	1976
V	V51	NA	8	42	Sc48	U	ENDF/B-4	1974
V	V51	NP	14	42	Ti51	U	ENDF/B-4	1974
V	V51	NG	42	42	V52	U	ENDF/B-4	1974
V	V50	NA	12	42	Sc47	U	N.D.T.11	1973
V	V50	N2N	5	42	V49	U	N.D.T.11	1973
V	V50	NG	42	42	V51	S	ENDF/B-4	1974
Cr	Cr54	NP	4	42	V54	U	KFK-2386	1977
Cr	Cr54	NA	7	42	Ti51	U	KFK-2386	1977
Cr	Cr54	NG	42	42	Cr55	U	ENDF/B-4	1974
Cr	Cr53	N2N	6	42	Cr52	S	KFK-2386	1977
Cr	Cr53	NNP	1	42	V52	U	JU-RR-3	1970
Cr	Cr53	NP	12	42	V53	U	KFK-2386	1977
Cr	Cr53	NA	12	42	Ti50	S	KFK-2386	1977
Cr	Cr53	NG	42	42	Cr54	S	ENDF/B-4	1974
Cr	Cr52	N2N	2	42	Cr51	U	ANL-75-34	1975
Cr	Cr52	NP	10	42	V52	U	KFK-2386	1977
Cr	Cr52	NA	10	42	Ti49	S	KFK-2386	1977
Cr	Cr52	NG	42	42	Cr53	S	ENDF/B-4	1974
Cr	Cr50	N2N	1	42	Cr49	U	ANL-75-34	1975
Cr	Cr50	NNP	5	42	V49	U	N.D.T.11	1973
Cr	Cr50	NP	15	42	V50	S	KFK-2386	1977
Cr	Cr50	NA	12	42	Ti47	S	KFK-2386	1977
Cr	Cr50	NG	42	42	Cr51	U	ENDF/B-4	1974
Mn	Mn55	NHE3	2	42	V53	U	ENDF/B-4	1974
Mn	Mn55	ND	8	42	Cr54	S	ENDF/B-4	1974
Mn	Mn55	NA	19	42	V52	U	ENDF/B-4	1974
Mn	Mn55	NNP	9	42	Cr54	S	ENDF/B-4	1974
Mn	Mn55	N2N	5	42	Mn54	U	ENDF/B-4	1974
Mn	Mn55	NP	16	42	Cr55	U	ENDF/B-4	1974
Mn	Mn55	NG	42	42	Mn56	U	ENDF/B-4	1974
Fe	Fe58	NP	12	42	Mn58	U	KFK-2386	1977
Fe	Fe58	NA	7	42	Cr55	U	N.D.T.11	1973

Search of parent nuclide   Search of daughter nuclide   Save your data   Open the selected data
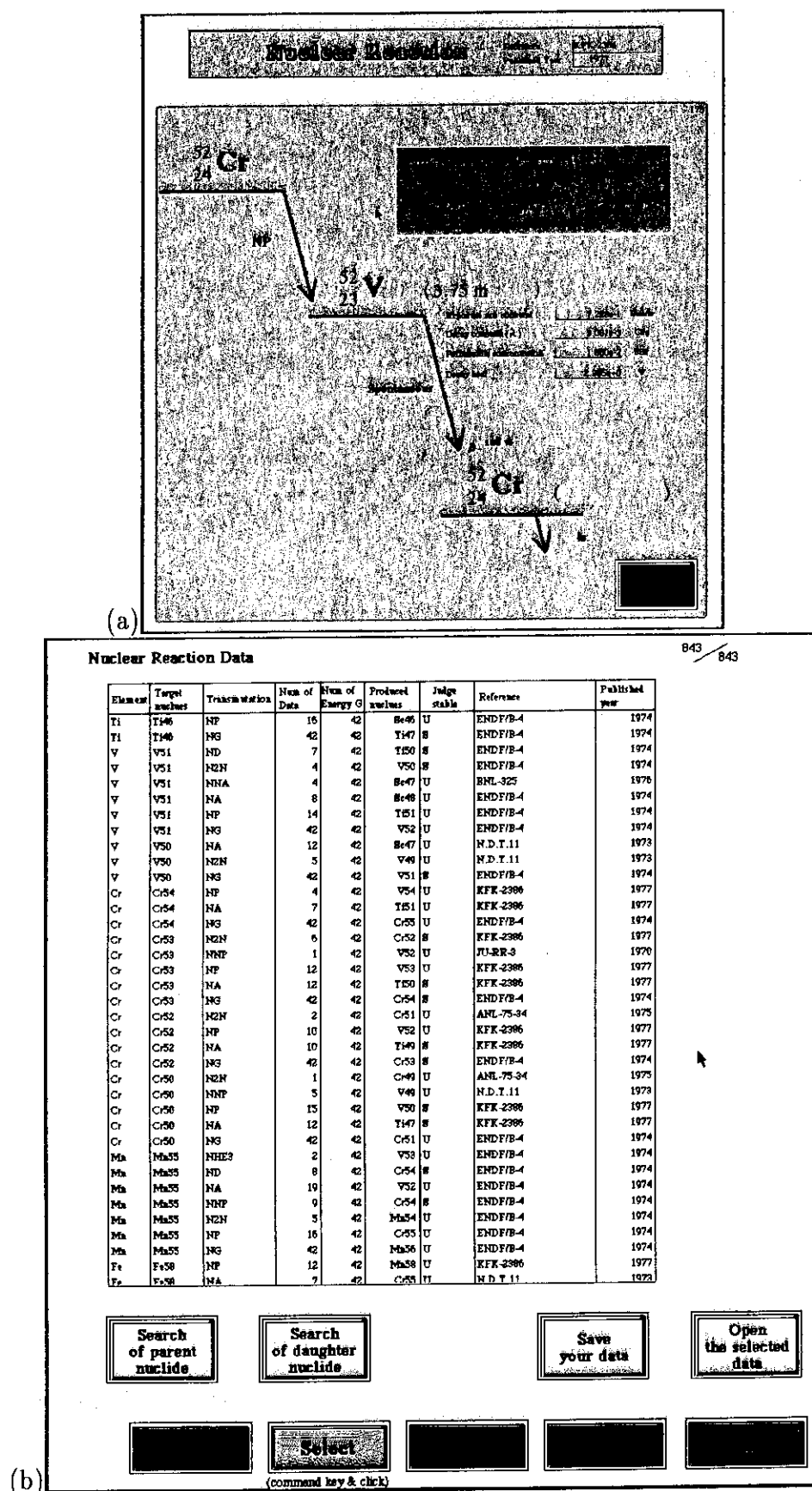
Select
(command key & click)

Figure 3: Retrieval folders of records on nuclear reaction. (a) : (List of records), (b) : (Transmutation and decay process)

Isotope Radiation Data

Element | N
Atomic weight | 14.0067
Density (g/cm3) | 0.81

Nuclear data

Transmission	Num of data	Reference	Publishing year

Isotope | N16

Num. of nucl. data | 0
Isotope abundance |
Judge stable or not | U
Half-Life | 7.13 s

Exposure rate constant | 1.460e+0 $19.45 \Sigma P_i E_i \frac{\mu_i}{\rho}$
Decay constant | 9.720e-2 $\log 2 / T$
Permissible concentration | 1.000e-9
Decay heat | 4.660e+0 $\Sigma E_\gamma P_\gamma + \frac{1}{3}\Sigma E_\beta P_\beta$

Decay Product | O16

Mode of decay

Mode	Decay ratio	MEMO
β-	100	

β or α Energy

Mode	Energy	Decay ratio	Intensity
	3.30e+0	4.9	6.39e-2
	4.29e+0	68	9.72e-1
	1.04e+1	26	9.03e-1
	1.70e+0		

γ Energy

Energy	Emission ratio	Intensity	Radiation dose
2.74e+0	7.50e-1	2.08e-2	4.42e-4
6.13e+0	6.90e+1	4.23e+0	6.90e-2
7.12e+0	5.01e+0	3.56e-1	3.81e-3

OK

(a)

Radioisotope Data

3517 / 3517

Element	Isotope	Isotopic abundance	Judge meta	Half-Life	Unit	Exposure rate constant	Decay constant (λ)	Permissible concentration	Decay heat	Mass Num.	Num. of Nucl. data	Decay product	Decay mode	Decay ratio
N	N1	100	S			0.000e+0	0.000e+0	0.000e+0	0.000e+0	1	0			
N	N2	0.02	S			0.000e+0	0.000e+0	0.000e+0	0.000e+0	2	0			
N	N3		U	1.233e+1	y	0.000e+0	1.763e-9	2.000e-6	6.200e-5	3	0	N<3	β-	100
He	He3	0	S			0.000e+0	0.000e+0	0.000e+0	0.000e+0	3	0			
He	He4	100	S			0.000e+0	0.000e+0	0.000e+0	0.000e+0	4	0			
He	He6		U	6.086e+2	ms	0.000e+0	8.579e-1	1.000e-9	1.189e+0	6	0	Li6	β-	100
He	He8		U	1.220e+2	ms	0.000e+0	5.661e+0	1.000e-9	0.000e+0	8	0	Li8	β-	100
Li	Li6	7.5	S			0.000e+0	0.000e+0	0.000e+0	0.000e+0	6	3			
Li	Li7	92.5	S			0.000e+0	0.000e+0	0.000e+0	0.000e+0	7	3			
Li	Li8		U	8.420e+2	ms	0.000e+0	8.202e-1	1.000e-9	4.333e+0	8	0	Be8	β-	100
Li	Li9		U	1.780e+2	ms	4.820e-1	3.894e+0	1.000e-9	6.150e+0	9	0	Be9	β-	100
Li	Li11		U	8.500e+0	ms	0.000e+0	8.155e+1	1.000e-9	0.000e+0	11	0	Be11	β-	100
Be	Be7		U	5.329e+1	d	2.830e-2	1.505e-7	4.000e-7	4.919e-2	7	0	Li7	ε	100
Be	Be8	0	U	6.717e-17	s	0.000e+0	8.998e-1	0.000e+0	0.000e+0	8	0			
Be	Be9	100	S			0.000e+0	0.000e+0	0.000e+0	0.000e+0	9	5			
Be	Be10		U	1.600e+6	y	0.000e+0	1.374e-14	1.000e-9	1.850e-1	10	0	B10	β-	100
Be	Be11		U	1.380e+1	s	8.208e-1	5.020e-2	1.000e-9	4.738e+0	11	0	B11	β-	100
Be	Be12		U	2.400e+1	ms	0.000e+0	2.888e+1	1.000e-9	0.000e+0	12	0	B12	β-	100
Be	Be14		U	5.000e+1	ms	0.000e+0	1.386e+1	1.000e-9	0.000e+0	14	0			
B	B8		U	7.700e+2	ms	5.882e-1	9.002e-1	1.000e-9	1.022e+0	8	0	Be8	ε	100
B	B9	0	U	8.000e-19	s	0.000e+0	8.664e+17	0.000e+0	0.000e+0	9	0			
B	B10	19.8	S			0.000e+0	0.000e+0	0.000e+0	0.000e+0	10	4			
B	B11	80.2	S			0.000e+0	0.000e+0	0.000e+0	0.000e+0	11	5			
B	B12		U	2.020e+1	ms	3.380e-1	3.431e+1	1.000e-9	4.520e+0	12	0	C12	β-	100
B	B13		U	1.740e+1	ms	0.000e+0	3.984e+1	1.000e-9	0.000e+0	13	0	C13	β-	100
B	B14		U	1.600e+1	ms	0.000e+0	4.332e+1	1.000e-9	0.000e+0	14	0	C14	β-	100
B	B15		U	6.000e+1	ms	0.000e+0	1.155e+1	1.000e-9	0.000e+0	15	0			
B	B17		U	2.000e+1	ms	0.000e+0	3.466e+1	1.000e-9	0.000e+0	17	0			
C	C8		U	3.000e+1	ms	0.000e+0	2.310e+1	1.000e-9	0.000e+0	8	0			
C	C9		U	1.265e+2	ms	0.000e+0	5.479e+0	1.600e-9	0.000e+0	9	0	B9	ε	100
C	C10		U	1.926e+1	s	9.973e-1	3.600e-2	1.000e-9	2.362e+0	10	0	B10	ε	100
C	C11		U	2.040e+1	s	5.868e-1	5.663e-4	6.000e-7	1.339e+0	11	0	B11	ε	100
C	C12	98.9	S			0.000e+0	0.000e+0	0.000e+0	0.000e+0	12	5			
C	C13	1.11	S			0.000e+0	0.000e+0	0.000e+0	0.000e+0	13	2			
C	C14		U	5.730e+3	y	0.000e+0	3.836e-12	1.000e-6	5.203e-2	14	0	N14	β-	100
C	C15		U	2.449e+0	s	1.199e+0	2.830e-1	1.000e-9	5.660e+0	15	0	N15	β-	100
C	C16		U	7.500e-1	s	0.000e+0	9.242e-1	1.000e-9	0.000e+0	16	0	N16	β-	100
C	C17		U	1.000e-1	s	0.000e+0	6.931e+0	1.000e-9	0.000e+0	17	0			
C	C18		U	1.500e-1	s	0.000e+0	4.621e+0	1.000e-9	0.000e+0	18	0			
C	C20		U	5.000e+1	ms	0.000e+0	1.386e+1	1.600e-9	0.000e+0	20	0			
N	N11		U	5.000e+1	ms	0.000e+0	1.386e+1	1.000e-9	0.000e+0	11	0			
N	N12		U	1.100e+1	ms	0.000e+0	6.301e+1	1.000e-9	0.000e+0	12	0	C12	ε	100
N	N13		U	9.960e+0	m	5.870e-1	1.200e-3	5.000e-7	1.416e+0	13	0	C13	ε	100
N	N14	99.6	S			0.000e+0	0.000e+0	0.000e+0	0.000e+0	14	8			
N	N15	0.37	S			0.000e+0	0.000e+0	0.000e+0	0.000e+0	15	0			
N	N16		U	7.130e+0	s	1.460e+0	9.720e-2	1.000e-9	4.660e+0	16	0	O16	β-	100
N	N17		U	4.170e+0	s	1.740e-2	1.662e-1	1.000e-9	1.307e+0	17	0	O17	β-	100

Search | RETURN

(command key & click)

(b)

Figure 4: Retrieval folders of records on isotope properties. (a) : (List of records), (b) : (Various properties of a isotope)

(a)

(b)

Figure 5: Retrieval folders of records on spontaneous decay. (a) : (Spontaneous decay of designated mass number), (b) : (Folder for input of a mass number)

Figure 6: Retrieval folders of records on decay after nuclear reaction and steps of transmutation. (a) : (decay and steps of transmutation), (b) : (Folder for input of a mass number)

properties. The list screen displays a listing of 3517 records of isotopes properties in folder, as shown Fig. 4(a). By selecting the desired isotope, it is possible to view the contents of properties of a isotope, as shown Fig. 4(b). Fig. 5 shows the retrieval folders of records on spontaneous decay. If the isotope is designated by the input of a mass number using the folder as show

Fig. 5(a), the spontaneous decay records of the radio isotope is obtained, as shown Fig. 5(b). Fig. 6 shows the retrieval folders of records on decay and transmutation processes after nuclear reaction. If the isotope is designated by the input of a element using the folder as shown Fig. 6(a), the decay of the produced nuclide and steps of transmutation is obtained, as shown Fig. 6(b). The user-interface (i.e. folder) of the database performs an important role either useful system or not. Using this user-interface, end-user can easily obtain the necessary nformation by the easy operation for retrieving, because a screen provided with pop-up and pull down menu, is employed to be mainly operated by micro-mouse in addition to keyboard.

4 Example of system operation

Type 316 stainless steel is used as the structural material of the fuel sub-assemblies in the sodium cooled fast breeder reactors. This steel is regarded as a candidate material for blanket structures of the fusion reactors. However it is required that materials should have a high resistance against swelling and low radioactivation under the high-energy neutron irradiation environment such as in fusion reactors. Ferritic 9Cr1WVTa steel is also being considered as an alternate candidate structural material to type 316 stainless steel /3/. An amount of He formation and radioactivity under neutron irradiation of both steels will be evaluated as an example of application of the present simulation system. Table 1 Results of retrieval for long half-life on the products of nuclear reaction of the first step caused by neutron irradiation to both type 316 stainless and ferritic steel.

(a) Compositional atom of type 316 stainless steel
(Fe,Cr,Ni,Ti,C,Mn,Si,S,P,O,N,B)

Element	Isotope	Reaction	Product	Half-life	Unit	Reference	Year
B	B10	NP	Be10	1.60E+06	y	ENDF/B-4	1974
C	C13	NA	Be10	1.60E+06	y	N.D.T.11	1973
C	C13	NG	C14	5.73E+03	y	ENDF/B-3	1970
N	N14	NP	C14	5.73E+03	y	ENDF/B-4	1974
Fe	Fe56	N2N	Fe55	2.70E+00	y	N.D.T.11	1973
Fe	Fe54	NNP	Mn53	3.70E+06	y	N.D.T.11	1973
Fe	Fe54	NG	Fe55	2.70E+00	y	ENDF/B-4	1974
Ni	Ni64	N2N	Ni63	1.00E+02	y	N.D.T.11	1973
Ni	Ni62	NG	Ni63	1.00E+02	y	ENDF/B-4	1974
Ni	Ni61	NNP	Co60	5.27E+00	y	N.D.T.11	1973
Ni	Ni60	N2N	Ni59	7.50E+04	y	N.D.T.11	1973
Ni	Ni60	NP	Co60	5.27E+00	y	ENDF/B-4	1974
Ni	Ni58	NA	Fe55	2.70E+00	y	KFK-2386	1977
Ni	Ni58	NG	Ni59	7.50E+04	y	ENDF/B-4	1974
Cu	Cu63	NP	Ni63	1.00E+02	y	N.D.T.11	1973
Cu	Cu63	NA	Co60	5.27E+00	y	ENDF/B-4	1974
Mo	Mo96	NA	Zr93	1.50E+06	y	N.D.T.11	1973
Mo	Mo95	NNP	Nb94	2.00E+04	y	N.D.T.11	1973
Mo	Mo94	N2N	Mo93	3.50E+03	y	N.D.T.11	1973
Mo	Mo94	NP	Nb94	2.00E+04	y	N.D.T.11	1973
Mo	Mo92	NNP	Nb91	6.80E+02	y	BNL-325	1976
Mo	Mo92	NP	Nb92	3.20E+07	y	N.D.T.11	1973
Mo	Mo92	NG	Mo93	3.50E+03	y	N.D.T.11	1973

(b) Compositional atom of ferritic 9Cr1WVTa steel
(Fe,Cr,W,V,Ta,C,Mn,Si,S,P,O,N,B)

Element	Isotope	Reaction	Product	Half-life	Unit	Reference	Year
B	B10	NP	Be10	1.6000E+06	y	ENDF/B-4	1974
C	C13	NA	Be10	1.6000E+06	y	N.D.T.11	1973
C	C13	NG	C14	5.7300E+03	y	ENDF/B-3	1970
N	N14	NP	C14	5.7300E+03	y	ENDF/B-4	1974
O	O17	NA	C14	5.7300E+03	y	N.D.T.11	1973
Fe	Fe56	N2N	Fe55	2.7000E+00	y	N.D.T.11	1973
Fe	Fe54	NNP	Mn53	3.7000E+06	y	N.D.T.11	1973
Fe	Fe54	NG	Fe55	2.7000E+00	y	ENDF/B-4	1974
Ta	Ta181	N3N	Ta179	1.8200E+00	y	ENDF/B-4	1974

Using the nuclide database, the possibility of large amount of He formation and radioactivity in the candidate materials can be easily evaluated qualitatively. The possibility of He formation is known by retrieving cross section size of (n, α) reaction on compositional atoms of materials. The radioactivity is known by retrieving half-life of transmuted products of compositional atoms of material. Table 1 shows transmuted products with half-life of more than one year in type 316 and ferritic steel. These result suggest that type 316 stainless steel has more radioactive nuclides and is radioactivated more easily than ferritic 9Cr-1WVTa steel under neutron irradiation. It is found that this

system will be frequently used by nuclear material scientists as a material information tool, if this system is jointed to networking system such as "Data-Free-Way" /1/−/3/.

5 Conclusion

The radioactivity is known by retrieving half-life of transmuted products of compositional atoms of material. Transmuted products with half-life of longer than one year in type 316 and ferritic steel. These result suggest that type 316 stainless steel has more radioactive nuclides and radioactivated more easily than ferritic 9Cr-1WVTa steel for reduced activation under neutron irradiation .

References

[1] Fujita M., Kurihara Y., Nakajima H., Yokoyama N., Ueno F., Kano S., Iwata S., *Proc. Int. Conf.on Computer Applications to Materials Science and Engineering,* **1992** p81-84 (Yokohama, Japan)

[2] Nakajima H., Yokoyama N., Ueno F., Kano S., Fujita M., Kurihara Y. and Iwata S., *J. Nucl. Mater.* **vol.212-215** (1994) p.1171-1714.

[3] Ueno F., Kano S., Iwata S.,Fujita M., Kurihara Y., Nakajima H.,Yokoyama N. and Iwata S., *J. Nucl. Sci. Technol,* **vol.31** (1994) p.1314-1334.

The First Internet Symposium on Nuclear Data: Paper No.021

3.21 Measurements of Double-differential Neutron Emission Cross Sections of Nb and Bi for 11.5 MeV Neutrons

Masanobu Ibaraki , Shigeo Matsuyama , Daisuke Soda, Mamoru Baba
and Naohiro Hirakawa
Department of Quantum Science and Energy Engineering, Tohoku University
Aramaki-Aza-Aoba, Aobaku, Sendai, 980-77, Japan
Email : iba@rpl.nucle.tohoku.ac.jp

Double-differential neutron emission cross sections (DDXs) of Nb and Bi have been measured for 11.5MeV neutrons using the $^{15}N(d,n)^{16}O$ quasi-monoenergetic neutron source at Tohoku University 4.5MV Dynamitron facility. For En' >6MeV, DDXs were measured by the conventional TOF method (single-TOF:S-TOF). For En' <6MeV, where the S-TOF spectra were distorted by the background neutrons, we adopted a double-TOF method (D-TOF). By applying D-TOF method, we obtained DDXs down to 1MeV.

1 Introduction

Double-differential neutron emission cross sections (DDXs) for fast neutrons are very important for the neutronics design of fusion reactors, shielding design of high energy accelerator facilities and so on. In the energy region between 8 - 13 MeV, there have been only very few DDX measurements despite of the importance for fusion reactor application. This paper describes DDX measurement at 11.5 MeV using the $^{15}N(d,n)^{16}O$ source /1/ as an extension of the systematic DDX studies for 14, 18 MeV and 1 - 6 MeV neutrons /2//3//4/. The 11.5 MeV neutron source by the $^{15}N(d,n)^{16}O$ reaction is not monoenergetic, and the low energy part of the spectrum measured by the conventional TOF (single-TOF : S-TOF) method is contaminated seriously by the events due to background neutrons in the source. In this study, we adopted the double-TOF (D-TOF) method /5/ that was similar to that employed at China Institute of Atomic Energy (CIAE) /6/ and eliminated experimentally the background events in the TOF spectrum. By this technique, we could obtain almost entire DDXs for 11.5 MeV neutrons. Experimental results are presented in comparison with evaluated data and calculations by the code EXIFON /7/.

2 Experiments and Data Reduction

Experiments were carried out using the Tohoku University Dynamitron time-of-flightspectrometer /8/. Scattering samples were cylinders of elemental niobium and bismuth(3 cm diam × 5 cm long). The neutrons were porduced by bombarding a $^{15}N_2$ gas target with a pulsed deuteron beam. Fig.1 shows energy spectrum of the source neutrons. Primary neutrons appear at 11.5 MeV with no appreciable background neutrons down to 6 MeV. In addition to the 11.5 MeV neutrons, however, there are intense several background neutron groups corresponding to the excited states of residual ^{16}O. These neutrons give rise to serious backgrounds overlapping with the spectrum by primary neutrons in the region En' < 6 MeV. Therefore, the D-TOF method was employed to obtain spectra for En' < 6 MeV by eliminating background events, as well as S-TOF method for En' > 6 MeV.
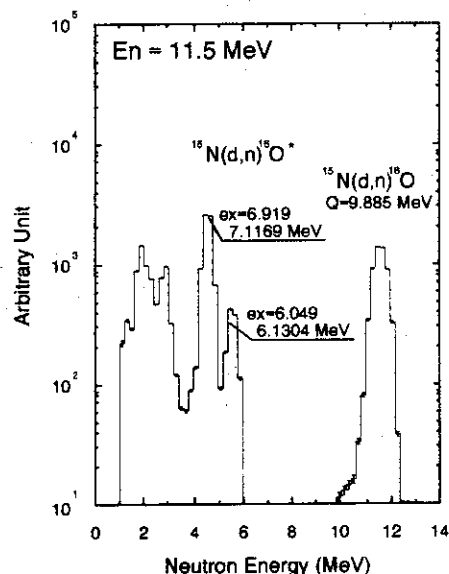
Figure 1: Energy spectrum of the source neutrons

2.1 S-TOF Experiment

The S-TOF experimental method was almost the same as that in previous studies for 14, 18 MeV and 1 - 6 MeV neutrons /2//3//4/. Fig.2 shows the experimental set up of the S-TOF method. The flight path length was around 6 m. A long liquid scintillation detector (LLSD) /9/ was used as a secondary neutron detector to compensate the low intensity of the neutron source. LLSD was housed in a massive shield placed vertically on a turning table. The neutron emission spectra were measured at 11 and 6 angles between 20 and 150-deg for Nb and Bi, respectively.
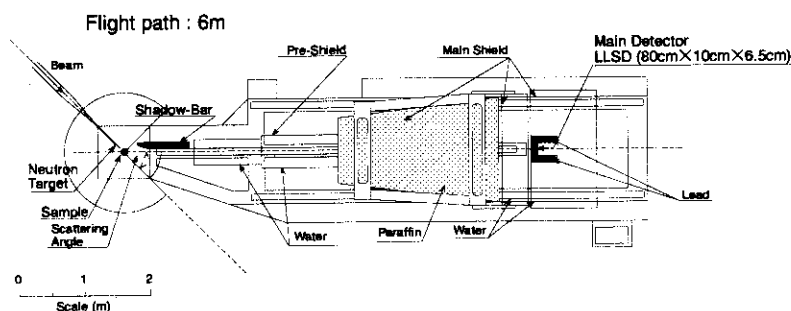

Figure 2: Experimental geometry of the S-TOF method

2.2 D-TOF Experiment

Fig.3 shows the experimental set up of the D-TOF method. The D-TOF method adopted a longer target-sample distance (3.2 m) and shorter sample-detector distance (85 cm) than in the S-TOF method. In this arrangement, the events by 11.5 MeV neutrons can be separated from those by background neutrons in TOF spectrum. The neutron target was shielded with iron, water and concrete to reduce sample independent backgrounds. Secondary neutrons were detected by a 14 cm diam × 10 cm long NE213 which was shielded with lead and paraffin. The neutron emission spectra were measured at 90-deg.
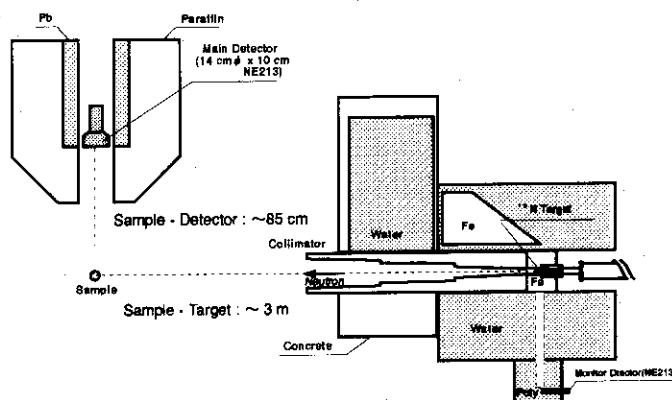
Figure 3: Experimental geometry of the D-TOF method

2.3 Data Reduction

The TOF spectra were converted into the energy spectra considering the effects of sample independent backgrounds and the detection efficiency. The energy spectra were corrected for the finite sample-size effects by a Monte-Carlo code SYNTHIA /10/. In the S-TOF measurement, absolute cross sections were determined by referring the n-p scattering cross section . In the D-TOF measurement, absolute cross sections were determined by normalizing the D-TOF data to the S-TOF data in 6 - 8 MeV region considering the resolution function in the experiments.

3 Results and Discussion

Fig.4 and 5 show high energy parts of measured DDXs of Nb and Bi derived by the S-TOF method in comparison with those derived from the evaluated nuclear data. Fig.6 shows overall DDXs at 90-deg derived by combining the D-TOF data for $En' < 6$ MeV. The data at one angular point will be enough since the angular distributions of continuum secondary neutrons can be described by Kalbach-Mann (K-M) or Kalbach systematics /2//11//12/.
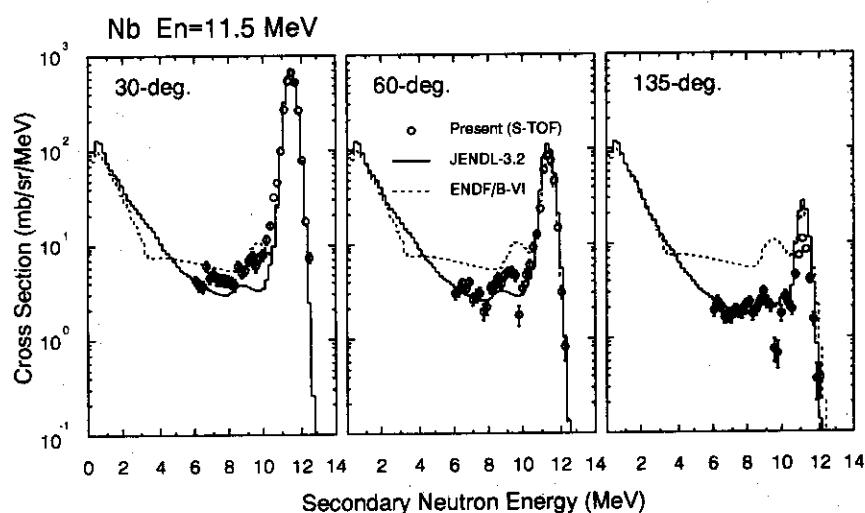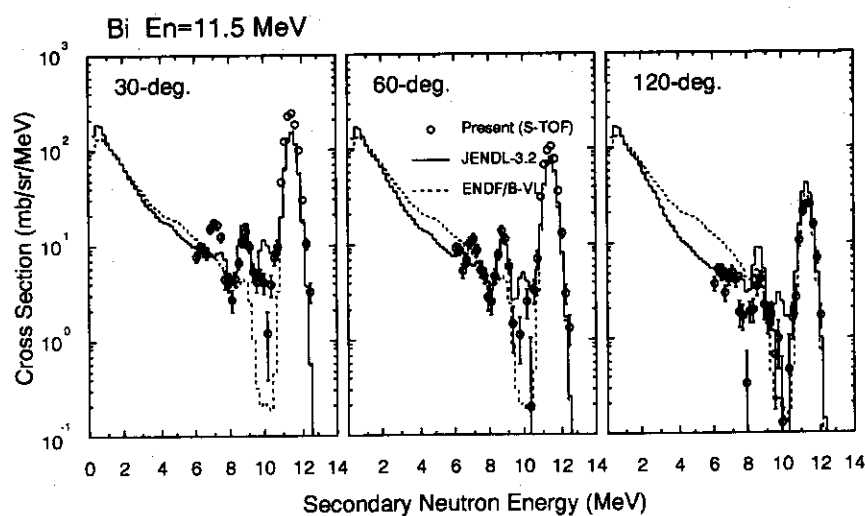

Figure 4: DDXs of Nb ($En' > 6$ MeV)

Figure 5: DDXs of Bi ($En' > 6$ MeV)
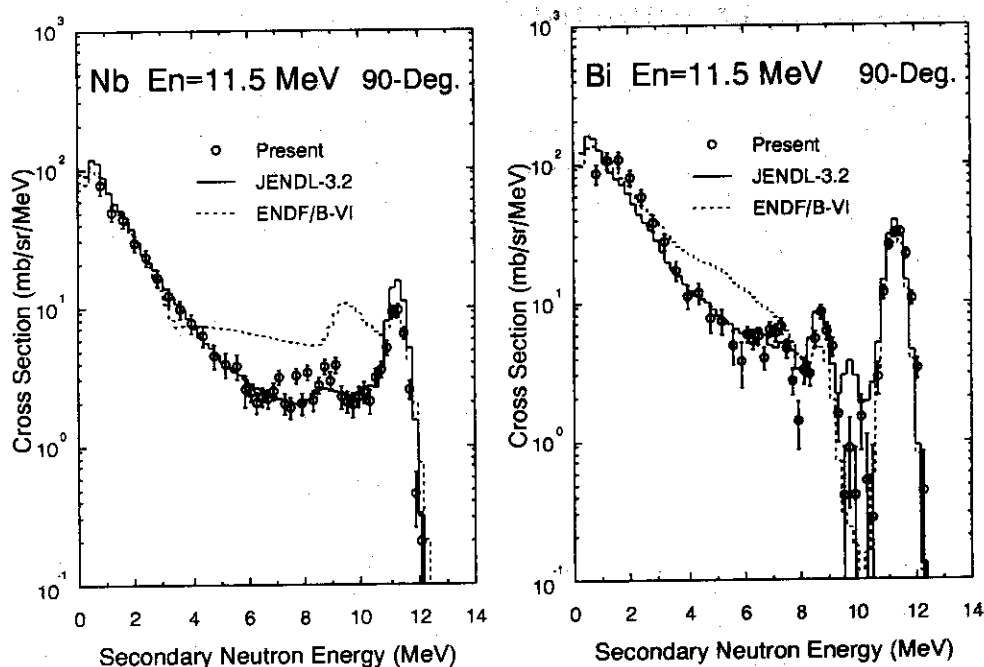
Figure 6: DDXs of Nb and Bi at 90 deg.

3.1 Comparison with evaluated data

For Nb, the JENDL-3.2 data reproduce the experimental data generally well except at forward angle, but the ENDF/B-VI data differ largely both in shape and magnitude from the experimental data. (Fig.4, 6) This large difference arises from the fact ENDF/B-VI assumes that angular distributions of continuum components to be isotropic in the laboratory system, and adopts inadequate energy spectrum.

For Bi, both data of JENDL-3.2 and ENDF/B-VI show marked discrepancies with the experimental data in 6 - 10 MeV. The inelastic peak observed around 7 MeV in experimental data is not considered in both evaluated data, and that around 10 MeV is overemphasized in JENDL-3.2. In low energy region corresponding to $(n, 2n)$ reaction, the JENDL-3.2 data is slightly lower than the experimental data. (Fig.5, 6) This trend was observed also for 14 MeV /2/.

A satisfactory agreement of the JENDL-3.2 data with the experimental data will be due to well examined model parameters at 14 and 18 MeV data.

3.2 Comparison with the code EXIFON

Fig.7 show energy differential cross sections (EDXs) deduced from the measured DDXs at 90-deg and K-M systematics, in comparison with the calculations by the code EXIFON /7/. The solid lines show total, and dashed lines represent MSD and MSC components.
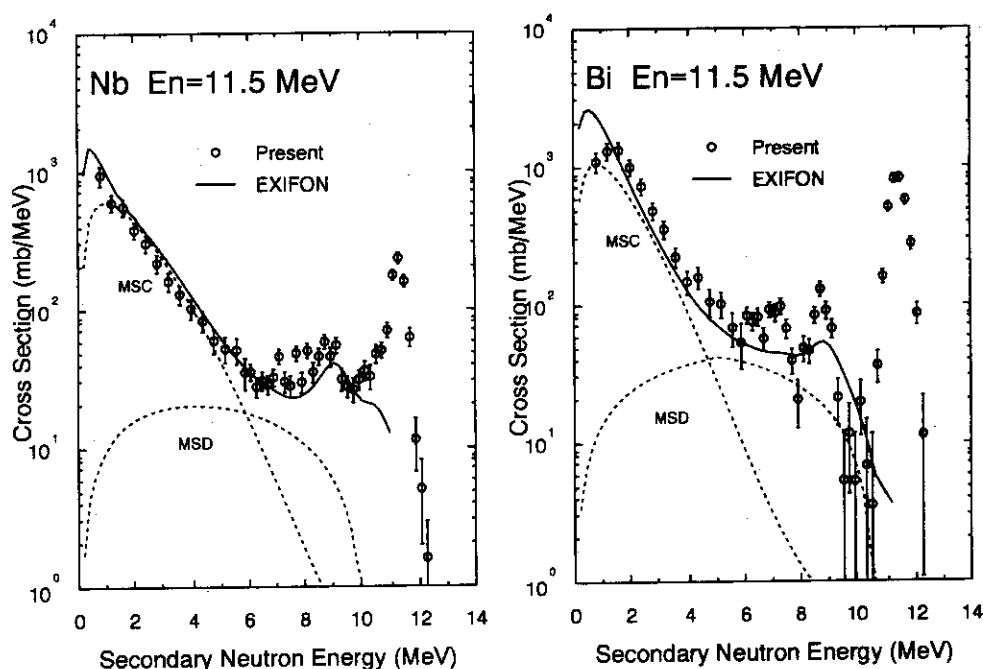

Figure 7: EDX of Nb and Bi deduced from measured DDX at 90-deg.

For Nb. EXIFON reproduces comparatively both in shape and magnitude the experimental data. For Bi, EXIFON underestimates the experimental data. Similar underestimation of EXIFON for Bi was observed in 14 MeV incident energy /2/ .

4 Summary

We have measured double-differential neutron emission cross sections of Nb and Bi for 11.5 MeV neutrons using the $^{15}N(d,n)^{16}O$ neutron source and compared with evaluated data and calculations by the code EXIFON. By combining the S-TOF and D-TOF method, we could obtain almost entire DDX data for 11.5 MeV neutrons. This method provides a powerful means for DDX measurements around 11 MeV, where only very few data are existing.

References

[1] S.Matsuyama et al., Proc. Int. Conf. Nuclear Data for Science and Technology (1994, Gatlinburg) p.400

[2] M.Baba et al., J. Nucl. Sci. Technol., 31(8) 757(1994)

[3] M.Baba et al., J. Nucl. Sci. Technol., 27(7) 601(1990)

[4] M.Baba et al., Proc. Int. Conf. Nuclear Data for Science and Technology (1991, Jeulich) p.349

[5] S.Matsuyama et al., JAERI-conf 95-008 (1995) p.157

[6] Q.Bujia et al., Proc. Int. Conf. on Nucl. Data for Sci. and Technology (1991 Jeulich) p.436

[7] H.Kalka et al., Phys. Rev., C40 1619(1989)

[8] S.Matsuyama et al., Nucl. Instrum. Methods A 348 (1994) 34-40

[9] S.Matsuyama et al., Nucl. Instrum. Methods A 372 (1996) 246-252

[10] M.Baba et al., Nucl. Instrum. Methods A 366 (1995) 354-365

[11] C.Kalbach and F.M.Mann, Phys. Rev., C23(1) 112(1981)

[12] C.Kalbach, Phys. Rev., C37(6) 2350(1988)

The First Internet Symposium on Nuclear Data: Paper No. 22

3.22 Measurement of Differential (n,xα) Cross Section using 4 π Gridded Ionization Chamber

Toshiya SANAMI, Mamoru BABA, Shigeo MATSUYAMA,
Toshihiko KAWANO*,Takehide KIYOSUMI, Yasushi NAUCHI,
Keiichiro SAITO and Naohiro HIRAKAWA
Quantum Science and Energy Engineering, Tohoku University
Aoba.Aramaki, Sendai 980-77, Japan
* *Energy Conversion Engineering, Kyushu University*
Kasuga-Kouen 6-1, Kasuga-shi,Fukuoka 816, Japan
(Presently at Forschungszentrum Karlsrhue)
E-mail : toshi@rpl.nucle.tohoku.ac.jp

We carried out the measurements of high resolution α emission spectra of ^{58}Ni and ^{nat}Ni between 4.5 and 6.5 MeV, and ^{12}C(n,xα) cross section using a 4π gridded ionization chamber. In Ni measurement, overall energy resolution was improved to around 200 keV by optimizing a sample thickness and a neutron source width. Measured alpha spectra showed separate peaks corresponding to the ground and low-lying excited states of the residual nucleus (^{55}Fe). These results were compared with another direct measurement and statistical model calculations. In ^{12}C measurement, GIC was applied for (n,xα) reactions of light nuclei. This appication is difficult to (n,xα) cross sections of light nuclei. because of the influences of large recoil energy and multi-body break-up. We developed new methods which eliminate the effects of recoil nuclei and multi-body break-up and applied them to ^{12}C(n,xα) reaction at En=14.1 MeV. In our experiment, the ^{12}C(n,α0)^{9}Be angular differential cross section and ^{12}C(n,n'3α) cross section were obtained.

1 Introduction

Neutron induced α emission data are important for the evaluation of radiation damage and nuclear heating in fusion and fast reactors. We have been conducting measurements of double differential (n,α) cross sections (DDXs) of structural elements, Fe, Ni, ^{50}Cr, Cu for 4.3 - 14.1 MeV neutrons using a specially designed gridded ionization chamber (GIC) /1/ /2/ /3/. The present GIC has advantages of a large geometrical efficiency (nearly 4π) and a capability of energy-angle determination.

In this paper, we present the measurements using the GIC for

1. high resolution α emission spectrum of ^{nat}Ni and ^{58}Ni(n,α) between 4.5 and 6.5 MeV and

2. ^{12}C(n,xα) cross section at 14.1 MeV.

In the former experiment, we measured (n,α) DDXs with an overall energy resolution around 200 keV and resolved α peaks to the low-lying levels of the residual nucleus, ^{55}Fe. The results were compared with statistical model calculations. The experiment was motivated by a large difference between our previous data /2/ /3/ and Goverdovski et al's one /4/. The data for each state will be interesting to assess the optical model potential and level density parameters employed in the calculation.

The latter experiment was the attempt to apply GIC to (n,xα) reactions of light nuclei. The present GIC was difficult to apply to (n,xα) reactions of light nuclei because of the influences of the large recoil energy and multi-body break-up (cf. Sect.3). To solve them, we developed new methods and obtained the data on angular differential ^{12}C(n,α_0)^{9}Be cross section and the sum α spectrum for the ^{12}C(n,n'3α) reaction.

2 High resolution α spectrum of ^{58}Ni and ^{nat}Ni(n,α)

2.1 Experiment

Experimental setup is shown in Fig.1, and is almost the same as in previous studies /1/ /2/ /3/. Samples were set in the center of GIC and bombarded with 4.5~6.5MeV neutrons. Source neutrons were produced at a D_2-gas target via the D(d,n) reaction using Tohoku University 4.5 MV Dynamitron accelerator. In this experiment, we employed thin samples and a neutron source with a low energy spread to improve the energy resolution of α spectra.

Figure 1: Experimental setup

Samples were made by vacuum evaporation on a Ta foil (10 μm), and about 280 μg/cm^2 thick (about 40 keV loss for 4 MeV α-particle). Neutron energy spread was reduced to about 150 keV by reducing the pressure of the gas target. Consequently, an overall energy resolution around 200 keV was achieved, which was good enough to separate α particles to the low lying levels of residual nucleus, ^{55}Fe, around 500 keV apart. Three signals for two anodes and the common cathode were gathered in the list mode.

Fig.2 shows two dimensional spectrum of ^{58}Ni at En=6.51 MeV. A satisfactory signal-to-noise ratio was achieved. The anode channel corresponds to the particle energy and the cathode one to the angle for each particle energy. The straight and curved lines in the figure represent the α emission angles of 90° and 0°, respectively. Owing to good energy resolution, a few stripes are observed clearly correspondingly to α particles to the ground and excited states. Because of the large solid angle of GIC, sufficient counting statistics was obtained within several hours of measurement with beam current around 4μA.
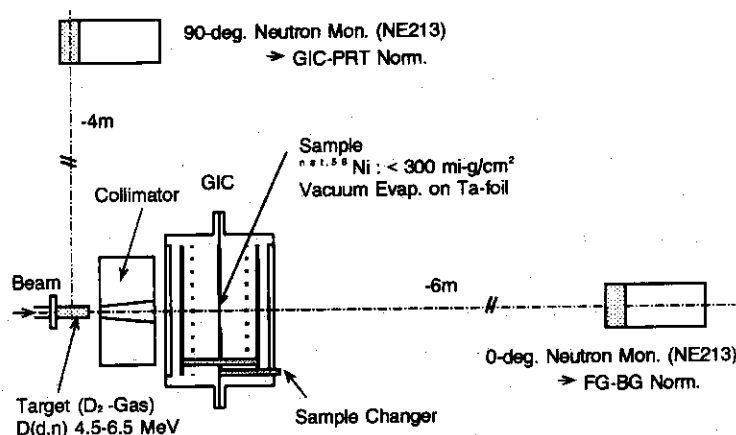
Neutron flux on the sample was determined using a single proton recoil telescope (PRT) consisting of a 20μm thick polyethylene radiator and a silicon surface barrier detector in a vacuum chamber /5/. DDXs were obtained by combining α particle yields for each angular mesh with the measured neutron flux. DDXs were corrected for the geometrical efficiency of GIC and the energy loss within the sample /1/.

The data errors were estimated considering the error sources of counting statistics, absolute normalization (8~9 %) and corrections. As shown later, the ^{nat}Ni data by a thin sample were confirmed to be consistent with those by a thick sample.
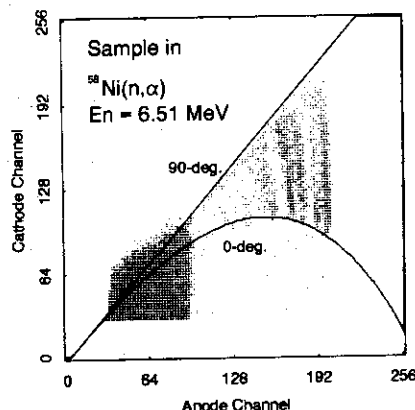

Figure 2: Two dimensional spectrum of ^{58}Ni at En=6.51 MeV

2.2 Statistical model calculation

For comparison with the experimental result, Hauser-Feshbach (HF) calculation was carried out. The calculation takes account of competition with neutron and proton emission channels. The parameters are as follows;

1. Neutron optical model potential (OMP) by A.B.Smith et al. /6/,

2. Proton OMP by Perey /7/ and α OMP by Lemos /8/,

3. Level density parameters by Gilbert-Cameron /9/.

Neutron OMP was that derived by fitting the total and scattering cross sections of ^{58}Ni. For ^{60}Ni and ^{61}Ni, the parameters were modified slightly using the global parameters by Rapaport et al./10/. The nuclear structure data are taken primarily from nuclear data sheet. The levels are treated as continuum above

- Ex=4.15, 3.7 and 3.0 MeV for ^{58}Ni, ^{60}Ni and ^{61}Ni(n,n'), respectively,

- Ex=0.440, 1.1 and 2.0 MeV for ^{58}Ni, ^{60}Ni and ^{61}Ni(n,p), respectively, and

- Ex=2.26, 2.6 and 4.8 MeV for ^{58}Ni, ^{60}Ni and ^{61}Ni(n,α), respectively.

The calculation by the parameters reproduces satisfactorily the total, (n,n') and (n,p) cross sections of ^{58}Ni.

2.3 Result and discussion

DDXs, ADX (Angular differential cross section) and integrated (n,α) cross sections are shown in comparison with the calculation and other data.
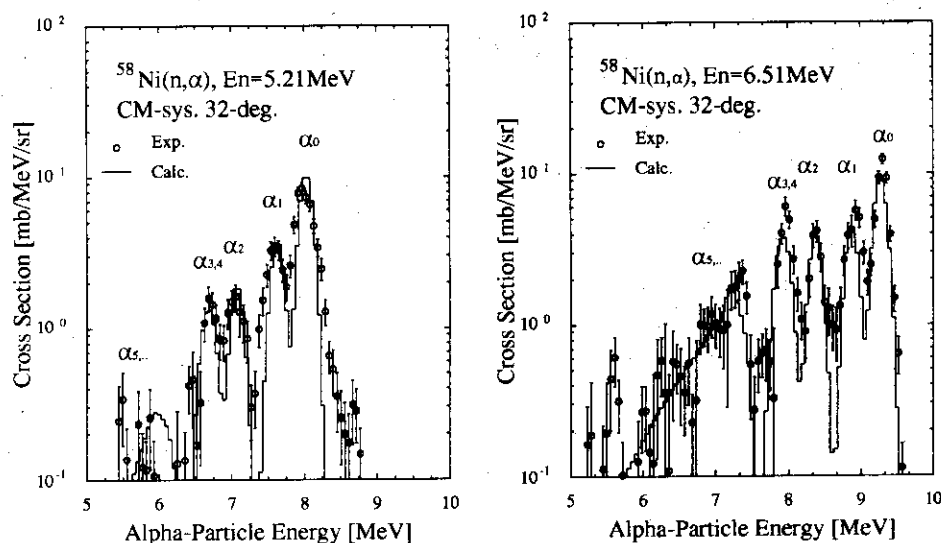
Figure 3: DDX at 5.21 and 6.51 MeV at 32°

2.3.1 DDX

Fig.3 shows the typical results of DDX at 5.21MeV and 6.51 MeV compared with HF results. The emission angle is 32° in cm-system. Our result is shown in circle and calculation result by solid histogram. The HF results are smeared with a gaussian function, 200 keV in FWHM. Naturally, α particles to higher states increase with the incident neutron energy. Our results are fairly close to the calculations in shape although the counting statistics is not high enough for higher levels. The comparison for each α group is shown in the next section.

Figure 4: Angular differential cross section at 5.21 MeV

2.3.2 ADX

Fig.4 shows angular differential cross section (ADX) at 5.21 MeV, for three components, α_0, α_1, $\alpha_{2,3}$... All the experimental ADXs are nearly 90° symmetric, and indicate that the reaction proceeds via the compound process in these neutron energy range. The shape of the experimental spectra are in fair agreement with HF calculations.
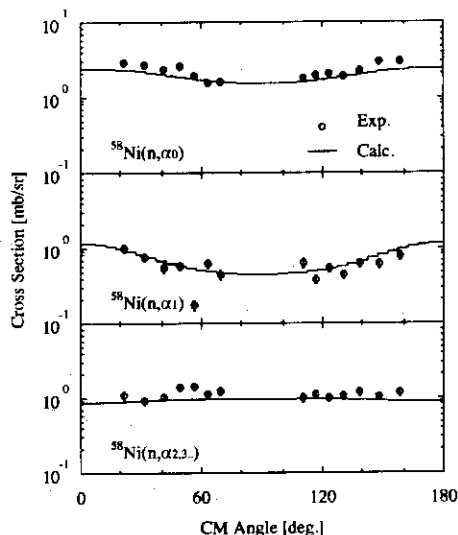
2.3.3 Excitation function of ^{58}Ni(n,α_0), (n,α_1), (n,$\alpha_{2,3}$..)

Fig.5 shows the excitation function of ^{58}Ni(n,α_0), (n,α_1), (n,$\alpha_{2,3}$..) in comparison with those by Goverdovski et al. /4/ and HF. The present data for (n,α_0) and (n,α_1)

include the results by the ^{nat}Ni samples as well as the ^{58}Ni one, because there is no contribution from ^{60}Ni. The $(n, \alpha_{2,3}..)$ component increases rapidly with neutron energy and it dominates the (n, α) cross section in higher neutron energy. Therefore, the calculation of (n, α) cross sections are sensitive to the level density parameter of ^{55}Fe.

Compared with the data by Goverdovski et al., our results are about twice as large as in (n, α_0) but smaller in $(n, \alpha_{2,3}..)$. This difference will be a main origin of the difference in (n, α) cross section between these experiments (Fig.6).

In comparison with HF calculation, the present values agree much better than Goverdovski et al.'s one, but tend to be larger above around 5 MeV in (n, α_0) and $(n, \alpha_{2,3}..)$ values. This leads to larger values of the present results in total (n, α) cross section than HF (cf.2.3.4).

Figure 5: Excitation function of ^{58}Ni(n, α_0), (n, α_1), $(n, \alpha_{2,3}..)$

2.3.4 Total (n,α) cross section of ^{58}Ni and ^{nat}Ni

Fig.6 shows the integrated ^{58}Ni(n, α) cross section in comparison with other experiment (Goverdovski /4/ and Wattecamps /11/), calculations (HF and EXIFON /13/ /14/) and the evaluations (JENDL-3R2 and ENDF/B-VI).

For ^{nat}Ni, the present results by the thin sample agree within error with our previous values by a thick sample. Therefore, it can be concluded that our previous data received no distortion by a sample thickness and an energy resolution.

Above 5.5 MeV, markedly discrepancies are existing among calculations and evaluations for the ^{58}Ni(n, α) cross section because of the ambiguity in model parameters. Therefore, experimental data are important to determine the magnitude. Our data support JENDL—3R2, but higher than both calculations in this region. The deviation between the present data and the calculations becomes larger with the neutron energy. This feature is seen too in the ^{nat}Ni(n, α) data, because ^{58}Ni is the dominant element of ^{nat}Ni. The lower values of HF will be attributed mainly to the problem of α OMP employed, but the effect of the level density parameters of ^{58}Ni and ^{55}Fe should be examined further.
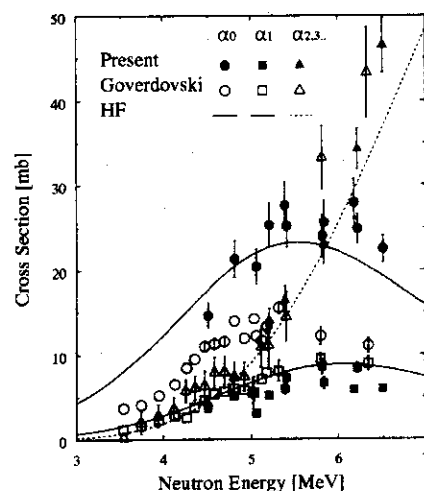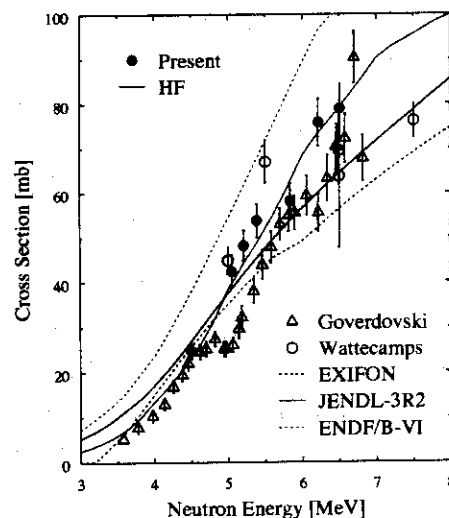

Figure 6: ^{58}Ni(n, α) cross section

3 ^{12}C(n,xα) cross section at 14.1 MeV

3.1 Experiment

In the fast neutron reactions with light nuclei, recoil particles have large energy and multi-body break up processes accompany in most cases. For the reason, as shown in the following, GIC can not be applied to light nuclei in 4 π geometry using a thin sample. Then, we developed a single hemisphere method (SH-method) and a forward-backward sum-coincidence method (FB-method), described below.

In the case of carbon, charged particle production reactions around 14 MeV, are (n,α_0)^{9}Be and (n,n'3α). (The ^{12}C(n,p) reaction is energetically possible but its cross section is negligibly small.) The former is two-body reaction and the latter is a four-body break-up process which contains sequential decay and three-body simultaneous decay /15/.

Figure 7: The response of GIC in the case of a two body reaction

Fig.7 shows the response of GIC in the case of a two body reaction, such as ^{12}C(n,α_0)^{9}Be. The recoil particle, ^{9}Be, has energy high enough to come out from the sample foil and contributes to the cathode signal. To remove the effect of recoil ^{9}Be, we operated separately the forward (FW) or backward (BW) hemisphere of GIC keeping inactive the other half (single hemisphere method: SH-method). In this mode, the energy-angle information can be obtained by the ordinary way.

Fig.8 shows the behavior of GIC for ^{12}C(n,n'3α). In most cases, one or two α particles are detected in both FW and BW. The anode and cathode outputs are the sum signal, and do not provide information on the energy and angle for each particle and the number of particles.

Nevertheless, instead, it is possible to detect the (n,n'3α) events with a very high geometrical efficiency and obtain the information on emission cross section and the sum energy of three alphas. We obtained sum spectrum by taking events which produce signals in both FW and BW (forward-backward sum-coincidence method: FB-method). The threshold energy for the coincidence was set around 200 keV to avoid count losses.
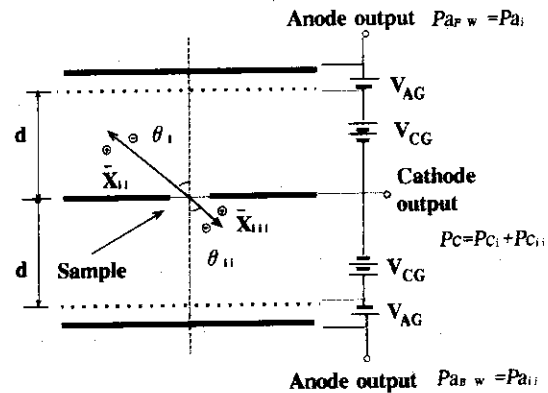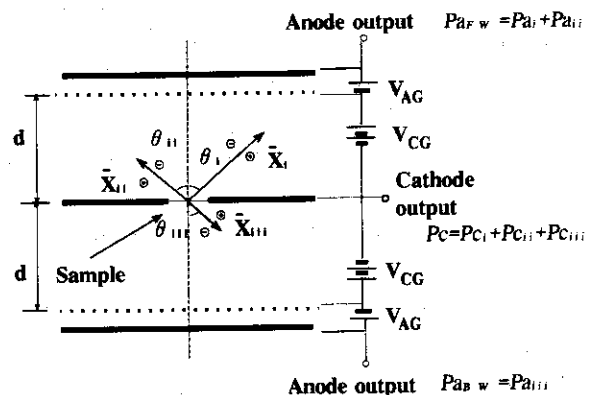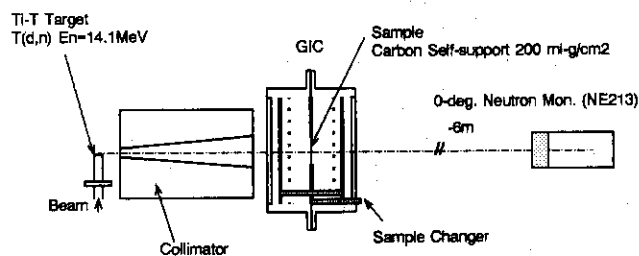

Figure 8: The behavior of GIC for ^{12}C(n,n'3α)

Figure 9: The experimental arrangement for ^{12}C(n,xα) measurement

The experimental setup is shown in Fig.9. The carbon sample was a self-supporting foil, 200 μg/cm^2 thick. Incident neutrons of 14.1 MeV were produced by T(d,n) reaction at 95°. Experimental setup is the same for both the SH and FB method. Neutron flux was measured using a δE-E type proton recoil telescope /5/.

3.2 ^{12}C(n,α_0)^{9}Be cross section

In the measured two-dimensional spectrum, the (n,α_0) events lie on a curved line between 0° and 90° lines because of a strong energy-angle correlation. But in the energy spectrum for each cm-angle deduced from the two-dimensional spectrum, the peaks of (n,α_0) events are observed clearly with constant energy. Fig.10 shows the present ADX of ^{12}C(n,α_0) in comparison with the data of Haight et al. by a magnetic spectrometer /16/ and those by the inverse reaction, ^{9}Be(α,n)^{12}C-gs /17/. Our result is in agreement with the result of inverse reaction within error.
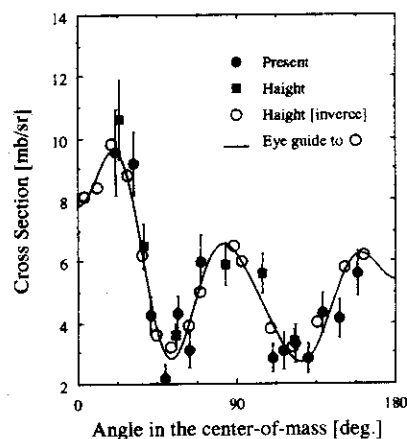

Figure 10: ADX of ^{12}C(n,α_0)^{9}Be

3.3 ^{12}C(n,n'3α) cross section

A sum energy spectrum of α particles from ^{12}C(n,n'3α) was deduced by processing the list data. Fig.11 shows the sum spectrum of FW-BW coincidence events for sample-in and sample-out cases. The peak around 7 MeV is due to ^{12}C(n,α_0)^{9}Be events. The events below 6 MeV are α particles from ^{12}C(n,n'3α) [Q=-7.2 MeV] reaction. To deduce the (n,n'3α) cross section, we have to estimate the detection efficiency (FW- BW coincidence probability), which depends on the geometrical efficiency of GIC and the energy and angle of α-particles. Here, we assumed simply that the detection efficiency was identical with the geometrical efficiency for two particles. Fig.12 shows the result in comparison with other data by the emulsion measurement /15/ /18/, neutron DDX /19/ and magnetic spectrometer /16/. The present result is consistent with other exper-
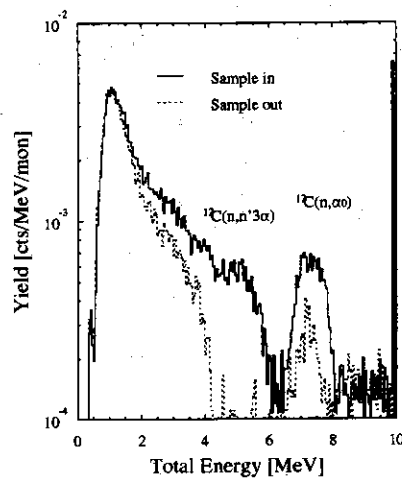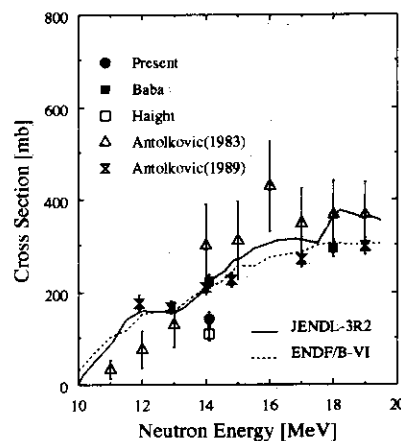
Figure 11: The sum spectrum of FW-BW coincidence events

Figure 12: ^{12}C(n,n'3α) Cross sections

iments, although more detailed estimation of detection efficiency will lead to a slightly higher value, because the above estimation ignores the count loss by the threshold level and self-absorption. More realistic detection efficiency can be obtained by the data on decaying scheme of ^{12}C studied by the emulsion measurement /18/.

Two methods described above will enable to study the (n,xα) cross sections of light nuclei in an almost 2 π or 4 π solid angle provided by GIC. For more efficient experiment, we will adopt the method of measurement using a grid signal /20/. By the method, we can obtain the data for both hemisphere in a single measurement.

References

[1] N.Ito M.Baba, S.Matsuyama, I.Matsuyama and N.Hirakawa, *Nucl. Instrum. Methods*, **A337**, 474 (1994)

[2] M.Baba, N.Ito, I.Matsuyama N.Hirakawa, S.Chiba, T.Fukahori, M.Mizumoto, K.Hasegawa and S.Meigo, *J. Nucl. Sci. Technol.*, **31**, 745(1994)

[3] M.Baba, N.Ito, S.Matsuyama, I.Matsuyama and N.Hirakawa, *Proc. Int. Conf. on Nucl.Data for Sci. and Technol.*, (1994 Gatlinburg) pp.941

[4] A.A.Goverdovski et al., *Proc.Int.Conf.Nucl.Data for Sci.Technol.*, (1994, Gatlinburg), p.117

[5] M.Baba, M.Takada, T.Iwasaki, S.Matsuyama, T.Nakamura, H.Ohguchi, T.Nakao, T.Sanami and N.Hirakawa, *Nucl. Instrum. Methods*, to be published.

[6] A.B.Smith et al., *"Fast Neutron Total and Scattering Cross Sections of ^{58}Ni and Nuclear Models"*, **ANL/ADM-120**

[7] F.G.Perey, *Phys. Rev.* **131**, 745 (1963)

[8] O.F.Lemos, *Orsay Report, Series A*, **No. 136** (1972)

[9] A.Gilbert and A.G.W.Cameron, *Can. J. Phys.*, **43**, 1446 (1965)

[10] J.Rapaport, V.Kulkarni and R.W.Finlay, *Nucl. Phys.*, **A330**, 15 (1979)

[11] E.Wattecamps, *Proc. Int. Conf. on Nucl. Data for Sci. and Technol.*, (Jülich, Germany 1991) pp.310

[12] A.Paulsen, H.Liskien, F.Arnotte and R.Widera, *Nucl. Sci. Eng.*, **78**, 377 (1981)

[13] H.Kalka, M.Torjiman and Seeliger, *Phys. Rev.* **C40**, 1619 (1989)

[14] H.Kalka, *Z. Phys.*, **A231**, 298 (1992)

[15] B.Antolkovic, I.Slaus and D.Plenkovic, *Nucl. Phys.* **A394**, 87 (1983)

[16] R.C.Haight, S.M.Grimes, R.G.Johnson and H.H.Barschall, *Nucl.Sci.Eng.*, **87**, 41 (1984)

[17] R.C.Haight and S.M.Grimes, unpublished.

[18] B.Antolkovic, G.Dietze and H.Klein, *Nucl. Sci. and Eng.*, **107**, 1 (1991)

[19] M.Baba, S.Matsuyama, M.Fujisawa, T.Iwasaki, S.Iwasaki and R.Sakamoto, *JAERI-M*, **90-025**, p.383

[20] C.Budtz-Jorgensen, H.-H.Knitter, Ch.Straede, F.-J.Hambsch and R.Vogt, *Nucl. Instrum. Meth.* **A258**, 209 (1987)

The First Internet Symposium on Nuclear Data: Paper No. 23

3.23 Comparision of decay and yield data between JNDC2 and ENDF/B-VI

K. Oyamatsu, M. Sagosaka and T. Miyazono

Department of Energy Engineering and Science, Nagoya University

Furo-cho , Chikusa-ku , Nagoya , 464-01 JAPAN

e-mail: oyak@luna.nucl.nagoya-u.ac.jp

This work is intended to be our first step to solve disagreements of the decay heat powers between measurements and summation calculations. We examine differences between nuclear data libraries to complement our uncertainty evaluation of the decay heat summation calculations only with ENDF/B-VI. The comparison is made mainly between JNDC2 and ENDF/B-VI while JEF2.2 decay data is also discussed. In this study, we propose and use a simple method which is an analogue of the overlap integral of two wave functions in quantum mechanics. As the first step, we compare the whole input nuclear data for the summation calculations as a whole. We find a slight difference of the fission yields especially for high-energy neutron induced fissions between JNDC2 and ENDF/B-VI. As for the decay energies, JNDC2, ENDF/B-VI are quite similar while JEF2.2 is found significantly different from these two libraries. We find substantial differences in the decay constant values among the three libraries. As the second step, we calculate the decay heat powers with FPGS90 using JNDC2 and ENDF/B-VI. The total decay heat powers with the two libraries differ by more than 10% at short cooling times while they agree well on the average at cooling times longer that 100 (s). We also point out nuclides whose contributions are significantly different between the two libraries even though the total decay heats agree well. These nuclides may cause some problems in predicting aggregate spectra of β and γ rays as well as delayed neutrons, and are to be reviewed in the future revision of decay and yield data.

1. Introduction

The calculated aggregate decay heat powers in the summation method have come to agree well with the measured decay powers at cooling times between 2 and 10^4 (s) in the cases of burst fissions for major actinide fissiles (e.g. ^{235}U, ^{238}U, ^{239}Pu and

241Pu). However the measurements have been performed only for these fissioning systems in the limited range of cooling times. Then, it is necessary to examine its prediction power at other cooling times and/or for other fissioning systems.

Our group has been evaluating the prediction power of the summation calculation with the present nuclear data libraries for various fissioning system. On one hand, Ohta et al. [1] and paper 012 in this symposium performed the conventional uncertainty analysis of the summation calculations with the evaluated nuclear data in ENDF/B-VI [2]. Paper 012 is intended to strengthen the justification of the approximation which was adopted in Ref. [1]. In this paper, we try to evaluate the difference among nuclear data libararies.

In Sec. 2, we review the decay heat summation calculations formally. In Sec. 3, we propose a simple method to measure the difference between two data sets. The analyses in the subsequent sections are performed with this method. In Sec. 4, we compare the yield and decay data of JNDC Version 2 [3], ENDF/B-VI and JEF2.2. In Sec. 5 we examine the decay heat powers from indivisual nuclides, which cause substantial difference in the total decay heat power between JNDC2 and ENDF/B-VI. We summarize the results of this paper in Sec. 6.

2. Review of decay heat summation calculations

In this section, we briefly review the summation calculation of the fission product decay heat power. For simplicity, we consider the case of burst fission and disregard the neutron reactions.

The total decay heat power from fission product nuclides, $P(t)$, are given by the sum of the contributions from all indivisual nuclides:

$$P(t) = \sum_i E_i \lambda_i n_i(t) .\tag{1}$$

Here, λ_i and E_i are the decay constant and the average decay energy of nuclide i, respectively. The number of atoms of nuclide i, $n_i(t)$, is the solution of the linear differential equation

$$\frac{dn_i(t)}{dt} = -\lambda_i n_i(t) + \sum_j a_{j \to i} \lambda_j n_j(t) ,\tag{2}$$

where $a_{j \to i}$ is the production ratio of nuclide i from a decay of nuclide j. For the burst fission, we solve Eq. (2) with initial condition

$$n_i(0) = y_i \tag{3}$$

with y_i being the independent yield of nuclide i.

The complications in solving Eqs. (2) and (3) lies in the dependence on the

decay constants. However, if we consider a verctor,

$$n(t) = \begin{pmatrix} n_1(t) \\ n_2(t) \\ \vdots \\ n_N(t) \end{pmatrix},$$ (4)

we can easily obtain the formal solution in the matrix representation. It is useful to define vectors of the independent yields and the average decay energies as

$$y = \begin{pmatrix} y_1 \\ y_2 \\ \vdots \\ y_N \end{pmatrix} \text{ and } E = \begin{pmatrix} E_1 \\ E_2 \\ \vdots \\ E_N \end{pmatrix},$$ (5)

respectively. We also define a matrix of decay constans as

$$\Lambda = \begin{pmatrix} -\lambda_1 & \lambda_{2 \to 1} & \cdots & \lambda_{N \to 1} \\ \lambda_{1 \to 2} & -\lambda_1 & \cdots & \lambda_{N \to 2} \\ \vdots & \vdots & \ddots & \vdots \\ \lambda_{1 \to N} & \lambda_{2 \to N} & \cdots & -\lambda_N \end{pmatrix}.$$ (6)

Here, the partial decay constant from nuclide j to nuclide i, $\lambda_{j \to i}$, is defined as

$$\lambda_{j \to i} = a_{j \to i} \lambda_j,$$ (7)

where

$$\lambda_j = \sum_{i \neq j} \lambda_{j \to i}.$$ (8)

Then, Eq. (2) can be written simply as

$$\frac{dn(t)}{dt} = \Lambda n(t)$$ (9)

with the initial condition

$$n(0) = y$$ (10)

in place of Eq.(3). The formal solution of Eqs. (9) and (10) is given by

$$n(t) = \exp(\Lambda t) y.$$ (11)

The total decay heat power can also be written in a simple form as

$$P(t) = {}^t E \begin{pmatrix} \lambda_1 & 0 & \cdots & 0 \\ 0 & \lambda_2 & \cdots & 0 \\ \vdots & \vdots & \ddots & \vdots \\ 0 & 0 & \cdots & \lambda_N \end{pmatrix} n(t) = {}^t E \Lambda_d \exp(\Lambda t) y$$ (12)

with

$$\Lambda_d = \begin{pmatrix} \lambda_1 & 0 & \cdots & 0 \\ 0 & \lambda_2 & \cdots & 0 \\ \vdots & \vdots & \ddots & \vdots \\ 0 & 0 & \cdots & \lambda_N \end{pmatrix}.$$

(13)

Although the numerical calculations of Eqs. (11) and (12) are not so easy due to complicated dependence on the decay constants, we see clearly that the expression for the total decay heat power is decomposed into three parts, E, $\Lambda_d \exp(\Lambda t)$, and y, which correspond to the average decay energies, decay constants and independent yields, respectively. It is also useful to define a vector of the decay heat powers from indivisual nuclides as

$$P(t) = \begin{pmatrix} E_1 & 0 & \cdots & 0 \\ 0 & E_2 & \cdots & 0 \\ \vdots & \vdots & \ddots & \vdots \\ 0 & 0 & \cdots & E_N \end{pmatrix} \begin{pmatrix} \lambda_1 & 0 & \cdots & 0 \\ 0 & \lambda_2 & \cdots & 0 \\ \vdots & \vdots & \ddots & \vdots \\ 0 & 0 & \cdots & \lambda_N \end{pmatrix} \exp(\Lambda t) y .$$

(14)

In the following, we make the comparision of the nuclear data libraries in two steps. First, we compare vectors of the average decay energies, E, the decay constants,

$$\lambda = \begin{pmatrix} \lambda_1 \\ \lambda_2 \\ \vdots \\ \lambda_N \end{pmatrix}$$

(15)

and independent yields, y, which are the components of the expression of the decay heat power (Eq. (12)). For simplicity, we consider a vector of the decay constants (Eq. (15)). Then, as the second step, we compare $n(t)$ and $P(t)$ which are calculated with the nuclear libraries as input data.

3. Method of comparison

In the previous section, we see that we need to compare pairs of vectors. Any pair of the vectors treated in this paper is not supposed to differ by an order of the magnitude because they represent the same physical quantity. Therefore, we use the direction cosine of two vectors as a measure of the difference between the two vectors.

In the following, we explain the method in the case of the independent yields although the other quantities can be treated in the same way. Let us write the independent yield vectors of different nuclear data libraries as y_i and y_i'. We define "overlap" of the two vectors as
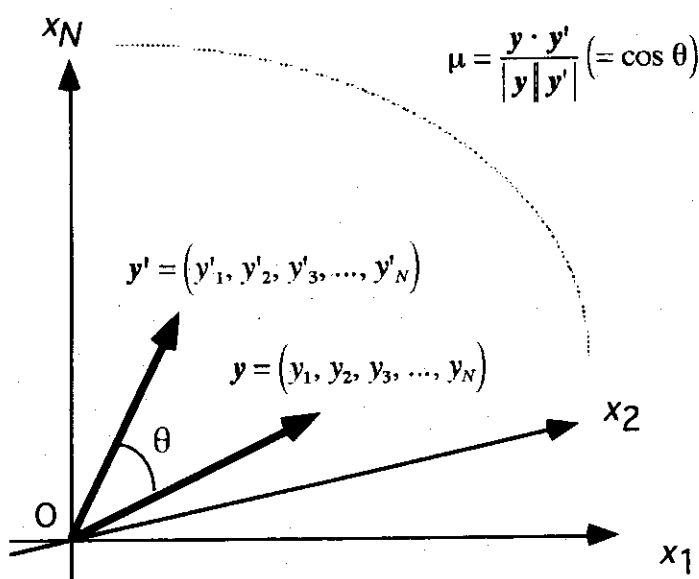
$$\mu = \frac{\boldsymbol{y} \cdot \boldsymbol{y}'}{|\boldsymbol{y}||\boldsymbol{y}'|} \left(= \cos \theta\right)$$

Fig. 1 Definition of overlap μ.

$$\mu = \frac{\boldsymbol{y} \cdot \boldsymbol{y}'}{|\boldsymbol{y}||\boldsymbol{y}'|} = \frac{\sum_{i=1}^{N} y_i \cdot y'_i}{\sqrt{\sum_{i=1}^{N} (y_i)^2 \sum_{j=1}^{N} (y'_j)^2}} \tag{16}$$

The overlap μ is the direction cosine of the two vectors as shown in Fig. 1. The deviation from the value $\mu=1$ ($\theta=0$) gives a measure of the difference between the fission yields. In the extreme cases, $\mu=1$ when y and y' are the same, and $\mu=0$ when they are perpendicular (completely different). The value μ is not very sensitive to the rotation angle in Fig. 1 because for a small angle θ,

$$\mu = \cos \theta \approx 1 - \theta^2 / 2 . \tag{17}$$

We note that $\mu=0.97$ ($\mu=0.866$) corresponds to $\theta=14°$ ($\theta=30°$). Therefore, the difference between the two vectors are considered to be appreciable when $\mu<0.97$.

The overlap μ in the above method is analogous to the overlap integral of two wave functions in quantumn mechanics:

$$\frac{\langle \phi_1 | \phi_2 \rangle}{\sqrt{\langle \phi_1 | \phi_1 \rangle \langle \phi_2 | \phi_2 \rangle}} . \tag{18}$$

4. Comparison between ENDF/B-VI and JNDC Version 2

In this section, we compare the yield and decay data in ENDF/B-VI with those in JNDC version 2. Since the number of fission product nuclides are different in these libraries (1227 in JNDC version 2 (JNDC2), 886 in ENDF/B-VI and 2345 in JEF2.2), care is taken in the following analyses.

4.1. Independent Fission Yield Values

For fission products whose data are not available in ENDF/B-VI, the yield values in ENDF/B-VI are taken to be zero:

$$y_{JNDC2} = \left(y_{1,J}, y_{2,J}, ..., y_{886,J}, y_{887,J}, ..., y_{1227,J} \right),$$

$$y_{ENDF/B-VI} = \left(y_{1,E}, y_{2,E}, ..., y_{886,E}, 0, ..., 0 \right). \tag{19}$$

Figure 2 shows values of the overlap μ for 20 fissioning systems that are available in both JNDC version 2 and ENDF/B-VI. From this figure we see that,

1. yields in the two libraies are different by 1-5.3 % ($0.947 \leq \mu \leq 0.99$). The best case is the ^{235}U thermal fission with $\mu=0.990$,
2. the agreement between the two libraries is the best for thermal fissions, and the worst for high energy fissions.

These yield differences probably reflect the fact that JNDC2 lists much more fission product nuclides because the sources of the yield values are almost the same [4].

The yield differences, together with differences in decay constants in the next subsection, affect the calculated decay heat powers at short cooling times.

Table 1. Comparison of yield data between JNDC2 and ENDF/B-VI

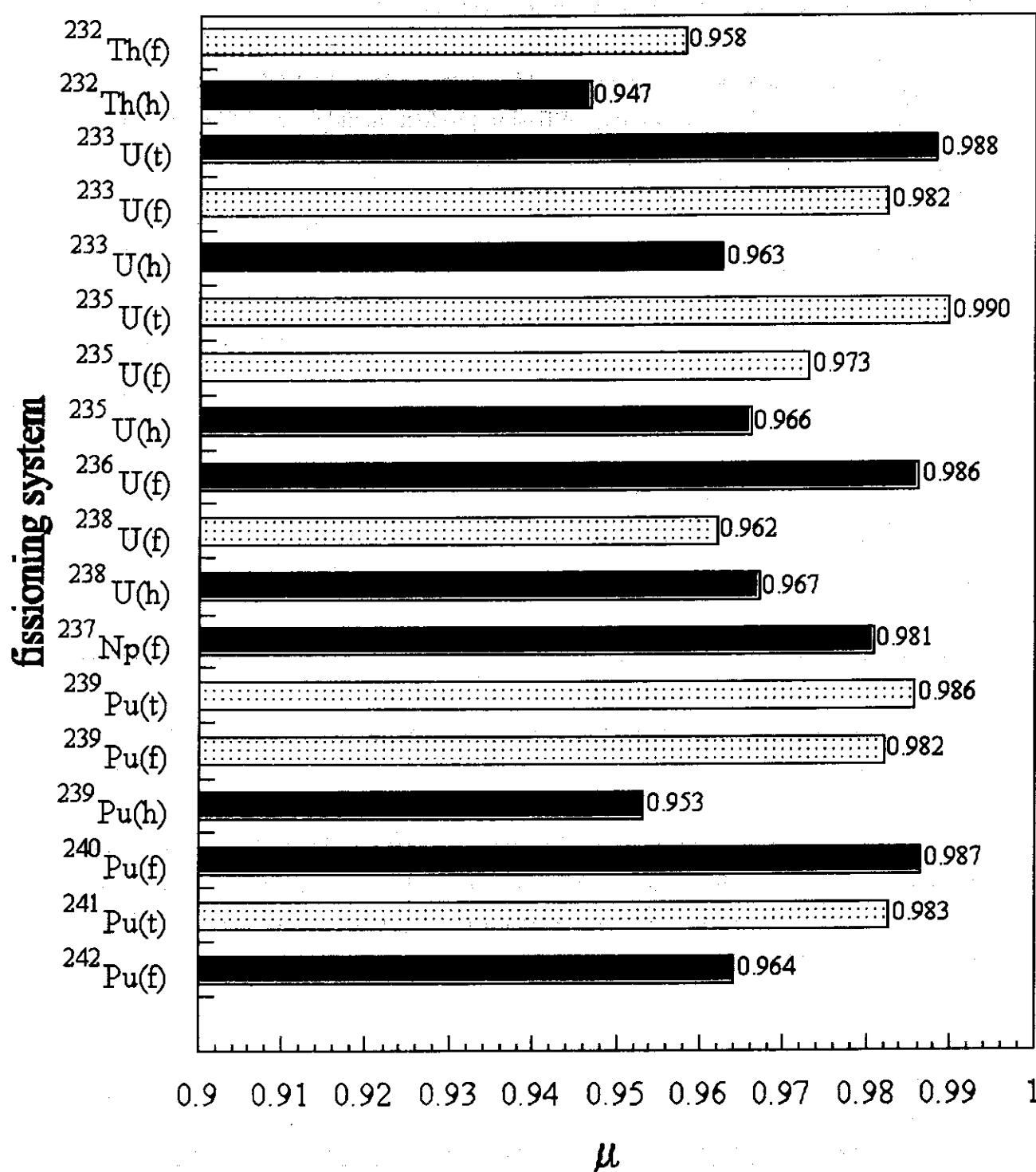|	thermal	fast	high energy
μ	0.983-0.990	0.958-0.987	0.947-0.967
difference (%)	1-2	1-4	3-5

Fig. 2. Values of the overlap μ of the independent fission yields between ENDF/B-VI and JNDC version 2 and ENDF/B-VI. Fissioning systems with lighter bars have the measured decay heat values at Ork Ridge and/or Yayoi. Abbreviations t, f and h stand for thermal, fast and high-energy neutron induced fissions, respectively.

Table 2. Comparison of decay data between JNDC2 and ENDF/B-VI (N=750)

	λ	E_β	E_γ	Q
μ	0.838	0.997	0.994	0.995
difference (%)	14.2	0.3	0.6	0.5

Table 3. Comparison of decay data between JNDC2 and JEF2.2 (N=782)

	λ	E_β	E_γ	Q
μ	0.853	0.934	0.841	0.996
difference (%)	14.7	6.6	15.9	0.4

Table 4. Comparison of decay data between ENDF/B-VI and JEF2.2 (N=634)

	λ	E_β	E_γ	Q
μ	0.877	0.940	0.887	0.997
difference (%)	12.3	6.0	11.3	0.3

4.2. Decay Constants, Decay Energies and Q Values

As for the comparison of decay constants, decay energies and Q values, we also consider JEF2.2. The comparison is made among the three libraries. We consider only fission products which are available in two libraries. For example, we consider the following two vectors

$$\lambda_{JNDC2} = \left(\lambda_{1,J}, \lambda_{2,J}, ..., \lambda_{886,J} \right) , \lambda_{ENDF/B-VI} = \left(\lambda_{1,E}, \lambda_{2,E}, ..., \lambda_{886,E} \right) \tag{20}$$

for the comparison of the decay constant between JNDC2 and ENDF/B-VI. The results are shown in Tables 2, 3 and 4 and are summerized as follows:

1. The decay constants are remarkably different among three libraries.
2. The decay energies in JNDC2 and ENDF/B-VI are almost equal.
3. The decay energies in JEF2.2, especially gamma decay energies, are substantially different from those in JNDC2 and ENDF/B-VI.

The decay constant differences are probably caused by short half-life nuclides whose extremely large decay constant values are uncertain. The differences in decay constants together with yield differences affect the decay heat calculations at short cooling times.

On one hand, between JNDC2 and ENDF/B-VI, there are small differences in yields and large differences in decay constants. On the other hand, JEF2.2 has different yields, decay constants and decay energies from JNDC2 and ENDF/B-VI. Therefore, the summation calculations with JEF2.2 are expected to give appreciably different results from those obtained with JNDC2 or ENDF/B-VI.

5. Difference in summation calculations

In this section we compare the results of the summation calculations between JNDC2 and ENDF/B-VI. Specifically, the comparision is made for the indivisual contributions $n(t)$ and $P(t)$, and the total decay heat power. The purpose of this comparison is to point out nuclear data which cause large differences in the total decay heat power. We also note that the differences of individual contributions affect more significantly the spectra of beta and gamma rays, and properties of delayed neutrons.

As an example, we show the case of the fast fission of ^{238}U. This is the case that the summation calculation with either library agrees well with the measured decay heat power at Yayoi. Figure 3 shows the ratio of the calculated total decay heat powers with the two libararies. Between cooling times 10 and 10^{10} (s), the calculated total decay heat powers agree well within a few %.
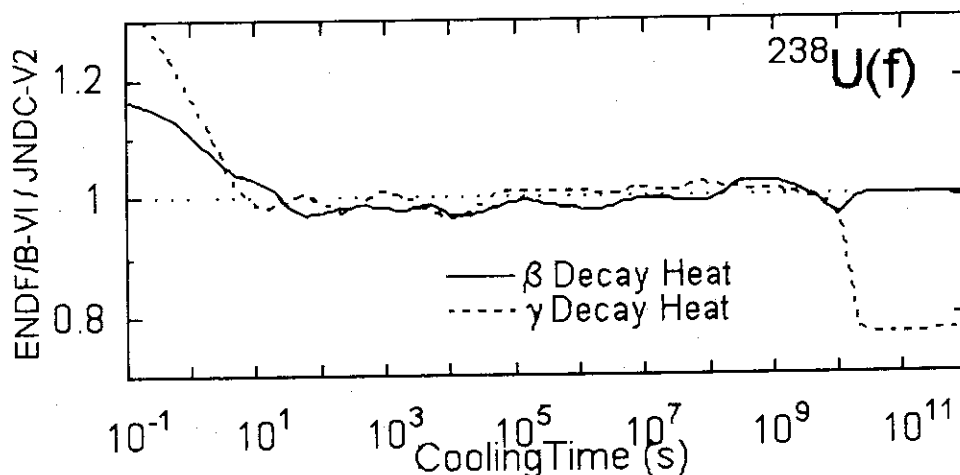

Fig. 3. Comparison of the calculated decay heat power between JNDC2 and ENDF/B-VI.
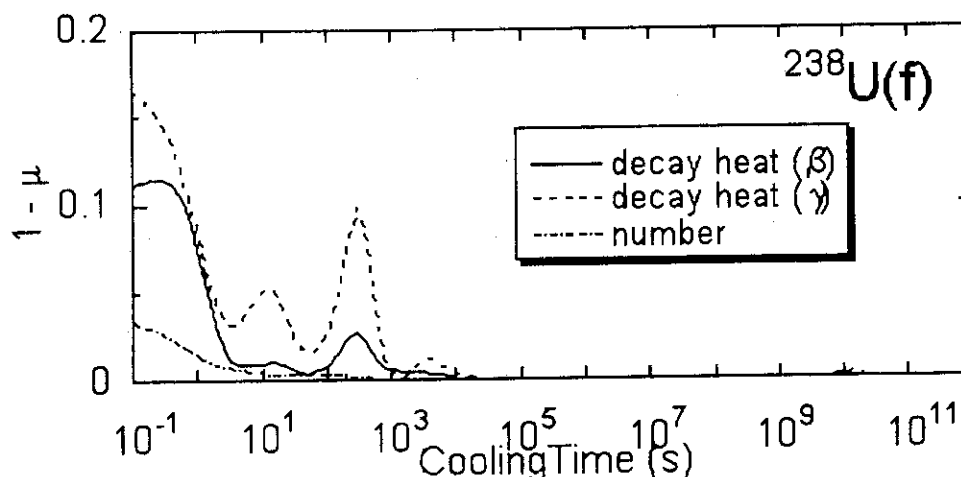
Fig. 4. Overlap μ for $n(t)$ and $P(t)$ in the case of the fast fission of ^{238}U. The summation calculations are performed with JNDC2 and ENDF/B-VI.

However, how about the contributions from indivisual nuclides? Figure 4 depicts overlap μ for $n(t)$ and $P(t)$. We see that indivisual contributions of decay power (especially gamma decay power) are substantially different at $t < 10^3$ (s) although the total decay power agrees well at $t > 10$ (s).

It is interesting to note that $P(t)$ differs more than $n(t)$. From the results of the previous section, we see that difference of $P(t)$ becomes larger due to the appreciable differences of decay constant values of short half-life nuclides.

The overlap μ for $P(t)$ has some peaks at short cooling times. These peaks are considered to be caused by a few nuclear data. It is interesting to note that there are some peaks in the overlap μ even if the total decay heat power is nearly equal. An example is the peak at 300 (s) in Fig.4. However, this peak is found not very interesting because it only reflects whether the ^{132}Sn decays to the ^{132}Sb isometric or ground states. In the case of the ^{238}U fast fission, the 4 % yield difference does not affect the total decay heat between 10 and 10^{10} (s). The differnces of $n(t)$ and $P(t)$, which seems to be caused mainly by differences of the decay constant and energy values, become sufficiently small at $t > 10^4$ (s).

As another example, we show the case of the ^{239}Pu high energy fission in

Figs. 5 and 6. In this case, the agreement of the total decay heat is worse than the case of the ^{238}U fast fission although the yield differences are almost the same (about 5 %). Furthermore, the differences of $n(t)$ and $P(t)$ are seen in the wider range of the cooling times. Even at 10^{10} (s), the $P(t)$ difference for the β decay heat is appreciable corresponding to the large difference of the total decay heat powers.
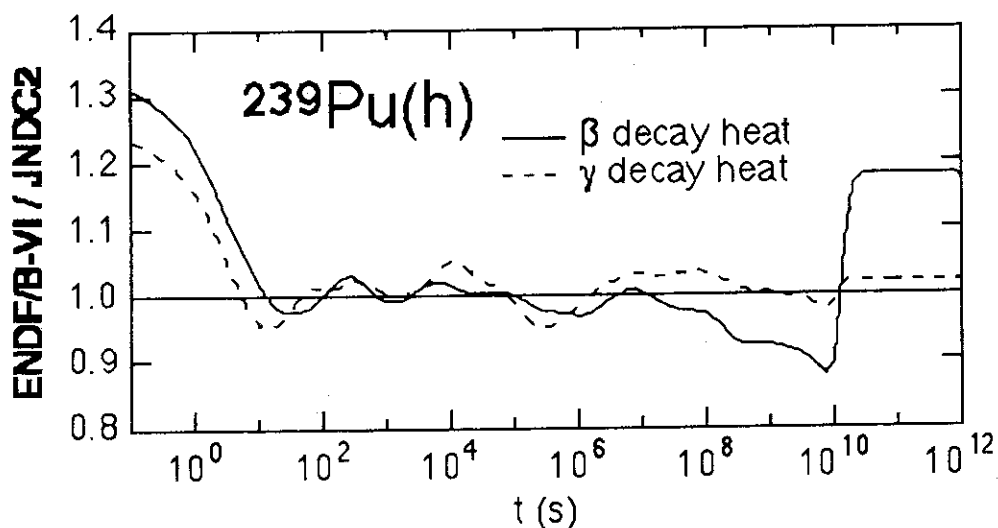

Fig. 5. Ratio of the calculated total decay heat powers in the case of the ^{239}Pu high energy fission. The summation calculations are performed with JNDC2 and ENDF/B-VI.
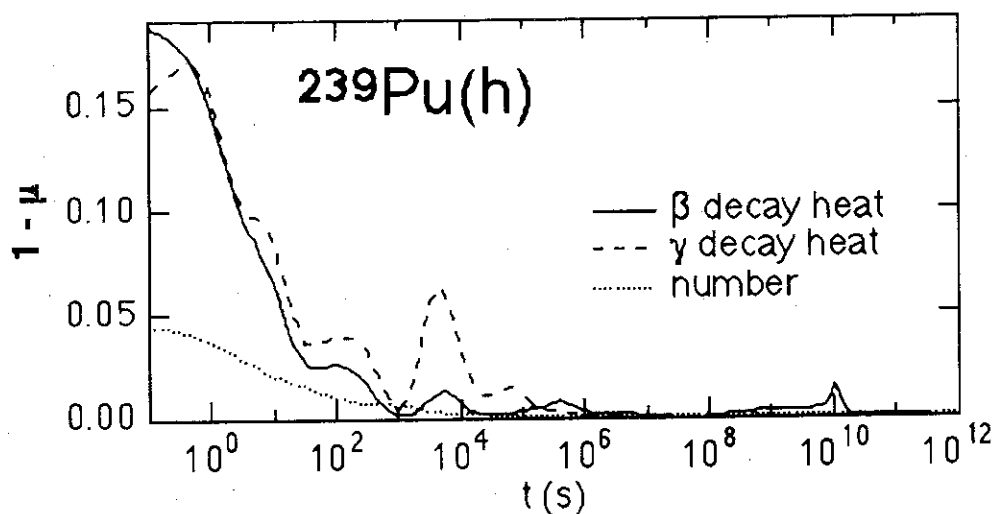

Fig. 6. Overlap μ for $n(t)$ and $P(t)$ in the case of the ^{239}Pu high energy fission. The summation calculations are performed with JNDC2 and ENDF/B-VI.

From the analyses using the overlap μ for $n(t)$ and $P(t)$, we find that:

1. The large differences of indivisual contributions can be seen as the peaks of the overlap μ as a function of the cooling time.

2. Each peak is considered to be caused by a few nuclides and can be used to point out the causal nuclear data.

3. The difference of $P(t)$ is larger than that of $n(t)$ reflecting the large differences of decay constants of short half-life nuclides.

4. Even at 10^{10} (s), the appreciable difference of $P(t)$ can be found for some fissioning systems.

6. Summary and future plan

We have seen the differences of yield and decay data for the decay heat summation calculations among nuclear data libraries, mainly between JNDC2 and ENDF/B-VI. The comparison has been also made for the results of the summation calculations between JNDC2 and ENDF/B-VI. The overlap μ is defined and utilized in this study. The major conclusions of this study are

1. As for yield data, JNDC2 and ENDF/B-VI differ by 1-5 %. (Thermal : 1-2 %, fast : 1-4 %, high energy : 3-5 %)

2. Decay energies of JNDC2 and ENDF/B-VI are almost equal.

3. However, decay energies (especially gamma decay energies) of JEF2.2 is substantially different from those of JNDC2 and ENDF/B-VI.

4. Decay constants are different among JNDC2, ENDF/B-VI and JEF2.2. Probably, the short half-life nuclides causes these large differences.

5. The decay heat power calculated with JEF2.2 will be substantially different from those with JNDC2 and ENDF/B-VI especially at short cooling times.

6. The difference of $P(t)$ can be seen as the peaks of the overlap μ as a function of the cooling time.

7. The difference of $P(t)$ is larger than that of $n(t)$ due to the large differences of decay constants of short half-life nuclides.

8. Even at 10^{10} (s), appreciable differences of $P(t)$ can be found for some fissioning systems.

The detailed list of nuclides which cause large differences between libraries is rather bulk and has not been completed yet. However, we are ready to answer the causal nuclides upon request if the fissioning systems and the cooling times are specified. We

also plan to publish the list elsewhere in order to help reviewing nuclear data for the future revison of the libraries.

We also intend to examine the yield data, $n(t)$ and $P(t)$ for JEF2.2 in order to complete the survey of the present uncertainties among libraries. These quantities are not treated in this paper simply because we have obtained JEF2.2 very recently.

In the next step of this study, we plan to examine the consistency among measurements performed at various places with the same method described in this paper so that we obtain the most relaible measured data. Then, we will be able to overcome the present disagreement among measured and calculated decay heat values by various authors.

Acknowledgements

References

1) Ohta, H., Oyamatsu, K.and Tasaka, K.:"A Simple Method for Evaluation of Uncertainties in Fission Product Decay Heat Summation Calculations", JAERI Conf96-008.

2) see, for example, Katakura, J. and England, J.R.:"Augmentation of ENDF/B Fission Product Gamma-Ray Spectra by Calculated Spectra", LA-12125-MS(1991).

3) Tasaka, K., Katakura, J., Ihara, H., Yoshida, T., Iijima, S., Nakashima, R., Nakagawa, T., and Takano, H.:"JNDC Nuclear Data Library of Fission Products - 2nd Version", JAERI 1320 (1988).

4) Yoshida, T., private communication.

The First Internet Symposium on Nuclear Data: Paper No. 24

3.24 **Measurements of Spallation Neutrons from a Thick Lead Target Bombarded with 0.5 and 1.5 GeV Protons**

Shin-ichiro Meigo[*], Hiroshi Takada[*], Satoshi Chiba[*], Tatsushi Nakamoto[**],
Kenji Ishibashi[**], Naruhiro Matsufuji[**], Keisuke Maehata[**], Nobuhiro Shigyo[**],
Yoshihisa Wakuta[**], Yukinobu Watanabe[†] and Masaharu Numajiri[††]

[*] Japan Atomic Energy Research Institute, Tokai-mura, Naka-gun, 319-11, Japan
[**] Department of Nuclear Engineering, Kyushu University, Hakozaki, Fukuoka, 812, Japan
[†] Energy Conversion Engineering, Kyushu University, Kasuga-koen, Kasuga, 816, Japan
[††] National Laboratory for High Energy Physics (KEK), Oho, Tsukuba, 305, Japan
(E-mail: meigo@linac.tokai.jaeri.go.jp)

Double differential neutron spectra from a thick lead target bombarded with 0.5 and 1.5 GeV protons have been measured with the time-of-flight technique. In order to obtain the neutron spectra without the effect of the flight time fluctuation by neutron scattering in the target, an unfolding technique has also been employed in the low energy region below 3 MeV. The measured data have been compared with the calculated results of NMTC/JAERI-MCNP-4A code system. It has been found that the code system gives about 50 % lower neutron yield than the experimental ones in the energy region between 20 and 80 MeV for both incident energies. The disagreements, however, have been improved well by taking account of the in-medium nucleon-nucleon scattering cross sections in the NMTC/JAERI code.

1. Introduction
With recent progress of the accelerator technology, various utilizations of a high energy and high current proton accelerator are proposed for various purposes such as neutron scattering study and accelerator driven actinide transmutation/1/. For the design of the target and shielding of the accelerator facilities, it is necessary to estimate the reaction rate and the neutron production in a thick medium in the energy region up to several GeV as accurately as possible. Nucleon-Meson Transport Codes such as NMTC/JAERI/2/ and LAHET/3/ have been widely employed for the neutronics calculation.

It is generally known that the codes can describe the particle productions and the transport in a thick medium. The accuracy of the codes is not completely satisfactory yet. In order to comprehend and improve the accuracy of the code, several studies/4,5/ have been performed from both the theoretical and the experimental points of view. A series of the measurements of neutron production double differential cross sections were carried out at LANL/6,7,8,9/ and KEK/10/. In LANL, the neutron yields in stopping-length targets were also measured with 113 and 256 MeV protons/5,6/. There is only a few data/11/ on the neutron spectra from thick targets bombarded with protons at incident energies higher than 256 MeV.

In this study, the neutron spectra from a thick lead target bombarded with 0.5 and 1.5 GeV protons have been measured at 6 angles between 15° and 150° using the TOF and unfolding techniques. The measured data were compared with calculated results of the NMTC/JAERI-MCNP-4A code system.

2. Experimental Procedure

2.1 *Incident Protons and Target*

The experiment was carried out at the π2 beam line of National Laboratory for High Energy Physics (KEK) in a series of double differential neutron production cross section measurements/10/. The illustration of the experimental arrangement is shown in Fig. 1. The incident proton was supplied as the secondary particle generated by an internal target which was placed in the accelerator ring of the 12 GeV proton synchrotron. The intensity of the incident particles was so weak ($<10^5$ particles/macro pulse) that incident protons were counted one by one with beam scintillators. The size of the incident beam was 2.0 cm in the perpendicular plane and 1.6 cm in the horizontal one in FWHM, respectively. The protons were identified from the pions produced at the internal target by the time-of-flight (TOF) technique with a pair of scintillators (Pilot U). That were located at a separation distance of 20 m. Each Pilot U scintillator was connected with two photomultipliers on opposite sides. The beam damp was a carbon block pile of 0.5×0.5 m^2 in the area and 1 m in thickness. The carbon was surrounded by sufficiently thick iron blocks except on the beam-incident surface. The distance from the target to the beam dump was 8.5 m.

The lead target was a rectangular parallelepiped $15 \times 15 \times 20$ cm^3 whose purity was 99.95%. It was thick enough to stop 0.5 GeV protons completely, while it caused the energy loss of 0.26 GeV on average for 1.5 GeV protons.

2.2 *Neutron Detector*

NE213 scintillators having the size of 12.7 cm in diameter and 12.7 cm in thickness were used as neutron detectors. The detectors were placed at angles of 30°, 60°, 90°, 120° and 150° to the beam axis and at a common distance of 1 m from the target. At the angle 15°, the distance was chosen 1.5m so that the higher energy resolution was achieved. In order to reject the events induced by the charged particles (i.e. π, p, d) produced in the lead target, NE102A scintillators of $17 \times 17 \times 1$ cm^3 were used as veto counters. They were placed in front of the NE213 scintillators at a distance of 2 cm.

The pulse height of the neutron detectors was calibrated by standard gamma ray measurements. The gamma ray energies are summarized in Table 1 with the light outputs at the half height of Compton edges. The light output was derived from the empirical formula of Dietze/12/ and expressed in the unit of electron equivalence. A good linearity between the light output and the measured signal was verified below 4.33 MeVee.

Table 1. Pulse height at the half height of Compton edge for the source gamma ray

Gamma Ray Source	Energy (MeV)	Pulse Height(MeVee) [a]
^{137}Cs	0.662	0.493
^{60}Co	1.173, 1.333	1.074 [b]
Am-Be	4.439	4.331

a 1 MeVee corresponds to the light output given by 1 MeV electron.

b Only one Compton edge is observed, because NE213 has poor resolution to distinguish 2 Compton edges. This light output is calculated with the average energy of 2 gamma rays.

2.3 *Electronic Circuit*

The diagram of the electronic circuit is shown in Fig. 2. When the coincidence of the signal from all beam detectors took place, a pulse with a time duration of 150 ns was sent to the next coincidence unit. The events arising from incident pions were eliminated in the

coincidence of all beam detectors. The number of incident protons was accumulated by the scaler. A good discrimination for the incident proton against the pion was achieved so that the uncertainty of the counting could be less than 1 %.

Anode signals of the photomultipliers, which were connected NE213 scintillators, were branched out to four pulses. One pulse was put into CFD to produce the start signal of TOF measurement. Three pulses were put into ADCs that collected the charge of pulse during the gate signal duration. In order to reject the events induced by gamma rays, the two-gate integration method/13/ was adopted. The conceptual diagram of this method is shown in Fig. 3. For the measurement of the fast and tail part of scintillation, two different gate signals was supplied to the ADCs. The total gate also employed to measure the pulse height of the scintillation. Data were taken event by event with a list mode and stored in the magnetic tape for an off-line analysis.

3. Data Analysis

3.1 TOF Analysis

An example of the TOF spectrum from the target is shown in Fig. 4. The horizontal axis of the TOF spectrum was reversed because the neutron detector made the start signal. A sharp peak due to prompt gamma rays is observed around 3100 channel. The width was typically 1.5 ns in FWHM. After the neutron events were distinguished from the gamma ray ones, the TOF spectrum of the neutrons was obtained as shown in the bottom of Fig. 4. By interposing an iron block of 50 cm in thickness between the target and detector, the room back ground was measured and found to be negligible.

The energy spectrum of the neutron is converted from the net TOF spectrum by the following expression,

$$\frac{d^2n}{dEd\Omega} = \frac{N_n}{N_p\ \varepsilon\Delta\Omega\ \Delta E}, \quad E = m_nc^2\left(1\Big/\sqrt{1 - L^2\Big/\left(c\left(t - t_0\right) + L\right)^2} - 1\right), \quad (1)$$

where N_n and N_p are the counts of neutrons and incident protons, respectively, e the detection efficiency for the neutron, DW the solid angle sustained by the detector to the center of the target, E the neutron energy, t the flight time, m_n the rest mass of the neutron, c the light speed, t_0 the flight time of the prompt gamma ray and L the distance from the center of target to the center of the detector. Here, the distance from the neutron producing point to the detection point is assumed to be L. This assumption was confirmed by a Monte-Carlo calculation which gave the standard deviation of the distance L smaller than 6 %.

The detection efficiencies were calculated for the energy range below 80 MeV with SCINFUL/14/ and up to 1.5 GeV with Cecil/17/. The results are shown with the experimental ones in Fig. 5. It is observed that SCINFUL results agree with the experimental data/15,16/ much better than Cecil. In the TOF analysis, therefore, the SCINFUL results were used as the detection efficiency below 80 MeV. Above 80 MeV, on the other hand, the calculated efficiency of Cecil adjusted to connect smoothly with that of SCINFUL at 80 MeV was employed. Two neutron spectra were obtained with the efficiency using the ^{137}Cs and ^{60}Co biases which were set at the half height of Compton edges for ^{137}Cs and ^{60}Co gamma rays, respectively. The neutron spectra determined with ^{137}Cs bias agreed with those determined with the ^{60}Co bias within the statistical errors. Since the statistical accuracy of the spectra obtained with the ^{137}Cs bias was better that of ^{60}Co bias, the results with the ^{137}Cs bias were adopted as the resultant neutron spectra.

3.2 *Unfolding Analysis*
Since the target was thicker than the mean free path for the neutrons with the energy below 200 MeV, most neutrons react with target nuclei more than once in the transport process. The scattered neutron has some delay in the flight time in comparison with the neutron which comes out the target without scattering. The delay makes apparent neutron energy spectrum obtained by the TOF technique softer than the real one. We analyzed the pulse height distribution to obtain the neutron spectrum by the unfolding technique independently. The unfolding analysis employed the code FORIST/18/ using a response matrix calculated with SCINFUL. The neutron spectra in the energy region below 14 MeV were obtained by the unfolding technique, because the pulse height was saturated above 14 MeV.

In Fig. 6, the neutron spectrum at the angle of 30° obtained by the unfolding technique is compared with the one by the TOF technique for 500 MeV proton incidence. In the region below 3 MeV, the difference of the neutron yield was larger than 50 % of that obtained by the TOF technique. This difference is ascribed to the ambiguity of the efficiency around the ^{137}Cs bias used in the TOF technique. Therefore, the neutron spectra reduced by the unfolding analysis is more reliable than those obtained by the TOF technique below 3 MeV. The results of unfolding analysis agree with those of TOF quite well between 3 and 14 MeV. This result indicates that the time fluctuation by the scattering is negligibly small above 3 MeV. In consequence, the neutron energy spectrum was determined by connecting the result of the TOF technique with that of the unfolding technique at 3 MeV. As for the neutron below 1.5 MeV, however, the error of the unfolding analysis was so large that the minimum energy of measured spectra were decided to be 1.6 MeV.

4. Calculation
The calculation was carried out with NMTC/JAERI/2/ and MCNP-4A/19/. NMTC/JAERI calculated the nuclear reactions and the particle transport above 20 MeV. MCNP-4A calculated the neutron transport below 15 MeV using a continuous energy cross section library FSXLIB-J3R2/20/ processed from the nuclear data file JENDL-3.2/21/. In NMTC/JAERI, the systematics of Pearlstein/22/ was implemented to estimate the total, the elastic and non-elastic nucleon-nucleus cross sections in the transport calculation part. The level density parameter derived by Baba/23/ was also employed in the statistical decay calculation in NMTC/JAERI.

Additional calculations were also performed by substituting the in-medium nucleon-nucleon cross sections (NNCS) for the free ones in the nuclear reaction calculation part of NMTC/JAERI. In this calculation, were employed the in-medium NNCS parametrized similarly to those of Cugnon/24/.

5. Results and Discussion
The present experimental spectra are shown in Figs. 7 and 8. The uncertainty of the present data is given in Table 2. The uncertainty of the neutron yield mainly comes from the statistical error and the uncertainty of the detection efficiency. The uncertainty of the detection efficiency is estimated at 3.0% for the neutron energy below 20 MeV. With the increase of neutron energy, the uncertainty becomes larger because of the increasing ambiguity the cross section used in the calculation.

The neutron energy resolution is also given in Table 2. It was determined from the uncertainty of the flight time and the flight path. The time uncertainty is derived from the

time resolution of the detector and the fluctuation of the time that the incident protons take to move from an incident point to a reaction point. The time resolution of the detector has been determined to be 0.4 ns in the standard deviation by the width of the prompt gamma peak of the thin target measurements/10/. The time fluctuation of 0.6 and 0.4 ns determined for the 0.5 and 1.5 GeV incident protons, respectively. The standard deviation was approximated to a half value of the transit time of protons in the target which was obtained by Janny/25/. The uncertainty of the flight path was estimated at 6.0 cm by the Monte-Carlo calculation on condition that the neutrons are produced uniformly in the target and detected uniformly in the detector. Since the condition is ignored the correlation between the time fluctuation for incident protons and the flight path, the real energy resolution are better than that of described here.

Table 2. Uncertainty and energy resolution of neutron spectra expressed in the standard

Neutron Energy (MeV)	Uncertainty (%)				Energy Resolution (%)
	Statistical Error	Detection Efficiency	Number of Incident Proton	Neutron Yield	
3	3 ~ 7	3		4 ~ 7	10 ~ 11
10	5 ~ 10	3		6 ~ 11	10 ~ 11
15	6 ~ 10	3		6 ~ 11	12 ~ 13
20	6 ~ 10	10	1	6 ~ 11	12 ~ 14
50	8 ~ 30	10		13 ~ 32	13 ~ 17
100	7 ~ 46	15		17 ~ 46	16 ~ 22
200	11 ~ 20*	15		19 ~ 25*	20 ~ 32

* For the angle smaller than 90°

The calculated results of the NMTC/JAERI-MCNP-4A code system, which are smeared with the energy resolution, are also shown in Figs. 7 and 8. It is observed that the results calculated with the free NNCS are in good agreement with the experimental ones in the lower energy region below 20 MeV at all angles for both incident energies. The calculated results, however, are about 50 % or more lower than the experimental data between 20 and 80 MeV at all angles. On the other hand, the results calculated with the in-medium NNCS shows much better agreement with the experimental ones. This improvement is ascribed to the fact that the increase of the high energy nucleon emission diminishes the excitation energy of a residual nucleus so that the neutron emission from the evaporation process is suppressed. The calculation with the in-medium NNCS successfully reproduces the overall measured neutron spectra in the angular region smaller than 60° for both incident energies although the codes give slightly lower neutron yields below 10 MeV. The underestimation for the backward neutron emission, however, still remains.

In order to investigate the cause of the discrepancy between the calculations and the experiments, the double differential neutron production cross sections were also calculated with the in-medium NNCS for the incident energies of 0.8 and 1.5 GeV, respectively. The results are compared with the experiments/9,10/ in Figs. 9 and 10. It is found that the agreement between the calculated and the experimental results for the thick target is as in the same level for that in the thin target. This indicates that the nuclear reaction calculation part should be improved in NMTC/JAERI. Some studies/5,26/ showed that the inclusion of the preequilibrium process or the refraction and reflection process improved the backward

neutron emission significantly. By the inclusion of those processes, the disagreement of the thick target will be more improved.

6. Conclusion

The neutron spectra from a thick lead target bombarded with 0.5 and 1.5 GeV protons were measured at 6 angles between 15° and 150°. We have obtained the accurate neutron spectra in the energy region above 1.6 MeV using the TOF and unfolding techniques with the neutron yield uncertainty of 7 % at 3 MeV and 25 % at 200 MeV. The calculation was also carried out with the NMTC/JAERI-MCNP-4A code system. It was found that results showed fairly good agreement with the experiments, but gave about 50 % lower neutron yield in the energy region between 20 and 80 MeV. The calculation with the in-medium NNCS achieved good agreement with the experiments. The calculation, however, could not reproduce the backward neutron emission. It is of interest to make systematic experiments with other targets for further investigation of the accuracy of NMTC/JAERI including the in-medium NNCS.

References
[1]   For example, T. Takizuka, et al., *Conceptual Design Study of an Accelerator-based Actinide Transmutation Plant with Sodium-cooled Solid Target/Core*, Proc. of OECD/NEA Mtg., Argonne, 398 (1993).
[2]   Y. Nakahara and T. Tsutsui, *A Code System for High Energy Nuclear Reactions and Nucleon-Meson Transport Code*, JAERI-M 82-198 (1982), [in Japanese].
[3]   R. E. Prael and H. Linchtenstein, *Users Guide to LCS: The LAHET Code System*, LA-UR 89-3014 (1989).
[4]   *Intermediate Energy Nuclear Data: Models and Code*, Proc. of OECD/NEA Mtg., Paris (1994).
[5]   N. Yoshizawa, et al., *J. Nucl. Sci. Technol.*, **32**, 601 (1995).
[6]   M. M. Meier, et al., *Nucl. Sci. and Eng.*, **102**, 309 (1989).
[7]   M. M. Meier, et al., ibid., **104** (1990) 339
[8]   S. Stamer, et al., *Phys. Rev.*, **C47**, 1647 (1993).
[9]   M. M. Meier, et al., *Rad. Eff.*, **96**, 73 (1986).
[10] K. Ishibashi, et al., *Measurement of Neutron-Production Double-Differential Cross Sections for Incident Protons of 0.8, 1.5 and 3 GeV*, Proc. Int. Conf, Gatlinburg (1994)
[11] S. Cierjacks, et al., *Phys. Rev.*, **C193**, 1976 (1987).
[12] G. Dietze and H. Klein, *Nucl. Instrum. Meth.* **193**, 529 (1982).
[13] Z. W. Bell, *Nucl. Instrum. Meth* **188**, 105 (1981).
[14] J. K. Dickens, *SCINFUL: A Monte Carlo Based Computer Program to Determine a Scintillator Full Energy Response to Neutron Detection for En Between 0.1 and 80 MeV*, ORNL-6436 (1988)
[15] V.V. Verbinski, et al., *The Response of Some Organic Scintillators to Fast Neutrons*, ORNL-P-993 (1965)
[16] S. Meigo, et al., private communication.
[17] R. A. Cecil, et al., *Nucl. Instrum. Meth.*, **161**, 439 (1979).
[18] R. H. Johnson and B. W. Wehring, *The FORIST UNFOLDING CODE*, ORNL/RSIC-40, p.33 (1976).
[19] J. F. Briesmeister (Ed.), *MCNP A General Monte Carlo N-Particle Transport Code Version 4A*, LA-12625 (1993).

[20] K. Kosako, et al., *A Continuous Energy Cross Section Library for MCNP Based on JENDL-3.2*, JAERI-Data/Code 94-020 (1994).

[21] K. Shibata, et al., *Japanese Evaluated Nuclear Data Library, Version-3 -JENDL-3-*, JAERI-1319 (1990).

[22] S. Pearlstein, *Astrophys. J.*, **346**, 1049 (1989).

[23] H. Baba, *Nucl. Phys.*, **A159**, 625 (1970).

[24] J. Cugnon, T. Mizutani and J. Vandermeulen, ibid., **A352**, 505 (1981).

[25] J. F. Janny, *Atom. Data and Nucl. Data Tables*, **27, 147** (1982).

[26] H. Takada, *J. Nucl. Sci Technol.*, **33**, 275 (1996).
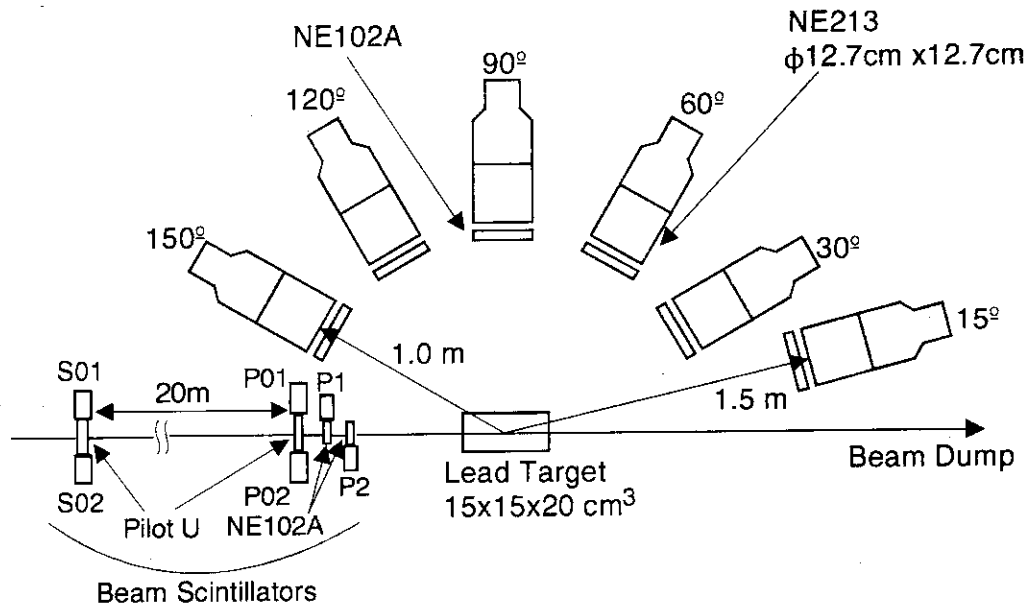
Fig. 1 Illustration of the experimental arrangement
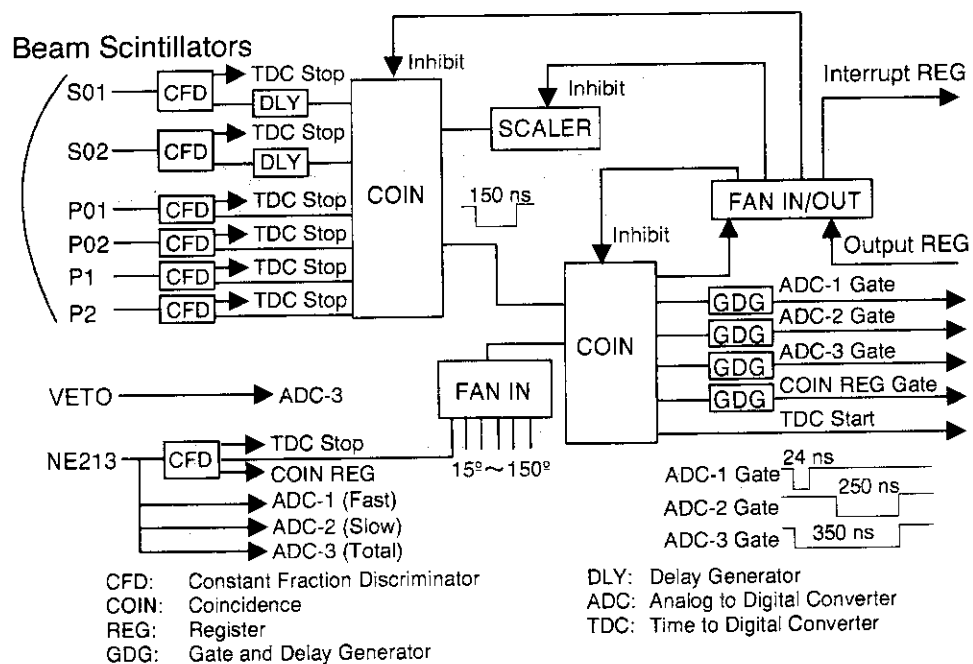
Fig. 2 Diagram of the electronic circuit used in the present experiment
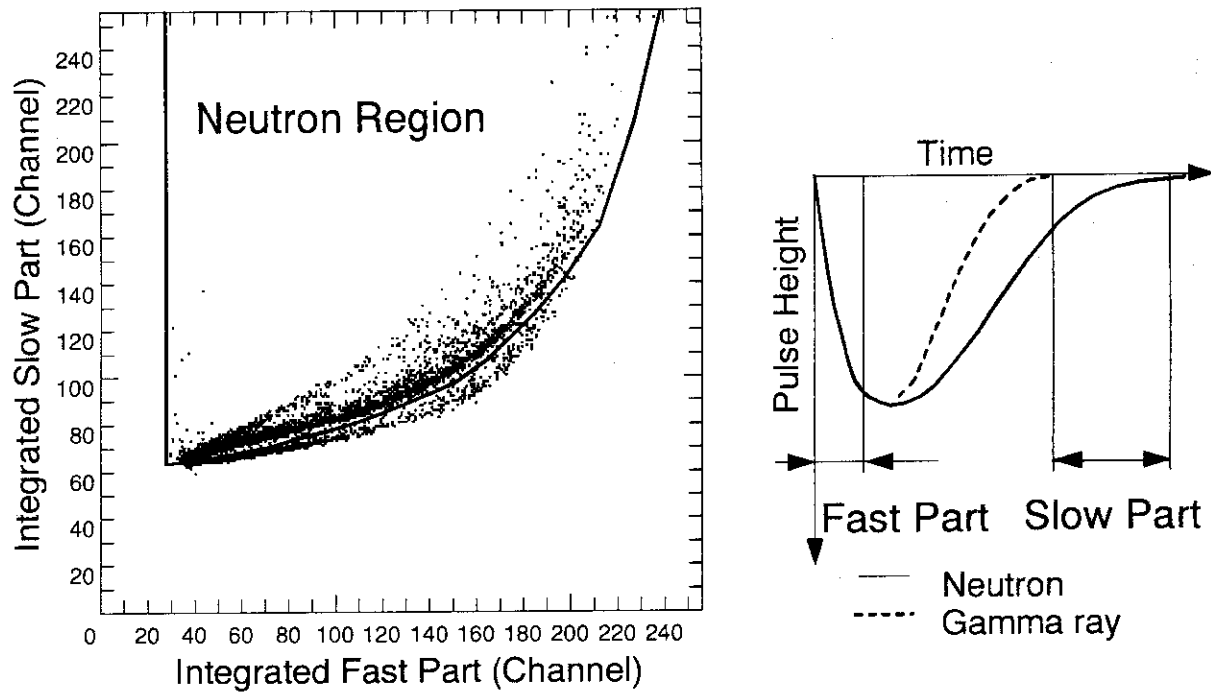
Fig. 3 Conceptual diagram of the two-gate integration method of neutron-gamma discrimination
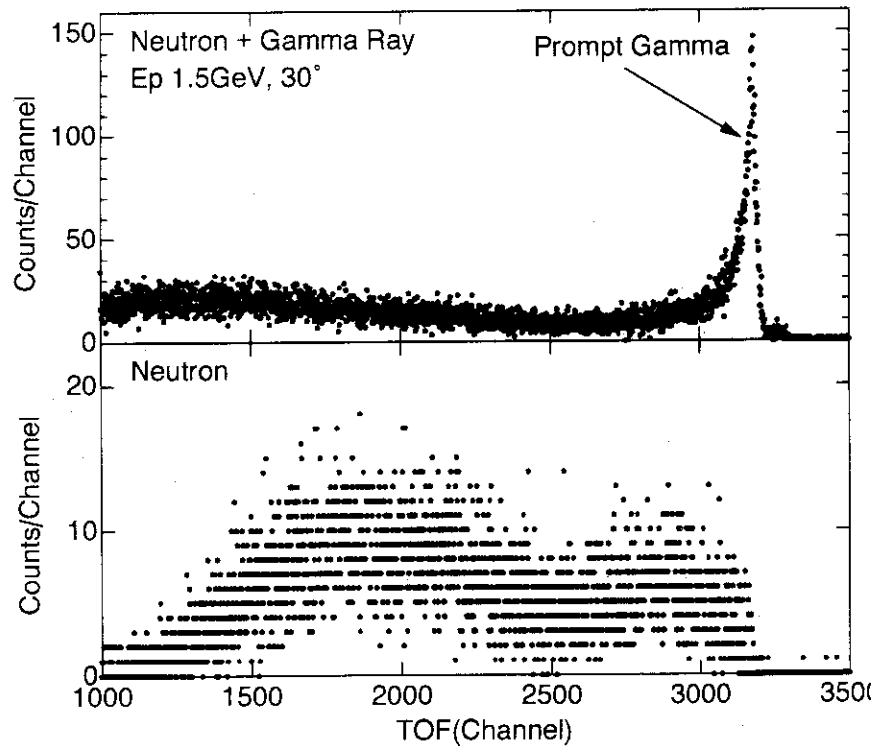
Fig. 4 Time-of-flight (TOF) spectrum measured at 30° bombarded with 1.5 GeV protons (top; for the neutron and the gamma ray, bottom; only for the neutron). Width of the TOF bin is 28 ps/channel.
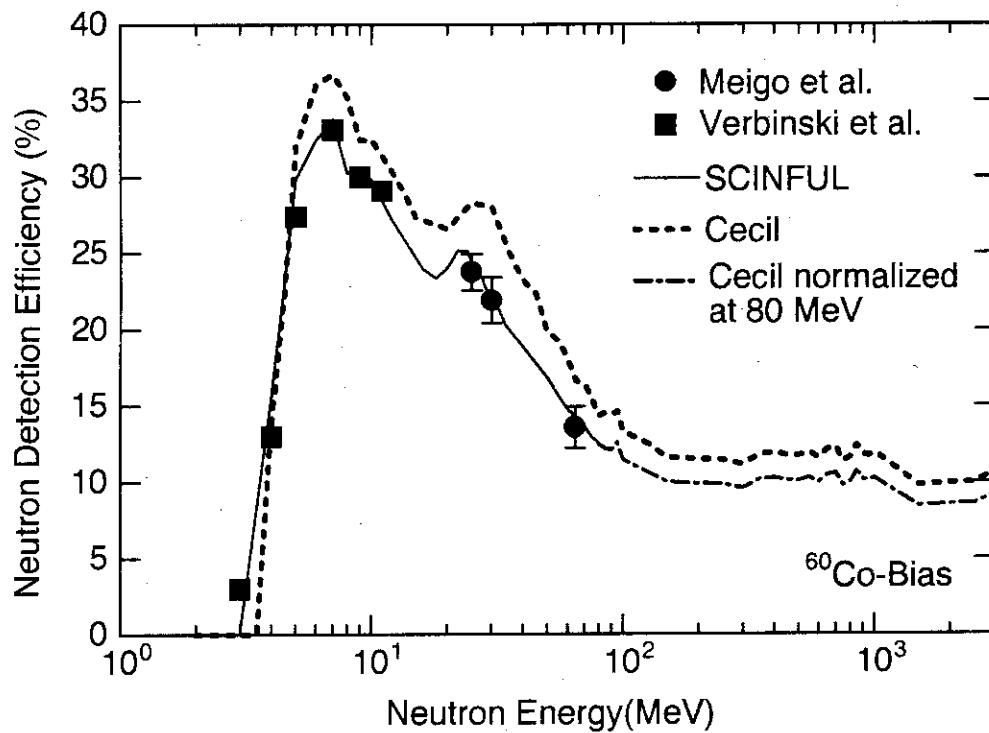
Fig. 5   Calculated and experimental neutron detection efficiency of the NE213 scintillator having the size of 12.7 cm in diameter and 12.7 cm in thickness
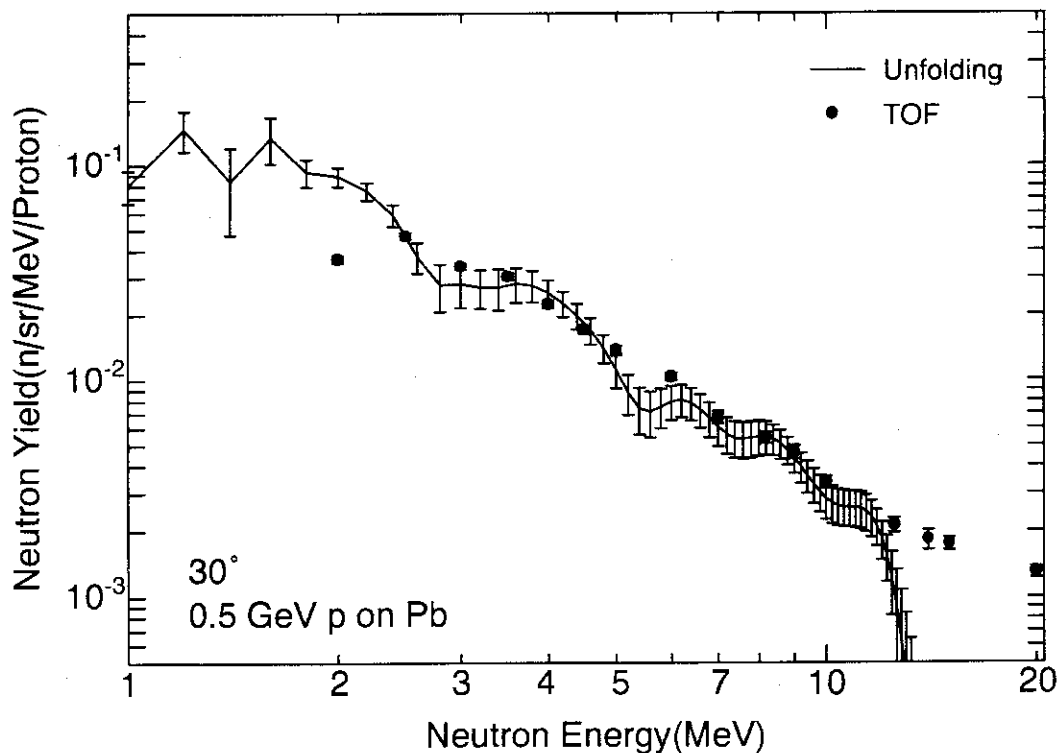

Fig. 6   Comparison of the neutron spectra at 30° obtained by TOF and unfolding methods for 0.5 GeV proton incident on thick lead target
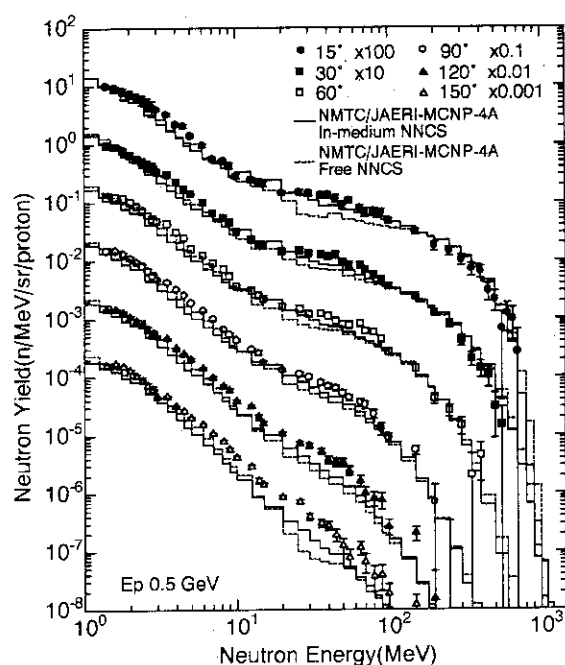
Fig. 7 Experimental and calculated neutron spectra in a lead target bombarded with 0.5 GeV protons. The marks are the experimental data. The lines indicate the calculated results of the code system.
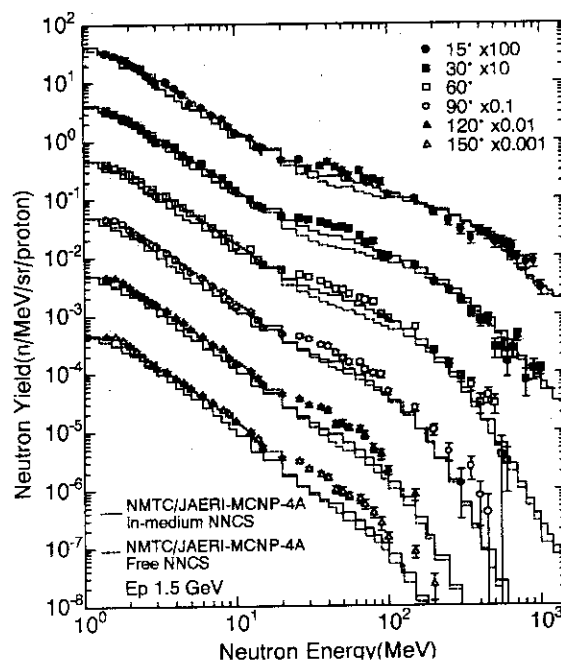
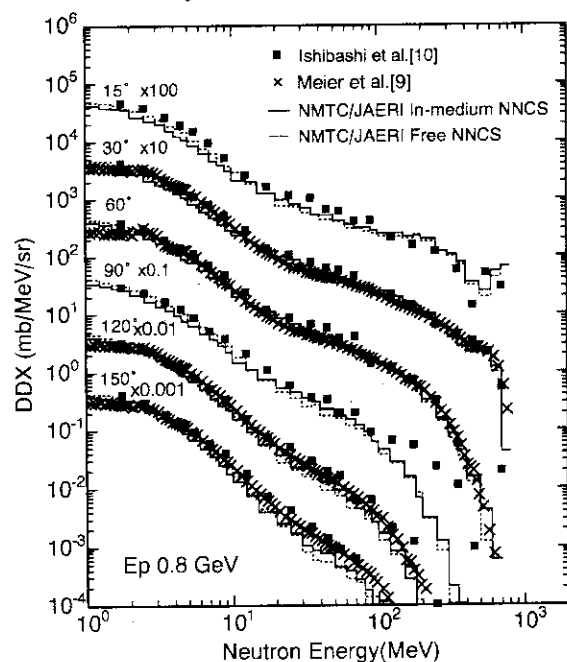Fig. 8 Same as for Fig. 7, except for proton energy, 1.5 GeV

Fig. 9 Double differential neutron production cross sections for 0.8 GeV protons. The solid marks indicate the experimental data/9,10/.
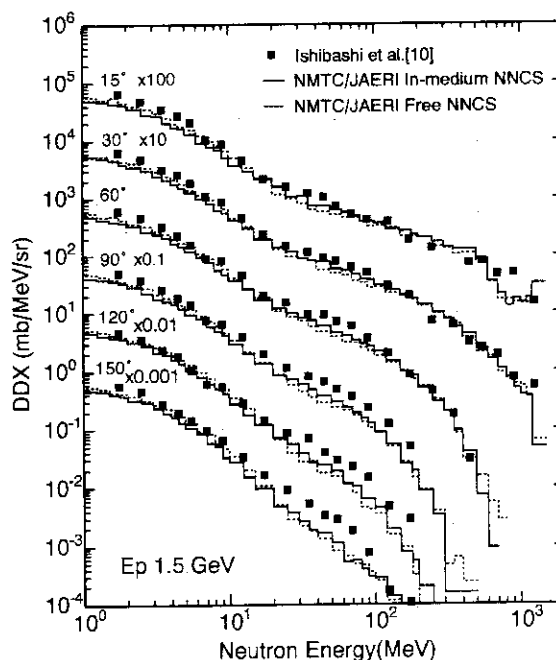
Fig. 10 Same as for Fig. 9, except for proton energy 1.5 GeV

The First Internet Symposium on Nuclear Data: Paper No. 25

3.25 Optical model calculation for the unresolved/resolved resonance region of Fe-56

KAWANO, Toshihiko
Energy Conversion Engineering, Kyushu University
6-1, Kasuga-kouen, Kasuga 816, Japan
Email : kawano@ence.kyushu-u.ac.jp

FRÖHNER, Fritz H.
Forschungszentrum Karlsruhe, Institut für Neutronenphysik und Reaktortechnik
Postfach 3640, 7500 Karlsruhe, Germany
Email : Fritz.Froehner@inr.fzk.de

We have studied optical model fits to total neutron cross sections of structural materials using the accurate data base for ^{56}Fe existing in the resolved and unresolved resonance region. Averages over resolved resonances were calculated with Lorentzian weighting in Reich-Moore (reduced R matrix) approximation. Starting from the best available optical potentials we found that adjustment of the real and imaginary well depths does not work satisfactorily with the conventional weak linear energy dependence of the well depths. If, however, the linear dependences are modified towards low energies, the average total cross sections can be fitted quite well, from the resolved resonance region up to 20 MeV and higher.

1 Introduction

A long-standing problem with optical model fits to total neutron cross sections of structural materials is the difficulty to reproduce the cross section minimum below about 2 MeV.

Figure 1 shows a comparison of the calculated total cross sections with some global optical potential parameters — Wilmore and Hodgson (WH)/1/, Becchetti and Greenlees (BG)/2/, Rapaport, Kulkarni, and Finlay (RKF)/3/, Walter and Guss (WG)/4/, and Varner et al. (CH89)/5/.

In this figure, IRK represents the evaluation by Vonach et al./6/, and GEEL is high-resolution Fe transmission data from Geel/7/ smoothed with a ± 5% energy window. A remarkable discrepancy between the evaluation and the calculation is seen below 3 MeV. This is not a typical characteristic of the global potential parameters only, since some specialized potential parameters adjusted to ^{56}Fe have the same problem too. The calculated cross sections with the potential parameters for iron derived by Arthur and Young/8/, Prince/9/, and Smith/10/ are shown in Fig.2.

We have studied the problem using the accurate data base for ^{56}Fe existing in the resolved and unresolved resonance region, namely high-resolution neutron transmission
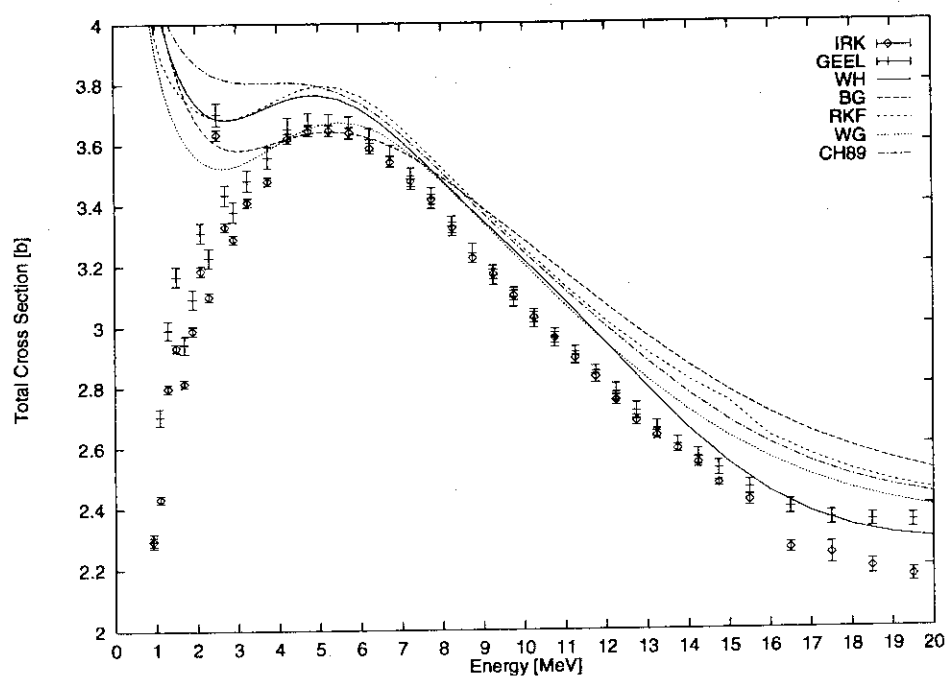
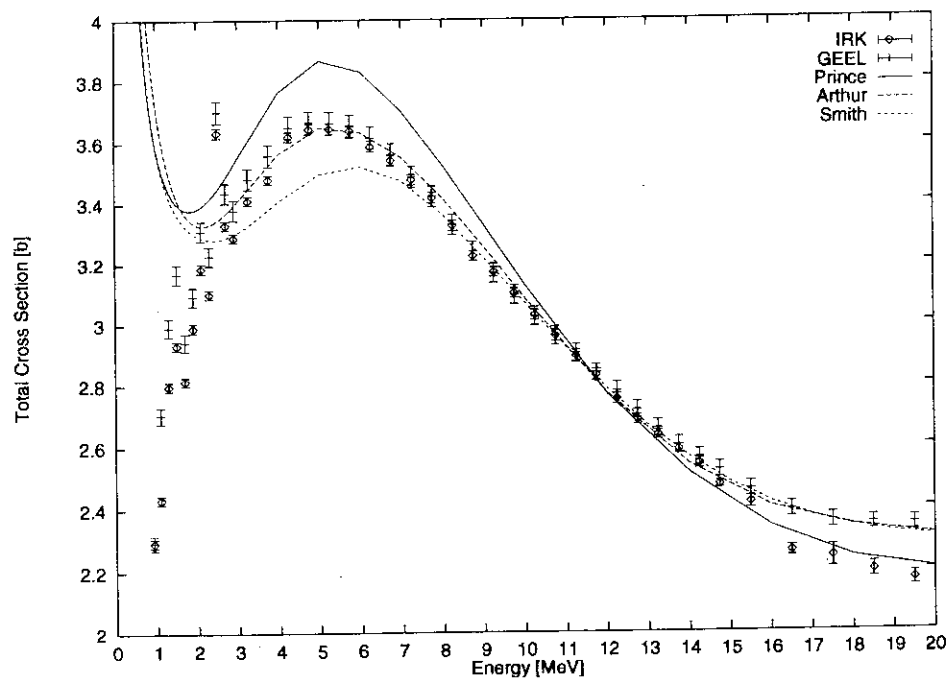Figure 1: calculated total cross sections with global set

Figure 2: calculated total cross sections with local set

measurements by ORNL/11/ and Geel/7/, resonance parameters by ORNL/11/ and Fröhner/12/.

The optical model gives energy averaged cross sections. In the resolved resonance region the averaged cross section can also be obtained from resonance parameters with Lorentzian weighting in Reich-Moore (reduced R matrix) approximation. At higher energies, where no resonance parameters are available but resonance structure persists, cross section averages in finite energy intervals can be compared with optical model calculations.

2 Data analysis

2.1 Unresolved region

Above 4 MeV the total cross section varies smoothly with neutron energy. The optical model is suitable for the evaluation of the cross section in this energy region, while below 4 MeV the cross section shows remarkable fluctuation, and the optical model gives an energy averaged cross section only. The energy averages were carried out with a $\pm$ 500 keV energy window and the result is shown in Fig.3. These averaged cross sections below 3 MeV are higher than similarly smoothed cross sections with $\pm$ 5% windows (50 keV at E_n=1 MeV), and they are also higher than the IRK evaluation.

The optical potential parameters were least-squares adjusted to fit the averaged total cross sections within their uncertainties. Note that we haven't paid attention to differential elastic scattering cross section data. The starting point of the parameter search is Rapaport's global set, (energies in MeV, lengths in fm)

$$
\begin{aligned}
V &= 52.57 - 0.316E & r_v &= 1.198 & a_v &= 0.663 \\
W_s &= 3.366 + 0.4E & r_w &= 1.295 & a_w &= 0.590
\end{aligned}
\tag{1}
$$

and the spin-orbit term is, $V_{so} = 6.2, r_{vso} = 1.01$ and $a_{vso} = 0.75$.

We employed a rather simple parametrization in order to avoid unnecessary complications. A volume type absorption term is ignored since the effect of the volume term can be replaced by the surface absorption term in this energy range.

We searched the above 6 parameters indicated by **boldface** with a computer program KALMAN/13/ and the optical model code ELIESE-3/14/. The results are,

$$
\begin{aligned}
V &= 45.37 - 0.316E & r_v &= 1.369 & a_v &= 0.318 \\
W_s &= 4.330 + 0.4E & r_w &= 1.483 & a_w &= 0.291
\end{aligned}
\tag{2}
$$

The calculated total cross sections are compared with the smoothed data in Fig.3.

As seen the calculation agrees with the data above 2 MeV, but it is still higher than the data below 2 MeV. It is difficult to reproduce the data both below and above 2 MeV at the same time with our parametrization. This would call for energy dependent geometrical parameters or a complicated energy dependence of the potential depths for the real and imaginary parts. In addition, the parameters do not guarantee to reproduce the angular distribution of the elastic scattering, because low energy data (below 4 MeV) require somewhat strange geometrical parameters — the radius parameters become large and the diffuseness parameters become small and they deviate too much from the global values. Only such unusual parameters insure the low total cross sections observed around 1 MeV.
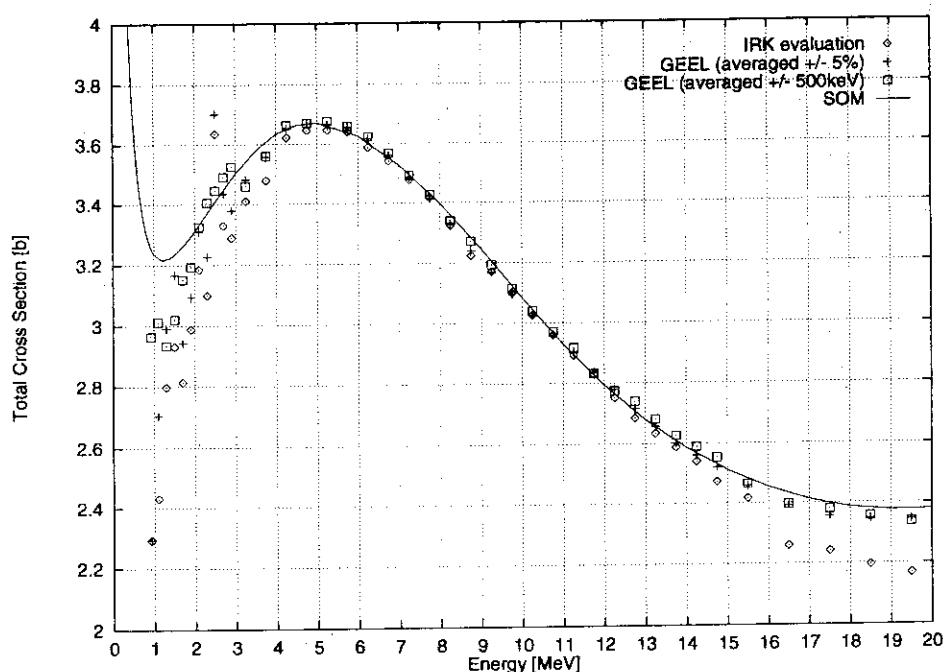
Figure 3: calculated total cross sections with the searched parameters

2.2 Resolved region

Precise resonance analyses with Reich-Moore reduced R matrix were made by Oak Ridge group/11/ and modified slightly by Fröhner/12/ for the ^{56}Fe total cross sections in the resonance region. These resonance parameters give an accurate representation of the data below the inelastic scattering threshold (850 keV).

The optical model gives cross sections averaged over resonances. The same average can be obtained in R matrix cross section representation when one replaces the neutron energy E in the R matrix by a complex energy $E + iI$ where $2I$ is the half width of the Lorentzian weight function. The I is taken to be 200 keV.

Averaged cross sections are calculated from the S matrix,

$$S = \frac{I(a)}{O(a)} \frac{1 - R(L^* - B)}{1 - R(L - B)} \tag{3}$$

where S is the scattering matrix, R the R matrix evaluated at the complex energy $E + iI$, a the channel radius, $I(r)$ the ingoing and $O(r)$ the outgoing radial wave function, L the logarithmic derivative of out-going wave function, and B the logarithmic derivative of the radial eigenfunctions (taken to be $= -\ell$, where ℓ is the orbital angular momentum).

The averaged total cross sections for each entrance channel (s-, p-, ... wave) are given by,

$$\sigma_T = \frac{2\pi}{k^2} g\{1 - \mathrm{Re}S\}, \tag{4}$$

where g is the spin factor, and k is the wave number, and they are shown in Fig.4.

Shape elastic scattering and reaction cross sections are also calculated from the S matrix. The averaged shape elastic scattering, and the reaction cross sections are given by

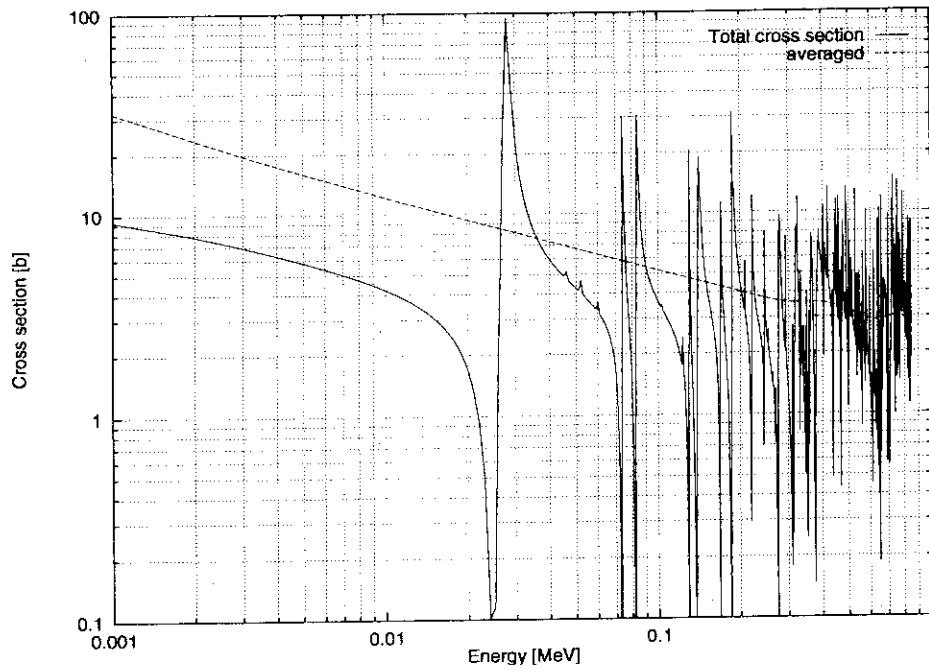$$\sigma_E = \frac{\pi}{k^2} g |1 - S|^2, \tag{5}$$

Figure 4: comparison of the total cross sections and the Lorentz-weighted averaged cross sections $E_n = 1 - 850$ keV

$$\sigma_R = \frac{\pi}{k^2} g \{1 - |S|^2\}. \tag{6}$$

The S matrix calculated with the optical model should be the same as the S matrix derived from the R matrix. We estimated the potential depths of the real/imaginary potential which give appropriate averaged elastic and non-elastic cross sections in the resonance region. The geometrical parameters and the spin-orbit interaction term are held constant and they are the same as the values obtained at the higher energies.

Parameter search was done with the optical model code CoH/13/, which searches the potential parameters not only for the angular distribution of elastic scattering but also for the total and the angle integrated scattering cross sections. The obtained real and imaginary potential depths are, $V = 44.61$ and $W_s = 0.1543 + 1.561E$.

These potential depths can be connected smoothly to the parameters obtained in the unresolved resonance region. The real depth is expressed by,

$$V = \begin{cases} 44.61 - 0.0329E^2 & E < 4.81 \text{ MeV} \\ 45.37 - 0.316E & \text{otherwise} \end{cases} \tag{7}$$

and the imaginary potential can be connected by a weighting function as follows.

$$\begin{aligned} W_{s1} &= 4.330 + 0.4E \\ W_{s2} &= 0.1543 + 1.561E \\ W_s &= W_{s1} f(E) + W_{s2}\{1 - f(E)\}, \end{aligned} \tag{8}$$

where $f(E)$ is the weighting function. A simple choice is $f(E) = \exp(-1/E)$, which assures smooth transition of W_{s1} and W_{s2} around $E = 1$ MeV.

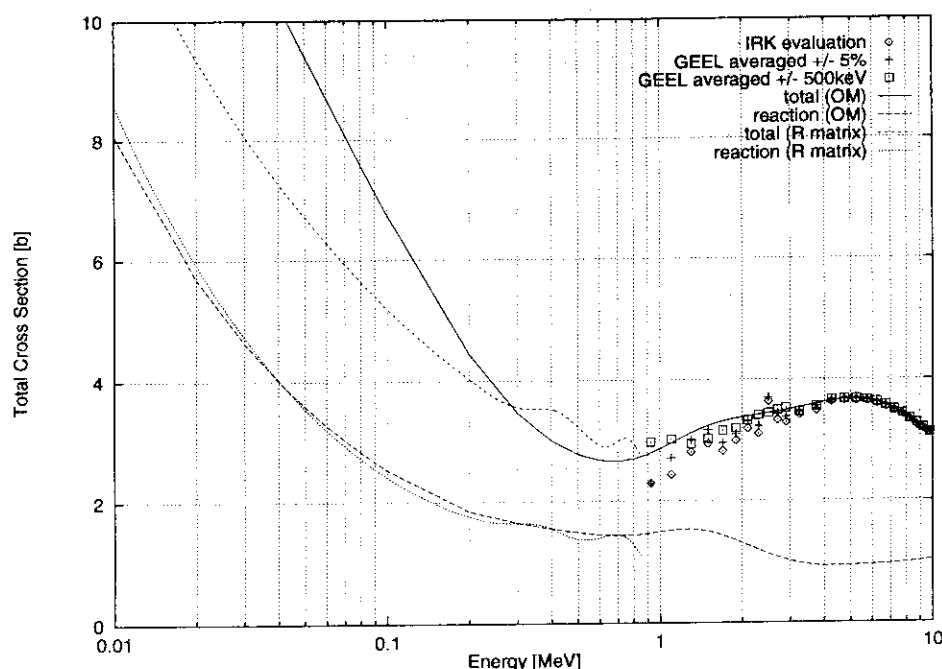The calculated cross sections are shown in Fig.5.

Figure 5: Comparison of the optical model calculation and smoothed cross sections in the resolved resonance region

3 Discussion

In the resolved resonance region the obtained absorption potential depth is much smaller than at higher energies, and it becomes very small (about 150 keV) when the neutron energy approaches zero. This is reasonable because at the neutron energy of 850 keV an inelastic scattering channel opens. This low-lying 2^+ state is assigned to a 1 phonon state which the spherical optical model cannot treat exactly. Therefore the strong excitation of this 2^+ state is regarded as a compound reaction.

At very low energies (less than 10 eV) the compound cross section, namely the radiative capture cross section, becomes large and the total cross section shows $1/v$ behavior. Above the $1/v$ region, the R matrix analysis implies that the averaged shape elastic scattering cross section is larger than the averaged compound formation cross section, as seen in Fig.5. This is a typical characteristic of ^{56}Fe. This nucleus is known as a *Scatterer* whose neutron capture cross section is quite small. This means, we should give small absorption cross sections in the optical model analysis of the ^{56}Fe below the inelastic scattering threshold.

Figure 6 shows a comparison of the calculated total/reaction cross sections with global optical potential parameters and resonance averaged cross sections.

As seen in this figure, the reaction cross sections calculated with the global set are larger than the resonance averaged cross section at the neutron energies below 3 MeV. Not only the global parameters but also localized parameters which are obtained from the ^{56}Fe data give large reaction cross sections below 3 MeV. For example, at 1 MeV Prince's parameters/9/ give 1.90 b, Arthur and Young's parameters/8/ 1.92 b, and Smith's parameters/10/ 2.17 b. This is the reason why the optical model fails to reproduce the total cross sections below several MeV for structural materials.

Konshin/15/ suggested that if a slightly larger real potential radius parameter is
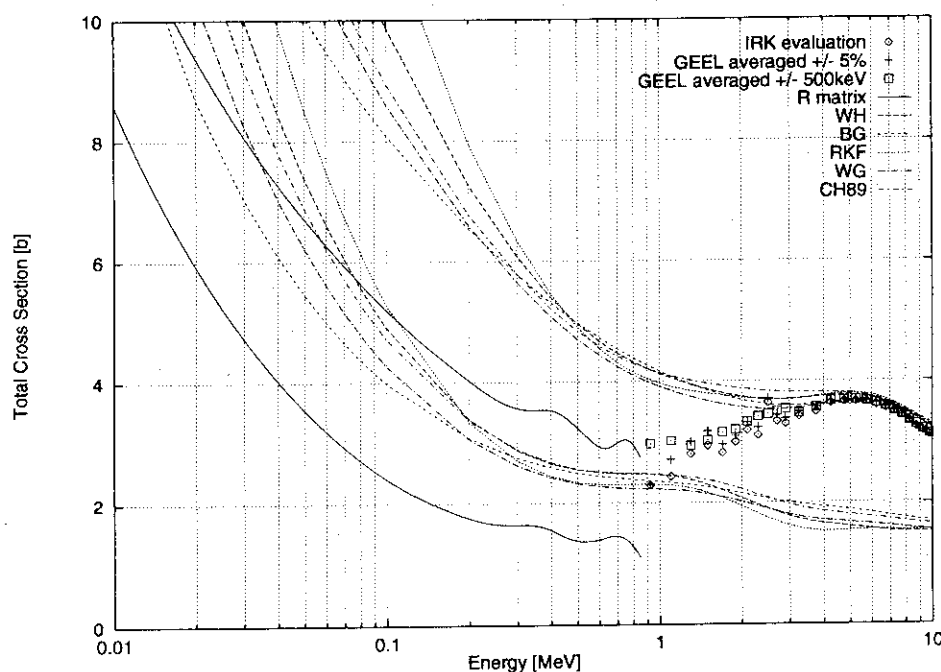
Figure 6: Comparison of the calculated total cross sections (upper curves) and reaction cross sections (lower curves) and the smoothed cross sections

given in the low energy region the discrepancy between the experimental data and the calculation becomes small. He derived an energy dependent real radius parameter, $r = 1.315 - 0.0167E$.

This can be understood from the S matrix properties at low energies. With the RKF global parameters/3/ we calculated S matrix elements at 2 MeV. Figure 7 shows their change when the real radius parameter is altered from 1.15 to 1.35 fm. When the radius parameter increases the elastic s-wave scattering increases, while the S matrix elements of the d-wave approaches 1. Since the d-wave dominates s- and p- waves at this energy, the change in the radius parameter results in a reduction of the elastic/reaction cross sections.

At the neutron energy of 1 MeV the sensitivity of the real radius parameter to the cross section becomes small as seen in Fig.8.

The total cross section does not change if the real radius parameter is varied. On the other hand, as seen in this figure, the imaginary diffuseness parameter has positive sensitivity to the total cross section because the volume integral per nucleon, J_w, is almost proportional to the imaginary diffuseness parameter, and the parameter is sensitive to the absorption cross section. The small imaginary diffuseness parameter ensures small absorption cross sections. The same effect is expected when one gives a small imaginary potential depth.

The complex potential from our study has small imaginary diffuseness ($a_w = 0.291$) and large real radius ($r_v = 1.369$). According to the previous discussion, these nonconventional values accomplish the desired reduction of the total cross section around 1 or 2 MeV.
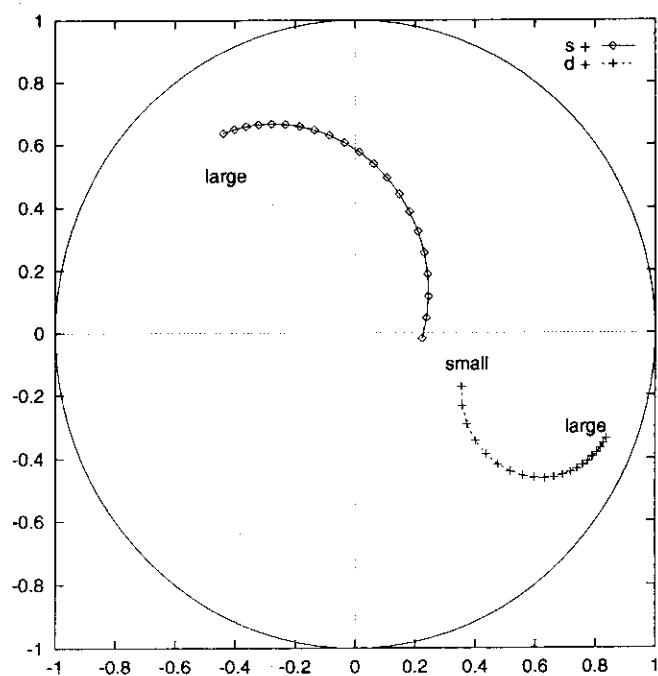
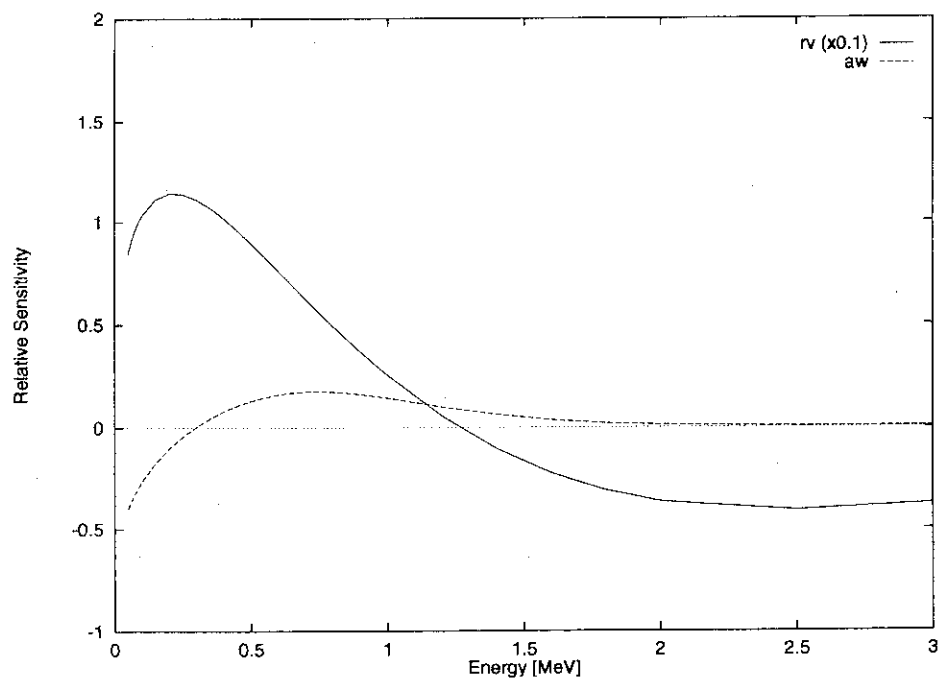Figure 7: Change of S matrix element on the complex plain when real radius parameter is varied from 1.15 to 1.35 fm

Figure 8: Relative sensitivity of the real radius parameter and imaginary diffuseness parameter

4 Conclusion

We derived an optical potential parameter set for ^{56}Fe from high-resolution total cross section data and resonance parameters, Eqs.(7) and (8) for $E < 20$ MeV, radius and diffuseness parameters as in Eq.(2). The average total cross sections can be fitted quite well with this parameter set, from the resolved resonance region up to 20 MeV. We showed that the discrepancy between the averaged total cross section and conventional optical model calculations comes from too large calculated absorption cross sections below 3 MeV. Small imaginary diffuseness parameter or small imaginary potential depth gives reasonable agreement with the data.

References

[1] D.Wilmore and P.E.Hodgson, *Nucl. Phys.*, **55**, 673 (1964)

[2] F.D.Becchetti and G.W.Greenlees, *Phys. Rev.*, **182**, 1190 (1969)

[3] J.Rapaport, V.Kulkarni, and R.W.Finlay, *Nucl. Phys.*, **A330**, 15 (1979)

[4] R.L.Walter and P.P.Guss, *Proc. Int. Conf. Nuclear Data for Basic and Applied Science*, Santa Fe, 1079 (1985)

[5] R.L.Varner *et al.*, *Phys. Rep.*, **201**, 57 (1991)

[6] V.Pronyaev, S.Tagesen, H.Vonach, and S.Badikov, *Physics Data*, **13-8** (1995)

[7] K.Berthold, C.Nazareth, G.Rohr, and H.Weigmann, *Proc. Int. Conf. Nuclear Data for Science and Technology*, Gatlinburg, 218 (1994)

[8] E.D.Arthur and P.G.Young, BNL-NCS-51245, 731 (1980)

[9] P.Prince, *Proc. Int. Conf. Nuclear Data for Science and Technology*, Antwerp, 574 (1982)

[10] A.B.Smith, ANL/NDM-136 (1995)

[11] C.M.Perey, F.G.Perey, J.A.Harvey, N.W.Hill and N.M.Larson, ORNL/TM-11742, (1990)

[12] F.H.Fröhner, *Proc. Int. Conf. Nuclear Data for Science and Technology*, Gatlinburg, 597 (1994)

[13] T.Kawano, unpublished

[14] S.Igarasi, JAERI-1224, (1972).

[15] C.A.Konshin, *Proc. Workshop on Computation and Analysis of Nuclear Data Relevant to Nuclear Energy and Safety*, Trieste, 775 (1992)

Appendix: Samples of WWW Pages of ISND-1

The First Internet Symposium on Nuclear Data

http://cracker.tokai.jaeri.go.jp/isnd/index.html
8 April 1996 - 15 July 1996

ISND Japanese Home Page

The First Announcement and Call for Papers

☐ Paper Registration Form

The Second Announcement

☐ How to make an HTML Paper for ISND
Complete your html paper and contact ISND secretariat before March 25.

Registration for Discussion

List of Papers submitted to ISND-1

General rules of ISND

Any comments and questions should be sent to ISND Secretariat.

The First Internet Symposium on Nuclear Data
Last modification; Monday, 01-Apr-96 10:44:28 JST

How to Make an HTML Paper for ISND

(1996/3/18 revised)

If you are not familiar with HTML (HyperText Markup Language), please read first the following document.

☐ A Beginner's Guide to HTML (NCSA)

General

HTML version
    It is better to use HTML 2.0, since some browsers do not support HTML 3.0.

Language
    The HTML paper should be written in ENGLISH.

Modification of the HTML Paper
    According to the discussion made during ISND, you may modify your HTML paper. However, it should be avoided that one submits an uncompleted paper, then correct it to a final one.

Format of HTML paper

(1) Heading part
    It should be in the following style:

```
<head>
<title>ISND-1 Paper </title>
</head>
Go to: <a href="http://133.53.24.51/isnd/paper_index.html">Paper Index</a> /
<a href="http://133.53.24.51/isnd/discussion/pNNN.html">Discussion panel</a>
<p>
<img src=".......  ">          <--- A photo of authors, if possible.
<center>
<h2> Title </h2>
 Authors name <br>
 Organization <br>
 Address <br>
 e-mail:         <br>
</center>
<hr>
Last modification: 1996/3/20       <-- date of last modification
<hr>
```

    The URL of your discussion panel will be informed later.

(2) Text part
    Text

    Tables
        If you use the <table> tag, then some browsers cannot display a proper table. It is better to use the <pre> tab.

    Equations
        In the case of complicated equation, it is recommend to use an inline image of a gif file.

List of Papers submitted to ISND-1

ISND-1-p001
Analysis of proton-induced fragment production cross sections by the Quantum Molecular Dynamics plus Statistical Decay Model
Satoshi Chiba, Osamu Iwamoto, Tokio Fukahori, Koji Niita, Toshiki Maruyama, Tomoyuki Maruyama and Akira Iwamoto

| Abstract | Paper | Discussion |

ISND-1-p002
Evaluation of cross sections and calculation of kerma factors for neutrons up to 80 MeV on ^{12}C
Masahide Harada, Yukinobu Watanabe, and Satoshi Chiba

| Abstract | Paper | Discussion |

ISND-1-p003
Effect of U-238 and U-235 Cross Sections on Nuclear Characteristics of Fast and Thermal Reactors
Hiroshi Akie, Hideki Takano and Kunio Kaneko

| Abstract | Paper | Discussion |

ISND-1-p004
Evaluation of the 2039 keV level property in ^{124}Te
Jun-ichi Katakura

| Abstract | Paper | Discussion |

ISND-1-p005
Measurement of Thermal Neutron Cross Section for $^{241}Am(n, f)$ Reaction
K. Kobayashi, S. Yamamoto, M. Miyoshi, I. Kimura, I. Kanno, N. Shinohara, and Y. Fujita

| Abstract | Paper | Discussion |

ISND-1-p006
Compositional Change of Some First Wall Materials by Considering Multiple Step Nuclear Reaction
Tetsuji Noda, Misako Utsumi and Mitsutane Fujita

| Abstract | Paper | Discussion |

ISND-1-p007

ISND-1-p001

Analysis of proton-induced fragment production cross sections
by the Quantum Molecular Dynamics plus Statistical Decay Model

Satoshi Chiba(*), Osamu Iwamoto, Tokio Fukahori, Koji Niita,
Toshiki Maruyama, Tomoyuki Maruyama and Akira Iwamoto

Japan Atomic Energy Research Institute,
Tokai-mura, Naka-gun, Ibaraki-ken 319-11, Japan

(*)E-mail: *chiba@cracker.tokai.jaeri.go.jp*

The production cross sections of various fragments from proton-induced reactions
on ^{56}Fe and ^{27}Al have been analyzed by the Quantum Molecular Dynamics (QMD) plus
Statistical Decay Model (SDM). It was found that the mass and charge distributions
calculated with and without the statistical decay have very different shapes.
These results also depend strongly on the impact parameter, showing an importance
of the dynamical treatment as realized by the QMD approach. The calculated results
were compared with experimental data in the energy region from 50 MeV to 5 GeV.
The QMD+SDM calculation could reproduce the production cross sections of the light
clusters and intermediate-mass to heavy fragments in a good accuracy. The
production cross section of ^{7}Be was, however, underpredicted by approximately 2
orders of magnitude, showing the necessity of another reaction mechanism not taken
into account in the present model.

Next List Previous

Next: Introduction

Go to: Program List / Discussion Panel

1 Advanced Science Research Center, Japan Atomic Energy Research Institute,
Tokai-mura, Naka-gun, Ibaraki-ken 319-11, Japan
2 Nuclear Data Center, Japan Atomic Energy Research Institute,
Tokai-mura, Naka-gun, Ibaraki-ken 319-11, Japan
3 Research Organization for Information Science and Technology
Tokai-mura, Naka-gun, Ibaraki-ken 319-11, Japan

Analysis of proton-induced fragment production cross sections by the Quantum Molecular Dynamics plus Statistical Decay Model

Satoshi Chiba (1,2) , Osamu Iwamoto (2) , Tokio Fukahori (1,2) , Koji Niita (1,3) ,
Toshiki Maruyama (1) , Tomoyuki Maruyama (1) and Akira Iwamoto (1)

Number of Visitors to this Page;

Last modification: 1996-Apr-18

Abstract:

The production cross sections of various fragments from proton-induced reactions on ^{56} Fe and ^{27} Al have been analyzed by the Quantum Molecular Dynamics (QMD) plus Statistical Decay Model (SDM). It was found that the mass and charge distributions calculated with and without the statistical decay have very different shapes. These results also depend strongly on the impact parameter, showing an importance of the dynamical treatment as realized by the QMD approach. The calculated results were compared with experimental data in the energy region from 50 MeV to 5 GeV. The QMD+SDM calculation could reproduce the production cross sections of the light clusters and intermediate-mass to heavy fragments in a good accuracy. The production cross section of ^{7} Be was, however, underpredicted by approximately 2 orders of magnitude, showing the necessity of another reaction mechanism not taken into account in the present model.

24. 10. -i, 02. 70. Ns, 25. 40. -h

ISND-1 Discussion Panel for p001

Analysis of proton-induced fragment production cross sections
by the Quantum Molecular Dynamics plus Statistical Decay Model

Satoshi Chiba, Osamu Iwamoto, Tokio Fukahori, Koji Niita,
Toshiki Maruyama, Tomoyuki Maruyama and Akira Iwamoto

Japan Atomic Energy Research Institute,
Tokai-mura, Naka-gun, Ibaraki-ken 319-11, Japan

Japanese Home Page / English Home Page
List of Papers submitted to ISND-1

For discussion send e-mail to isnd-p001@cracker.tokai.jaeri.go.jp.

General rules

How to access;

- ☐ Papers can be seen by any World Wide Web browsers. I The abstracts and papers are linked from a paper list (List of Papers submitted to ISND-1). Anyone can access them by clicking [Abstract] or [Paper] .
- ☐ Discussions are done in discussion panels. They can be accessed by clicking [Discussion] ·
- ☐ Abstracts, papers and discussion panels are open to everybody.

How to access the discussion panel;

1. If you want to post questions or comments, you should register first. The registration can be done by the "Registration for Discussion" in the ISND home page. The registered names are listed in a proceedings of ISND. The registration is needed only once.
2. Questions and comments should be sent to each e-mail address of the paper. This e-mail addresses are displayed in each abstract, paper and discussion panel.
3. The questions and comments will be displayed in the discussion panel and also forwarded to the author of the paper.
4. The author sends his answers to the discussion panel, then his answer will be displayed on the discussion panel.

General attentions;

To authors

- ☐ Authors should send their answers as soon as possible.
- ☐ Authors may modify their paper at any time.
- ☐ Copyrights of abstracts and papers are held by original authors.
- ☐ By submitting abstracts and papers to the ISND, there are possibility of being copied by anybody without explicit permission. The organizers of ISND are in no way responsible for the further use of the submitted materials.
- ☐ The proceedings will be published as one of "JAERI-Conf" reports which is a report published by the Japan Atomic Energy Research Institute. Authors are requested to submit manuscripts to the symposium secretariat before June 28 and to transmit the copyright to Japan Atomic Energy Research Institute.

To participants

- ☐ The authors reserve all copyrights of abstracts and papers which are made open in the ISND.
- ☐ Please send questions and comments for papers above by e-mail to the address of each paper as described.

ISND-1 Registration Form for Discussion Panel

Access to all of our symposium is free of charge. We would like to get a good count of our participants though, so please take a few minutes to tell us your e-mail address and some information for registration.

We'll add your e-mail address into a registration list and permit you to join to discussion.

What's your E-mail Address?

NOTE: In order to receive authorization, your E-Mail Address MUST be reachable. This must be your COMPLETE INTERNET e-mail address. No embedded spaces or commas.

See ISND home page for the detailed information.

We'd also like to have a bit more information, so we can keep in touch about proceedings and news, but it's not required. If you fill out the following form, your name will be appear on a participant list of the ISND proceedings:

First Name:
Middle Name:
Last Name:
Affiliation 1:
Affiliation 2:
Address 1:
Address 2:
City:
State/Province:
Country:
Zip/International Postal Code:

Phone Number:
FAX Number:

The First Internet Symposium on Nuclear Data, April 8 – June 15, 1996
http://cracker.tokai.jaeri.go.jp/isnd/index.html
e-mail: isnd@cracker.tokai.jaeri.go.jp